Magnetic resonance of a single electron spin and its magnetic environment by photon counting

Léo Balembois

Léo Balembois. Magnetic resonance of a single electron spin and its magnetic environment by photon counting. Quantum Physics [quant-ph]. Université Paris-Saclay, 2023. English. NNT : 2023UPASP056 . tel-04165482

HAL Id: tel-04165482
https://theses.hal.science/tel-04165482v1

Submitted on 19 Jul 2023

Magnetic resonance of a single electron spin and its magnetic environment by photon counting

Résonance magnétique d'un spin électronique unique et de son environnement magnétique par comptage de photons

Thèse de doctorat de l'université Paris-Saclay

École doctorale n° 564, Physique en Ile-de-France (EDPIF)
Spécialité de doctorat : Physique
Graduate School : physique, Référent : Faculté des sciences d'Orsay

Thèse préparée dans l'unité de recherche **SPEC** (Université Paris-Saclay, CEA,CNRS), sous la direction de **Daniel ESTEVE**, directeur de recherche au CEA-Saclay, le co-encadrement de **Emmanuel FLURIN**, chargé de recherche, CEA Saclay et le co-encadrement de **Patrice BERTET** directeur de recherche, CEA Saclay

Thèse soutenue à Paris-Saclay, le 12 juin 2023, par

Léo BALEMBOIS

Composition du jury

Membres du jury avec voix délibérative

Eleni DIAMANTI Directrice de recherche, Sorbonne Université	Présidente
Vincent JACQUES Directeur de recherche, Université de Montpellier	Rapporteur & Examinateur
Ioan POP Professeur, Karlsruher Institut für Technologie	Rapporteur & Examinateur
Alain ASPECT Professeur à l'Institut d'Optique, Université Paris-Saclay	Examinateur
Mazyar MIRRAHI Directeur de recherche, INRIA	Examinateur
Jean-François ROCH Professeur, ENS Paris-Saclay	Examinateur

THESE DE DOCTORAT

NNT : 2023UPASP056

À Elise, à mes parents

Remerciements

Je tiens tout d'abord à remercier les membres de mon jury, Ioan, Vincent, Eleni, Mazyar, Jean-François et Alain qui ont accepté de prendre le temps de lire et d'évaluer mon travail.

Mes remerciements vont ensuite aux personnes qui ont travaillé avec moi tout au long de ces presque quatre ans de thèse. Merci en premier lieu à mes encadrants qui m'ont soutenu et accompagné durant cette période. Merci Emmanuel de m'avoir lancé en 2019 sur ce projet ambitieux de détection de photon micro-onde. La route a été (un peu) plus longue que prévue, mais on a fini par aboutir, et cela tient largement à ton enthousiasme et ton optimisme. Merci Patrice de m'avoir guidé à travers les expériences de détection de spin une fois que le détecteur a été opérationnel. Ta compréhension profonde de la physique et ton sens de la pédagogie m'ont fait progresser à pas de géant dans cet univers de cristaux glacés. Merci Denis de m'avoir aidé à rationaliser mes processus de fabrication à un moment où je commençais à diverger, ton aide a été incroyablement précieuse. Enfin, merci à Daniel pour toute l'aide que tu m'as apportée dans la rédaction de ce manuscrit, tes conseils et tes relectures l'ont grandement amélioré.

Je tiens ensuite à remercier les doctorants qui ont travaillé sur les expériences avant mon arrivée et qui m'ont transmis leur expertise. Merci Emanuele pour tous tes conseils sur les bonnes pratiques en salle blanche. Merci Marianne, pour toutes tes explications sur les instruments de mesure, les logiciels d'acquisition de données et plus généralement pour tous les conseils que tu m'as apportés.

Ce travail a avant tout été collectif, et je remercie grandement Zhiren et Eric qui ont travaillé sur la fabrication des échantillons de spin. Nous avons formé une belle équipe, et cela a été un plaisir de vous fournir des détecteurs de photons micro-ondes et de mesurer avec vous. Mention spéciale à Eric, mon co-thésard et co-bureau, merci pour tous les fous rire partagés dans ce bureau du fond du couloir, et pour toutes ces discussions passionnantes sur des sujets plus ou moins sérieux. Merci également aux plus jeunes doctorants, Louis, Alexandre et Jaime, avec qui j'ai pu travailler avant mon départ. Bonne chance avec l'expérience et je vous souhaite le meilleur pour la suite.

Comme pour tout travail de recherche, nous avons eu besoin de support technique et j'adresse un grand merci à Pascal pour toute l'aide apportée sur le montage des pièces mécaniques. Merci à Dominique, Jean-Claude et Vincent de l'atelier mécanique du SPEC pour la conception des pièces et (parfois) pour les réparations faites sur mon vélo. Merci également à Pief et Sébastien, mes deux anges gardiens en salle blanche, vous formez un duo de choc pour guider le jeune thésard novice (et un peu maladroit).

Plus généralement, merci à tout le groupe Quatronique de m'avoir accueilli et de m'avoir fait découvrir le monde de la recherche. Merci Hélène, Philippe, Marcelo, Hugues, Patrick et Christian pour votre sympathie et pour toutes les discussions intéressantes autour d'un café ou d'une mousse au chocolat de Mélissa. Merci aux doctorants et post-doctorants du groupe, Brian, Alexander, Nicolas, Joan, Anil, Boris et Yutian avec qui j'ai pu passer de bons moments.

Enfin, merci à la direction du SPEC d'organiser tout ce petit monde et d'avoir su nous permettre de continuer à travailler dans de bonnes conditions malgré les difficultés liées aux divers confinements et couvre-feux. Un grand merci également à François Ladieu, le responsable des thèses au SPEC, pour ta qualité d'écoute, ta vision philosophique de la vie et le support que tu apportes aux doctorants du SPEC.

En dehors du laboratoire, je tiens à remercier mes proches qui m'ont apporté un soutien indéfectible pendant cette thèse. Merci à mes parents et à mon frère de m'avoir écouté quand le moral était un peu bas et d'avoir su me faire prendre du recul et me remettre en selle. Enfin, merci à Elise d'avoir partagé cette aventure avec moi, la vie est plus douce à tes côtés, et ça m'a permis d'arriver au bout de ce long périple.

Contents

Useful physical constants

Constants in SI units [1] :

- vacuum magnetic permeability, $\mu_0 = 4\pi \times 10^{-7}$ H/m
- Planck constant, $h = 6.63 \times 10^{-34}$ Js
- reduced Planck constant, $\hbar = h/2\pi = 1.05 \times 10^{-34}$ Js
- Bohr magneton, $\mu_B = 9.274 \times 10^{-24}$ J/T, $\mu_B/h = 13.996$ GHz/T
- nuclear magneton, $\mu_N = 5.051 \times 10^{-27}$ J/T, $\mu_N/h = 7.622$ MHz/T
- Boltzmann constant, $k_B = 1.38 \times 10^{-23}$ J/K

---

[1] Values from NIST (https://physics.nist.gov/cuu/Constants/index.html)

List of abbreviations

- EPR: electron paramagnetic resonance
- ESR: electron spin resonance
- FID: free induction decay
- FWHM: full-width-at-half-maximum
- HEMT: high electron mobility transitor
- HWHM: half-width-at-half-maximum
- ID: instantaneous diffusion
- JTWPA: Josephson traveling-wave parametric amplifier
- LO: local oscillator
- PCB: printed circuit board
- ppb: part per billion
- REI: rare-earth ion
- rms: root-mean-square
- SEM: scanning electron microscope
- SMPD: Single microwave photon detector
- SNR: signal to noise ratio
- VNA: vector network analyzer

Chapter 1

Résumé détaillé

1.1 Contexte général de la résonance paramagnétique électronique

La résonance paramagnétique électronique (RPE) est une technique qui permet d'étudier la structure et le comportement des substances contenant des électrons non appariés. Lorsqu'un champ magnétique statique est appliqué, la dégénérescence des niveaux de spin des électrons non appariés est levée et le spin électronique va précesser autour du champ magnétique à la fréquence de Larmor. Cette fréquence est déterminée par le facteur (ou le tenseur dans les solides) gyromagnétique de l'électron qui relie son moment magnétique à son moment angulaire. La prédiction du rapport gyromagnétique de l'électron libre par la théorie quantique des champs est une des grandes réussites de la physique du XXème siècle. L'accord entre la théorie et l'expérience atteint une précision de 12 chiffres significatifs. Selon le "National Institute of Standards and Technology" (NIST), la valeur du facteur gyromagnétique de l'électron libre est de 28,0249514242(85) $\mathrm{GHz} \cdot \mathrm{T}^{-1}$.

Par conséquent, en présence d'un champ magnétique statique, les électrons non appariés réagissent de manière résonnante au rayonnement électromagnétique. Compte tenu de la valeur du facteur gyromagnétique de l'électron libre, les fréquences de résonance se situent généralement dans la gamme des micro-ondes pour des champs magnétiques modérés. Lorsque l'échantillon est exposé à un champ électromagnétique de la bonne fréquence, les électrons non appariés peuvent en absorber l'énergie, ce qui entraîne un phénomène de résonance qui peut être sondé expérimentalement à l'aide de différentes techniques. Ce processus d'absorption est à la base de la RPE, qui permet aux scientifiques d'obtenir des informations précieuses sur les propriétés des impuretés paramagnétiques et de leur environnement [SJ01b].

Il existe deux techniques principales de spectroscopie RPE : à ondes continues et à ondes pulsées. Dans la spectroscopie RPE à onde continue, un signal micro-ondes continu irradie l'échantillon et son coefficient de transmission/réflexion est analysé. Cette méthode est polyvalente mais présente des limites en termes de résolution spectrale et temporelle. La RPE pulsée, que nous utiliserons dans cette thèse, consiste à exciter l'ensemble des spins par de courtes impulsions électromagnétiques résonnantes. L'information sur les spins est contenue dans le signal qu'ils réémettent après avoir été excités [SJ01b]. De nombreuses séquences d'impulsions ont été mises au point pour répondre à diverses questions.

Parmis elles, la détection inductive (ID-ESR) est la méthode la plus répandue pour réaliser des spectroscopies RPE [Rab+38; Blo46; PTP46]. Dans cette approche, l'échantillon contenant les spins est placé à l'intérieur d'un résonateur micro-ondes, accordé à une fréquence spécifique ω_0. Des impulsions résonnantes sont appliquées pour créer d'abord une magnétisation transverse transitoire, puis pour induire la formation d'un signal micro-ondes pulsé, notamment un écho de spin. Les propriétés caractéristiques de l'ensemble de spin

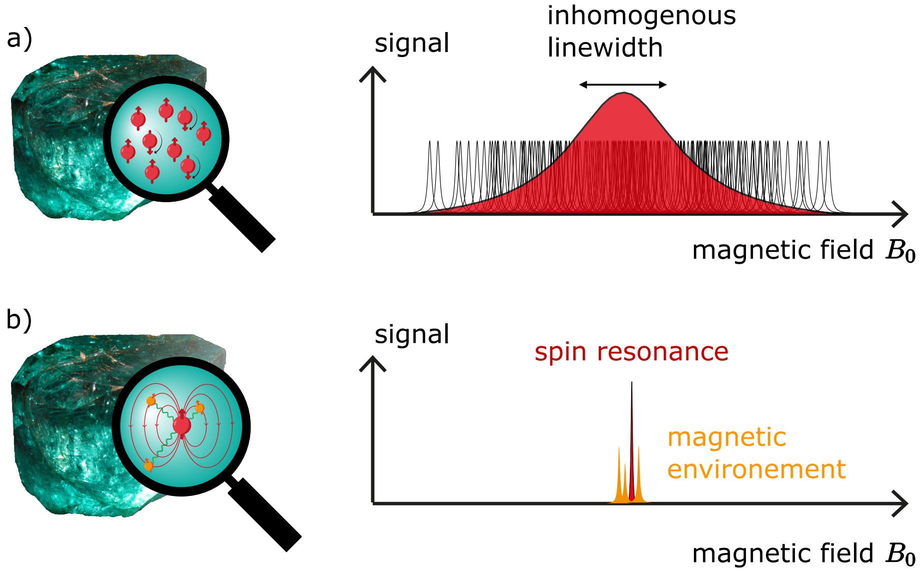

Figure 1.1: Illustration du signal fourni par un ensemble d'impuretés paramagnétiques contenues dans un cristal en fonction du champ magnétique statique B_0. L'environnement électromagnétique propre à chaque spin illustré en (b) provoque une dispersion inhomogène des fréquences de résonance. Les mesures d'ensemble ne tiennent pas compte de ces caractéristiques locales.

peuvent être extraites à partir de la phase et de l'amplitude de cet écho.

Cette technique permet aux chercheurs de déterminer les propriétés essentielles des spins et de leur environnement, avec des applications dans divers domaines tels que la biologie [Yos+96], la biochimie [Pol06] et les sciences des solides [Sli55].

En termes de sensibilité de détection, les spectromètres utilisant la ID-ESR sont confrontés à des limitations strictes en raison du faible couplage entre les spins et le champ magnétique micro-ondes appliqué. En une seconde de temps d'intégration, les spectromètres actuels ne peuvent détecter que de grands ensembles de spins contenant environ 10^9 spins [Abh+22], ce qui rend la caractérisation des propriétés locales très difficile. A titre d'exemple, l'élargissement inhomogène de la fréquence est un problème courant en spectroscopie RPE, où les facteurs gyromagnétiques des spins individuels varient en raison de leurs différents environnements locaux (voir Figure 1.1). Il en résulte une distribution des fréquences de résonance, ce qui fait qu'il est difficile pour les spectromètres commerciaux de tenir compte de toutes les interactions locales. Au lieu de cela, ils ont tendance à donner une moyenne de l'effet global de l'élargissement inhomogène, ce qui limite leur capacité à fournir des informations détaillées sur les propriétés locales.

De nombreuses méthodes ont été mises au point pour améliorer la sensibilité de la détection par RPE. L'une d'entre elles consiste à tirer parti de la charge de l'électron pour se coupler au champ électrique, ce qui permet d'obtenir de forts couplages spin-photon [Xia+04]. Ce concept a été mis en œuvre dans des matériaux semi-conducteurs en utilisant des architectures de transistors. Cette spécificité limite son application. Une autre technique consiste à exploiter les impuretés qui possèdent des transitions optiques, comme les célèbres centres NV du diamant ou les ions erbium [Riz+22]. Cette détection optique de la résonance de spin électronique a même permis aux physiciens d'atteindre la détection d'un spin unique [Gru+97]. Bien que cette méthode soit limitée aux ions présentant des transitions optiques appropriées, elle a donné lieu à un nombre important d'applications, notamment pour la magnétométrie à haute résolution spatiale.

Le groupe Quantronics s'est inséré dans cet effort de recherche en proposant d'utiliser l'électrodynamique quantique des circuits (cQED) [HR06; Bla+21] pour obtenir une RPE de haute sensibilité. La cQED utilise des circuits électriques bidimensionnels refroidis à une température de l'ordre du millikelvin. Dans ces conditions, il est possible de produire des micro-résonateurs supraconducteurs à facteur de qualité élevé qui génèrent des champs magnétiques localisés intenses. Un couplage spin-photon record de 3 kHz [Ran+20] a été obtenu par ce bias, à comparer à la force de couplage inférieure au Hz dans les cavités résonantes conventionnelles.

Un faible volume de mode améliore également le taux d'émission spontanée de photons micro-ondes par les spins via l'effet Purcell [Bie+16]. Les temps d'acquisition son par conséquent réduit ce qui améliore la sensibilité. Par ailleurs, le traitement du signal est effectué à l'aide d'amplificateurs paramétriques Josephson (JPA), qui nous permettent d'amplifier les signaux micro-ondes avec le bruit minimal imposé par la mécanique quantique. En outre, le fonctionnement à des températures extrêmement basses (10-20 mK) permet une grande polarisation du spin, ce qui augmente les signaux.

La combinaison de ces avantages a permis au groupe Quantronics d'atteindre une sensibilité de détection de 12 spin/$\sqrt{\mathrm{Hz}}$ en 2020 pour la spectroscopie ID-ESR en utilisant une plateforme d'ions bismuth intégrés dans un cristal de silicium [Ran+20]. Cependant, malgré un progrès de cinq ordres de grandeur par rapport à l'état de l'art, le régime de spin unique reste hors de portée. Les méthodes de détection inductive sont en effet confrontées à un problème de bruit intrinsèque. L'information de l'ensemble de spin est contenue dans les quadratures du champ électromagnétique de l'écho de spin. Comme ces quadratures sont mesurées directement, le bruit minimal associé à leur détection correspond aux fluctuations du vide dans la largeur de bande de détection. C'est propriété fondamentale de la mécanique quantique. Même en supposant qu'aucun bruit n'est ajouté par les amplificateurs, ce bruit du vide ne peut être réduit. Dans ce contexte, la détection d'un spin unique par le photon micro-onde qu'il émet pendant sa relaxation correspond à une petite augmentation transitoire du niveau de bruit (voir Figure 2.2a). Le rapport signal/bruit de l'ID-ESR est donc fondamentalement limité, et la détection d'un spin unique nécessite une nouvelle stratégie.

Afin de relever ce défi, notre groupe a proposé une nouvelle méthode de RPE basée sur la détection de la fluorescence (FD-ESR), qui consiste à détecter directement le photon micro-onde émis par un spin à l'aide d'un détecteur de photon micro-onde unique (SMPD).

Cette approche repose sur le concept de dualité onde-particule. Dans le cas de la détection inductive, la lumière est traitée comme une onde avec les fluctuations associées, même dans l'état du vide. Le fait de considérer la lumière comme un flux de particules nous permet de ne plus être sensible à ces fluctuations (voir Figure 2.2). Pour un compteur de photons, l'absence de photon incident se traduit par une absence de signal. Le bruit dépend uniquement des imperfections du détecteur, telles que la présence de photons parasites, et peut en principe être extrêmement faible. Le rapport signal/bruit n'est alors limité que par notre capacité à concevoir et à fabriquer un détecteur de photons à micro-ondes ayant une efficacité élevée η_{d} et un faible taux de faux positifs α_{d}. Cette nouvelle méthode est donc mieux adaptée à la détection d'un spin unique.

Une preuve de principe de la FD-ESR a été obtenue pour la première fois par Emanuele Albertinale [Alb+21] en utilisant un SMPD développé par Emmanuel Flurin [Les+20]. L'expérience a ensuite été développé et amélioré par Eric Billaud [Bil+22], mais le régime de sensibilité de 1 spin/$\sqrt{\mathrm{Hz}}$ n'a pas été atteint en raison de certaines imperfections structurelles du détecteur.

Cette thèse s'appuie sur ces travaux antérieurs et présente la conception et la mise en œuvre d'un SMPD amélioré doté d'une sensibilité de détection record de 10^{-22} W/$\sqrt{\mathrm{Hz}}$, et atteignant le régime de détection du spin unique. Ce nouveau détecteur a été utilisé pour effectuer la spectroscopie d'ions erbium dans un cristal de scheelite. Ce système cristal-ion

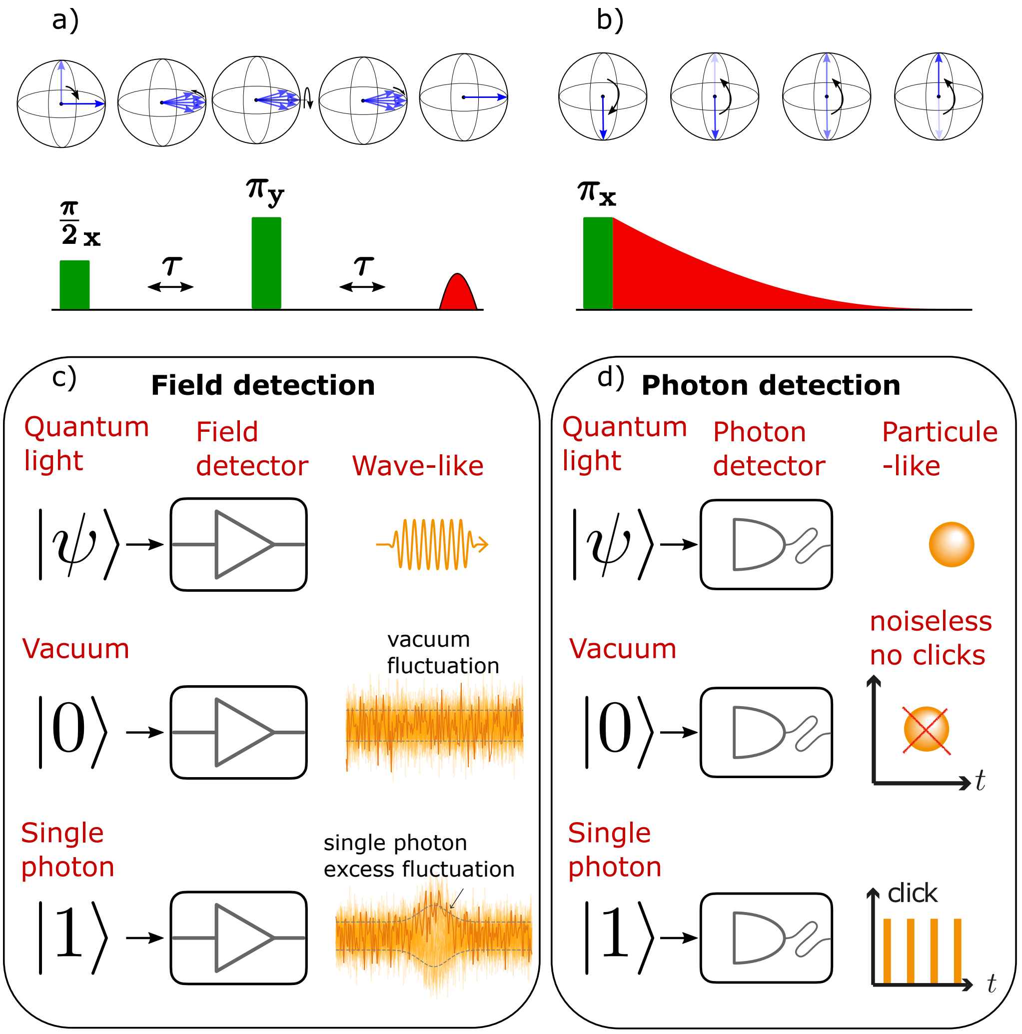

Figure 1.2: **Différence entre la détection inductive et la détection par fluorescence** a) Séquence d'écho, typique de l'ID-ESR. Les spins sont placés sur l'équateur par une impulsion de $\pi/2$. Ils évoluent ensuite selon leur fréquence de Larmor individuelle. Une impulsion π les refocalise, ce qui provoque un écho (en rouge). b) Détection d'un spin par son signal de fluorescence. La séquence consiste à exciter un spin avec une impulsion π et à collecter le photon issu de sa désexcitation radiative avec un compteur de photons. c) Détection du champs electromagnétique. L'information sur l'ensemble des spins est contenue dans la phase et l'amplitude du signal, nous considérons ici la lumière comme une onde. Cette méthode est intrinsèquement bruyante du fait des fluctuations du vide. La détection d'un état de Fock $|1\rangle$ correspondant simplement à une augmentation du bruit moyen engendré. d) Détection de photons. La présence d'un photon se traduit par un clic du détecteur. Cette méthode est fondamentalement non-bruitée, l'absence de photon se traduisant par une absence de détection.

a été choisi en raison de ses longs temps de cohérence de spin, comme l'a démontré la caractérisation initiale complète réalisée par Marianne Le Dantec et Milos Rancic à l'aide de l'ID-ESR [Dan22; Le +21]. Une optimisation du couplage entre le résonateur micro-ondes et les spins d'erbium a ensuite été réalisée par Zhiren Wang, permettant d'obtenir un couplage spin-résonateur de $g_0 = 3$ kHz.

Cette thèse démontre la détection d'un ion erbium unique dans un cristal de scheelite par FD-ESR grâce à la mise en œuvre d'un SMPD suffisamment

sensible. Cette détection pousse la résonance paramagnétique électronique à sa sensibilité ultime. En outre, elle montre que ce niveau de sensibilité nous permet d'obtenir un aperçu de l'environnement local du spin, avec en particulier la signature des spins nucléaires de ^{183}W entourant l'ion d'erbium.

Ce manuscrit est divisé en deux parties. La première est consacrée au compteur de photons micro-ondes. Le Chapter 3 fournit le contexte théorique nécessaire pour comprendre les différents concepts des circuits cQED impliqués dans notre SMPD. Le Chapter 4 traite spécifiquement de la théorie et du principe de fonctionnement du détecteur. Le Chapter 5 et le Chapter 6 présentent la fabrication et les caractéristiques du compteur.

La deuxième partie est consacrée à la détection des ions erbium. Le Chapter 7 décrit théoriquement la plateforme expérimentale comprenant le système de cristal/ion Er^{3+} : $CaWO_4$ et le résonateur supraconducteur qui permet un fort couplage spin-photon. Le Chapter 8 démontre que notre système de mesure peut détecter des spins individuels et fournit une description complète de leurs caractéristiques (tenseur g, temps de cohérence, etc.). Enfin, le Chapter 9 se concentre sur la sélection d'un spin électronique spécifique et étudie son environnement immédiat. Nous mettons en évidence son couplage avec le bain de spin nucléaire ^{183}W et émettons plusieurs hypothèses concernant les positions des atomes ^{183}W qui contribuent à son environnement magnétique.

1.2 Résultats expérimentaux

1.2.1 Détecteur de photons micro-ondes uniques avec une sensibilité record: $\mathcal{S} = 10^{-22}\ \mathrm{W}/\sqrt{\mathrm{Hz}}$.

Dans le domaine optique, la conception d'un détecteur de photons est rendue possible par l'existence de matériaux, tels que les semi-conducteurs ou les supraconducteurs, dont l'écart énergétique est inférieur à l'énergie des photons à détecter. L'absorption des photons par effet photoélectrique crée un grand nombre de quasiparticules (paires électron-trou dans les semi-conducteurs et quasiparticules supraconductrices, associées à des paires de Cooper brisées, dans les supraconducteurs) qui peuvent être facilement détectées. Dans le domaine des micro-ondes, en revanche, ce concept n'est pas directement transposable. Les photons micro-ondes ont en effet une énergie inférieure de 5 ordres de grandeur à celle des photons optiques et ne pourront pas combler le gap énergétique des matériaux semi-conducteurs. Une autre stratégie doit être envisagée.

Une autre approche consiste à considérer la détection des photons comme une tâche de traitement de l'information quantique. Dans ce cas, la tâche consiste à faire correspondre l'état d'un photon qui se propage avec l'état d'un bit quantique qui peut être manipulé et mesuré selon les protocoles cQED. Afin d'imiter le caractère irréversible de l'absorption des photons, cette correspondance doit être conçu de manière à être indépendant de la forme d'onde et du temps d'arrivée du photon. Dans ce travail, nous utilisons une architecture de circuit SMPD développée par Raphaël Lescanne et Emmanuel Flurin [Les+20] exploitée plus tard dans la thèse de doctorat d'Emanuele Albertinale [Alb+21] pour la détection par fluorescence micro-ondes d'un ensemble d'impuretés de bismuth dans le silicium.

Notre architecture de compteur exploite le développement rapide des circuits QED et notamment des qubits "transmon". Ces systèmes à deux niveaux, dont la fréquence de transition typique se situe entre 5 et 10 GHz, peuvent être utilisé pour la détection des photons micro-ondes. Près de deux décennies de recherche en informatique quantique ont permis de les manipuler en quelques nanosecondes et d'effectuer la lecture de leur état quantique avec une grande fidélité à l'aide d'un amplificateur paramétrique Josephson fonctionnant à la limite minimale du bruit quantique.

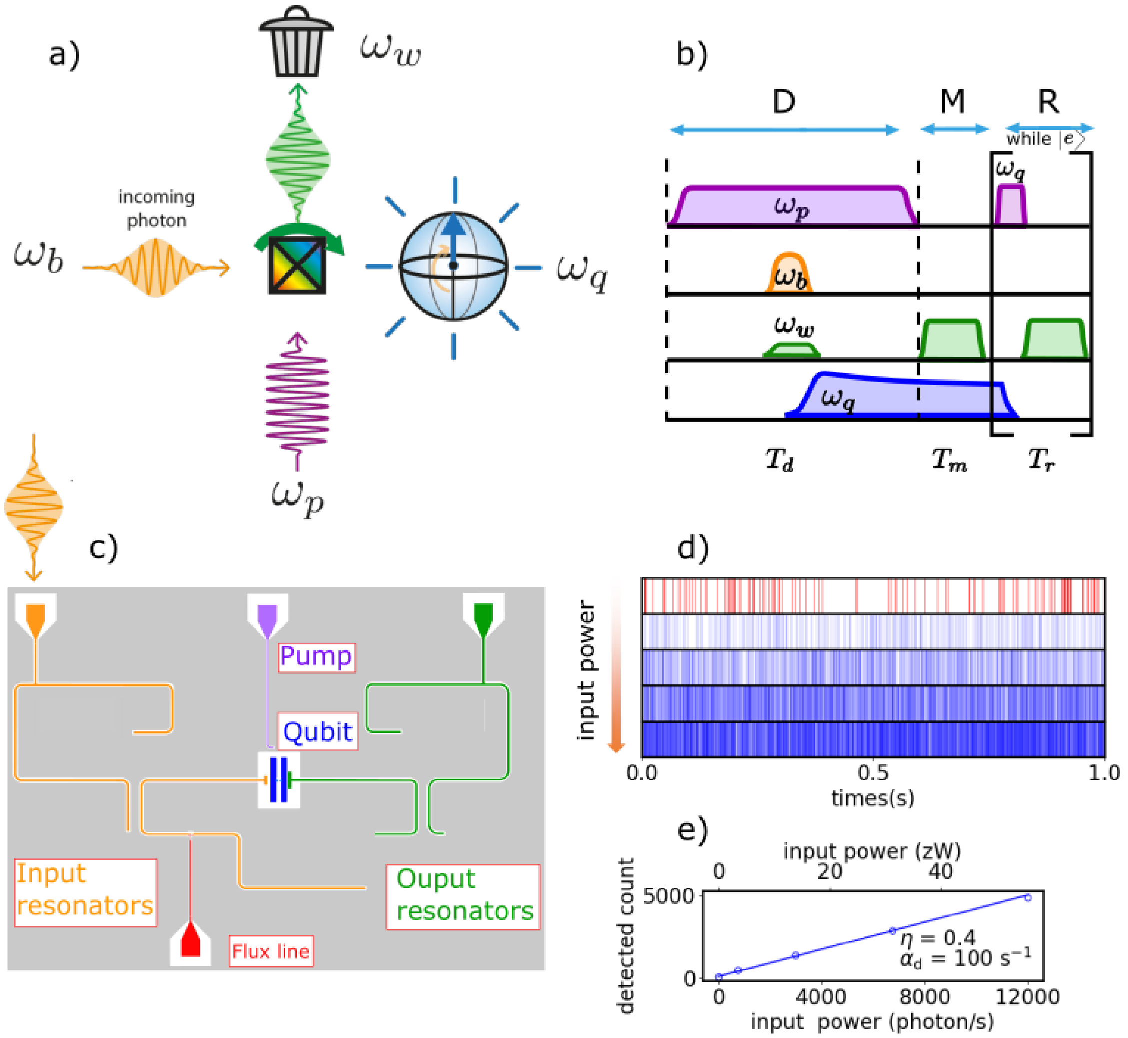

Figure 1.3: **SMPD : Principe de fonctionnement et caractérisation** a) Principe de fonctionnement. La non linéarité fournie par un qubit supraconducteur (carré noir barré) permet une conversion non linéaire transformant un photon incident à la fréquence ω_b et un photon de pompe à la fréquence ω_p en une excitation du qubit à la fréquence ω_q et un photon dans le résonateur de sortie à la fréquence ω_w. L'activation du processus n'est possible que si les fréquence des ondes incidentes correspondent à celle des ondes sortante tel que, $\omega_\mathrm{b} + \omega_\mathrm{p} = \omega_\mathrm{q} + \omega_\mathrm{w}$. b) Cycle du SMPD. Le cycle de détection (D) est défini par l'application du ton de pompe (violet) sur le qubit. Le qubit est ensuite lu de manière dispersive (M) et réinitialisé (R). c) Puce du SMPD. Les modes sont définis par des résonateurs CPW. Le résonateur d'entré (orange) est un résonateur $\lambda/2$, rendu accordable grace à un SQUID contrôlé par une ligne de courant continu (rouge). La fréquence au sommet de l'arche est $\omega_\mathrm{b}/2\pi = 7.005$ GHz. Un résonateur à large bande $\lambda/2$ (orange), en résonance avec le résonateur d'entrée, est placé avant la ligne de sortie et se comporte comme un filtre passe-bande. Le mode de sortie (vert) est un résonateur $\lambda/4$ de fréquence $\omega_\mathrm{w}/2\pi = 7.704$ GHz. Il est également équipé d'un filtre passe-bande (vert). Le qubit de fréquence $\omega_\mathrm{q}/2\pi = 6.183$ GHz est représenté en bleu. La ligne de pompe permettant la conversion à 4 ondes est représentée en violet. d) Traces temporelles montrant la réponse du SMPD lorsqu'un état cohérent est envoyé sur le résonateur d'entrée. Chaque ligne verticale représente la détection d'un photon. Le nombre de photon envoyé augmente progressivement de 0 photon·s^{-1} (trace rouge) à 12000 photon·s^{-1} (dernière trace bleue). Cette puissance correspond à 55 zW. e) Relation entre le nombre de photons détectés et le nombre de photons incidents permettant d'extraire l'efficacité $\eta = 0.43$ et $\alpha_\mathrm{d} = 84$ s^{-1}.

La mise en correspondance irréversible du photon entrant avec l'état du qubit est assurée par un processus de mélange à 4 ondes. Nous introduisons à cette fin deux modes intermédiaires appelés respectivement "buffer" et "waste". En pompant le qubit avec un ton micro-ondes, la non-linéarité fournie par le transmon nous permet de mélanger ces modes afin de convertir le photon entrant dans le buffer en une excitation du qubit et un photon dans le waste (voir Figure 2.3a). Ce dernier est ensuite rapidement dissipé dans les lignes, ce qui rend la conversion inverse impossible. En raison de l'alternance entre les phases de pompage et de lecture du qubit, le détecteur fonctionne de manière cyclique (voir Figure 2.3b).

Une grande partie de cette thèse est consacrée à l'amélioration de la sensibilité de ce détecteur de photons. Nous avons profité des progrès récents dans la fabrication des transmons ainsi que de l'amélioration de la compréhension des circuits cQED pour affiner la conception du détecteur. En un mot, nous avons utilisé les mêmes éléments de base que ceux utilisés dans la recherche de l'ordinateur quantique, mais cette fois pour concevoir un meilleur détecteur. Par rapport à la version originale, nous avons gagné un ordre de grandeur en sensibilité pour atteindre $\mathcal{S} = 10^{-22}\ \mathrm{W}/\sqrt{\mathrm{Hz}}$. Cette amélioration est due à une réduction drastique du taux de faux positifs ($\alpha_\mathrm{d} = 84\ \mathrm{s}^{-1}$ contre $\alpha_\mathrm{d,old} = 1500\ \mathrm{s}^{-1}$), et à une augmentation de l'efficacité ($\eta_\mathrm{d} = 0.43$ contre $\eta_\mathrm{d,old} = 0.2$). La caractérisation de ces paramètres cruciaux pour le SMPD est présentée dans Figure 2.3d,e.

Dans le Chapter 5, nous détaillons la conception et le processus de fabrication du détecteur. La Figure 2.3c donne un aperçu de la puce SMPD. Les résonateurs orange (resp. verts) correspondent aux modes buffer (resp. waste). Le qubit transmon est représenté en bleu, avec sa ligne de pompe en violet. La caractérisation complète du SMPD est présentée dans Chapter 6.

1.2.2 Détection d'un spin électronique unique Er^{3+} dans un cristal de scheelite

Le nouveau SMPD décrit dans la première partie de la thèse est ensuite utilisé pour détecter des spins uniques à partir du signal de fluorescence qu'ils émettent pendant leur relaxation. Comme le bruit de fond des micro-ondes est fortement atténué à 10 mK, le comptage de photons est la méthode appropriée pour détecter ce signal, qui consiste en un flux de photons uniques.

Pour atteindre la sensibilité de détection d'un spin unique en 1 seconde de temps d'intégration, la puissance émise par le spin doit être du même ordre de grandeur que la puissance minimale détectable par le SMPD en 1 s : 10^{-22} W (voir la dernière section). Un spin électronique dans l'espace libre à la fréquence typique $\omega/2\pi = 8$ GHZ possède un taux d'émission spontannée de $10^{-12}\ \mathrm{s}^{-1}$, soit ≈ 30000 ans. Lorsqu'il est inséré dans un cristal hôte, la relaxation par génération de phonons devient dominante, augmentant le taux de relaxation spontanée à $\approx 1\ \mathrm{s}^{-1}$. Pour que le taux de relaxation radiative soit le canal de perte dominant, il faut utiliser l'effet Purcell [Pur46] en couplant les spins à un résonateur à fort facteur de qualité. Ce régime dit de Purcell a été atteint en 2016 dans notre groupe [Bie+16] pour des impuretés de bismuth incorporées dans du silicium.

Notre système expérimental consiste en un cristal de scheelite pure $\mathrm{CaWO_4}$ contenant des traces d'erbium (~ 1 ppb). Les ions Er^{3+} qui remplacent les Ca^{2+} (voir Figure 2.4a), forment un défaut paramagnétique avec un degré de liberté de spin. La structure électronique d'un ion erbium est complexe. Les fonctions d'onde des onze électrons de sa bande de valence s'hybrident fortement pour donner une première échelle d'énergie dégénérée avec une transition optique fondamentale à une longueur d'onde de 1.5 μm. Le champ cristallin à l'intérieur du $\mathrm{CaWO_4}$ perturbe faiblement cette structure énergétique et lève la dégénérescence des niveaux de l'état fondamental en huit doublets de Kramers [Kra30]. La dégénérescence restante est assurée par le théorème de Kramers : les espèces ayant

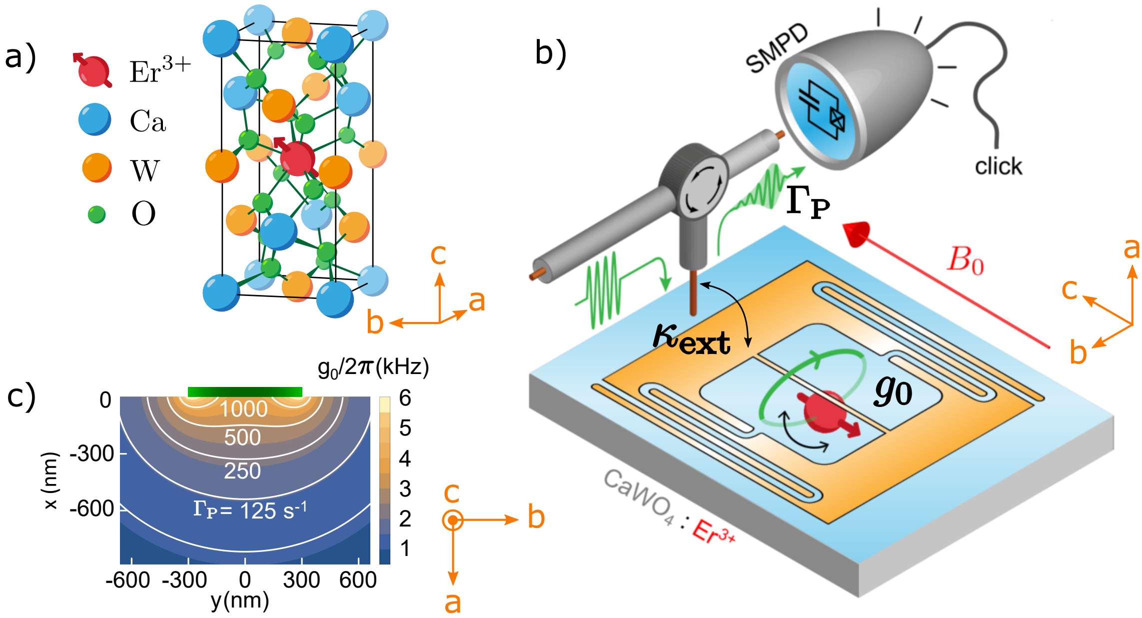

Figure 1.4: **Plate-forme expérimentale** a) Schéma de la maille élémentaire de $CaWO_4$ centrée sur un ion Er^{3+} substituant un ion Ca^{2+}. Les oxygènes sont supprimés pour plus de clarté. Un degré de liberté de spin est représenté pour l'ion Er^{3+}. La symétrie du cristal est tétragonale autour de l'axe c, ce qui signifie que les axes a et b sont équivalents. b) Schéma de l'expérience globale. Un résonateur micro-ondes (orange) composé d'un condensateur interdigité court-circuité par un nanofil est modelé dans une couche de niobium (bleu) au sommet du cristal (gris). Le résonateur est couplé ç la ligne micro-onde au taux κ_{ext}. Le nanofil permet de coupler le spin au résonateur avec la force g_0. Les spins sont excités en envoyant une impulsion micro-onde sur le résonateur. ils se relaxent ensuite radiativement grâce à l'effet Purcell généré par le couplage. Enfin, les photons résultants sont acheminés vers le SMPD à l'aide d'un circulateur. c) Simulation de la force de couplage g_0 et du taux de Purcell correspondant Γ_{P} en fonction de la position du spin dans le plan (a, b). Le rectangle vert représente la section transversale du nanofil..

un nombre impair d'électrons restent doublement dégénérées en raison de la symétrie de renversement du temps. Chacun des doublets de Kramers se comporte donc comme un spin-1/2 effectif dont la dégénérescence peut être levée par un champ magnétique qui brise la symétrie de renversement du temps, c'est-à-dire par effet Zeeman. Le facteur de Landé du système dépend fortement de la symétrie du cristal [Enr71; Ber+09] car le spin effectif résulte d'une interaction entre l'ion et le champ cristallin. Le tenseur **g** est donc anisotrope avec $\mathrm{g_c} = 8.38$ et $\mathrm{g_{a,b}} = 1.25$ (voir Figure 2.4a pour la définition des axes).

Le choix du cristal $CaWO_4$ est intéressant en raison de sa faible teneur en impuretés magnétiques, dominée par la fraction 0.143 des isotopes ^{183}W qui ont un spin nucléaire. Les propriétés de cette plate-forme expérimentale ont été étudiées en détail par Marianne Le Dantec en utilisant des méthodes ID-ESR [Le +21] et ensuite par Eric Billaud en utilisant FD-ESR [Bil+22; Bil23].

Le couplage spin-photon a lieu via un résonateur micro-onde supraconducteur 2D de fréquence $\omega_0/2\pi = 7.3$ GHz fabriqué au sommet du cristal dans un film de niobium. Comme le montre Figure 2.4b, il se compose d'un condensateur interdigité court-circuité par un nanofil parallèle à l'axe c du cristal. Le champ magnétique statique $\boldsymbol{B_0}$ appliqué parallèlement au fil permet aux spins d'entrer en résonance avec le résonateur. Le champ magnétique généré par le nanofil permet le couplage avec les spins. Il est transverse au nanofil et se situe donc dans le plan (a, b) où le facteur g est maximal. Le Figure 2.4c

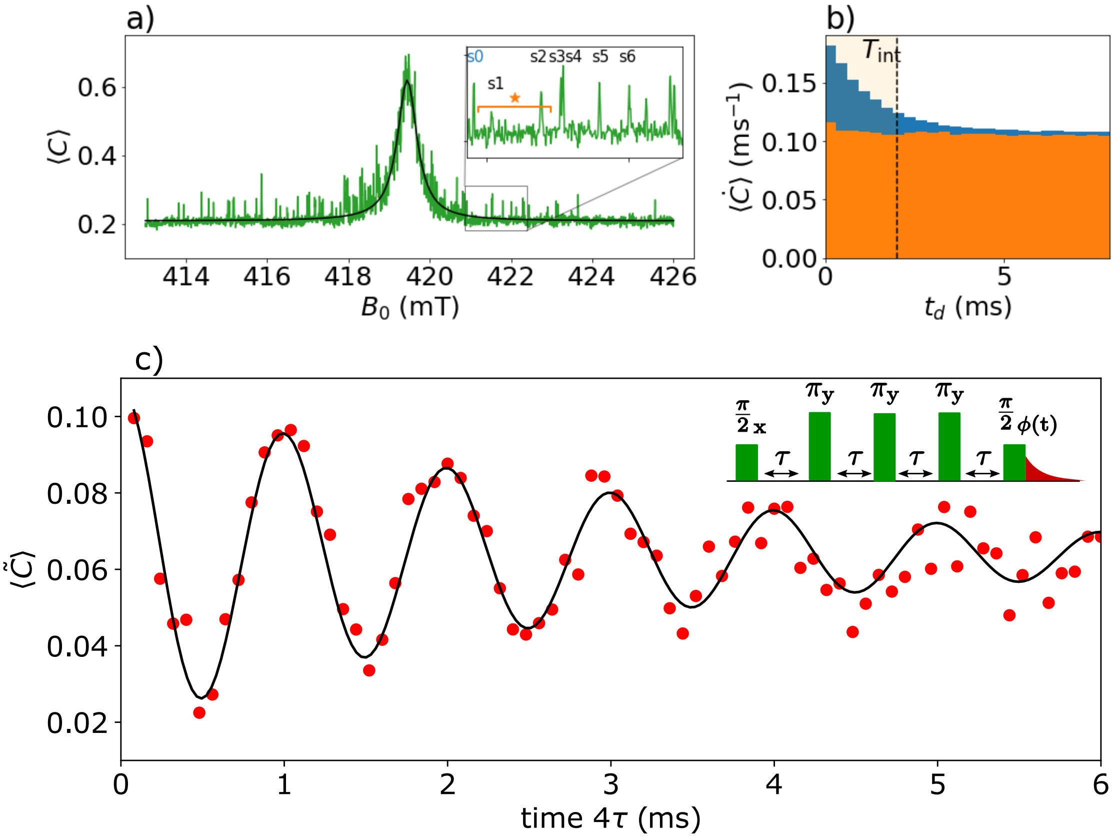

Figure 1.5: **Détection de spin unique par FD-ESR** a) Spectroscopie de spin à faible puissance (~ -107 dBm à l'entrée de l'échantillon), avec une fenêtre d'intégration de 2 ms. Le $\langle C \rangle$ représente le nombre moyen de clics pendant le temps d'intégration T_{int}, B_0 est l'amplitude du champ magnétique statique appliqué. La courbe verte représente les données mesurées, la courbe noire est un fit lorentzien. L'angle θ varie linéairement entre $-0.016°$ et $0.016°$ au cours du balayage. b) Taux de clic moyen $\langle \dot{C} \rangle$ en fonction du temps. L'histogramme bleu représente le signal de fluorescence provenant du spin étiqueté s_0 dans l'encadré de (a). L'histogramme orange représente le bruit de fond et correspond au comptage sombre du SMPD. c) Expérience de découplage dynamique avec 3 impulsions π de refocalisation. Le nombre moyen de clics corrigé de l'arrière-plan $\langle \tilde{C} \rangle$ est représenté en fonction du temps 4τ entre les impulsions $\pi/2$. Une phase linéaire croissante $\phi(\tau) = 2\pi\Delta\tau$ avec $\Delta = 0,001\,\text{MHz}$ est appliquée à la dernière impulsion. Les points rouges sont les données tandis que la courbe noire est un fit sinusoidale permettant d'extraire le temps de cohérence. $T_2^{\text{DD}} = 2.99 \pm 0.03\,\text{ms}$. Données prises à $B_0 = 422.085$ mT et $\theta = -0.003°$.

montre une simulation de la force de couplage $g_0/2\pi$ en fonction de la position du spin dans le voisinage du nanofil. Avec nos paramètres expérimentaux, nous atteignons des couplages de quelques kHz, ce qui donne un taux de Purcell $\Gamma_{\text{P}} \sim 1000$ s^{-1} pour les spins les plus fortement couplés. La puissance instantanée correspondante $P = 5 \cdot 10^{-21} W$ nous place dans une situation favorable pour la détection d'un seul spin. La conception et la fabrication du résonateur micro-ondes ont été réalisées par Zhiren Wang [Wan+23]. L'expérience complète, esquissée dans Figure 2.4b, consiste à exciter l'ensemble de spin avec une impulsion micro-onde appliquée sur le résonateur et à collecter les photons micro-ondes émis. L'échantillon de spin est simplement connecté au SMPD par un câble coaxial à faible perte. Un simple circulateur guide les photons collectés vers le détecteur.

La Figure 2.5a représente une spectroscopie en champ magnétique réalisée avec cette configuration expérimentale. Pour chaque valeur de l'amplitude du champ magnétique B_0, l'ensemble des spins est excité à faible puissance afin de sélectionner les spins les plus fortement couplés. Les photons micro-onde émis sont ensuite collectés par le SMPD. Nous définissons une fenêtre d'intégration d'une durée de T_{int} sur laquelle nous faisons la moyenne du nombre d'événements de détection (ou clics) $\langle C \rangle$. Le spectre résultant se présente comme une somme de pics étroits et inégalement répartis, centrés autour de $B_0 = \omega_0/(\mathrm{g_c}\mu_{\mathrm{B}})$. Nous montrons dans la thèse que chaque pic individuel correspond à un spin unique en étudiant les statistiques d'émission de photons. Ce résultat est comparable à la première détection d'une molécule unique à l'aide d'un détecteur de photons optiques [OB90], mais pour un spin émettant dans le domaine des micro-ondes.

Le signal de fluorescence associé à un spin unique est représenté dans Figure 2.4b. Le temps de relaxation radiative observé $T_1 \approx 1.5$ ms est en bon accord avec la valeur attendue. Des mesures de cohérence sont effectuées sur différents spins uniques. La Figure 2.4c montre par exemple les résultats d'une expérience de découplage dynamique réalisée sur le spin étiqueté s_0 dans Figure 2.4a. Un temps de cohérence de ~ 3 ms est atteint, ce qui correspond à la limite radiative $2T_1$.

1.2.3 Sonder les spins nucléaires $^{183}\mathrm{W}$ avec le spin électronique de l'erbium

Le contrôle d'un spin électronique unique ouvre la voie à la mesure de son environnement local. En particulier, le spin électronique peut être utilisé pour mesurer et contrôler le bain de spin nucléaire environnant grâce au couplage hyperfin lié à l'interaction dipôle-dipôle magnétique entre les spins nucléaires et électroniques.

Ce concept a été démontré pour la première fois en 2012 pour les centres NV du diamant [Tam+12; Kol+12; Lon+13], mesurés individuellement à l'aide d'une transition optique. Le principe de l'expérience est de détourner le concept de découplage dynamique introduit en 1999 [VKL99] pour les systèmes quantiques ouverts. Au lieu d'utiliser la séquence de découplage dynamique pour isoler le spin de l'électron de son environnement bruyant, on l'utilise pour le mettre en résonance avec un spin nucléaire spécifique.

Dans le cas de notre expérience, le bain de spin nucléaire est constitué des noyaux de l'isotopes de tungstène $I = 1/2^{183}\mathrm{W}$, dont l'abondance naturelle est de 0.145. Ils occupent aléatoirement les sites de tungstène et interagissent avec le spin électronique Er^{3+} par couplage dipolaire magnétique (voir Figure 2.6a,b). Comme le moment magnétique du spin électronique est 4 à 5 ordres de grandeur plus grand que celui du spin nucléaire, nous pouvons appliquer l'approximation séculaire. Le spin électronique entraîne les spins nucléaires dont les axes de quantification dépendent de l'état de son état, comme le montre Figure 2.6b. Cet effet est au cœur de l'expérience. Bien que le spin électronique ne puisse pas être inversé par l'interaction hyperfine, il peut choisir une phase, ce qui permet de connaître l'état quantique du spin nucléaire.

La séquence de découplage dynamique que nous avons utilisée consiste en une séquence CPMG de 24 impulsions de refocalisation π (voir Figure 2.6c). Le spin de l'électron, placé dans une superposition d'états par l'impulsion initiale $\pi/2-$, est ensuite basculé 24 fois par la série d'impulsions π, puis reprojeté sur l'axe z de la sphère de Bloch par la dernière impulsion $\pi/2-$. Nous mesurons ensuite son signal de fluorescence avec le SMPD.

Chaque fois qu'une impulsion π est appliquée au spin électronique, l'axe de quantification du spin nucléaire change. Si la fréquence de modification de l'axe l'inclinaison de cet axe est en phase avec la fréquence de Larmor ω_{L} du spin nucléaire, ce dernier subira une rotation progressive après chaque impulsion π. Cette condition de résonance peut être exprimée en termes du temps 2τ entre les impulsions π, comme $2\tau_k = (2k+1)\pi/\omega_{\mathrm{L}}$ pour $k \in \mathbb{N}$. Pour ces temps inter-impulsion spécifiques, la séquence CPMG intrique progressivement

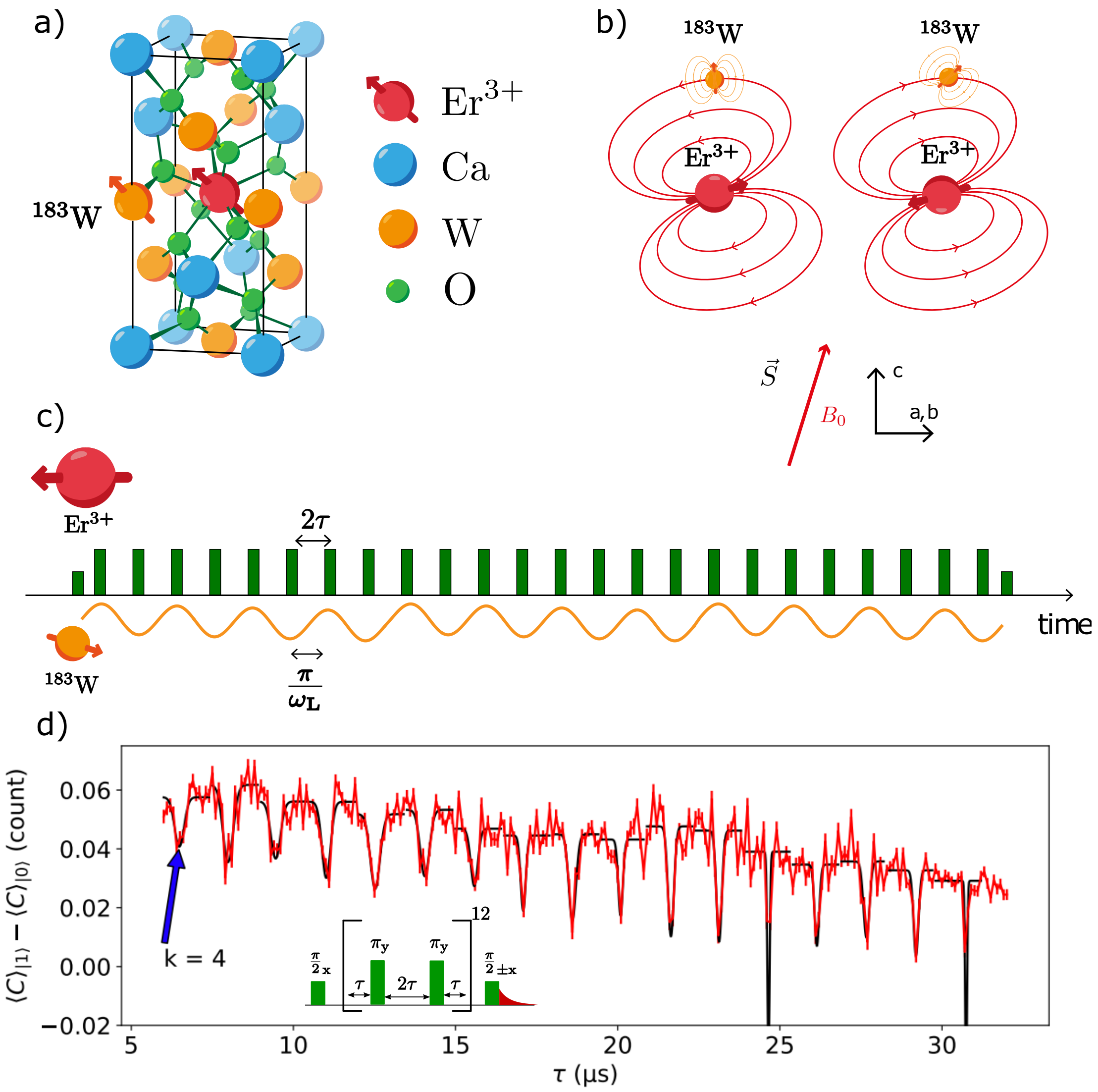

Figure 1.6: **Détection de spin nucléaire ^{183}W avec une séquence de découplage dynamique.** a) Spin électronique Er^{3+} possédant un spin nucléaire ^{183}W 1/2 dans son environnement immédiat. b) Interaction electro-nucléaire. L'état du spin de l'électron influence l'axe de quantification du spin nucléaire en raison de son moment magnétique plus important. Le tenseur **g** anisotrope provoque un désalignement entre la direction de quantification du spin de l'électron et l'orientation du champ magnétique. c) Séquence de découplage dynamique avec 24 impulsions de refocalisation π appliquées au spin de l'électron. En raison de la dépendance de la quantification du spin nucléaire par rapport à l'état du spin électronique, il existe une condition de résonance entre le délai d'interpulsion 2τ et la fréquence de Larmor du spin nucléaire ω_L. d) Expérience de découplage dynamique correspondante. La dernière impulsion projette l'état final alternativement sur l'état excité ou l'état fondamental. Le nombre moyen de clics est noté $\langle C\rangle_{|0\rangle}$ et $\langle C\rangle_{|1\rangle}$. Le contraste entre les projections est représenté en fonction du temps τ. Les creux espacés de $\Delta\tau = \pi/\omega_L = 1,52$ μs sont dus à l'interaction avec le bain de spin nucléaire ^{183}W. Le premier creux à $\tau_4 = 6,44$ μs correspond à la résonance d'ordre 4. Les lignes rouges sont les données, les lignes noires pleines représentent le fit gaussien de chaque creux.

les spins nucléaires et électroniques. Le niveau d'intrication est contrôlé par le nombre d'impulsions π.

L'information d'intrication peut être récupérée grâce à l'état de l'électron. En effet, si τ est hors résonance, les spins ne sont pas intriqués après les 24 impulsions et le spin de l'électron reste dans l'état de superposition initial. La décohérence est le seul mécanisme qui influence le résultat final. Au contraire, si $\tau = \tau_k$, une intrication se produit et l'état final du système change. Du point de vue du spin de l'électron, cela peut être vu comme une perte rapide de cohérence qui se produit pour chaque τ_k.

Il suffit donc de mesurer l'état final du spin de l'électron pour reconstruire la dynamique de l'intrication. La mesure de la probabilité P_{x} que le spin de l'électron reste dans sa superposition initiale est illustrée dans Figure 2.6d en fonction du temps τ. Comme prévu, nous observons un schéma régulier de creux, espacés de $\Delta\tau = \pi/\omega_{\mathrm{L}} = 1.52$ confirmant l'interaction entre le spin de l'électron et un bain de spin nucléaire ^{183}W. Cette expérience constitue la première détection des spins nucléaires ^{183}W à l'aide d'un spin électronique individuel.

Pour conclure cette introduction, il est intéressant de prendre du recul et d'examiner la chaîne de concepts qui a conduit à ce résultat final. Nous utilisons un amplificateur paramétrique Josephson pour lire en une seule fois l'état d'un qubit transmon. Cet atome artificiel, inséré dans une architecture cQED, permet de signaler le passage d'un photon micro-onde. En travaillant sur le couplage spin-photon, nous sommes capables d'utiliser cette architecture de détection de photons pour détecter un spin électronique Er^{3+} unique intégré dans un cristal $CaWO_4$. Enfin, nous approfondissons la description de la matière en utilisant le spin de l'électron lui-même comme indicateur pour détecter son environnement local et en particulier les spins nucléaires ^{183}W. Cette nouvelle chaîne, combinant circuits supraconducteurs, comptage de photons et spectroscopie RPE, offre une sensibilité de détection inégalée et ouvre la voie à de nombreuses applications dans le domaine de la détection et de l'informatique quantiques.

Chapter 2

Introduction

2.1 The general context of high sensitivity Electron Spin Resonance

Electron Spin Resonance (ESR) is an insightful technique that allows researchers to investigate the structure and behavior of substances containing unpaired electron paramagnetic impurities. When a static magnetic field is applied, the degeneracy of the unpaired electron spin levels is lifted, and the spin dynamics follows a precession around the applied magnetic field at the Larmor frequency. This frequency is determined by the electron's gyromagnetic ratio, more precisely a gyromagnetic tensor in solids, that links the magnetic moment of the electron to its angular momentum. Remarkably, the prediction of the free electron's gyromagnetic ratio by quantum field theory has been an extraordinary achievement, with an experimental and theoretical agreement reaching a 12-digit precision. As documented by the National Institute of Standards and Technology (NIST), the value of the free electron gyromagnetic ratio is $-28.0249514242(85)\ \mathrm{GHz} \cdot \mathrm{T}^{-1}$.

As a consequence, in presence of a static magnetic field, unpaired electrons are resonantly responsive to electromagnetic radiation. Given the intrinsic electron's gyromagnetic factor value, the resonance frequencies are typically in the microwave range for moderate magnetic fields. When the sample is exposed to an electromagnetic field with the right frequency, the unpaired electrons can absorb energy from it, leading to a resonance phenomenon that can be probed experimentally with different techniques. This absorption process is the basis of ESR, enabling scientists to gain valuable insights into the properties of paramagnetic impurities and their surroundings [SJ01b].

There are two main ESR spectroscopy techniques : continuous wave (CW) and pulsed. In CW-ESR, a continuous microwave signal irradiates the sample, and its transmission/reflection coefficient is analyzed. This method is versatile but faces limitations in terms of spectral and temporal resolution. Pulsed ESR, on the other hand, involves exciting the spin ensemble with short bursts of resonant electromagnetic fields. The information about the spins is contained in the signal they re-emit after being excited by the pulses [SJ01b]. Numerous pulse sequences have been developed for addressing various questions.

Inductive detection electron spin resonance (ID-ESR) is the most prevalent method for performing ESR spectroscopy [Rab+38; Blo46; PTP46]. In this approach, the sample containing the spins is placed inside a microwave resonator, tuned to a specific frequency ω_0. Resonant pulses are applied to first create a transient transverse magnetization, and later induce the formation of a microwave pulsed signal, noticeably a spin echo. Characteristic properties of the spin ensemble can be extracted from the phase and amplitude of this echo.

ESR allows researchers to determine key properties of spins and their surroundings, with applications in various fields such as biology [Yos+96], biochemistry [Pol06], and

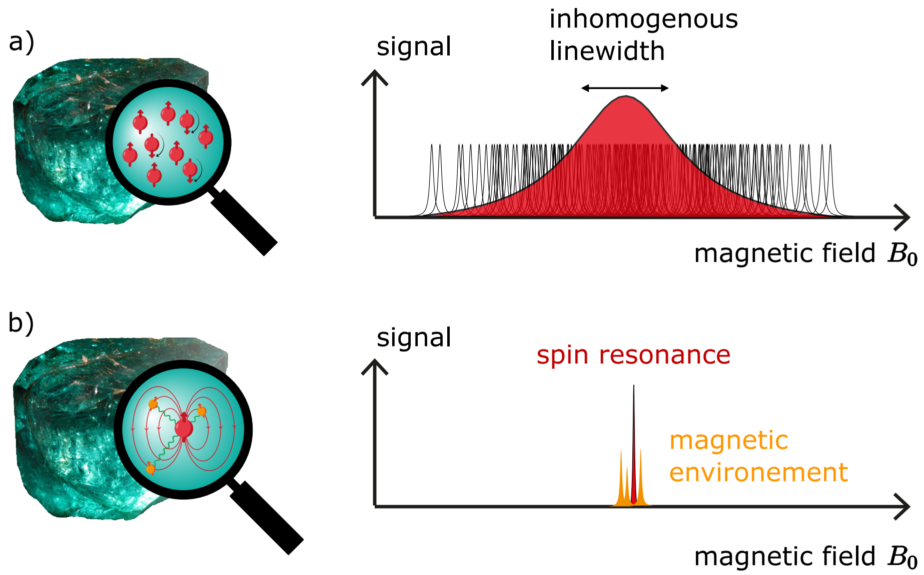

Figure 2.1: **Electron spin resonance.** a) Illustration of the signal provided by a set of paramagnetic impurities contained in a crystal as the function of the static magnetic field B_0. The electromagnetic environment specific to each spin shown in (b) causes an inhomogeneous dispersion of the resonance frequencies. The ensemble measurements do not account for these local characteristics.

solid-state science [Sli55].

In terms of spin detection sensitivity, conventional ID-ESR spectrometers face stringent limitations due to the weak coupling between the spins and the applied microwave magnetic field. In a one second averaging time, current ESR spectrometers can only detect large spin ensembles containing about 10^9 spins [Abh+22], which makes the characterization of local properties very challenging.

Inhomogeneous frequency broadening is a common issue in ESR spectroscopy, where the gyromagnetic factors of individual spins vary due to their different local environments. This leads to a distribution of resonance frequencies, making it difficult for commercial spectrometers to account for all the local interactions. Instead, they tend to average out the overall effect of the inhomogeneous broadening, limiting their ability to provide detailed insight into local properties.

Numerous methods have been developed in order to enhance the sensitivity of ESR detection. One approach involves leveraging the electron's charge to couple with the electric field, which can yield couplings several orders of magnitude higher [Xia+04]. This concept has been implemented in semiconductor materials using transistor architectures, a specificity that limits its application. Another technique involves exploiting impurities that possess optical transitions, such as the celebrated diamond's NV centres or erbium ions [Riz+22]. This optical detection of electron spin resonance has even enabled physicists to reach single-spin detection [Gru+97]. Despite the fact that this method is limited to ions with suitable optical transitions, it has yielded to a significant number of applications, noticeably for high spatial resolution magnetometry.

The Quantronics group has been pursuing the use of circuit Quantum Electrodynamics (cQED) [HR06; Bla+21] to achieve high sensitivity ESR. This approach employs two-dimensional electrical circuits cooled to millikelvin temperature. In these conditions, high quality factor superconducting micro-resonators that generate intense localized magnetic fields can reach a record-breaking coupling strength of 3 kHz [Ran+20] between spins and the resonator mode, to be compared to the sub-Hz coupling strength in conventional ESR resonant cavities.

A low mode volume also enhances the spontaneous emission rate of microwave photons by the spins via the Purcell effect [Bie+16], which reduces the acquisition time and the sensitivity. Moreover, signal processing is performed using great cQED devices, the Josephson Parametric Amplifiers (JPA), that allow us to mplify microwave signals with the minimal noise imposed by quantum mechanics. Additionally, operation at extremely low temperatures (10 -20 mK) provides a large spin polarization, which increases the signals.

These combined advantages allowed the Quantronics group to reach a detection sensitivity of 12 spin/$\sqrt{\mathrm{Hz}}$ in 2020 for ID-ESR spectroscopy using a platform of bismuth ions embedded in a silicon crystal [Ran+20]. However, despite a progress of five orders of magnitude compared to the previous state of the art, the single spin regime was still out of reach. Inductive detection methods indeed face an intrinsic noise challenge, as the spin ensemble's information is contained in the spin echo's electromagnetic field quadratures. Since these quadratures are measured directly, the minimal noise associated with their detection corresponds to vacuum fluctuations within the detection bandwidth, a fundamental property of quantum mechanics. Even assuming that no noise is added by the amplifiers, this vacuum noise level cannot be reduced. In this context, detecting a single spin via the microwave photon it emits during its Purcell relaxation corresponds to a small transient increase in noise level (see Figure 2.2a). The signal-to-noise ratio of ID-ESR is thus fundamentally limited, and reaching the single-spin regime calls for a new strategy.

In order to address this challenge, our group has proposed a new ESR method based on Fluorescence Detection (FD-ESR), which consists in the direct detection of the microwave photon emitted by a spin using a Single Microwave Photon Detector (SMPD), rather than measuring the photon field.

This approach relies on the wave-particle duality concept. In the case of inductive detection, light is treated as a wave with associated fluctuations, even in the vacuum state. In contrast, considering light as a stream of particles frees us from considering the vacuum state fluctuations (see Figure 2.2). Indeed, for a photon counter, the absence of an incoming photon results in the absence of a signal. Noise depends solely on detector imperfections, such as the presence of spurious photons reaching the detector, and can be in principle, be extremely low. The signal-to-noise ratio is then solely limited only by our ability to design and make a microwave photon detector with high efficiency η_{d} and a low false positive rate α_{d}. This new detection paradigm is therefore better suited for single spin detection.

A proof of principle of FD-ESR was first obtained by Emanuele Albertinale [Alb+21] using a SMPD developed by Emmanuel Flurin [Les+20]. The experiment was then developed and improved by Eric Billaud, but the sensitivity regime of 1 spin/$mathrmsqrtHz$ was not achieved due to certain structural imperfections in the detector.

This thesis builds on these previous works, presenting the design and implementation of an improved SMPD that achieves a record detection sensitivity of 10^{-22} W/$\sqrt{\mathrm{Hz}}$, and reaches the single-spin detection regime. This new detector was employed to perform spectroscopy of erbium ions in a scheelite crystal. This crystal-ion system was chosen due to its long spin coherence times, as demonstrated in the initial comprehensive characterization performed by Marianne Le Dantec and Milos Rancic using ID-ESR [Dan22; Le +21]. An optimization of the coupling between the microwave resonator and erbium spins was then carried out by Zhiren Wang, resulting in a large spin-resonator coupling $g_0 = 3$ kHz.

This thesis demonstrates the detection of a single erbium ion in a scheelite crystal by FD-ESR through the implementation of a sufficiently sensitive SMPD. This detection pushes electron spin resonance to its ultimate sensitivity. Additionally, it shows that this level of sensitivity allows us to obtain insight into the local spin environment, particularly regarding the nuclear spins of ^{183}W surrounding the erbium ion.

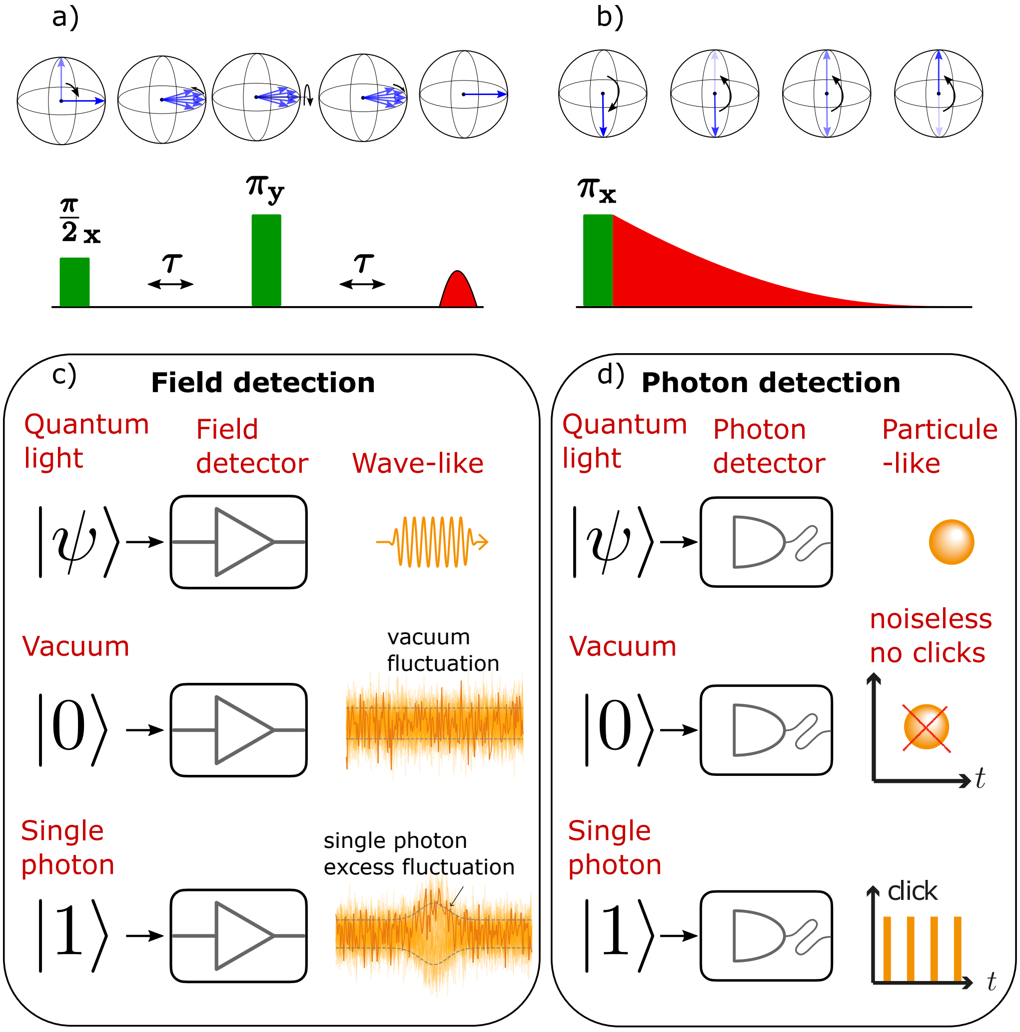

Figure 2.2: **Difference between inductive detection and fluorescence detection** a) Echo sequence, typical of the ID-ESR. The spins are placed on the equator by a $\pi/2$ pulse. They then evolve according to their individual Larmor frequency. A π pulse refocuses them, which causes an echo (in red). b) Detection of spin by its fluorescence signal. The sequence consists of exciting a spin with a π pulse and collecting the photon from its radiative de-excitation with a photon counter. c) Field detection. The information on the spin ensemble is contained in the phase and amplitude of the signal, we consider here the light as a wave. This method is intrinsically noisy due to vacuum fluctuations. the detection of a Fock $|1\rangle$ state simply corresponding to an increase in the average noise caused. d) Photon detection. The presence of a photon translates in a detector click. This method is basically noiseless, an absence of photon translating into an absence of detection.

This manuscript is divided into two parts. The first part is devoted to the microwave photon counter. Chapter 3 provides the theoretical background necessary to understand the various concepts of cQED circuits involved in our SMPD. Chapter 4 specifically discusses the detector's theory and operating principle. Chapter 5 and Chapter 6 present the counter's fabrication and characteristics.

The second part is dedicated to erbium spin detection. Chapter 7 theoretically describes the experimental platform comprising the ion-crystal $Er^{3+} : CaWO_4$ system and the superconducting resonator that enables a strong spin-photon coupling. Chapter 8 demonstrates that our measurement system can detect individual spins and provides a thorough description of their characteristics (g-tensor, coherence time, etc.). Lastly, Chapter 9 focuses on the selection of a specific electron spin and investigates its immediate environment. We highlight its coupling with the ^{183}W nuclear spin bath and put forth several hypotheses regarding the positions of the ^{183}W atoms that contribute to its magnetic environment.

2.2 Experimental results

2.2.1 Single microwave photon detector with a record sensibility: $\mathcal{S} = 10^{-22}\ \mathrm{W}/\sqrt{\mathrm{Hz}}$

In the optical domain, the design of a photon detector is made possible by the existence of materials, such as semiconductors or superconductors, with an energy gap smaller than the energy of the photons to be detected. The absorption of the photons through the photoelectric effect creates a large number of quasiparticles (electron-hole pairs in semiconductors and superconducting quasiparticles, associated to broken Cooper pairs, in superconductors) that can easily be detected. In the microwave range, however, this concept cannot be directly transposed. Microwave photons indeed have an energy 5 orders of magnitude lower than optical photons and won't be able to bridge the gap of semiconducting materials. Another approach has to be considered.

An alternative approach consists in considering the detection of photons as a quantum information processing task. Here, the task consists of mapping the state of a propagating photon onto the state of quantum bit that can be manipulated and readout following cQED protocols. In order to mimic the irreversible character of photon absorption, this mapping should be designed such that it is independent of the waveform and arrival time of the photon. In this work, we use a SMPD circuit architecture developed by Raphaël Lescanne and Emmanuel Flurin [Les+20] later exploited in Emanuele Albertinale's PhD thesis [Alb+21] for the microwave fluorescence detection of an ensemble of bismuth impurities in silicon.

Our SMPD architecture exploits the rapid development of QED circuits and noticeably the "transmon" qubits. These two-level systems with a typical transition frequency in the 5-10 GHz range can be placed in speaking terms with microwave photons. Almost two decades of quantum computing research has enabled to manipulate this qubit in a few nanoseconds and perform the single shot readout of its quantum state with a high fidelity using a Josephson parametric amplifier operated at the minimal quantum noise limit.

The irreversible mapping of the incoming photon onto the qubit state is then ensured by a 4 wave mixing process. We introduce for this purpose two intermediate modes called respectively the "buffer" and the "waste". By pumping the qubit with a microwave drive, the non linearity provided by the transmon allows us to mix these modes in order to convert the incoming buffer photon into a qubit excitation and a waste photon (see Figure 2.3a). The latter is then quickly dissipated in the lines, which making the reverse conversion impossible. Due to the alternation between the pumping and readout phases of the qubit, the detector operates cyclically (see Figure 2.3b).

A large part of this thesis is dedicated to improving the sensitivity of this single microwave photon detector (SMPD) for allowing us to achieve single spin detection. We took advantage of the recent progress in transmon qubit fabrication, and of the improved understanding of cQED circuits to refine the design of the detector. In a nut, we used the same basic building blocks as those used in the quest for the quantum computer, but this time to design a better detector. Compared to the original version, we gained one order of magnitude in sensitivity to reach $\mathcal{S} = 10^{-22}\ \mathrm{W}/\sqrt{\mathrm{Hz}}$. This improvement is due to a drastic reduction in the false positive rate ($\alpha_\mathrm{d} = 84\ \mathrm{s}^{-1}$ vs $\alpha_{\mathrm{d,old}} = 1500\ \mathrm{s}^{-1}$), and to

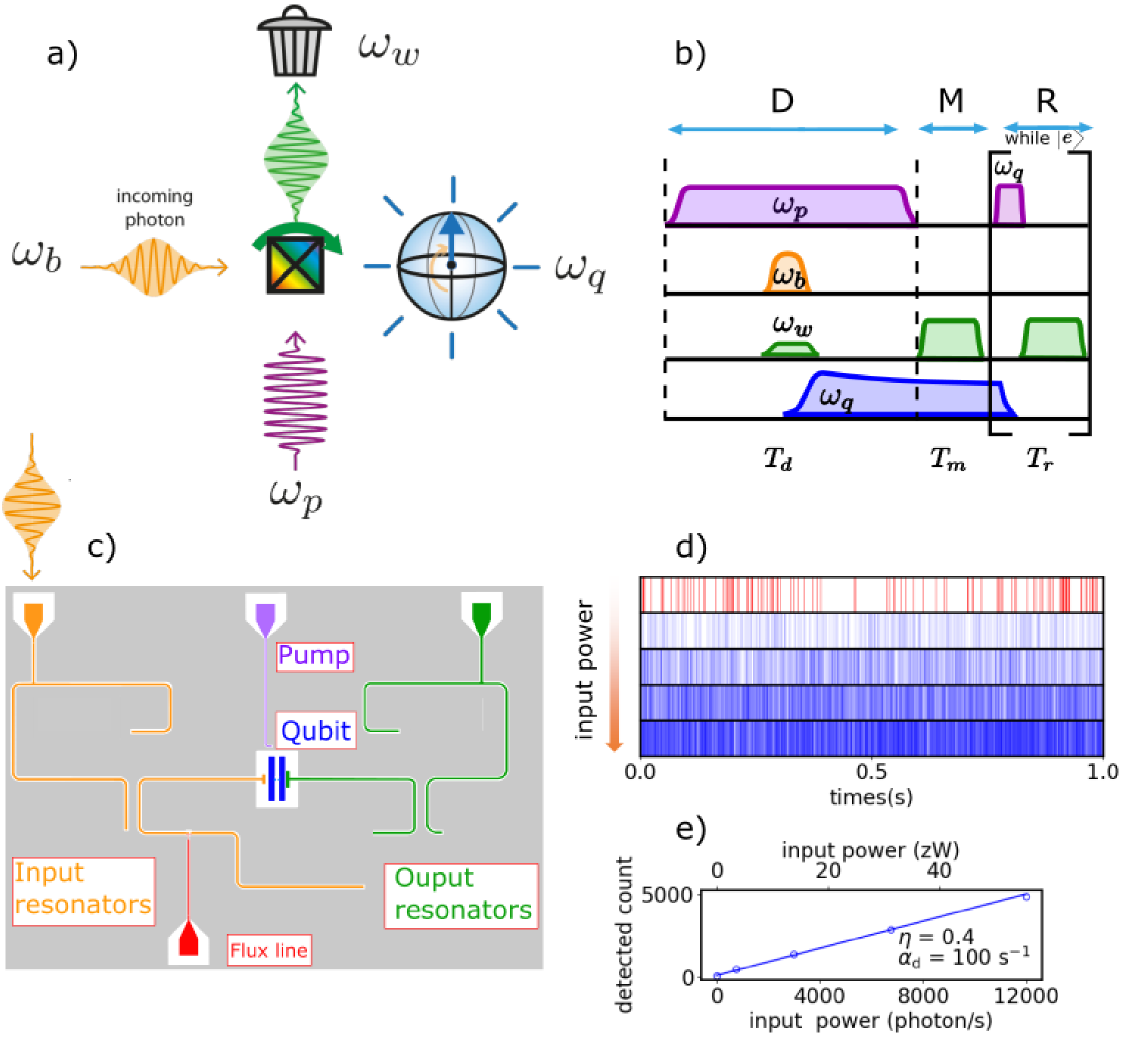

Figure 2.3: **SMPD: Operating principle and characterization** a) Operating principle. The non linearity provided by a superconducting qubit (black crossed square) allows frequency mixing of an incoming photon at frequency ω_b and a pump tone at frequency ω_p promoting the excitation of the qubit at frequency ω_q and the releasing of a photon in an overdamped waste mode at frequency ω_w.The activation of the process is submitted to the frequency matching condition $\omega_\mathrm{b} + \omega_\mathrm{p} = \omega_\mathrm{q} + \omega_\mathrm{w}$. b) SMPD cycle. The detection cycle (D) is define by the the application of the pump tone (purple). The qubit is then dispersively readout (M) and reset (R). c) SMPD chip. The modes are defined by CPW-resonators. The buffer (orange) is a $\lambda/2$ resonator, made tunable with a SQUID bias by a DC-current line (red). The top arch frequency is $\omega_\mathrm{b}/2\pi = 7.005$ GHz A broadband resonator $\lambda/2$ (orange), resonant with the buffer resonator is placed before the output line and behaves as a band pass filter. The waste mode (green) is a $\lambda/4$ resonator of frequency $\omega_\mathrm{w}/2\pi = 7.704$ GHz. It also comes with a bandpass filter (green). The qubit of frequency $\omega_\mathrm{q}/2\pi = 6.183$ GHz is represented in blue. The pump line allowing the 4 wave mixing is represented in purple. d) Time traces showing the response of the SMPD when a coherent tone is applied to the buffer resonator. Each vertical line represent the detection of a photon. The power of the tone is gradually increases starting from 0 photon$\cdot$s^{-1} (red trace) to reach 12000 photon$\cdot$s^{-1}(last blue trace). This power corresponds to 55 zW. e) Relation between the number of detected photon and the number of incident photon allowing to extract the efficiency $\eta = 0.43$ and $\alpha_\mathrm{d} = 84$ s^{-1}.

an increase in efficiency ($\eta_{\mathrm{d}} = 0.43$ vs $\eta_{\mathrm{d,old}} = 0.2$). The characterization of these SMPD crucial figures of merit is shown in Figure 2.3d,e.

In the Chapter 5, we detail the design and fabrication process of the detector. The Figure 2.3c gives an overview of the SMPD chip. The orange (resp. green) resonators correspond to the buffer (resp. waste) modes. The transmon qubit with its characteristic large capacitor is represented in blue, with its dedicated pump line in purple. The full characterisation of the SMPD is reported in Chapter 6.

2.2.2 Detecting a single Er^{3+} electron spin in a scheelite crystal

The new SMPD design described in the first part of the thesis is then used to detect single spins from the fluorescence signal they emit during their relaxation. Since the microwave background is strongly attenuated at 10 mK, photon counting is the appropriate method to detect this signal, which consists of a stream of single photons.

To achieve single-spin detection sensitivity in 1 second, the corresponding power should be of the same order of magnitude as the minimum power detectable by the SMPD in 1 s: 10^{-22} W (see last section). An electron spin in free space at the typical frequency $\omega/2\pi = 8$ GHZ spontaneously emits a photon at a rate of 10^{-12} s^{-1}, i.e a life-time of ≈ 30000 years. When inserted into a host crystal, relaxation by phonon generation becomes dominant, increasing the spontaneous relaxation rate to ≈ 1 s^{-1}. To make the radiative relaxation rate dominant, one has to use the Purcell effect [Pur46] by coupling the spins to a small mode volume and low loss resonator. Reaching this so-called Purcell regime was achieved in 2016 in our group [Bie+16] for bismuth impurities embedded in silicon.

Our experimental system consists of a pure Scheelite crystal $\mathrm{CaWO_4}$ containing traces of erbium (~ 1 ppb). The Er^{3+} ions that replace the Ca^{2+} (see Figure 2.4a), form a paramagnetic defect with a spin degree of freedom. The electronic structure of an erbium ion is complex. The wave functions of the eleven electrons in its valence band hybridise strongly to give a first degenerated energy scale with a fundamental optical transition at a of 1.5 μm wavelength. The crystal field within the $\mathrm{CaWO_4}$ weakly perturbs this energy structure and lifts the degeneracy of the ground state levels into eight Kramers doublets [Kra30]. The remaining degeneracy is ensured by the Kramers theorem: species with an odd number of electrons remain doubly degenerate due to time-reversal symmetry. Each of the Kramers doublets therefore behaves as effective spin-1/2 whose degeneracy can be lifted by a magnetic field which breaks the time reversal symmetry, i.e. the Zeeman effect. The Landé factor of the system depends strongly on the symmetry of the crystal [Enr71; Ber+09] as the effective spin results from an interaction between the ion and the crystal field. The $\mathbf{g}$ tensor is therefore anisotropic with $\mathrm{g_c} = 8.38$ and $\mathrm{g_{a,b}} = 1.25$ (see Figure 2.4a for axis definition).

The choice of the $\mathrm{CaWO_4}$ crystal is interesting because of its low magnetic impurity content, dominated by the 0.143 fraction of $^{183}\mathrm{W}$ isotopes that have a nuclear spin. The properties of this experimental platform were investigated in great detail by Marianne Le Dantec using ID-ESR methods [Le +21] and then by Eric Billaud using FD-ESR [Bil+22; Bil23].

The spin-photon coupling takes place in a 2D superconducting microwave resonator of frequency $\omega_0/2\pi = 7.3$ GHz patterned at the top of the crystal in a niobium film. As shown in Figure 2.4b, it consists of a large interdigitated capacitor shunted by a nanowire aligned along the crystal c-axis, that makes an inductor. The static magnetic field $\boldsymbol{B_0}$ applied parallel to the wire allows the spins to be brought into resonance with the resonator. The nanowire magnetic field that makes the coupling to the spins, transverse to the nanowire, thus lies in the (a, b) plane where the g factor is maximum. The Figure 2.4c shows a simulation of the coupling strength $g_0/2\pi$ in function of the spin position in the neighborhood of the nanowire. With our experimental parameters, we reach couplings of a

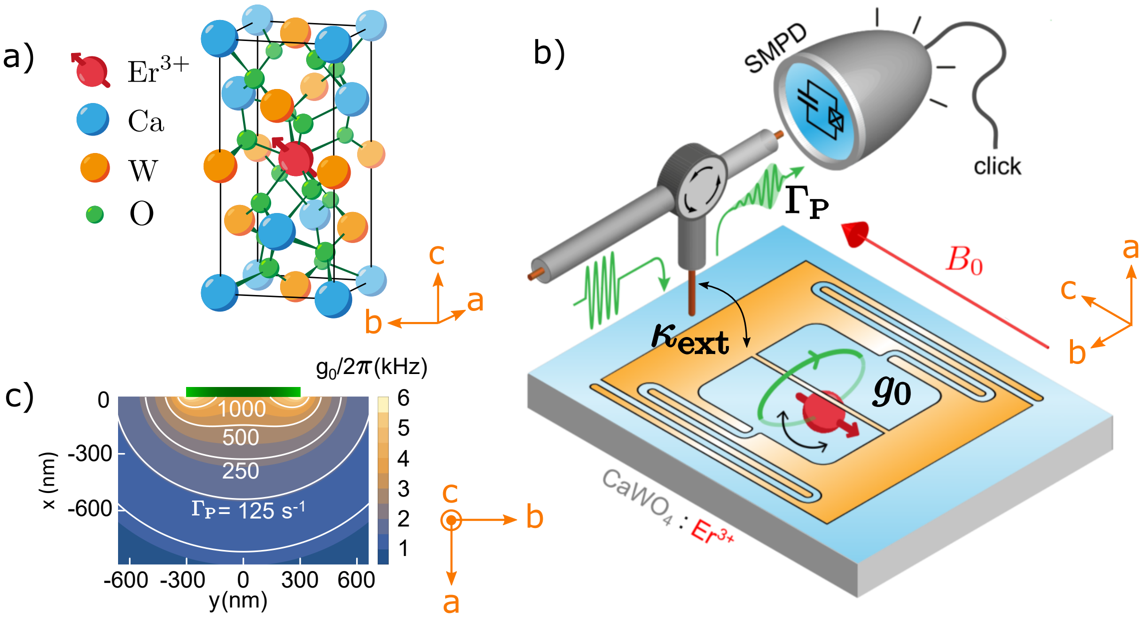

Figure 2.4: **Experimental platform** a) Schematic of the $CaWO_4$ lattice centered around a Er^{3+} ion that have replaced a Ca^{2+}. Oxygens are removed for clarity. A spin degree of freedom is represented for the Er^{3+} ion. The crystal symmetry is tetragonal around the axis c, which means axis a and b are equivalent. b) Schematic of the overall experiment. A microwave resonator (orange) composed of an interdigitated capacitor shunted by a nanowire is patterned in niobium layer (blue) at the top of the crystal (grey). The resonator is couple the line with the strength κ_{ext}. The nanowire allows the coupling of the spin to the resonator with the strength g_0. The spins are excited by populating the microwave resonator with a microwave pulse. Then, they relaxes radiatively due to the Purcell effect generated by the coupling. Finally, the resulting photons are routed to the SMPD with a circulator. c) Simulation of the coupling strength g_0 and the corresponding Purcell rate Γ_P as the function of the spin position in the (a, b) plane. The green rectangle represents the nanowire cross section.

few kHz, which yields a Purcell rate $\Gamma_\text{P} \sim 1000\ \text{s}^{-1}$ for the most strongly coupled spins. The corresponding instantaneous power $P = 5 \cdot 10^{-21} W$ puts us in a favorable situation for single spin detection. The design and the fabrication of the microwave resonator was realized by Zhiren Wang [Wan+23]. The full experiment, sketched in Figure 2.4b, consists in exciting the spin ensemble with a microwave pulse applied on the resonator and collecting the emitted microwave photons. The spin sample is simply connected to the SMPD with a low loss coaxial cable. A simple microwave circulator orients the collected fluorescence photons to the detector.

The Figure 2.5a represents a spectroscopy in the magnetic field realized with this experimental configuration. For each value of the magnetic field amplitude B_0, the spin ensemble is excited at low power in order to select the most strongly coupled spins. The fluorescence photons are then collected by the SMPD. We define an integration window with a duration of T_{int} over which we average the number of detection events (or clicks) $\langle C \rangle$. The resulting spectrum appears as a sum of narrow, unevenly distributed peaks centered around $B_0 = \omega_0/(\text{g}_\text{c}\mu_\text{B})$. We show in the thesis that each individual peak corresponds to a single spin by studying the photon emission statistics. This result is comparable to the first detection of a single molecule using an optical photon detector [OB90], but for a spin emitting in the microwave domain.

The fluorescence signal associated with a single spin is shown in Figure 2.4b. The

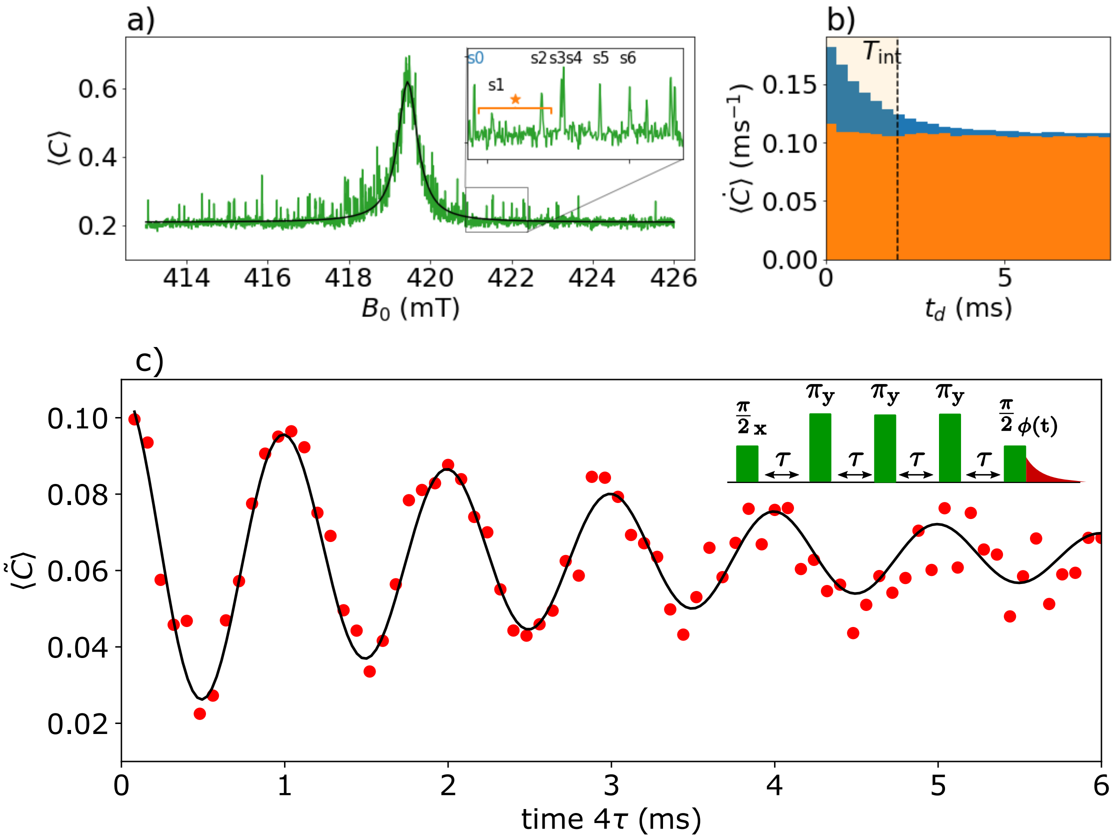

Figure 2.5: **Single spin detection with FD-ESR** a) Spin spectroscopy at low power (~ -107 dBm at sample input), with an integration window of 2 ms. $\langle C\rangle$ represents the average number of clicks during the integration time T_{int}, B_0 is the amplitude of the static magnetic field applied. Green line is measured data, black line is a Lorentzian fit. Note that the angle θ varies linearly between $-0.016°$ and $0.016°$ over the scan. b) Average click rate $\langle\dot{C}\rangle$ as the function of the time. Blue histogram represents the fluorescence signal coming from the spin labeled s_0 on the inset of (a). Orange histogram is the background and correspond to the SMPD dark count. c) Dynamical decoupling experiment with 3 refocusing π-pulses. The background corrected average number of clicks $\langle\tilde{C}\rangle$ is plotted as the function of the time 4τ between the $\pi/2$ pulses. A linearly increasing phase $\phi(\tau) = 2\pi\Delta\tau$ with $\Delta = 0.001\,\mathrm{MHz}$ is imparted on the last pulse. Corresponding fit and its envelope (solid and dash lines) are shown, yielding the coherence time $T_2^{\mathrm{DD}} = 2.99 \pm 0.03\,\mathrm{ms}$. Data taken at $B_0 = 422.085$ mT and $\theta = -0.003°$.

observed radiative relaxation time $T_1 \approx 1.5$ ms is in good agreement with the expected value. Coherence measurements are performed on various single spins. The Figure 2.4c shows the results of a dynamical decoupling experiment carried out on the spin labeled s_0 in Figure 2.4a. A coherence time of ~ 3 ms is reached, thus reaching the radiative limit $2T_1$.

2.2.3 Probing the ^{183}W nuclear spins with the electronic erbium spin

Controlling a single electronic spin opens the way to measuring its local environment. In particular, the electron spin can be used to measure and control the surrounding bath of nuclear spin thanks to the hyperfine coupling, the magnetic dipole-dipole interaction between the nuclear and electronic spins.

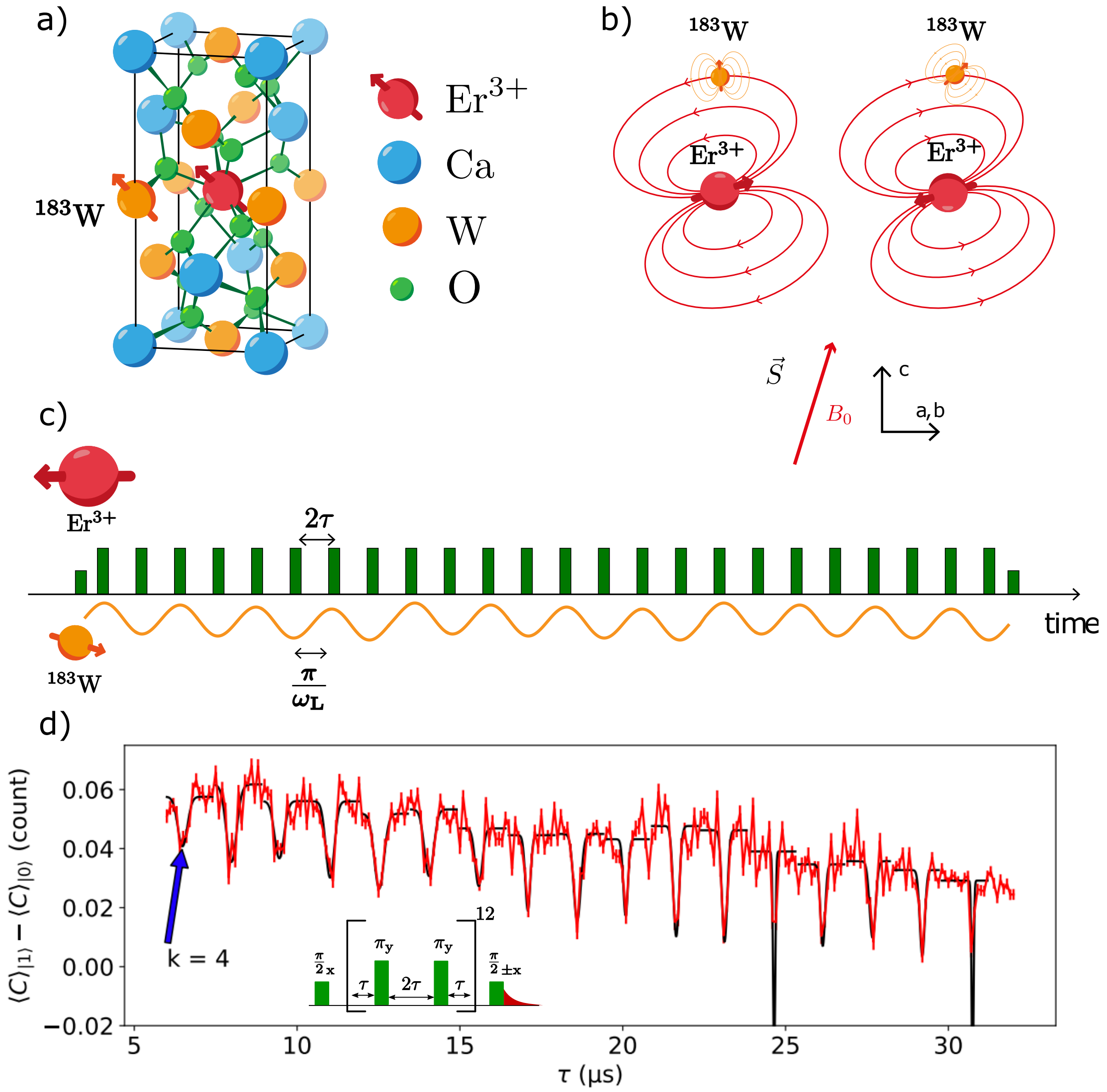

Figure 2.6: ^{183}W **nuclear spin detection with dynamical decoupling sequence.** a) Er^{3+} electron spin with a ^{183}W nuclear spin 1/2 in its immediate environment. b) electron-nuclear spin interaction. The electron spin state influences the quantization axis of the nuclear spin due to its larger magnetic moment. The anisotropic **g**-tensor causes a misalignment between the electron spin quantization direction and the magnetic field orientation. c) Dynamical decoupling sequence with 24 refocusing $\pi-$pulses applied to the electron spin. Due to the nuclear spin quantization dependence with the electron spin state, a resonance condition exists between the interpulse delay 2τ and the nuclear spin Larmor frequency ω_L. d) Corresponding dynamical decoupling experiment. The last pulse projects the final either on the ground of the excited state. The associated average number of clicks is noted $\langle C\rangle_{|0\rangle}$ and $\langle C\rangle_{|1\rangle}$. The contrast between the projection is plotted as the function of the time τ. the dips spaced by $\Delta\tau = \pi/\omega_L = 1.52$ μs are caused by interaction with the ^{183}W nuclear spin bath. The first dip at $\tau_4 = 6.44$ μs is the fourth order resonance. Red lines are data, solid black lines are Gaussian fit of each dips.

This concept was first demonstrated in 2012 for the NV centres of diamond [Tam+12; Kol+12; Lon+13], individually readout using an optical transition. The principle of the experiment is to divert the concept of dynamical decoupling introduced in 1999 [VKL99] for open quantum system. Instead of using the dynamical decoupling sequence to isolate the electron spin from its noisy environment, it is used to bring it into resonance with a specific nuclear spin.

In the case of our experiment, the nuclear spin bath consists of the $I = 1/2^{183}$W isotope nuclei, with 0.145 natural abundance. They randomly occupy the tungsten sites and interact with the Er^{3+} electron spin by magnetic dipolar coupling (see Figure 2.6a,b). Since the magnetic moment of the electron spin is 4 to 5 orders of magnitude larger than that of the nuclear spin, we can apply the secular approximation. The electron spin drives the nuclear spins whose quantization axes depend on the electron spin state as shown in Figure 2.6b. The effect is at the heart of the experiment. Although the electronic spin cannot be flipped by the hyperfine interaction, it can pick a phase, which provides a hand on the nuclear spin quantum state.

The dynamical decoupling sequence we have used consists in a CPMG sequence with of 24 refocusing $\pi-$pulses (see Figure 2.6c). The electron spin, placed in a superposition of states by the initial $\pi/2-$pulse, it is then tilted 24 times by the series of π-pulses, and then reprojected on the z-axis of the Bloch sphere by the last $\pi/2-$pulse. We then measure its fluorescence signal with the SMPD.

Each time a $\pi-$pulse is applied to the electron spin, the rotation axis of the nuclear spin changes. If this axis tilt is in phase with the Larmor frequency ω_{L} of the nuclear spin, the latter will be gradually rotated after each $\pi-$pulse. This resonance condition can be expressed in terms of 2τ, the inter-pulse time in the CPMG sequence, as $2\tau_k = (2k+1)\pi/\omega_{\mathrm{L}}$ for $k \in \mathbb{N}$. For these specific inter-pulse times, the CPMG sequence entangles progressively the nuclear and the electron spins. The entanglement level being controlled by the the number of π-pulses.

The entanglement information can be retrieved thanks to the electron state. Indeed, if τ is out of resonance, the spins are not entangled after the 24 π pulses and the electron spin remains in the initial superposition state. Decoherence is the only mechanism that influences the final result. On the contrary, if $\tau = \tau_k$, an entanglement occurs and the final state of the system change. From the point of view of the electron spin, this can be seen as a rapid loss of coherence which appends for each τ_k.

It is therefore sufficient to measure the final state of the electron spin to reconstruct the dynamics of the entanglement. The measurement of the probability P_{x} that the electron spin remains in its initial superposition is shown in Figure 2.6d. As expected, we observe a regular pattern of dips, spaced by $\Delta\tau = \pi/\omega_{\mathrm{L}} = 1.52$ confirming the interaction between the electron spin and a ^{183}W nuclear spin bath. This experiment is the first report on the detection of ^{183}W nuclear spins using an individual electron spin.

To conclude this introduction, it is interesting to step back and look at the chain of concepts that lead to this end result. We use a state-of-the-art Josephson parametric amplifier to single-shot readout the state of a high-coherence transmon qubit. This artificial atom, inserted in a cQED architecture, allows to signal the passage of a microwave photon. By working on the spin-photon coupling, we are able to use this photon detector architecture to detect a single Er^{3+} electron spin embedded in a $CaWO_4$ crystal. Finally, we dive deeper into the description of matter by using the electron spin itself as a proxy to detect its local environment and in particular the ^{183}W nuclear spins. This new chain, combining superconducting circuits, photon counting and ESR spectroscopy, provides unequaled detection sensitivity and opens the way to numerous applications in quantum sensing and quantum computing.

Part I

Single microwave photon detector with an absolute power sensitivity of 10^{-22} W/$\sqrt{\text{Hz}}$

Chapter 3

Circuit QED

The research work carried out in this thesis belongs to the field of circuit quantum electrodynamics (cQED) , i.e. the domain of quantum superconducting circuits in interaction with quantized electromagnetic fields in the microwave frequency domain. Circuit QED itself belongs to the domain of Quantum electrical circuits that was initiated in the early 1980s, for addressing the following question: Can electrical circuits that are unquestionably macroscopic compared to atoms reach a quantum regime ? This issue was first addressed following a clever suggestion of A.J. Leggett [Leg80]. Leggett made the point that a Josephson junction, i.e. a tunnel junction between superconducting electrodes, is an electrical component with a single degree of freedom, the superconducting phase difference across it, and that the knowledge of the classical dynamics of this variable is sufficient for predicting its properties in the quantum regime of the Josephson junction, if such a quantum regime exists. Leggett noticeably considered the non classical phenomenon of Macroscopic Quantum Tunnelling (MQT). MQT predicts that a Josephson junction current biased below its critical current can escape out of the zero-voltage state by quantum tunneling of the superconducting phase difference out of its potential well. Different experiments indeed observed this phenomenon, but the most conclusive ones were carried out at U.C. Berkeley in the group of John Clarke [Cla+88]. In the course of these experiments, Devoret, Martinis and Clarke furthermore provided evidence for the quantum levels of a current-biased Josephson junction. Research in this domain was further developed at Saclay in Quantronics group ([Est+89]) by coupling a current-biased Josephson junction to a tunable microwave resonator, i.e. already a circuit QED device, but quantum coherence was not considered as good enough for quantum state manipulation.

The interest in quantum electrical circuits got suddenly boosted by the theoretical developments of quantum information and of quantum computing, which triggered a very active search of physical systems suitable for implementing the quantum bits requested for making a quantum processor. In the late 1990s, Bouchiat et al. from Quantronics [Bou+98] made a simple circuit consisting of a charge biased superconducting electrode in contact with a superconducting reservoir via a Josephson junction. This circuit was nicknamed the single Cooper pair box. They demonstrated that its ground state can be placed in a coherent superposition of two charge states of the superconducting electrode differing by a single Cooper pair passed through the junction. A quantum coherent superposition of the ground state of this circuit and of its first excited state was demonstrated soon after at NEC by Nakamura, Pashkin and Tsai [NPT99]. This was the first quantum bit circuit. An improved version of the single Cooper pair box circuit fitted with single-shot readout and partial protection against decoherence allowed Quantronics to reproduce all the basic quantum manipulations made on atoms [Vio+02], with a coherence time in the microsecond range.

Inspired by the cavity QED experiments carried out on atoms coupled to resonant cavities [HR06], [Kim98] noticeably at the LKB of the ENS Paris in the Haroche-Raimond team, Wallraff et al. [Wal+04] first demonstrated at Yale in 2004 the strong coupling regime between a Cooper pair box and a quantum microwave resonator. Addresing the Cooper pair bow with microwave signals allowed them to manipulate the qubit, to perform its readout, and to filter out the noise coupled to the qubit. In order to further reduce decoherence due to the charge noise acting on the Cooper pair box, Koch et al. [Koc+07] operated the Cooper pair box in the so-called phase regime, in which it behaves as an anharmonic oscillator. This is the Transmon version of the Cooper pair box which is presently the most widely used superconducting qubit for making quantum processors. From then on, the performance of superconducting qubits increased year by year, and individual Transmon qubits presently (early 2023) reach a coherence time in the millisecond range [Wan+22], [Som+21], obtained thanks to the use of tantalum in the superconducting circuit connected to the Josephson junction.

The single microwave photon detector (SMPD) at the heart of this thesis is part of this research area. Here we take advantage of the progress achieved in circuit QED research to build a detector with ultimate single spin sensitivity. The elements of circuit theory needed to understand the SMPD design are introduced in this chapter.

3.1 Quantum oscillator and transmission line

3.1.1 Quantum LC oscillator

The harmonic LC resonator is a central building block in circuit QED. It is composed of an inductor L and a capacitor C (see Figure 3.1). This system has a single degree of freedom with two conjugated electrical variables, the flux in the inductor and the charge on the capacitor. These variables are linked to the current and voltage by the Faraday law and the current-charge relation:

$$\Phi = \int_{-\infty}^{t} v(t^{'})\mathrm{d}t^{'} \tag{3.1}$$

$$Q = \int_{-\infty}^{t} i(t^{'})\mathrm{d}t^{'}. \tag{3.2}$$

The constitutive relations linking the voltage and current at the terminals of the coil and capacitor set the relations between the flux and the charge:

$$Q = C\dot{\Phi} \qquad\qquad \Phi = -L\dot{Q} \tag{3.3}$$

These equations can be used to write the Lagrangian of the system as the function of the flux Φ:

$$\mathcal{L} = \frac{C\dot{\Phi}^2}{2} - \frac{\Phi^2}{2L} \tag{3.4}$$

We then write the momentum associated to Φ and Q as:

$$\frac{\partial \mathcal{L}}{\partial \dot{Q}} = \Phi \qquad\qquad \frac{\partial \mathcal{L}}{\partial \dot{\Phi}} = Q \tag{3.5}$$

These definitions lead to the Poisson bracket $\{\Phi, Q\} = 1$, proving that these variables are conjugate. Using the Dirac quantization method, also called canonical quantization, one

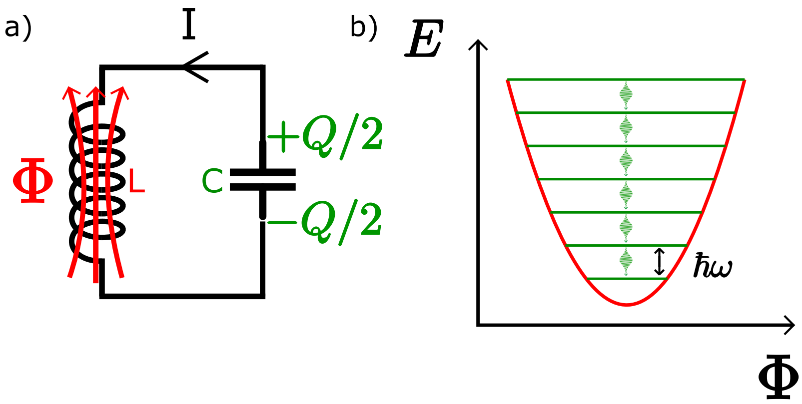

Figure 3.1: **LC resonator.** (a) Electrical representation of a LC resonator with flux Φ passing through the inductance L. The capacitor C has a charge Q distributed on its two electrodes. (b) Energy of the LC oscillator as the function of Φ. The energy levels are spaced by $\hbar\omega_0$.

can promote the flux Φ and its conjugate momentum Q into quantum operators obeying the commutation relation:

$$[\hat{\Phi}, \hat{Q}] = i\hbar \tag{3.6}$$

The Hamiltonian of the system obtained from the Legendre transformation $\mathcal{H}_\mathrm{r} = \dot{\Phi}Q - \mathcal{L}$ is :

$$\mathcal{H}_\mathrm{r} = \frac{\hat{Q}^2}{2C} + \frac{\hat{\Phi}^2}{2L}. \tag{3.7}$$

With the inductance L and the capacitance C, one can construct two different physical parameters, the characteristic impedance of the circuit $Z_\mathrm{c} = \sqrt{L/C}$ and the resonance frequency of the oscillator $\omega_0 = 1/\sqrt{LC}$.

In the same way as done for a mechanical oscillator, one defines the ladder operators $\hat{a}$ and $\hat{a}^\dagger$:

$$\hat{a}^\dagger = \frac{1}{\sqrt{2\hbar Z_\mathrm{c}}}(\hat{\Phi} - iZ_\mathrm{c}\hat{Q}) \tag{3.8}$$

$$\hat{a} = \frac{1}{\sqrt{2\hbar Z_\mathrm{c}}}(\hat{\Phi} + iZ_\mathrm{c}\hat{Q}) \tag{3.9}$$

$$\tag{3.10}$$

These operators satisfy the usual relation $[\hat{a}, \hat{a}^\dagger] = 1$. Their eigenstates are the coherent states $|\alpha\rangle$. The Hamiltonian can be rewritten as:

$$\mathcal{H}_\mathrm{r} = \hbar\omega_0 \left(\hat{a}^\dagger\hat{a} + \frac{1}{2}\right) \tag{3.11}$$

The eigenvalues of this Hamiltonian are $E_\mathrm{n} = \hbar\omega_0(n + 1/2)$ and are associated with the eigenstates $|n\rangle$, called Fock states. The parameter n is the number of photons in the cavity. We can also express the voltage and current operators in terms of ladder operators using the relations: $\hat{V} = \hat{Q}/C$ and $\hat{I} = \hat{\Phi}/L$. This gives the expressions:

$$\hat{V} = i\omega_0\sqrt{\frac{\hbar Z_c}{2}}(\hat{a}^\dagger - \hat{a}) = i\delta V(\hat{a}^\dagger - \hat{a}) \tag{3.12}$$

$$\hat{I} = \omega_0\sqrt{\frac{\hbar}{2Z_c}}(\hat{a}^\dagger + \hat{a}) = \delta I(\hat{a}^\dagger + \hat{a}) \tag{3.13}$$

where $\delta V = \omega_0\sqrt{\hbar Z_0/2}$ and $\delta I = \omega_0\sqrt{\hbar/(2Z_0)}$ are the root-mean-square (rms) fluctuations of the voltage and current in the resonator ground state, i.e. the rms vacuum fluctuations.

The electromagnetic field at position $\boldsymbol{r}$ near the LC resonator depends on the resonator geometry and on the position, but always takes the following form:

$$\hat{\boldsymbol{E}}_1(\boldsymbol{r}) = i\boldsymbol{\delta E}(\boldsymbol{r})(\hat{a}^\dagger - \hat{a}) \tag{3.14}$$

$$\hat{\boldsymbol{B}}_1(\boldsymbol{r}) = \boldsymbol{\delta B}(\boldsymbol{r})(\hat{a}^\dagger + \hat{a}) \tag{3.15}$$

Here $\boldsymbol{\delta E}(\boldsymbol{r})$ and $\boldsymbol{\delta B}(\boldsymbol{r})$ are the root-mean-square (rms) vacuum fluctuations of the electric and magnetic field. These fluctuations will play an important role in our experiments because they directly give the coupling constant to a microscopic object placed in the field of the resonator. It is important to note that these quantities directly involve the characteristic impedance of the LC oscillator that can be controlled by design.

3.1.2 Lumped element and co-planar waveguide

As just mentioned above, the electromagnetic field generated by the oscillating current and voltage in the resonator is determined by the resonator geometry. In this thesis, we use two types of geometry depending on the function of the resonator.

The first type corresponds to "lumped-resonators". In this configuration, the capacitor and inductance size is significantly smaller than the wavelength $\lambda_0 = 2\pi c/\omega_0$ where c is the speed of light in the medium.

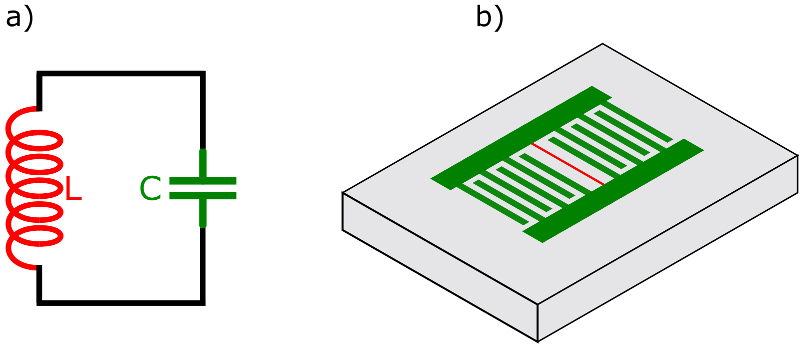

Figure 3.2: **Lumped-element.** (a) Lumped-elements model of an LC resonator, the current passing through the inductance L generates a spatially-dependent magnetic field $\hat{\mathbf{B}}(\mathbf{r})$. (b) Realistic illustration of an LC resonator design, here the role of the inductance (red) is played by a wire shunting the two capacitor plates (green).

The figure Figure 3.2b shows an example of physical implementation: an interdigitated capacitor (in green) patterned in a a thin metallic film, is connected to a nanowire which plays the role of the inductance (in red). The electric field is concentrated between the capacitor electrodes, whereas the magnetic field is localized in the vicinity of the nanowire.

Such a spatially well defined magnetic field is suitable for coupling the resonator to a small ensemble of spins in the substrate of the resonator, and eventually to a single one.

The second type of resonator we use is based on coplanar waveguide (CPW) transmission line sections with boundary conditions at the ends. A CPW transmission line consists of a central conducting line separated from the ground plane by two insulating gaps (Figure 3.3a).

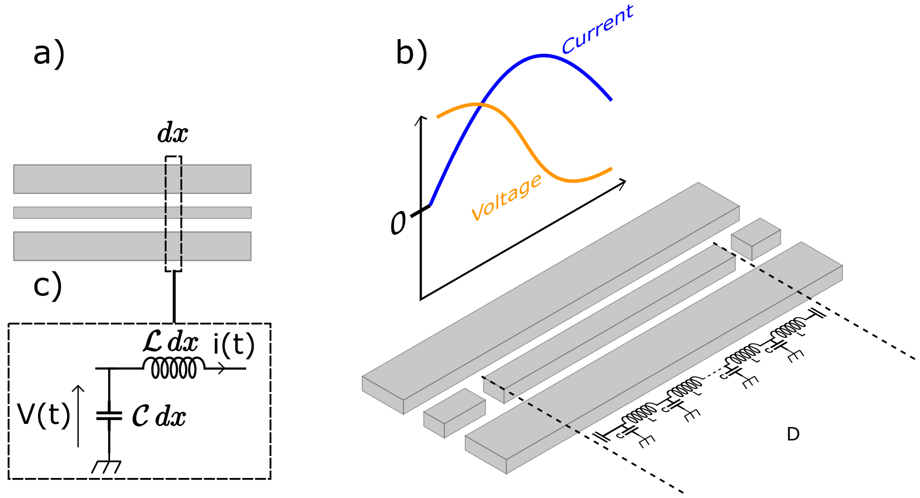

Figure 3.3: **LC resonator.** (a) Coplanar waveguide, the central conductor track is separated from the ground plane by two gaps. (b) Electrical diagram of a section of coplanar waveguide consisting of a LC oscillator with an inductance $\mathcal{L}dx$ and a capacitance $\mathcal{C}dx$. The quantity $\sqrt{\mathcal{L}/\mathcal{C}}$ defined the line impedance. (c) Representation of a CPW resonator. The conducting track is interrupted on both side by a gap. The edges correspond to current node and voltage maximum. This open-open boundary conditions defined a $\lambda/2$ resonator.

This ensemble is patterned on the top of a dielectric substrate and can be modeled by a chain of infinitesimal lumped LC elements. Each segment of length $\mathrm{d}x$ has a series inductance $\mathcal{L}\mathrm{d}x$ and a parallel capacitance $\mathcal{C}\mathrm{d}x$ with $\mathcal{L}$ and $\mathcal{C}$ The inductance and capacitance per unit of length (Figure 3.3b). The characteristic impedance of the line is $Z_\mathrm{c} = \sqrt{\mathcal{L}/\mathcal{C}}$. The impedance mismatch at the two edges yields different boundary conditions and determines the standing wave resonant modes of the structure, with a fundamental mode ω_0 and a series of harmonics.

In this thesis we use two kinds of boundary conditions. The first one will be a open-open configuration in which the fundamental mode of a CPW section with length D corresponds to the length $D = \lambda/2$. The frequencies of the modes are $\omega_\mathrm{n}/2\pi = nc/2D$ with $n = 1, 2...$ and c the speed of light in the transmission line. This configuration is shown in (Figure 3.3c).

The second configuration is the open-short configuration, yielding to a $D = \lambda/4$ length for the fundamental mode. In this case the mode frequencies are $\omega_\mathrm{n}/2\pi = (2n-1)c/4D$ with $n = 1, 2....$ This configuration in which $\omega_2 = 3\omega_1$ is interesting in order to avoid cross-talk between different elements of a more complex circuit.

A great advantage of CPW resonators is the easy control of the frequency by adjusting the length D. This geometry is thus well suited when this control is important, as is case for the resonators in the SMPD device.

3.1.3 Propagating modes in lossless transmission lines

In our experiment, the different quantum devices including the resonators described in Section 3.1.1 are interconnected with lossless CPW transmission lines modeled by a chain of lumped-elements as sketched in Figure 3.3a. This section sums up the main results on the modeling of lossless lines following the review [Cle+10].

3.1.3.1 Classical description

One readily obtains the telegrapher's equations from the analysis of an elementary LC cell with infinitesimal length as sketched in Figure 3.3b.

The well-known solutions to this equation are a superposition of waves propagating to the right and left:

$$V(x,t) = V^{\rightharpoondown}(x,t) + V^{\leftharpoonup}(x,t) \tag{3.16}$$

$$I(x,t) = \frac{V^{\rightharpoondown}(x,t) - V^{\leftharpoonup}(x,t)}{Z_{\mathrm{c}}} \tag{3.17}$$

$$V^{\leftrightharpoons}(x,t) = V_0^{\leftrightharpoons}\cos(\omega t \pm x\omega/c + \phi_0^{\leftrightharpoons}) \tag{3.18}$$

With the phase velocity $c = 1/\sqrt{\mathcal{L}\mathcal{C}}$ and the initial phases $\phi_0^{\leftrightharpoons}$. The current flowing in the infinitesimal inductance $\mathcal{L}\,dx$ is related to $V^{\leftrightharpoons}$ via the characteristic impedance $Z_{\mathrm{c}} = \sqrt{\mathcal{L}/\mathcal{C}}$.

In the case of an infinite line, the left and right propagating waves are independent. On the contrary, if the line is connected to a load impedance Z_l (as for a CPW resonator), the current and voltage respect Ohm's law at the boundary (taken at $x = 0$ for simplicity), which yields to:

$$Z_l = \frac{V(0,t)}{I(0,t)} = \frac{V^{\rightharpoondown}(t) + V^{\leftharpoonup}(t)}{V^{\rightharpoondown}(t) - V^{\leftharpoonup}(t)} Z_{\mathrm{c}} \tag{3.19}$$

The presence of an impedance mismatch between the line and the load generates a reflected wave. From the equation Equation 3.19 , one obtains the reflection coefficient R :

$$\frac{V^{\leftharpoonup}(t)}{V^{\rightharpoondown}(t)} = \frac{Z_{\mathrm{c}} - Z_{\mathrm{l}}}{Z_{\mathrm{c}} + Z_{\mathrm{l}}} =: R \tag{3.20}$$

R can be measured with a Virtual Analyzer Network (VNA). If the load is an LC resonator, the R value taken for different frequencies $\omega/2\pi$ gives the resonance frequency and the quality factor.

3.1.3.2 Quantum description

We now consider a quantum description of the line following refs. [Cle+10] and [Flu14]. For each direction of propagation along a transmission line (left and right), and for each monochromatic mode of the electromagnetic field (identified by its frequency ω), one can associate a pair of operators $\hat{a}^{\leftrightharpoons}(\omega)$ and $\hat{a}^{\leftrightharpoons\dagger}(\omega)$ which respectively annihilate and create a photon in that mode and propagation direction. These operators satisfy the commutation relation $[\hat{a}^{\leftrightharpoons}(\omega), \hat{a}^{\leftrightharpoons\dagger}(\omega')] = 2\pi\delta(\omega - \omega')$.

Typically, we are interested in a narrow-band frequency region centered around ω_0. In this case it is interesting to perform a Fourier-transform of $\hat{a}^{\leftrightharpoons}(\omega)$ in order to work in the time domain. In addition, we move in the rotating frame at the considered frequency $\omega_0/2\pi$. The new operators $\hat{a}^{\leftrightharpoons}(t)$ satisfy the commutation relation $[\hat{a}^{\leftrightharpoons}(t), \hat{a}^{\leftrightharpoons\dagger}(t')] = \delta(t-t')$. Under these conditions, the propagating voltage can be expressed at $x = 0$ as:

$$\hat{V}^{\leftrightharpoons}(t) = \sqrt{\frac{\hbar\omega_0 Z_\mathrm{c}}{2}} \left(\hat{a}^{\leftrightharpoons}(t) + \hat{a}^{\leftrightharpoons\dagger}(t)\right) \tag{3.21}$$

The propagating current is easily calculated using Equation 3.17.

The $\hat{a}^{\leftrightharpoons}(t)$ are operators describing the field amplitude flux associated to a propagating mode, thus the power carried by the quasi-monochromatic wave of frequency ω_0 is described by the quantum observable

$$\hat{P}^{\leftrightharpoons}(t) = \hbar\omega_0 \hat{a}^{\leftrightharpoons\dagger}(t)\hat{a}^{\leftrightharpoons}(t). \tag{3.22}$$

It is interesting to note that the basis chosen to write the operators $\hat{a}^{\leftrightharpoons}(\omega)$ and $\hat{a}^{\leftrightharpoons}(t)$ represent two extreme ways of dividing the frequency-time plan. It's either an infinitesimal time tiling or an infinitesimal frequency tiling. This representation is not realistic insofar as our measuring equipment (typically a VNA) have a certain frequency and temporal resolution. A more practical choice is to use a wavelet basis where each wavelet is defined on a cell of area $\Delta\omega\Delta t = 2\pi$ in order to preserve the time-energy Heisenberg uncertainty: $\Delta E \Delta t \geq \hbar/2$. Each cell can be labeled with two indices representing its position in time and frequency. To form a correct basis for the frequency-time plane, the wavelet collection $u_\mathrm{ij}(t)$ (i and j labeling the wavelet area in the frequency-time plan) must be orthogonal which results in the orthogonality relations:

$$\int_{-\infty}^{+\infty} u_{n,k}(t) u^*_{p,l}(t) dt = \delta_{n,p}\delta_{k,l} \tag{3.23}$$

$$\int_{-\infty}^{+\infty} u_{n,k}(\omega) u^*_{p,l}(\omega) d\omega = \delta_{n,p}\delta_{k,l}. \tag{3.24}$$

This basis can then be used to represent the operators $\hat{a}^{\leftrightharpoons}(t)$:

$$\hat{a}^{\leftrightharpoons}_{i,j} = \int \hat{a}^{\leftrightharpoons}(t) u_{i,j}(t) dt. \tag{3.25}$$

Where i labels the time position and$j$ the frequency position. Each $\hat{a}^{\leftrightharpoons}_{i,j}$, $\hat{a}^{\leftrightharpoons\dagger}_{i,j}$ describes a pair of creation/annihilation operators which create/destroy photons of frequency centered around ω_0 at the time t_i. These operators satisfy the commutation relation $[\hat{a}_i, \hat{a}_i{}^\dagger] = 1$ which is similar to the one describe for the harmonic oscillator in Section 3.1.1. In the following of this manuscript, we will consider the propagating operator at the entrance of the circuit (chosen at x=0). We therefore rename the operators $\hat{a}^{\leftharpoonup}(x=0)$ (resp $\hat{a}^{\rightharpoonup}(x=0)$) as $\hat{a}_\mathrm{in}$ (resp $\hat{a}_\mathrm{out}$).

3.1.4 LC resonator connected to a transmission line

3.1.4.1 Resonator coupling and losses

In our experiment, the transmission lines are both used to measure and inter-connect the resonators. As shown in Figure 3.4a, the model consists in a parallel RLC resonator connected to the transmission line of impedance $Z_\mathrm{c} = 50\Omega$ with the capacitance C_c.

The cavity has internal losses modeled by the resistor R. These losses result in a decrease of the intra-cavity field at the rate κ_int. They are typically caused by dissipation at the dielectric-metal or metal-air interfaces. From the cavity, the coupling to the line also corresponds to losses, as it gives rise to a rate of energy leakage κ_ext through the capacity C_c.

The total impedance of this circuit is:

$$\frac{1}{Z_t} = \frac{1}{R} + iC\omega + \frac{1}{iL\omega} + \frac{1}{Z_\mathrm{c} + \frac{1}{iC\omega}} \tag{3.26}$$

$$= \frac{1}{R} + \frac{Z_\mathrm{c} C_\mathrm{c}^2 \omega^2}{1 + (Z_\mathrm{c} C_\mathrm{c} \omega)^2} + i\left[\left(C + \frac{C_\mathrm{c}}{1 + (Z_\mathrm{c} C_\mathrm{c} \omega)^2}\right)\omega - \frac{1}{L\omega}\right] \tag{3.27}$$

In most of cases, the circuit is operated in the high quality factor limit $Z_\mathrm{c} C_\mathrm{c} \omega \ll 1$, In this limit and close to the resonance frequency of the uncoupled RLC resonator $\omega_0 = 1/\sqrt{LC}$, one can define an equivalent $R'L'C'$ circuit (see Figure 3.4b) with:

$$L' = L \tag{3.28}$$

$$C' \approx C + C_\mathrm{c} \tag{3.29}$$

$$\frac{1}{R'} = \frac{1}{R} + \frac{1}{R_\mathrm{ext}} \tag{3.30}$$

$$R_\mathrm{ext} \approx \frac{1}{Z_\mathrm{c}'(C_\mathrm{c}\omega_0)^2} \tag{3.31}$$

The resonance frequency is now $\omega_0' = 1/\sqrt{L(C + Cc)}$. The line slightly re-normalizes the frequency of the uncoupled resonator. The quality factor, limited by energy leakage in the environment is $Q = R'\sqrt{C'/L'}$ [Poz11]. The decomposition of Q^{-1} into coupling and intrinsic losses gives the internal and external quality factors:

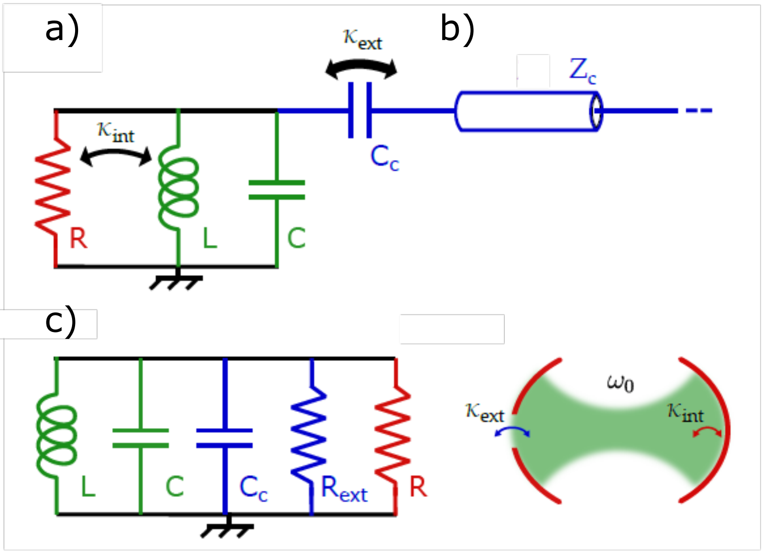

Figure 3.4: **LC resonator.** (a) RLC resonator connected to a transmission line of impedance Z_c through a capacitor. The field is dissipated inside the internal resistor R (red) at the rate κ_int. The connection to the line creates an energy leak to the outside at the rate κ_ext. (b) Equivalent circuit in the high quality factor limit and near of the frequency resonance. (c) Optics representation of the cavity with a semi-reflecting mirror.

$$Q_{\text{int}}^{-1} = R^{-1}\sqrt{\frac{L}{C'}} \tag{3.32}$$

$$Q_{\text{ext}}^{-1} = R_{\text{ext}}^{-1}\sqrt{\frac{L}{C'}} \tag{3.33}$$

The corresponding energy dissipation rates are $\kappa_{\text{int}} = \omega_0'/Q_{\text{int}}$ and $\kappa_{\text{ext}} = \omega_0'/Q_{\text{ext}}$.

In the rest of this manuscript we will write the different resonator frequencies ω to refer to the resonance frequency renormalized by the lines.

3.1.4.2 Input-output theory

In this section we derive the input-output equation which links the intra cavity field $\hat{a}$ introduced in Section 3.1.1 to the propagating operators $\hat{a}_{\text{in}}$ and $\hat{a}_{\text{out}}$ introduced in Section 3.1.3.2.

As shown in Section 3.1.4.1, in the high quality factor regime and close to the frequency resonance, the RLC circuit coupled to the line is equivalent to a renormalized R'L'C' circuit. In this regime, the circuit shown in Figure 3.5a can be considered as the general case. For simplicity, we will first consider the case without internal losses.

The Hamiltonian of the circuit obtained from a canonical quantization is:

$$\hat{H}_{\text{c}} = \frac{\hat{Q}^2}{2C} + \frac{\hat{\Phi}^2}{2L} - \hat{\Phi}\hat{I}(x=0) \tag{3.34}$$

where $\hat{I}(x=0) = \frac{\hat{V}(x=0)^{\rightharpoonup} - \hat{V}(x=0)^{\leftharpoonup}}{Z_{\text{c}}}$ is the propagating current operator at the entrance of the circuit. We first write the expression of $\hat{H_{\text{int}}} = -\hat{\Phi}\hat{I}$ as the function of the ladder operators in the vicinity of the resonance frequency ω_0:

$$\hat{H}_{\text{int}} = \sqrt{\frac{\hbar Z_{\text{c}}}{2}}(\hat{a}+\hat{a}^\dagger)\sqrt{\frac{\hbar\omega_0}{2R_{\text{ext}}}}(\hat{a}_{\text{in}} - \hat{a}_{\text{out}} + \hat{a}_{\text{in}}^\dagger - \hat{a}_{\text{out}}^\dagger) \tag{3.35}$$

A rotating wave approximation (RWA) then leads to:

$$\hat{H}_{\text{int}} = -\frac{\hbar}{2}\sqrt{\kappa_{\text{ext}}}(\hat{a}^\dagger(\hat{a}_{\text{in}} - \hat{a}_{\text{out}}) + \hat{a}(\hat{a}_{\text{in}}^\dagger - \hat{a}_{\text{out}}^\dagger)) \tag{3.36}$$

Here $\kappa_{\text{ext}} = Z_{\text{c}}\omega_0/R_{\text{ext}}$ which is the same definition given in Section 3.1.4.1.

The boundary conditions imposes that the circuit voltage and the line voltage at the input to the circuit are equal. Therefore, in terms of quantum operators:

$$\frac{\hat{Q}}{C} = \hat{V}^{\leftharpoonup}(t) + \hat{V}^{\rightharpoonup}(t) \tag{3.37}$$

Which can be decomposed in term of ladder operators:

$$-iC(\hat{a} - \hat{a}^\dagger) = \sqrt{\frac{\hbar\omega_0 R_{\text{ext}}}{2}}(\hat{a}_{\text{in}} + \hat{a}_{\text{out}} + \hat{a}_{\text{in}}^\dagger + \hat{a}_{\text{out}}^\dagger) \tag{3.38}$$

Separating the contribution of oscillating and counter-oscillating operators in the RWA, we get:

$$\boxed{\sqrt{\kappa_{\text{ext}}}\hat{a} = i(\hat{a}_{\text{out}} + \hat{a}_{\text{in}})} \tag{3.39}$$

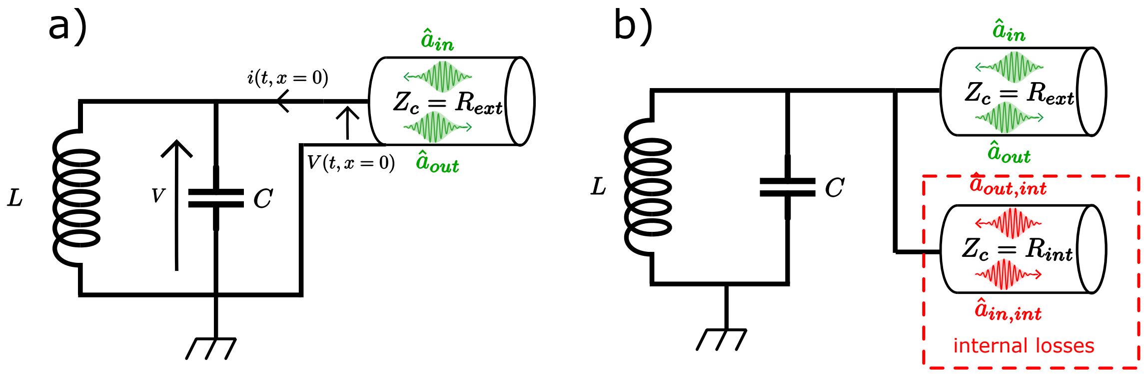

Figure 3.5: **input output illustration.** (a) Lossless resonator coupled to a transmission line. The operator $\hat{a}_{\text{in}}$ and $\hat{a}_{\text{out}}$ represent the propagating field. V represents the LC circuit voltage. $V(t,x=0)$ and $i(t,x=0)$ are the oscillating current and voltage at the line output. (b) modeling of the internal losses as an additional transmission line

We now describe the temporal evolution of the system. The dynamics is governed by the Heisenberg equation:

$$-i\hbar\frac{\partial\hat{a}}{\partial t} = [\hat{H}_r,\hat{a}] + [\hat{H}_{\text{int}},\hat{a}] + [\hat{H}_{\text{bath}},\hat{a}] \tag{3.40}$$

where $\hat{H}_r$ is defined in Equation 3.11 and H_{bath} represents the continuum of modes in the transmission line. This bath and the resonator are distinct modes, so $[\hat{H}_{\text{bath}},\hat{a}] = 0$. Calculating the commutator yields the following Heisenberg evolution equation:

$$\frac{\partial\hat{a}}{\partial t} = -i\omega_0\hat{a} + \frac{i\sqrt{\kappa_{\text{ext}}}}{2}(\hat{a}_{\text{in}} - \hat{a}_{\text{out}}) \tag{3.41}$$

Now, by injecting Equation 3.39, we obtain the well known form of the input-output relation involving the cavity field $\hat{a}$ and the input field $\hat{a}_{\text{in}}$:

$$\frac{\partial\hat{a}}{\partial t} = -i\omega_0\hat{a} - \frac{\kappa_{\text{ext}}}{2}\hat{a} + \sqrt{\kappa_{\text{ext}}}\hat{a}_{\text{in}} \tag{3.42}$$

Note that in the last relation, we have changed the phase definition of $\hat{a}_{\text{in}}$ such as: $\hat{a}_{\text{in}} \leftarrow e^{\frac{i\pi}{2}}\hat{a}_{\text{in}}$. This transformation does not involve any loss of generality and allows us to simplify the expression.

The last point of the derivation is to integrate the losses into the model. We take it into account by coupling a fictitious transmission line with a coupling rate κ_{int} identical to the internal energy leakage rate (see Figure 3.5). Hence, the final form of the input-output equation of the system is:

$$\boxed{\frac{\partial\hat{a}}{\partial t} = -i\omega_0\hat{a} - \frac{\kappa_{\text{ext}}+\kappa_{\text{int}}}{2}\hat{a} + \sqrt{\kappa_{\text{ext}}}\hat{a}_{\text{in}} + \sqrt{\kappa_{\text{int}}}\hat{a}_{\text{in,int}}} \tag{3.43}$$

3.1.5 Cavity driven by a coherent state

Now that we have introduced the theoretical framework of a cavity coupled to a transmission line, we show in this section the comportment of the cavity driven by a coherent state. In this case, the mode at the input of the cavity is $|\alpha_{\text{in}}\rangle$, an eigenstate of $\hat{a_{\text{in}}}$. The power carried by the mode is $P_{\text{in}} = \hbar\omega\,|\alpha_{\text{in}}|^2$. Under this drive, the cavity state is displaced from the vacuum state $|0\rangle$ to the coherent state $|\alpha\rangle$ (eigenstate of $\hat{a}$). By taking the average of

Equation 3.43 with the ket $|\alpha, \alpha_{\text{in}}\rangle$, we obtain the evolution equation of the intra-cavity field:

$$\partial_t \alpha(t) = -i\omega_0 \alpha(t) - \frac{1}{2}(\kappa_{\text{ext}} + \kappa_{\text{int}})\alpha(t) + \sqrt{\kappa_{\text{ext}}}\alpha_{\text{in}}(t) \tag{3.44}$$

where have taken into account that $\langle \hat{a}_{\text{in,int}}(t) \rangle = 0$. By taking the Fourier transform of this equation, we obtain the expression of the intra-cavity field as a function of the input field:

$$\alpha(\omega) = \frac{2\sqrt{\kappa_{\text{ext}}}}{\kappa_{\text{int}} + \kappa_{\text{ext}} - 2i(\omega - \omega_0)} \alpha_{\text{in}}(\omega) \tag{3.45}$$

It is interesting to write the number of intra-cavity photons as the function of the input power at resonance ($\omega = \omega_0$). For a coherent state, the relation $\bar{n} = |\alpha|^2$ leads to:

$$\bar{n} = \frac{4\kappa_{\text{ext}} P_{\text{in}}}{\hbar\omega_0 (\kappa_{\text{ext}} + \kappa_{\text{int}})^2} \tag{3.46}$$

In the next sections of the chapter we use this relation to quantify the input power of the coherent drive.

3.1.6 Scattering matrix

In a more general multi-port system, one considers a more general framework based on a scattering matrix S of size $n \cdot n$, with n the number of ports. The elements of this matrix are given by:

$$\hat{S}_{\text{ij}} = \frac{\hat{a}_{out,i}}{\hat{a}_{in,j}} \tag{3.47}$$

In this thesis we only use reflection measurements. In the case of a resonator coupled to a transmission line, we can write:

$$S_{11}(\omega) = \frac{\sqrt{\kappa_{\text{ext}}}\alpha(\omega) - \alpha_{\text{in}}}{\alpha_{\text{in}}} = \frac{\kappa_{\text{ext}} - \kappa_{\text{int}} + 2i(\omega - \omega_0)}{\kappa_{\text{ext}} + \kappa_{\text{int}} - 2i(\omega - \omega_0)}. \tag{3.48}$$

A VNA is commonly used for measuring S_{11} parameter. The relative values of κ_{ext} and κ_{int} define three different regimes (see Figure 3.6):

1. **under-coupled regime** where $\kappa_{\text{int}} \gg \kappa_{\text{ext}}$. The circuit impedance is much higher than the line one. The signal is almost completely reflected. Only a small absorption dip and phase shift are observed.

2. **over-coupled regime** where $\kappa_{\text{int}} \ll \kappa_{\text{ext}}$. The circuit impedance is much smaller than the line one. A fraction of the signal is absorbed whereas the other part is reflected with a 2π phase shift across the resonance.

3. **critical coupling condition** where $\kappa_{\text{int}} = \kappa_{\text{ext}}$. Impedances are equal, The majority of the signal impinging on the resonator is absorbed. The absorption dip is maximal and the phase change is not well defined.

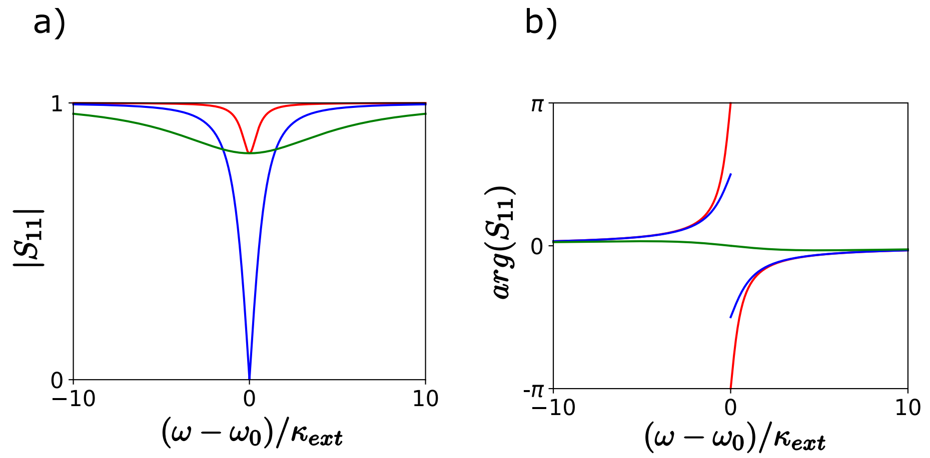

Figure 3.6: **Reflective mesurement** (a) $|S_{11}|$ (b) phase of S_{11}. red color corresponds to $\kappa_{\text{int}} = 0.1\kappa_{\text{c}}$, blue to $\kappa_{\text{int}} = \kappa_{\text{c}}$ and green to $\kappa_{\text{int}} = 10\kappa_{\text{c}}$.

3.2 The Josephson junction

The Josephson junction is a key element in circuit QED devices.it is composed by a tunnel junction with a thin insulating barrier between two superconducting electrodes.

B. Josephson demonstrated theoretically in 1962 [Jos62] that, in opposition to the common belief at that time, a super-current of Cooper pairs driven by the superconducting phase difference $\varphi = \varphi_{\text{b}} - \varphi_{\text{a}}$ (see Figure 3.7) and proportional to the normal state tunnel conductance can flow through the junction, even when the tunnel barrier transmission of single electrons in the normal state is very small . Josephson established the celebrated Josephson relations that determine the electrical behavior of a junction:

$$I = I_{\text{c}} \sin\varphi \tag{3.49}$$

$$\frac{\partial\varphi}{\partial t} = \frac{2e}{\hbar}V \tag{3.50}$$

Where I_{c} is a parameter called the critical current and e the charge of the electron. In the case of BCS superconductors, Josephson found that the critical current is $I_{\text{c}} = \pi\Delta/2eR_{\text{N}}$, where Δ is the BCS gap energy and R_{N} the normal state resistance of the junction. The flux across the junction is still given by the Faraday law $V = \partial_t\Phi$. Using the Equation 3.50, one obtains a relation between this flux and the superconducting phase difference: $\Phi = (\hbar/2e)\varphi = \Phi_0\varphi/2\pi$ with Φ_0 the flux quantum. We have shown in Section 3.1.1 that $\hat{\Phi}$ was a good quantum operator, thus, one can define by extension the phase operator: $\hat{\varphi} = 2\pi\hat{\Phi}/\Phi_0$.

By using Equation 3.49 and Equation 3.50 one can relate the derivative of the current to the voltage:

$$\frac{\partial I}{\partial t} = \frac{\partial I}{\partial\varphi}\frac{\partial\varphi}{\partial t} = I_{\text{c}}\cos(\varphi)\frac{2\pi V}{\Phi_0} \tag{3.51}$$

One deduces that the junction behaves as an inductor $V = L\partial_t I$, with an inductance that depends on the phase and thus on the current:

$$L(\varphi) = \frac{\Phi_0}{2\pi I_{\text{c}}\cos(\varphi)} = \frac{\Phi_0}{2\pi I_{\text{c}}\sqrt{1-\frac{I^2}{I_{\text{c}}^2}}} \tag{3.52}$$

In the weak current regime where $I/I_{\text{c}} \ll 1$, a Taylor expansion of the inductance as the function of the ratio I/I_{c} yields to:

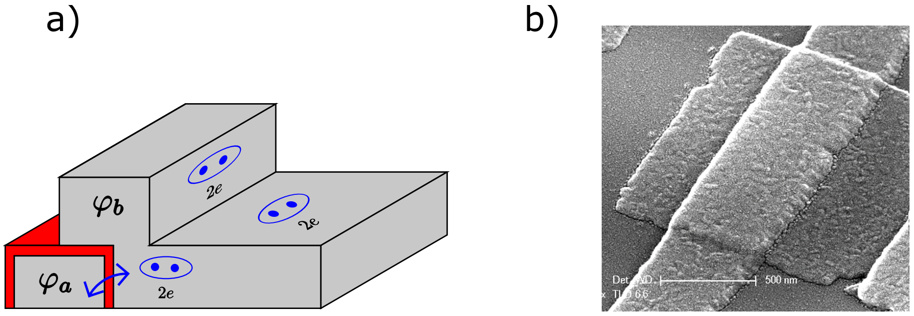

Figure 3.7: **Josephson junction** (a) Schematic of a realistic Josephson junction. The grey layer represents the superconducting films with the phase φ_{a} and φ_{b}. The red layer materializes the insulator. (b) Scanning electron microscope (SEM) picture of a Josephson junction. The superconducting electrodes are made in aluminum while the insulating layer is composed of alumina (Al_2O_3)

$$L(I) \sim \frac{\Phi_0}{2\pi I_{\text{c}}}(1 + \frac{(I/I_{\text{c}})^2}{2} + O((I/I_{\text{c}})^4)) \tag{3.53}$$

which shows the non-linear character of the Josephson junction as the function of the current. The junctions used in our experiments are operated in this weak current regime.

The energy stored in a linear inductor takes the form $E = \int dt V(t)I(t) = \Phi^2/2L$. This energy term appears in the Hamiltonian in Section 3.1.1 of a resonator. A similar calculation of the energy stored in a Josephson junction yields to :

$$E = \int \frac{\partial \Phi}{\partial t} I_{\text{c}} \sin\left(\frac{2\pi\Phi}{\Phi_0}\right) = -E_{\text{j}} \cos\left(\frac{2\pi\Phi}{\Phi_0}\right) \tag{3.54}$$

where $E_{\text{j}} = \Phi_0 I_{\text{c}}/2\pi$ is the Josephson energy. In the case of BCS superconductors, the Josephson energy is related to the critical current by the relation $E_{\text{j}} = (2e/\hbar)I_{\text{c}}$

3.2.1 The Superconducting Quantum Interference Device

The Superconducting Quantum interference device (SQUID) consists of 2 Josephson junctions connected in parallel (see Figure 3.8). We only consider here SQUIDs with negligible loop inductance i.e. with a sufficiently small loop, so that the voltages across the two junctions are equal. In this condition, the SQUID can be considered as a Josephson junction with adjustable inductance as detailed below.

The total current is the sum of the current flowing in the two branches. By defining φ_1 and φ_2 the phase difference differences across the 2 junctions (see Figure 3.8), the total current reads:

$$I = I_1 \sin(\varphi_1) + I_2 \sin(\varphi_2) \tag{3.55}$$

We consider here a symmetric SQUID with $I_1 = I_2 = I_{\text{c}}$. Therefore, the total current is:

$$I = 2I_{\text{c}} \cos\left(\frac{\varphi_2 - \varphi_1}{2}\right) \sin\left(\frac{\varphi_2 + \varphi_1}{2}\right) \tag{3.56}$$

Due to the flux quantization in the superconducting SQUID loop, the phase difference φ_1 and φ_2 are link to the total flux threading across the loop:

$$\varphi_2 - \varphi_1 = 2\pi \frac{\Phi_{\text{tot}}}{\Phi_0} \tag{3.57}$$

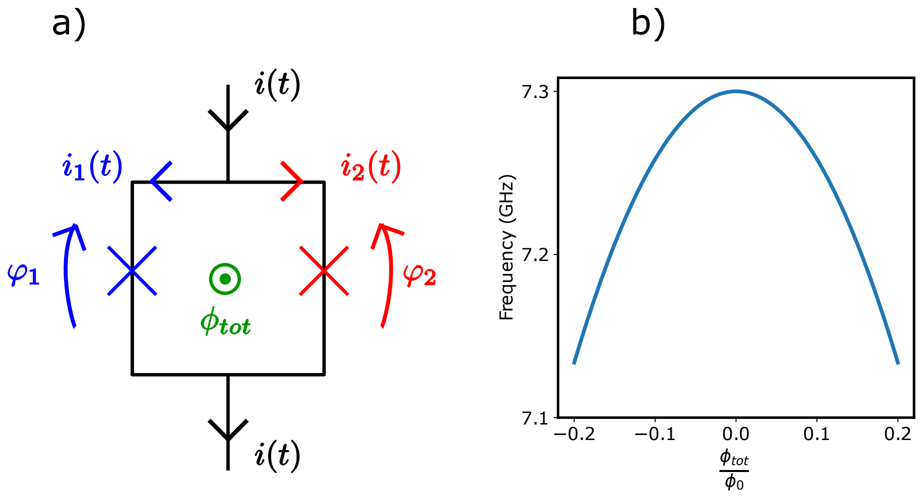

Figure 3.8: **Squid and tunable resonator.** (a) Schematic of a SQUID circuit with the electrical symbol of the Josephson junction. (b) Tunability curve of a resonator with an integrated SQUID with participation ration $p = 0.3$ and $\omega(0) = 7.3\text{GHz}$. The curve is obtained from the Taylor development of the resonance frequency $\omega(\Phi_{\text{tot}})$.

Φ_{tot} represents the sum of a flux due to an external magnetic field and the flux generated by the current flowing in the loop. By defining $\varphi_{12} = (\varphi_1 + \varphi_2)/2$ The final form for the total current is:

$$I = 2I_{\text{c}} \cos\left(\pi \frac{\Phi_{\text{tot}}}{\Phi_0}\right) \sin(\varphi_{12}) \tag{3.58}$$

Therefore, the SQUID can be seen as a Josephson junction with a tunable superconducting current $I_{cs} = 2I_{\text{c}} \cos\left(\pi \frac{\Phi_{\text{tot}}}{\Phi_0}\right)$. From Equation 3.53 we can directly define the tunable inductance in the weak current limit:

$$L_s(\Phi_{\text{tot}}) = \frac{\Phi_0}{2\pi I_{cs}(\Phi_{\text{tot}})} \tag{3.59}$$

The control of an inductance with a magnetic flux threading a SQUID loop makes the SQUID a useful tool for many applications. In circuit QED, it is noticeably used for tuning the resonance frequency of superconducting microwave resonators.

3.2.2 Tunable resonator

For tuning a microwave resonator, one incorporates a flux-tunable SQUID inductor in the resonator. For instance, when a SQUID with inductance $L_s(\Phi_{\text{tot}})$ is inserted in the middle of a $\lambda/2$ resonator, its resonance frequency becomes:

$$\omega(\Phi_{\text{tot}}) = 1/(\sqrt{(L + L_s(\Phi_{\text{tot}}))C}) \tag{3.60}$$

L_s varying periodically between $\Phi_0/4\pi I_{\text{c}} = L_{\text{j}}$ and $+\infty$, the resonator frequency shows several arches when the flux is swept. The resonance frequency reaches minima when $\Phi_{\text{tot}} = (2n+1)\Phi_0/2$ with $n \in \mathbb{Z}$. Since in our experiment we stay in the regime where $\Phi_{\text{tot}} \ll \Phi_0$, we can realise a Taylor expansion:

$$\frac{\omega(\Phi_{\text{tot}})}{\omega(0)} \sim 1 - \frac{p}{4(1+p)} (\frac{\Phi_{\text{tot}}\pi}{\Phi_0})^2 \tag{3.61}$$

where $p = L_\mathrm{j}/L$ is the participation ratio of the SQUID to the total circuit inductance. A typical tunability curve is given in Figure 3.8b.

Experimentally this tunability is obtained by placing a flux line nearby the SQUID loop. The resonators used in the photon detector have a resonance frequency close to 7 GHz and can be tuned over a range a several hundred of MHz.

The main drawback of integrating a SQUID into a resonator is the additional noise due to flux fluctuations in the SQUID loop. This flux noise can be caused by current instability in the flux line or by vortices in the thin film. The consequence is an extra decrease of the quality factor of the cavity.

3.3 Transmon qubit

3.3.1 System Hamiltonian

The operating principle of the photon counter is to record the arrival of a photon from the passage of a qubit from its ground state to its excited state. Building upon the non linearity provided by Josephson junctions, one can create a wide variety of circuit that behave as artificial atoms and qubits. A fairly complete review of the state of the art can be found in [Bla+21]. We summarize here the points necessary for this thesis.

The basic Cooper Pair Box circuit consists of a Josephson junction in parallel with a capacitor (see Figure 3.9a).

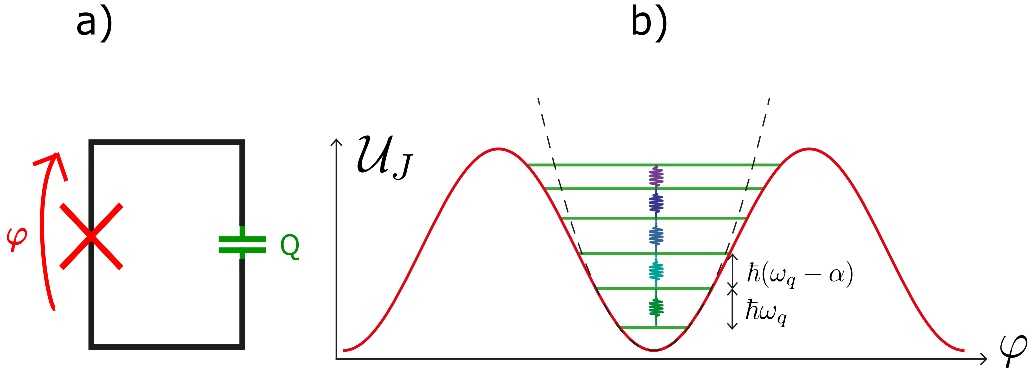

Figure 3.9: **Transmon qubit** (a) Electrical representation of a transmon qubit. φ represents the phase difference across the junction and Q the capacitor charge (b) Energy levels of a transmon qubit. The cosine (red) represents the energy evolution as the function of the phase φ. The anharmonicity α cause a non-constant spacing between the levels.

This circuit can be quantized in the same way as the LC circuit by defining the operators $\hat{\Phi}$ (flux across the junction) and $\hat{Q}$ (capacitor charge). The Hamiltonian is derived from a canonical quantization (see Section 3.1.1) is:

$$\hat{H} = \frac{\hat{Q}^2}{2C} - E_\mathrm{J} \cos\left(2\pi\hat{\Phi}/\Phi_0\right) \tag{3.62}$$

with the usual relations of commutation: $[\hat{\Phi}, \hat{Q}] = i\hbar$. It is more natural to express this Hamiltonian as the function of the phase operator $\hat{\varphi} = 2\pi\hat{\Phi}/\Phi_0$ and the number of extra Cooper pairs on the capacitor $\hat{N} = \hat{Q}/2e$. The Hamiltonian then reads:

$$\hat{H} = 4E_\mathrm{C}\hat{N}^2 - E_\mathrm{J}\cos\hat{\varphi} \tag{3.63}$$

with $E_\mathrm{C} = e^2/2C$ the charging energy, E_j the Josephson energy, and $[\hat{\varphi}, \hat{N}] = i$. The spectrum of this Hamiltonian is controlled by the ratio $E_\mathrm{j}/E_\mathrm{c}$. When $E_\mathrm{j}/E_\mathrm{c} \ll 1$ the eigenstates correspond roughly to number states. This regime was used in 1998 to prove the quantum character of superconducting circuits [Bou+98]. Nevertheless, this regime exposes the system to charge noise which causes the frequency to fluctuate, limiting qubit coherence. The best strategy for overcoming this problem is to operate the Cooper pair box in the so called transmon regime $E_\mathrm{j}/E_\mathrm{c} \gg 1$ (typically $E_\mathrm{j}/E_\mathrm{c} \approx 50$). A transmon is best described as an anharmonic resonator almost completely insensitive to charge noise [Koc+07], a major benefit obtained at the expense of a greatly reduced spectrum anharmonicity. The state of the art of individual transmon coherence time is above 1 ms, i.e. about a progress of six orders of magnitude compared to the superconducting qubit. All superconducting quantum computing architectures presently developed are based on transmons and this element is also at the core of our SMPD.

Taking into account that the ratio $E_\mathrm{j}/E_\mathrm{c}$ is the quantity that characterizes the comportment of the Hamiltonian, and using the expression of $\hat{N}$ and $\hat{\varphi}$ in function of the ladder operators $\hat{q}$ and $\hat{q}^\dagger$, the Hamiltonian can be written as:

$$\hat{H} = -4E_\mathrm{C}N_\mathrm{ZPF}^2(\hat{q}-\hat{q}^\dagger)^2 - E_\mathrm{J}\cos\left(\varphi_\mathrm{ZPF}(\hat{q}+\hat{q}^\dagger)\right) \tag{3.64}$$

Where $N_\mathrm{ZPF} = (E_\mathrm{J}/32E_\mathrm{C})^{1/4}$ and $\varphi_\mathrm{ZPF} = (2E_\mathrm{C}/E_\mathrm{J})^{1/4}$ refer to quantum fluctuations in the ground state. Knowing that we work in the transmon regime, we can now rightfully perform a series expansion of the Hamiltonian :

$$\hat{H} = \underbrace{\sqrt{\frac{E_\mathrm{J}E_\mathrm{C}}{2}}(\hat{q}-\hat{q}^\dagger)^2 + \sqrt{\frac{E_\mathrm{J}E_\mathrm{C}}{2}}(\hat{q}+\hat{q}^\dagger)^2}_{\text{harmonic oscillator}} - \underbrace{\frac{E_\mathrm{C}}{24}\varphi_\mathrm{ZPF}^4(\hat{q}+\hat{q}^\dagger)^4}_{\text{non-linearity}} + O(E_\mathrm{C}\sqrt{\frac{E_\mathrm{C}}{E_\mathrm{J}}}) \tag{3.65}$$

The transmon Hamiltonian can be seen as a quantum harmonic oscillator perturbed by a weak non linearity. We can organize the terms so that the Josephson plasma frequency $\omega_\mathrm{p} = \sqrt{8E_\mathrm{J}E_\mathrm{C}}/\hbar$ appears:

$$\boxed{\hat{H} = \sqrt{8E_\mathrm{J}E_\mathrm{C}}\hat{q}^\dagger\hat{q} - \frac{E_\mathrm{C}}{12}(\hat{q}+\hat{q}^\dagger)^4} \tag{3.66}$$

The non-linear term can be developed y using the rotating wave approximation (RWA). Keeping terms with the same number of creation and annihilation operators yields to:

$$\boxed{\hat{H} = (\sqrt{8E_\mathrm{J}E_\mathrm{C}} - E_\mathrm{C})\hat{q}^\dagger\hat{q} - \frac{E_\mathrm{C}}{2}\hat{q}^{\dagger 2}\hat{q}^2} \tag{3.67}$$

With this equation, we can define the transmon frequency $\omega_\mathrm{q} = \omega_\mathrm{p} - E_\mathrm{c}/\hbar$ defined as the energy difference between the two first levels. The renormalization due to $E_\mathrm{c}/\hbar$ is called the Lamb shift. To match with the literature, the eigenstates of the Hamiltonian will be note: $|g\rangle, |e\rangle, |f\rangle ....$

The non-linear term induces a variation of the energy difference between subsequent levels: The energy difference between the state $|e\rangle$ and $|f\rangle$ is $\hbar\omega_\mathrm{ef} = (\sqrt{8E_\mathrm{J}E_\mathrm{C}} - 2E_\mathrm{C})$ that we can write $\omega_\mathrm{ef} = \omega_\mathrm{q} - \alpha$ with $\alpha = E_\mathrm{c}/\hbar$ the anharmonicity of the transmon. The Figure 3.9b shows the evolution of the level energies with anharmonicity. Typically $\alpha/2\pi$ is in the range of a few hundred MHz.

The key point of this spectrum is that it allows us to define an effective two level system. Indeed, the non-constant energy difference between levels mitigates the risk to excite higher transitions with a pulse tuned on the first one. Therefore a transmon can be legitimately seen as a qubit.

It is therefore often convenient to use the Pauli matrix formalism to descripe operators acting on the qubit. In the ($|g\rangle$,$|e\rangle$) basis, Pauli matrix are expressed as: $\hat{\sigma}_\mathrm{z} = |g\rangle\langle g| - |e\rangle\langle e|$,

$\hat{\sigma}_\mathrm{x} = |g\rangle\langle e| + |e\rangle\langle g|$ and $\hat{\sigma}_\mathrm{y} = i|e\rangle\langle g| - i|g\rangle\langle e|$. The annihilation operator is $\hat{\sigma} = |g\rangle\langle e|$. In this framework the qubit Hamiltonian is simply:

$$\hat{H}_\mathrm{q} = \frac{\hbar}{2}\omega_\mathrm{q}\hat{\sigma_\mathrm{z}}. \tag{3.68}$$

We will use it to describe the decoherence mechanism in the next section.

3.3.2 Decoherence mechanisms

In the last section, we have shown that the transmon states $|g\rangle$ and $|e\rangle$ can be seen as a qubit. In this section, we describe the decoherence of the qubit induced by the interaction with its environment.

Here we will consider two mechanisms, relaxation and dephasing. Relaxation is an energy exchange between the qubit and the environment that occurs at a rate γ_1. Dephasing corresponds to the loss of information about the phase of the superposition of the qubit basis states at a rate of γ_ϕ. It is caused by fluctuations in the qubit frequency due to fluctuations in the environment state.

Both effects can be described by a master equation which introduces decoherence terms, namely Lindbladian operators, in the Schrödinger evolution equation of the density matrix:

$$\frac{\partial\hat{\rho}}{\partial t} = \frac{-i}{\hbar}[\hat{H},\hat{\rho}] + \sum_{\hat{L}} \mathcal{D}_{\hat{L}}(\hat{\rho}) \tag{3.69}$$

with:

$$\mathcal{D}_{\hat{L}}(\hat{\rho}) = \hat{L}\hat{\rho}\hat{L}^\dagger - \frac{1}{2}\hat{L}^\dagger\hat{L}\hat{\rho} - \frac{1}{2}\hat{\rho}\hat{L}^\dagger\hat{L}. \tag{3.70}$$

The relaxation and dephasing operators (resp $\hat{L_\mathrm{r}}$ and $\hat{L_\Phi}$) are:

$$\hat{L_\mathrm{r}} = \sqrt{\gamma_1}\hat{\sigma} \tag{3.71}$$

$$\hat{L_\Phi} = \sqrt{\frac{\gamma_\Phi}{2}}\hat{\sigma_\mathrm{z}} \tag{3.72}$$

From these Lindbladian operators and the Hamiltonian of the qubit $\hat{H}_\mathrm{q}$ defined above, one can solve the master equation. The final density matrix reads:

$$\rho = \begin{pmatrix} A_1 e^{\gamma_1 t} & A_2 e^{-i\omega_\mathrm{q} - \frac{\gamma_1}{2} - \gamma_\Phi t} \\ A_3 e^{i\omega_\mathrm{q} - \frac{\gamma_1}{2} - \gamma_\Phi t} & A_4 e^{-\gamma_1 t} \end{pmatrix} \tag{3.73}$$

From this result, one can define several characteristic times for the coherence properties of the system. $T_1 = 1/\gamma_1$ is the relaxation time of the qubit. It will take a prominent role in the SMPD operations (see Chapter 4). $T_\Phi = 1/\gamma_\Phi$ is the pure dephasing time. The total dephasing time define as $1/T_2 = 1/2T_1 + 1/T_\Phi$ includes the pure dephasing time but also an energy relaxation component which ultimately limits its value to $2T_1$.

3.4 Transmon dispersively coupled to a resonator

As it will be developed in Chapter 4, the SMPD architecture is based on the dispersive coupling between a transmon qubit and two resonators. This section describes how this interaction allows us to readout the state of the qubit.

3.4.1 Hamiltonian of the coupled system

The full treatment of the transmon-cavity Hamiltonian is well described in [Alb21]. Here we will recall the main steps of the derivation based on a Bogoliubov transformation.

From the Section 3.1.1 and Section 3.3, we can write the Hamiltonian of the system in terms of ladder operators:

$$\hat{H} = \underbrace{\hbar\omega_0\hat{a}^\dagger\hat{a}}_{\text{oscillator}} + \underbrace{\hbar(\omega_{\mathrm{q}}+\alpha)\hat{q}^\dagger\hat{q} - \frac{\alpha}{12}(\hat{q}+\hat{q}^\dagger)^4}_{\text{transmon}} + \underbrace{\hbar g(\hat{a}^\dagger\hat{q}+\hat{a}\hat{q}^\dagger)}_{\text{capacitive coupling}} \tag{3.74}$$

Where ω_0 is the resonator frequency and g is the coupling strength driving the hybridization between the modes $\hat{a}$ and $\hat{q}$. This parameter can be exactly obtained from the electrical parameters of the circuit [Alb21]. The dispersive coupling regime takes place when the coupling strength g is much smaller than the frequency difference between the qubit and the cavity mode, ie: $g \ll \Delta$, where $\Delta = \omega_{\mathrm{q}} - \omega_0$.

The first step of the derivation consists in finding a dressed state basis in which the "linear" Hamiltonian with the quartic term removed :

$$\hat{H}_{\mathrm{lin}} = \hbar\omega_0\hat{a}^\dagger\hat{a} + \hbar(\omega_{\mathrm{q}}+\alpha)\hat{q}^\dagger\hat{q} + \hbar g(\hat{a}^\dagger\hat{q}+\hat{a}\hat{q}^\dagger) \tag{3.75}$$

consists of uncoupled modes, i.e. a basis where the term $\hbar g(\hat{a}^\dagger\hat{q}+\hat{a}\hat{q}^\dagger)$ is canceled. This is done thanks to a Bogoliubov transformation with the unitary operator : $\hat{U} = \exp\Big[\theta(\hat{a}^\dagger\hat{q}-\hat{a}\hat{q}^\dagger)\Big]$. Under this transformation, the ladder operators transform as : $\hat{U}^\dagger\hat{a}\hat{U} = \cos\theta\hat{a} + \sin\theta\hat{q}$ and $\hat{U}^\dagger\hat{q}\hat{U} = \cos\theta\hat{q} - \sin\theta\hat{a}$. The transformed Hamiltonian is:

$$\hat{U}^\dagger\hat{H}_{\mathrm{lin}}\hat{U} = \hbar\tilde{\omega_0}\hat{a}^\dagger\hat{a} + \hbar(\tilde{\omega_{\mathrm{q}}}+\alpha)\hat{q}^\dagger\hat{q} + \hbar(g\cos 2\theta - \frac{\Delta}{2}\sin\theta)(\hat{a}^\dagger\hat{q}+\hat{a}\hat{q}^\dagger) \tag{3.76}$$

To cancel the coupling term, one has to choose $\theta = \frac{1}{2}\arctan 2g/\Delta$. In the dispersive regime, $\Delta \gg g$, one gets $\theta \approx g/\Delta$ and the dressed modes and frequencies:

$$\hat{a} \leftarrow \hat{a} + \frac{g}{\Delta}\hat{q} \tag{3.77}$$

$$\hat{q} \leftarrow \hat{q} - \frac{g}{\Delta}\hat{a} \tag{3.78}$$

$$\omega_{\mathrm{q}} \leftarrow \omega_{\mathrm{q}} - \tfrac{g^2}{2\Delta} \tag{3.79}$$

$$\omega_0 \leftarrow \omega_0 + \tfrac{g^2}{2\Delta} \tag{3.80}$$

The second step of the derivation consists in applying the unitary $\hat{U}$ to the full Hamiltonian $\hat{H}$. Given that $\hat{U}$ is unitary, the quartic term is readily transformed since $\hat{U}^\dagger(\hat{q^\dagger}+\hat{q})^4\hat{U} = (\hat{U}^\dagger[\hat{q^\dagger}+\hat{q}]\hat{U})^4$. The full transformed Hamiltonian reads:

$$\hat{H}/\hbar = \omega_0\hat{a}^\dagger\hat{a} + (\omega_{\mathrm{q}}+\alpha)\hat{q}^\dagger\hat{q} - \frac{\alpha}{12}\left(\hat{q}+\hat{q}^\dagger + \frac{g}{\Delta}(\hat{a}+\hat{a}^\dagger)\right)^4 \tag{3.81}$$

The important point to note is that the non linearity provided by the Josephson junction mixes the dressed states in a non trivial way. We can expand the non linear term and perform a RWA approximation in order to only keep the terms which conserve the energy of the qubit and the resonator mode in the Hamiltonian:

$$\boxed{\hat{H}/\hbar = \omega_0\hat{a}^\dagger\hat{a} + \omega_{\mathrm{q}}\hat{q}^\dagger\hat{q} - \frac{\alpha}{2}\hat{q}^{\dagger 2}\hat{q}^2 - \frac{K}{2}\hat{a}^{\dagger 2}\hat{a}^2 - \chi\hat{a}^\dagger\hat{a}\hat{q}^\dagger\hat{q}} \tag{3.82}$$

with

$$K \quad = \alpha \frac{g^4}{\Delta^4} \tag{3.83}$$

$$\chi \quad = 2\alpha \frac{g^2}{\Delta^2} \tag{3.84}$$

K and χ are referred to as the self-Kerr of the resonator and cross-Kerr between the transmon and the resonator. For typical parameters such as $\alpha = 2\pi \times 200$ MHz, $g = 2\pi \times 100$ MHz and $\Delta = 2\pi \times 1$ GHz, The self-Kerr is of the order of $K \sim 2\pi \times 10$ kHz, whereas the resonator linewidth is typically $\kappa = 2\pi \times 1$ MHz. The self-Kerr can thus be usually neglected in the circuit dynamics.

The cross-Kerr term can be seen as a dispersive frequency shift of the qubit or resonator mode caused by the state of the other one. This so-called dispersive shift that has a typical value of the order of $\chi \sim 2\pi \times 1$ MHz, plays a crucial role in the oscillator-qubit dynamics. Indeed, it allows to readout non-destructively the state of the qubit by measuring the resonator frequency. Another important use of the dispersive shift is the determination of the average photon number in the cavity from qubit decoherence. We will return to these two points in the following sections.

3.4.2 Qubit Quantum non demolition readout

We can recast the Equation 3.82 by neglecting the self-Kerr term as:

$$\hat{H}/\hbar = \hat{a}^\dagger \hat{a}(\omega_0 - \chi \hat{q}^\dagger \hat{q}) + \omega_\mathrm{q} \hat{q}^\dagger \hat{q} - \frac{\alpha}{2} \hat{q}^{\dagger 2} \hat{q}^2 \tag{3.85}$$

This expression shows that the cavity frequency depends on the qubit state. It takes the value $\omega_\mathrm{b}^\mathrm{g} = \omega_\mathrm{b}$, $\omega_\mathrm{b}^\mathrm{e} = \omega_\mathrm{b} - \chi$ for the qubit in the ground $|g\rangle$, excited $|e\rangle$ state.

A reflective measurement of the cavity thus yields a measurement of the qubit state. To do so, a coherent tone is sent on the cavity through the line, which creates an intra-cavity coherent state as seen in Section 3.1.5. These coherent states are conditioned by the state of the qubit, and one obtains their expression using Equation 3.40 by replacing $\hat{H}_r$ by the Hamiltonian given by Equation 3.85:

$$\alpha_g \quad = \frac{\epsilon}{\kappa/2 + i(\delta + \chi/2)} \tag{3.86}$$

$$\alpha_e \quad = \frac{\epsilon}{\kappa/2 + i(\delta - \chi/2)} \tag{3.87}$$

With κ the oscillator linewitdh, $\delta = \omega - \omega_0 + \chi/2$ (chosen to symetrize the cavity field) and $\epsilon = \sqrt{\kappa_\mathrm{ext}}\alpha_\mathrm{in}$ the tone amplitude seen by the cavity. In order to obtain a graphical representation of these states in the phase plane, we evaluate the intra cavity field quadratures, $\langle \hat{X} \rangle_{e/g} = (\alpha_{e/g} + \alpha_{e/g}^*)/2$ and $\langle \hat{Y}_{e/g} \rangle = (\alpha_{e/g} - \alpha_{e/g}^*)/2i$:

$$\langle \hat{X} \rangle_{e/g} = \frac{\epsilon\kappa/2}{(\kappa/2)^2 + (\delta \mp \chi/2)^2} \tag{3.88}$$

$$\langle \hat{Y} \rangle_{e/g} = \frac{\epsilon(\delta \mp \chi/2)}{(\kappa/2)^2 + (\delta \mp \chi/2)^2} \tag{3.89}$$

Interestingly, the information on qubit state is exclusively on the $\langle \hat{Y} \rangle$ quadrature as shown on Figure 3.10a. The corresponding phase of the intra-cavity field is:

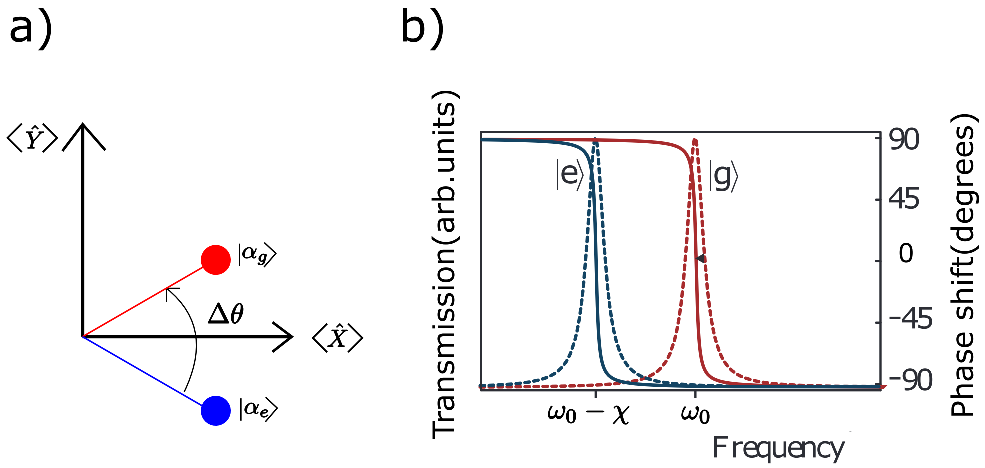

Figure 3.10: **Dispersive readout** (a)Phase plan representation with the two qubit-conditioned coherent states of the cavity create by the input coherent tone. This phase plan can be rebuild from a heterodyne measurement of the cavity. (b) Amplitude and phase of the intra-cavity state as the function of the frequency of the input signal. The coupling with the qubit imposes a cavity frequency shift of χ conditioned by the qubit state ($|e\rangle$ *or* $|g\rangle$). The signal is mostly absorbed at frequency ω_0 (resp $\omega_0-\chi$) when the qubit is in the ground (resp excited) state. figure adapted from [Bla+07].

$$\theta_{e/g} = \arctan\left(\frac{\langle\hat{Y}\rangle_{e/g}}{\langle\hat{X}\rangle_{e/g}}\right) = \arctan\left(\frac{\delta \mp \chi/2}{\kappa/2}\right) \tag{3.90}$$

This expression yields the phase shift in the phase plan. The variations with the frequency tone of the amplitude and phase of the intra-cavity coherent state are displayed in Figure 3.10b .

The intra-cavity state described on this plot is linked to the output signal $\hat{a}_{\text{out}}$ by the input-output equation Equation 3.43. A measurement of the reflected signal thus gives access to the phase space representation in Figure 3.10a and to qubit state. Here, we use an heterodyne measurement technique described more detail in the experimental part.

In the measurement regime considered here, this measurement is projective and leaves the qubit in a state corresponding to the measured value. Ideally, it is a quantum non-demolition measurement : a subsequent measurement of the qubit should ideally give the same answer.

3.4.3 Transmon measurement induces dephasing

In the previous section we took advantage of the fact that the qubit imposes a frequency shift on the resonator to make a non-destructive measurement. In this section we will use the symetric effect in order to calibrate the intra-cavity number of photons for a given drive. This measurement will give us an precise calibration of the input power.

The effect of the cavity photon number on the qubit is best seen by rewriting Equation 3.82 in the form:

$$\hat{H}/\hbar = \omega_0\hat{a}^\dagger\hat{a} + (\omega_{\text{q}} - \chi\hat{a}^\dagger\hat{a})\hat{q}^\dagger\hat{q} - \frac{\alpha}{2}\hat{q}^{\dagger 2}\hat{q}^2 \tag{3.91}$$

When the resonator is driven by a coherent tone, the photons present in the cavity shift the qubit frequency by $\bar{n}\chi$, with $\bar{n}$ the average number of photons in the cavity. This effect is called a Stark shift in analogy with the Stark shift in atomic levels.

In addition, the fluctuations in photon population yields qubit dephasing, and thus decoherence. The added decoherence rate is of the order of $\kappa\bar{n}$ with κ the cavity linewidth. A derivation of the expressions of the dephasing rate γ_2 and of the frequency shift Δ_s can be found in [Gam+06]. These quantities are related to the coherent field state in the cavity defined in Equation 3.87 by :

$$\Delta_\mathrm{s} + i\gamma_2 = -\chi\alpha_g\bar{\alpha}_e = \frac{-4\chi|\epsilon|^2}{(\kappa_\mathrm{b} + 2i\delta)^2 + \chi^2} \tag{3.92}$$

The value of the left side term Δ_s and γ_2 can be obtained from a Ramsey fringe experiment starting from a superposition of states $|+\rangle = (|g\rangle + |e\rangle)/\sqrt{2}$, in presence of photons in the cavity. The fringe oscillation frequency yields Δ_s, and their decay with time γ_2.

The knowledge of Δ_s and γ_2 when the microwave drive is at resonance with the cavity ($\omega = \omega_0$) gives us access to the average number of intra-cavity photons. Then, using Equation 3.46 , one obtains a calibration of the incoming power:

$$P_\mathrm{in} = \hbar\omega_0\bar{n}\frac{\kappa^2}{4\kappa_\mathrm{ext}} \tag{3.93}$$

This absolute calibration of the power impinging on the cavity will be exploited for the determination of the SMPD efficiency.

3.5 Purcell effect

3.5.1 General case

We have seen how the cavity can induce qubit dephasing, and is thus a source of decoherence with a rate γ_2 for the qubit. This is however not the only way the cavity induce qubit decoherence. Indeed, Edwin Purcell [Pur46] had shown that, in the strong coupling regime of a quantum system to a cavity, the effective density of modes for relaxation between its levels by emission of a photon in the cavity is so enhanced that this relaxation channel can become the dominant one with a rate γ_1 . A step by step derivation of Purcell relaxation based on the master equation is given in [Alb21]. We only recall here the assumptions made and the main steps.

For the sake of simplicity, we reduce the transmon to a two-level system and use the Pauli operator formalism. The Hamiltonian of the coupled system in the rotating frame of the qubit is given by:

$$\hat{H} = \hbar\Delta\hat{a}^\dagger\hat{a} + \hbar g(\hat{a}^\dagger\hat{\sigma} + \hat{a}\hat{\sigma^\dagger}) \tag{3.94}$$

where g represents the qubit/resonator coupling and $\Delta = \omega_0 - \omega_\mathrm{q}$. The master equation leading the evolution of the system reads:

$$\frac{\partial\hat{\rho}}{\partial t} = \frac{-i}{\hbar}[\hat{H}, \hat{\rho}] + \mathcal{D}_{\hat{L_\Phi}}(\hat{\rho}) + \mathcal{D}_{\hat{L_\mathrm{r}}}(\hat{\rho}) + \mathcal{D}_{\hat{L_\kappa}}(\hat{\rho}) \tag{3.95}$$

where: $\hat{L_\mathrm{r}} = \sqrt{\gamma_1}\hat{\sigma}$, $\hat{L_\Phi} = \sqrt{\frac{\gamma_\Phi}{2}}\hat{\sigma}_\mathrm{z}$ (already introduced in Section 3.1.4.2) and $L_{\hat{\kappa}} = \sqrt{\kappa}\hat{a}$ with κ the cavity linewidth.

The derivation of this master equation is based on the adiabatic elimination of the cavity. The cavity degree of freedom will be removed by taking the trace of the cavity operator. Such an approximation is correct when the number of photons in the cavity remains small, so that $\kappa \gg \gamma_1, \Phi, g$. By injecting a solution of the form:

$$\hat{\rho} = \hat{\rho}_{00} \otimes |0\rangle\langle 0| + \lambda\left(\hat{\rho}_{10} \otimes |1\rangle\langle 0| + \hat{\rho}_{01} \otimes |0\rangle\langle 1|\right) +$$

$$+ \lambda^2\left(\hat{\rho}_{11} \otimes |1\rangle\langle 1| + \hat{\rho}_{02} \otimes |0\rangle\langle 2| + \hat{\rho}_{20} \otimes |2\rangle\langle 0|\right) + O(\lambda^3). \tag{3.96}$$

in the master equation, we can solve the different component ρ_{mn}. Then we take the trace $\rho_{\mathrm{s}} = \rho_{00} + \lambda^2\rho_{11}$ and we write the reduced master equation for the qubit degree of freedom:

$$\frac{\partial \hat{\rho}_{\mathrm{s}}}{\partial t} = \frac{-i}{\hbar}[\hat{H}_{\mathrm{s}}, \hat{\rho}_{\mathrm{s}}] + \mathcal{D}_{\hat{L_\Phi}}(\hat{\rho}_{\mathrm{s}}) + \mathcal{D}_{\hat{L_{\mathrm{r}}}}(\hat{\rho}_{\mathrm{s}}) + \mathcal{D}_{\hat{L_\kappa}}(\hat{\rho}_{\mathrm{s}}) + \mathcal{D}_{\hat{L_{\mathrm{P}}}}(\hat{\rho}_{\mathrm{s}}) \tag{3.97}$$

Where, $\hat{H}_{\mathrm{s}}$ is the Hamiltonian reduced to the cavity ground state $\langle 0|\hat{H}|0\rangle \approx \hat{H}_{\mathrm{s}}$. The new Lindbladian term $\hat{L}_{\mathrm{P}} = \sqrt{\Gamma_{\mathrm{p}}}\sigma$ represents the enhanced relaxation rate of the qubit due to photon emission, the so-called Purcell effect. Its rate is given by the expression:

$$\Gamma_{\mathrm{p}} = \frac{g^2\kappa}{\frac{\kappa^2}{4} + \Delta^2}. \tag{3.98}$$

This effect can be used to increase the radiative relaxation rate of a system where photon emission is not the main de-excitation channel. Two different regimes can be identified:

- **strong coupling regime**: for $g \gg \kappa$, an excitation can be coherently exchanged back and forth between the spin and the resonator before its energy gets transmitted in the line or dissipated by resonator losses.
- **weak coupling regime**: if $g \ll \kappa$, an excitation gets damped quickly in the resonator. If $\kappa_{\mathrm{ext}} \gg \kappa_{\mathrm{int}}$, the photon emitted by the spin is completely transmitted in the line.

This use will be important in the detection of spin coupled to superconducting microwave resonators in Chapter 8.

The Purcell effect can also be used to protect a qubit from the external environment by using it as a filter. In this case the Purcell effect decreases the radiative emission rate and thus increases the coherence time of the qubit. The following section details more precisely this configuration

3.5.2 Purcell filters

While the Purcell effect is interesting for increasing the photon emission rate in the case of spin detection, it can become the limiting factor for the coherence of a superconducting qubit coupled to a readout resonator. One can try to reduce this effect by decreasing the qubit-resonator coupling, by increasing the frequency detuning or by reducing the bandwidth of the resonator. However, all these methods imply a slower reading of the qubit. A compromise must be found between qubit relaxation and measurement time.

A method to avoid this trade-off is to add an additional resonator between the readout resonator and the line [Jef+14]. This additional element, called a Purcell filter, is frequency tuned to the readout resonator and has a low quality factor.

The theory of the full system is done in [SMK15]. The interest of this architecture is the decoupling between the energy decay rate of the qubit towards the line and the effective bandwidth of the readout resonator.

More precesely, The effective decay rate of the readout resonator to the transmission line through the filter is given by Equation 3.98:

$$\kappa_{\mathrm{r}} = \frac{4G^2}{\kappa_{\mathrm{Pr}}} \frac{1}{1 + (2[\omega_{\mathrm{r}} - \omega_{\mathrm{Pr}}]/\kappa_{\mathrm{Pr}})^2} \approx \frac{4G^2}{\kappa_{\mathrm{Pr}}}. \tag{3.99}$$

with ω_{Pr} (resp. ω_{r}) and κ_{Pr} (resp. κ_{r}) the Purcell filter (resp. readout resonator) frequency and linewidth. Here, G is the coupling between the readout resonator and its Purcell filter.

On the other hand, due to the filter, the cavity rate involved in the qubit Purcell rate equation Equation 3.98 is not given by Equation 3.99 but rather by the expression:

$$\kappa_{\mathrm{r}}^{\mathrm{q}} = \frac{4G^2}{\kappa_{\mathrm{Pr}}} \frac{1}{1 + (2[\omega_{\mathrm{q}} - \omega_{\mathrm{Pr}}]/\kappa_{\mathrm{Pr}})^2} \approx \frac{G^2 \kappa_{\mathrm{Pr}}}{\Delta_{\mathrm{r}}^2}. \tag{3.100}$$

with $\Delta_{\mathrm{r}} = \omega_{\mathrm{q}} - \omega_{\mathrm{Pr}}$. By inserting this expression in the Purcell rate, we obtain the residual decay of the qubit through the waste channel:

$$\Gamma_{\mathrm{P}}^{\mathrm{q}} = \frac{G^2 g_{\mathrm{r}}^2 \kappa_{\mathrm{Pr}}}{\Delta_{\mathrm{r}}^4}. \tag{3.101}$$

Therefore, the effect of the frequency detuning between the qubit and the resonators separating it from the transmission line is reinforced. The qubit relaxation time T_1 is preserved whereas the readout resonator can be strongly coupled to the line.

These Purcell filters will play a key role in the SMPD architecture as we will need a long-T_1 transmon qubit as well as strongly damped coupled resonators.

Chapter 4

Single microwave photon detector theoretical concepts

A photon counter is a device that reveals the presence of photons by triggering a phenomenon that can be registered at the macroscopic scale. In optics, photon counters are based on an avalanche photodiode. This device is a reverse-biased PN junction in which a photoelectron, produced by an impinging photon, triggers an electron avalanche that reaches a large current during a short ns duration. This "click" is easily registered with a current amplifier. Single photon avalanche detectors (SPADs) with a very low dark count rate are now commonly used to detect single atoms or molecules using their fluorescence, with important applications in microscopy [Bru+19] and more broadly in quantum technologies [KDM77; WEH18].

The detection of an optical photon in a SAPD is possible because photon energy can exceed the gap of a semiconductor. This method thus cannot work for photons in the microwave domain with an energy about 5 orders of magnitude smaller in energy than the optical domain. Nevertheless, the rapid development of circuit-QED introduced in Chapter 3 has unlocked the research on the subject, and several devices have been proposed and sometimes successfully implemented ([Gri+20; Kos+15; Roy+18]). Among them, the proof of concept of a Single Microwave Photon Detector (SMPD) demonstrated by Lescannes et al [Les+20] has been implemented in Quantronics during the PhD research of Emanuele Albertinale [Alb21] for detecting the fluorescence of electronic spins. The operating principle of this circuit is to register the arrival of a microwave photon by triggering an irreversible transition of a transmon qubit from its ground state to its excited state. The transmon of course needs to have a long enough relaxation time so that it can be later measured before returning to its ground state. A high fidelity readout is also requested. This technology has been shown to be sensitive enough to perform ESR experiments on a small one-thousand electronic spin ensemble [Alb+21], establishing this way the state of the art of ESR.

In this thesis work, we use the same circuit architecture and further improve it enough in order to gain at least one order of magnitude in sensitivity. The achieved progress has allowed us to perform measurements on a single electron spin as described in Chapter 8. This chapter presents the operating principle of our SMPD and its architecture.

4.1 SMPD based on a four-wave mixing process

4.1.1 SMPD working principle

The photon detection strategy presented here exploits a transmon qubit as a marker of the passage of a photon. From the point of view of quantum information processing it can be seen as the reliable transfer of the quantum information carried by an incoming photon wave-packet onto the qubit state.

The architecture described in this chapter is based on the irreversible evolution between a superconducting resonator and the qubit. Indeed, these two quantum systems should not interact in a coherent way as this would lead to a reversible evolution. Instead, they share a common dissipative mechanism to a cold bath: the qubit irreversibly switches to its excited state if and only if a photon enters the resonator, and the reverse process cannot occur. We use this highly correlated dissipation mechanism to detect itinerant photons impinging on the resonator.

Dissipation engineering is a new paradigm for the manipulation of individual quantum systems. Counter-intuitively, the loss of information or energy to the external environment opens up new possibilities for quantum circuits. In contrast to Hamiltonian-driven coherent evolution, the irreversible leakage of information to an external bath is modeled by the jump operators (also called dissipators) $\hat{L}$ already described in Section 3.3.2. Similarly to the Hamiltonian, they describe transition between quantum states but like in general $\hat{L} \neq \hat{L}^\dagger$ the dynamic is irreversible.

Our SMPD is composed of an input superconducting resonator called "buffer" coupled to a transmon qubit. The cavity is described by the bosonic operators $\hat{b}$ and $\hat{b}^\dagger$, and the qubit by its raising and lowering operators $\hat{\sigma}$ and $\hat{\sigma}^\dagger$. In the Jaynes-Cumming framework, the intertaction Hamiltonian that couples the qubit to the cavity is $\hat{H}_{\text{int}} = g(\hat{a}\hat{\sigma}^\dagger + \hat{a}^\dagger\hat{\sigma})$, which yields on resonance a coherent and continuous oscillation between the qubit and the cavity, thus making impossible photon detection. A solution for escaping this limitation is to replace the interaction $\hat{H}_{\text{int}}$ by an irreversible dissipation operator $\hat{L}_{\text{nl}} = \sqrt{\kappa_{\text{nl}}}\hat{b}\hat{\sigma}^\dagger$. This non trivial dissipator describes an irreversible quantum jump, in which the annihilation of a photon gets associated to the excitation of the qubit, without a reverse term enabling the decay of the qubit associated with the creation of a photon. In contrast to the dissipators discussed in Section Section 3.3.2, the operator $\hat{L}_{\text{nl}}$ has the unique property of being both non-local, as it affects modes in different spatial locations, and non-linear, as it involves the product of operators.

The general procedure to create such a dissipator is to engineer a coherent interaction $\hat{H}_{\text{aux}}$ between the system of interest (here the couple buffer/qubit) and an auxiliary resonator, strongly damped into the environment. The additional resonator is called the "waste" and is described by the ladder operators $\hat{w}$ and $\hat{w}^\dagger$. The procedure, based on the adiabatic elimination of the waste degree of freedom can be summarized as:

$$\begin{cases} \hat{H}_{\text{aux}} = \hat{L}_{\text{nl}}\hat{w}^\dagger + \hat{L}_{\text{nl}}^\dagger\hat{w} \\ \hat{L}_{\text{aux}} = \sqrt{\kappa_{\text{w}}}\hat{w} \end{cases} \quad \rightarrow \quad \hat{L}_{\text{nl}}. \tag{4.1}$$

Similar ideas have been recently used for the stabilization of quantum states [Mur+12; Sha+13] or manifolds [Leg+15], and for the fabrication of non-reciprocal components [MC15; Sli+15].

Practically, the non-linearity of the transmon junction allows for the creation of non-linear combinations of modes $\hat{\sigma}$, $\hat{b}$, and $\hat{w}$, including a four-wave mixing process that can be activated by applying a pump tone with an appropriate frequency ω_{p} to the qubit. These processes associated to the terms $\hat{b}\hat{\sigma}^\dagger\hat{w}^\dagger$ and $\hat{b}^\dagger\hat{\sigma}\hat{w}$ describe the energy transfer between the buffer and the couple qubit/waste caused by the pump. The waste resonator being always closed to its ground state, the conversion involving an energy transfer from the waste/qubit pair to the buffer is inhibited. This adiabatic elimination of the waste implies that $\kappa_{\text{nl}} \ll \kappa_{\text{w}}$. Under these conditions, the buffer photon is transferred irreversibly into the qubit excitation and the dissipator $\hat{L}_{\text{nl}}$ becomes effective.

In the following sections, we will detail the expression of the SMPD Hamiltonian and highlight the four-wave mixing term that is at the heart of the detector concept. We then

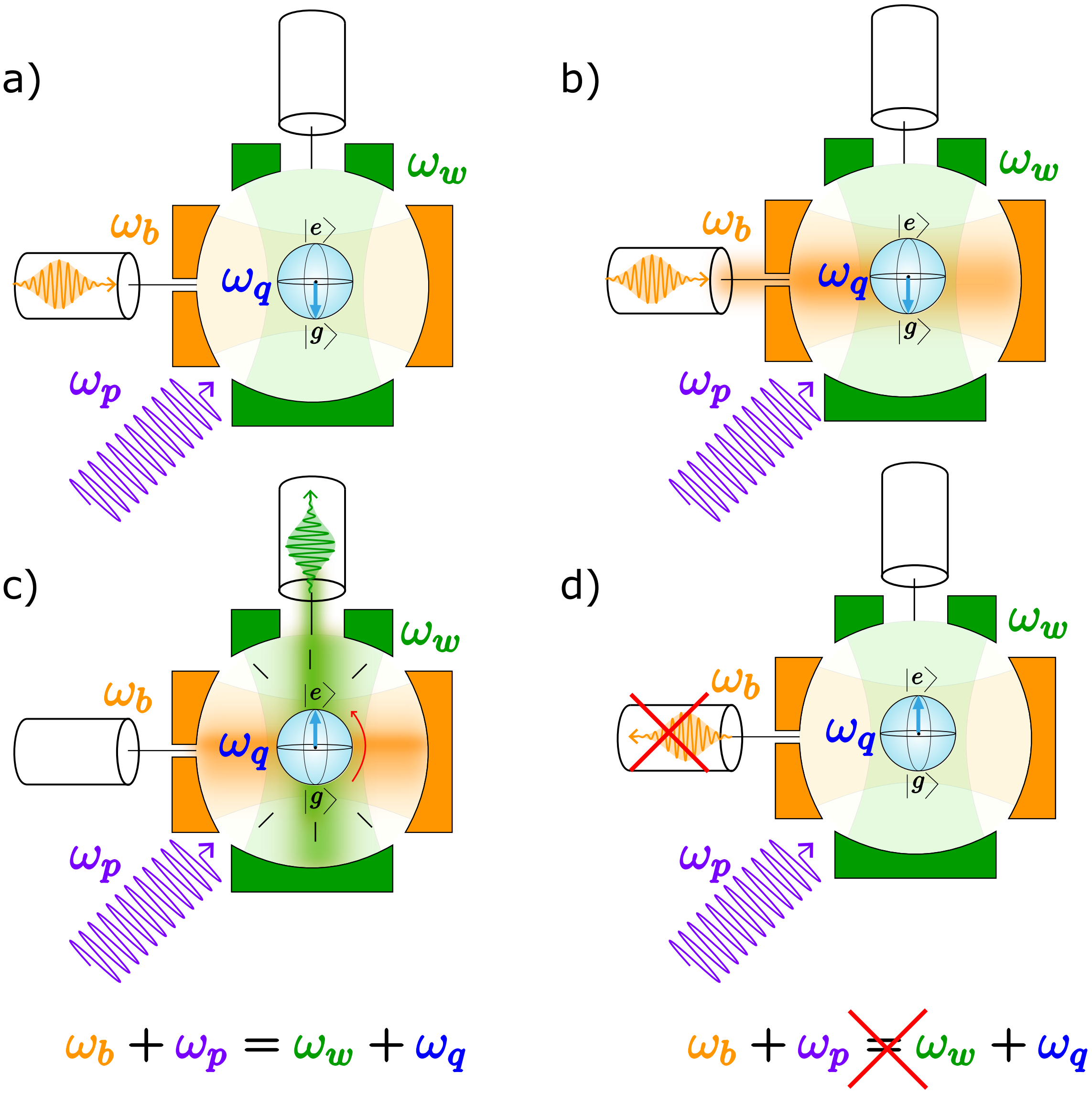

Figure 4.1: **SMDP working principle** (a) A transmon qubit at frequency ω_{q} is coupled to two cavities, namely the buffer at frequency ω_{b} and the waste at frequency ω_{w}. The waste resonator is strongly coupled to its output line. In addition, a pump tone at frequency ω_{p} is continuously shined on the qubit during the detection phase. (b) The incoming photon enters the buffer resonator whose frequency is adjusted to match the frequency of the photon. (c) The four-waves mixing occurs due to the pump tone tuned to match the frequency condition : $\omega_{\mathrm{b}} + \omega_{\mathrm{p}} = \omega_{\mathrm{w}} + \omega_{\mathrm{q}}$. A buffer photon plus a pump photon are converted in a qubit excitation and a waste photon. The waste photon is quickly dissipated into the environment due to the strong coupling. (d) Photon counter state after the passage of a photon. The absence of waste photon inhibits the reverse parametric process that would have converted the qubit excitation in a buffer photon.

solve the master equation in the framework of adiabatic elimination to obtain an explicit expression of $\hat{L}_{\mathrm{nl}}$. Finally, we will develop an analogy between the 4-wave mixing process and a 2 coupled-cavity model to obtain the bandwidth of the detector.

4.1.2 SMPD Hamiltonian

The derivation of the SMPD Hamiltonian is similar to the one of the transmon-resonator system developed in Section 3.4 and is also based on the Bogoliubov approach.

The full SMPD Hamiltonian reads:

$$\begin{aligned}\hat{H}/\hbar = \sum_{m=w,b} \omega_{\rm m}\hat{m}^\dagger\hat{m} + g_{\rm m}(\hat{m}^\dagger\hat{q}+\hat{q}^\dagger\hat{m}) + (\omega_{\rm q}+\alpha)\hat{q}^\dagger\hat{q} \\ - \frac{\alpha}{12}(\hat{q}^\dagger+\hat{q})^4 + \epsilon_{\rm p}(\hat{q}^\dagger e^{-i\omega_{\rm p}t} + \hat{q}e^{i\omega_{\rm p}t}) + \epsilon_{\rm d}(\hat{b}e^{i\omega_{\rm d}t}+\hat{b}^\dagger e^{-i\omega_{\rm d}t})\end{aligned} \tag{4.2}$$

The transmon qubit is capacitively coupled to two distinct harmonic modes: the buffer mode $\hat{b}$ at a frequency $\omega_{\rm b}$ with a coupling constant $g_{\rm b}$ and the waste mode $\hat{w}$ at a frequency $\omega_{\rm w}$ with a coupling constant $g_{\rm w}$. The pump term with amplitude $\epsilon_{\rm p}$ and frequency $\omega_{\rm p}$ represents the microwave tone that triggers the four-wave mixing. An incoming photon impinging the detector at a frequency $\omega_{\rm d}$ is modeled by a buffer drive with amplitude amplitude $\epsilon_{\rm d}$.

In the dispersive regime, and with the appropriate Bogoliubov transformation, the transmon qubit is displaced by the pump tone and hybridizes with the buffer and the waste leading to a dressed qubit mode:

$$\hat{q} \leftarrow \hat{q} + \frac{g_{\rm b}}{\Delta_{\rm b}}\hat{b} + \frac{g_{\rm w}}{\Delta_{\rm w}}\hat{w} + \frac{\epsilon_{\rm p}e^{-i\omega_{\rm p}t}}{\Delta_{\rm p}} \tag{4.3}$$

where, $\Delta_{\rm m} = \omega_{\rm m} - \omega_{\rm q}$ with $m = (b, w, p)$. Considering that $\epsilon_{\rm d} \ll 1$, the Hamiltonian written in the dressed basis is:

$$\begin{aligned}\hat{H}/\hbar = \omega_{\rm b}\hat{b}^\dagger\hat{b} + \omega_{\rm w}\hat{w}^\dagger\hat{w} + (\omega_{\rm q}+\alpha)\hat{q}^\dagger\hat{q} + \epsilon_{\rm d}(\hat{b}e^{i\omega_{\rm d}t}+\hat{b}^\dagger e^{-i\omega_{\rm d}t}) \\ - \frac{\alpha}{12}\left[\hat{q}+\hat{q}^\dagger + \frac{g_{\rm b}}{\Delta_{\rm b}}(\hat{b}+\hat{b}^\dagger) + \frac{g_{\rm w}}{\Delta_{\rm w}}(\hat{w}+\hat{w}^\dagger) + \frac{\epsilon_{\rm p}}{\Delta_{\rm p}}(e^{i\omega_{\rm p}t}+e^{-i\omega_{\rm p}t})\right]^4\end{aligned} \tag{4.4}$$

where the $\omega_{\rm i}/2\pi$ are the measured frequencies shifted by the mode hybridization.

The expansion of the nonlinear term gives rise to hundreds of terms among which only a few of them conserve the energy. These a the terms composed of the $\hat{O}^\dagger\hat{O}$ monomials. We can classify them in two different Hamiltonians according to the physical effect they describe: $\hat{H}_{\rm Starck}$ for the frequency shifts due to the pump and $\hat{H}_{\rm Kerr}$ for all the Kerr effects between the circuit elements.

The other monomials of the expansion describe energy non-conserving terms. They include the four-wave mixing terms of interest to us for the SMPD, but also more exotic terms. We will classify them in the non conservative Hamiltonian $\hat{H}_{\rm nc}$. Finally, with the drive term $\hat{H}_{\rm drive}$ introduced, the full Hamiltonian is:

$$\hat{H} = \hat{H}_{\rm Starck} + \hat{H}_{\rm Kerr} + \hat{H}_{\rm nc} + \hat{H}_{\rm drive} \tag{4.5}$$

where:

$$\hat{H}_{\rm drive} = \epsilon_{\rm d}(\hat{b}e^{i\omega_{\rm d}t}+\hat{b}^\dagger e^{-i\omega_{\rm d}t}) \tag{4.6}$$

$$\hat{H}_{\rm Stark}/\hbar = \sum_{\rm m=b,w}\left(\omega_{\rm m} - \chi_{\rm qm}\left|\xi_{\rm p}\right|^2\right)\hat{m}^\dagger\hat{m} + \left(\omega_{\rm q} - 2\chi_{\rm qq}\left|\xi_{\rm p}\right|^2\right)\hat{q}^\dagger\hat{q}, \tag{4.7}$$

$$\hat{H}_{\rm Kerr}\hbar = \sum_{\rm m=b,w,q} -\frac{\chi_{\rm mm}}{2}\hat{m}^{\dagger 2}\hat{m}^2 - \chi_{\rm qb}\hat{b}^\dagger\hat{b}\hat{q}^\dagger\hat{q} - \chi_{\rm qw}\hat{w}^\dagger\hat{w}\hat{q}^\dagger\hat{q} - \chi_{\rm bw}\hat{w}^\dagger\hat{w}\hat{b}^\dagger\hat{b}, \tag{4.8}$$

$$\hat{H}_{\rm nc}/\hbar = \underbrace{g_3\hat{b}\hat{w}^\dagger\hat{q}^\dagger e^{-i\omega_{\rm p}t} + g_3\hat{b}^\dagger\hat{w}\hat{q}e^{i\omega_{\rm p}t}}_{\text{SMPD 4-waves mixing terms}} + \cdots + \underbrace{g_3\hat{b}^\dagger\hat{w}^\dagger\hat{q}^\dagger e^{i\omega_{\rm p}t}}_{\text{other 4wm terms}} + \cdots \underbrace{-2\alpha\frac{g_{\rm b}}{\Delta_{\rm b}}\frac{g_{\rm w}}{\Delta_{\rm w}}\hat{q}^\dagger\hat{q}\hat{b}\hat{w}^\dagger}_{\text{other terms}} \tag{4.9}$$

with:

$$\chi_{\mathrm{qq}} = \frac{\alpha}{2} \qquad \chi_{\mathrm{ww}} = \frac{\alpha}{2}\frac{g_{\mathrm{w}}^4}{\Delta_{\mathrm{w}}^4} \qquad \chi_{\mathrm{bb}} = \frac{\alpha}{2}\frac{g_{\mathrm{b}}^4}{\Delta_{\mathrm{b}}^4} \tag{4.10}$$

$$\chi_{\mathrm{qm}} = 2\alpha\frac{g_{\mathrm{m}}^2}{\Delta_{\mathrm{m}^2}} \qquad \chi_{\mathrm{bw}} = 2\alpha\frac{g_{\mathrm{b}}^2}{\Delta_{\mathrm{b}}^2}\frac{g_{\mathrm{w}}^2}{\Delta_{\mathrm{w}}^2} \qquad g_3 = -\xi_{\mathrm{p}}\sqrt{\chi_{\mathrm{qb}}\chi_{\mathrm{qw}}} \tag{4.11}$$

$$\xi_{\mathrm{p}} = \frac{\epsilon_{\mathrm{p}}}{\Delta_{\mathrm{p}}} \tag{4.12}$$

We have neglected the terms $\hat{m}^\dagger\hat{m}$ arising from the normal ordering of the fourth-order term since their effect is just to shift the bare frequencies ω_m by a constant amount. In the following, we will disregard the terms $\chi_{\mathrm{bw}}, \chi_{\mathrm{bb}}, \chi_{\mathrm{ww}}$ as well as the frequency shift of the resonator, $\chi_{\mathrm{qm}}|\xi_{\mathrm{p}}|^2$, caused by the pump, as they are much smaller than the other terms in the equation.

We then move to a rotating frame defined by the following the unitary transformation:

$$\hat{U}^\dagger = e^{i\omega_{\mathrm{d}}\hat{b}^\dagger\hat{b}}e^{i(\omega_{\mathrm{w}}-\delta_{\mathrm{w}})\hat{w}^\dagger\hat{w}}e^{i(\omega_{\mathrm{q}}-2\chi_{\mathrm{qq}}|\xi_{\mathrm{p}}|^2)\hat{q}^\dagger\hat{q}} \tag{4.13}$$

The purpose of this transformation is to make the driving term $\hat{H}_{\mathrm{drive}}$ (ω_{d} term) independent of time, to introduce the parameter δ_{w} that marks the relation between the output photon frequency and the pump and drive frequencies, and finally to move in the qubit rotating frame, considering that its bandwidth is infinitely narrow.

In this new frame, the rotating-wave approximation (RWA) allows us to remove the fast-rotating terms, whereas one keeps the four-wave mixing terms that are essential for SMPD operation (see Equation 4.9) when they are quasi-static in the rotating frame. These terms transform as:

$$\hat{U}^\dagger(g_3\hat{b}\hat{w}^\dagger\hat{q}^\dagger e^{-i\omega_{\mathrm{p}}t} + hc)\hat{U} = e^{-i(\omega_{\mathrm{p}}+\omega_{\mathrm{d}}-\omega_{\mathrm{w}}+\delta_{\mathrm{w}}-\omega_{\mathrm{q}}+2|\xi_{\mathrm{p}}|^2)t}g_3\hat{b}\hat{w}^\dagger\hat{q}^\dagger + hc \tag{4.14}$$

The condition on the pump frequency to stop the rotation is thus:

$$\omega_p = \omega_{\mathrm{q}} + \omega_{\mathrm{w}} - \omega_{\mathrm{b}} - \delta_{\mathrm{w}} + \delta_{\mathrm{b}} - 2\left|\xi_{\mathrm{p}}\right|^2\chi_{\mathrm{qq}}. \tag{4.15}$$

where we have taken into account that $\omega_{\mathrm{d}} = \omega_{\mathrm{b}} - \delta_{\mathrm{b}}$. We define $\delta_{\mathrm{p}} = \delta_{\mathrm{b}} - \delta_{\mathrm{w}}$ as the frequency detuning of the pump. The parameter δ_{w} introduced earlier is now well defined as the function of the experiment parameters: $\delta_{\mathrm{w}} = \delta_{\mathrm{b}} - \delta_{\mathrm{p}}$. The frequency of the waste photon produced by the four-wave mixing is dependent on the frequency of the input photon but also on the pump frequency.

By replacing the bosonic operator $\hat{q}$ by the two level-level lowering operator $\hat{\sigma}$, the final Hamiltonian reads:

$$\hat{H}/\hbar = \delta_{\mathrm{b}}\hat{b}^\dagger\hat{b} + (\delta_{\mathrm{b}} - \delta_{\mathrm{p}})\hat{w}^\dagger\hat{w} + \underbrace{g_3\hat{b}\hat{w}^\dagger\hat{\sigma}^\dagger + g_3\hat{b}^\dagger\hat{w}\hat{\sigma}}_{\text{four-wave mixing terms}} - \chi_{\mathrm{qb}}\hat{b}^\dagger\hat{b}\hat{\sigma}^\dagger\hat{\sigma} - \chi_{\mathrm{qw}}\hat{w}^\dagger\hat{w}\hat{\sigma}^\dagger\hat{\sigma} + \xi_{\mathrm{p}}(\hat{b} + \hat{b^\dagger}) \tag{4.16}$$

4.2 Adiabatic elimination of the output resonator

4.2.1 Dynamic of the reduced system

The Hamiltonian described in the last section provides a four-wave mixing process when the frequency matching condition Equation 4.15 is satisfied. When the pump tone is applied, a buffer photon is then converted in a qubit excitation and a waste photon. As introduced in Section 4.1.1, this conversion has to be irreversible in order to avoid the reverse process.

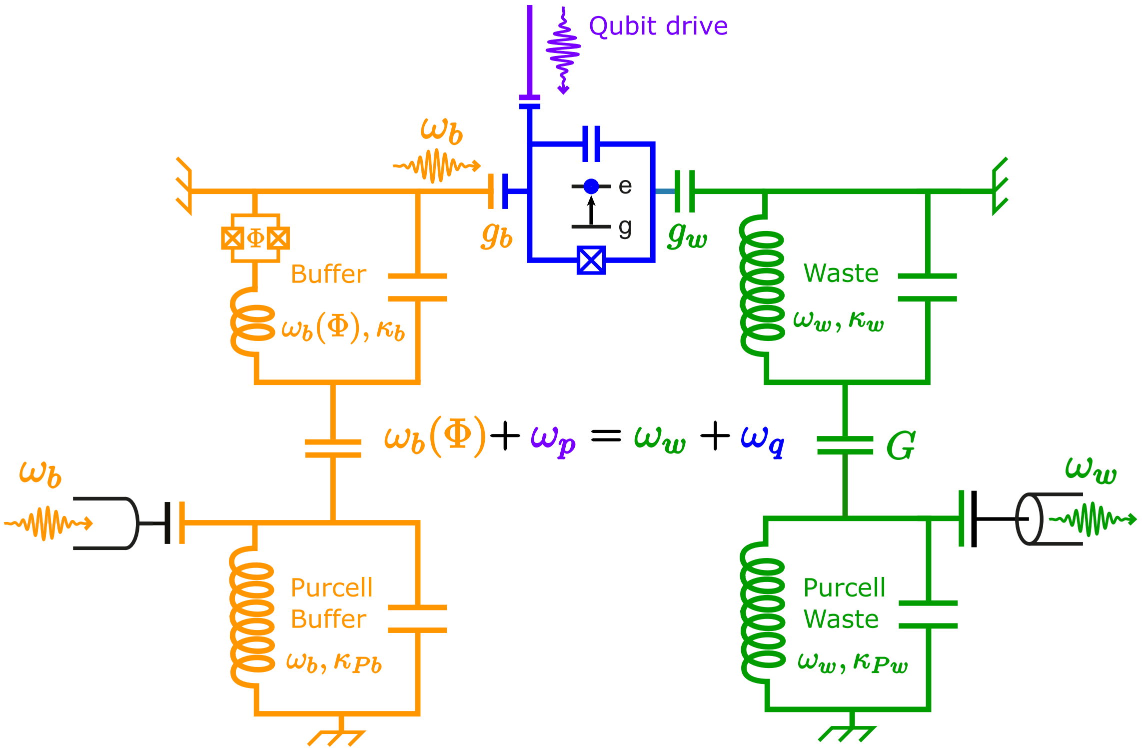

Figure 4.2: **SMPD electrical representation** The buffer resonator (orange), capacitively coupled to the transmon qubit (coupling strength g_b) incorporates a SQUID to adapt its frequency to that of the photon. The buffer Purcell resonator (same color) is used to protect the qubit from the line environment and increase the T_1. The waste resonator (green) also capacitively coupled to the qubit (coupling strength g_w) interacts more strongly with the line so that its state remains close to the ground state $|0\rangle$. The Purcell waste allows this strong coupling in addition to its role in protecting the qubit. An other benefit of the Purcell filter is to reduce the readout time of the qubit. The transmon qubit (blue) allows the mixing between the circuit elements thanks to the non linearity provided by the Josephson junction. The 4-waves mixing process is triggered by the pump tone (purple) when the frequency condition: $\omega_\mathrm{b} + \omega_\mathrm{p} = \omega_\mathrm{q} + \omega_\mathrm{w}$ is realized.

This irreversibility can be simply obtained by making a waste resonator with an energy decay rate κ_w much larger than the coupling strength g_3 between the buffer and the waste through the qubit. In a semi-classical picture, one could say that the photon created in the waste mode disappears so quickly that the reverse process can never occur. In these conditions, the number of photons in the waste resonator photons always remains close to zero, i.e. the waste resonator stays close to its ground state, and the adiabatic elimination of the waste mode is possible. This approximation simply consists in tracing out the state of the system on the waste degree of freedom. The evolution of the remaining system will give us the dynamics of the four-waves mixing process.

We approach the problem using the Lindblad formalism by inserting a dissipation channel to the waste resonator. The full Lindblad equation then writes:

$$\dot{\hat{\rho}} = \frac{1}{i\hbar}[\hat{H}, \hat{\rho}] + \kappa_\mathrm{w}\mathcal{D}_{\hat{w}}(\hat{\rho}) + \kappa_\mathrm{b}\mathcal{D}_{\hat{b}}(\hat{\rho}) \tag{4.17}$$

In the adiabatic elimination framework, we search for a solution of Equation 4.17 in the form:

$$\begin{aligned}\hat{\rho} =&\hat{\rho}_{00} \otimes |0\rangle \langle 0| + \lambda \left(\hat{\rho}_{10} \otimes |1\rangle \langle 0| + \hat{\rho}_{01} \otimes |0\rangle \langle 1|\right) + \\ &+ \lambda^2 \left(\hat{\rho}_{11} \otimes |1\rangle \langle 1| + \hat{\rho}_{02} \otimes |0\rangle \langle 2| + \hat{\rho}_{20} \otimes |2\rangle \langle 0|\right) + O(\lambda^3).\end{aligned} \tag{4.18}$$

The operators $|m\rangle \langle n|$ act on the waste Hilbert space. The reduced density matrix $\hat{\rho}_{\mathrm{mn}}$ describes the system evolution in which the degrees of freedom of the waste have been projected. The λ parameter accounts for the fact that the waste is close to its vacuum state, thus $\lambda \ll 1$. The derivation consists in extracting the dynamics of the reduced density matrix $\hat{\rho}_{\mathrm{qb}} = \mathrm{Tr}_{\mathrm{w}}(\rho) = \rho_{00} + \lambda^2 \rho_{11}$.

As we can only calculate the impact of $\hat{w}$ and $\hat{w}^\dagger$ on the $|n\rangle \langle m|$, it is useful to rewrite the Hamiltonian in the following form:

$$\hat{H} = \hbar g_3 \hat{b} \hat{\sigma}^\dagger \hat{w}^\dagger + \hbar g_3^* \hat{b}^\dagger \hat{\sigma} \hat{w} + \left(\delta_{\mathrm{b}} - \delta_{\mathrm{p}} - \hbar \chi_{qw} \hat{\sigma}^\dagger \hat{\sigma}\right) \hat{w}^\dagger \hat{w} + \hat{H}_{qb} \tag{4.19}$$

with:

$$\hat{H}_{qb} = -\hbar \chi_{qb} \hat{b}^\dagger \hat{b} \hat{\sigma}^\dagger \hat{\sigma} + \hbar \delta_{\mathrm{b}} \hat{b}^\dagger \hat{b} + \epsilon_{\mathrm{d}} (\hat{b} + \hat{b}^\dagger). \tag{4.20}$$

By injecting Equation 4.18 in Equation 4.17 and projecting on $\langle 0| \cdot |0\rangle$, $\langle 0| \cdot |1\rangle$ and $\langle 1| \cdot |0\rangle$ respectively, we get the following system of equations:

$$\frac{\dot{\hat{\rho}}_{00}}{\kappa_w} = \lambda^2 \left(i\rho_{01} \hat{A} - i\hat{A}^\dagger \rho_{10} + \rho_{11}\right) + \frac{1}{i\hbar} [\hat{H}_{\mathrm{qb}}, \hat{\rho}] + O(\lambda^3) \tag{4.21}$$

$$\frac{\dot{\hat{\rho}}_{01}}{\kappa_w} = i\rho_{00} \hat{A}^\dagger - \rho_{01} \left(\frac{1}{2} - i\hat{\Delta}\right) + O(\lambda) \tag{4.22}$$

$$\frac{\dot{\hat{\rho}}_{11}}{\kappa_w} = i\rho_{10} \hat{A}^\dagger - i\hat{A}\rho_{01} - i[\hat{\Delta}, \rho_{11}] - \rho_{11} + O(\lambda) \tag{4.23}$$

where

$$\hat{A} = \frac{g_3}{\kappa_w \delta} \hat{b} \hat{\sigma}^\dagger \tag{4.24}$$

$$\hat{\Delta} = \frac{\delta_{\mathrm{b}} - \delta_{\mathrm{p}} - \chi_{qw} \hat{\sigma}^\dagger \hat{\sigma}}{\kappa_w} \tag{4.25}$$

The key point is to invoke the adiabatic approximation for assuming that ρ_{11} and ρ_{01} are continuously in the steady state. One can then solve the above system and obtain an evolution equation for the reduced density matrix $\hat{\rho}_{\mathrm{qb}} \sim \hat{\rho}_{00}$:

$$\boxed{\frac{d}{dt} \hat{\rho}_{\mathrm{qb}} = -i\Delta_{\mathrm{nl}} [\hat{b}^\dagger \hat{b} \hat{\sigma} \sigma^\dagger, \hat{\rho}_{\mathrm{qb}}] + \kappa_{\mathrm{nl}} \mathcal{D}_{\hat{b}\hat{\sigma}^\dagger}(\hat{\rho}_{\mathrm{qb}}) + \kappa_{\mathrm{b}} \mathcal{D}_{\hat{b}}(\hat{\rho}_{\mathrm{qb}}) + [\hat{H}_{\mathrm{qb}}, \hat{\rho}_{\mathrm{qb}}] + O(\delta^3)}. \tag{4.26}$$

with:

$$\kappa_{\mathrm{nl}} = \frac{4|g_3|^2/\kappa_{\mathrm{w}}}{1 + 4|\frac{\delta_{\mathrm{b}} - \delta_{\mathrm{p}} - \chi_{\mathrm{qw}}}{\kappa_{\mathrm{w}}}|^2}, \tag{4.27}$$

$$\Delta_{\mathrm{nl}} = \frac{4|g_3|^2/\kappa_{\mathrm{w}}}{1 + 4|\frac{\delta_{\mathrm{p}} - \delta_{\mathrm{b}} - \chi_{\mathrm{qw}}}{\kappa_{\mathrm{w}}}|^2} \frac{\chi_{\mathrm{qw}} - (\delta_{\mathrm{p}} - \delta_{\mathrm{b}})}{\kappa_{\mathrm{w}}}, \tag{4.28}$$

$$\tag{4.29}$$

The dissipating term κ_{nl} is the core of the SMPD. It allows for the irreversible transformation of a buffer photon in a qubit excitation. This dissipation is maximum for $\delta_{\mathrm{p}} - \delta_{\mathrm{b}} = \chi_{\mathrm{qw}}$. As a consequence the frequency condition for best inducing the four-wave mixing process becomes:

$$\boxed{\omega_p = \omega_{\mathrm{q}} + \omega_{\mathrm{w}} - \omega_{\mathrm{b}} - \chi_{\mathrm{qw}} - |\xi_{\mathrm{p}}|^2\, 2\chi_{\mathrm{qq}}} \tag{4.30}$$

With this condition, we define the SMPD dissipation rate as:

$$\boxed{\Gamma_{\mathrm{SMPD}} = \kappa_{\mathrm{nl}}|_{\delta_{\mathrm{p}}+\delta_{\mathrm{b}}=\chi_{\mathrm{qw}}} = 4|\xi_{\mathrm{p}}|^2 \frac{\chi_{\mathrm{qb}}\chi_{\mathrm{qw}}}{\kappa_{\mathrm{w}}}} \tag{4.31}$$

This quantity will be used in the next section for defining an important physical concept, the cooperativity.

4.2.2 Efficiency and cooperativity

In this section we derive the efficiency of conversion $\eta_{4\mathrm{wm}}$ between the state $|1\rangle$ of the buffer and the qubit state $|e\rangle$.

In our experiments, the quantum state of the light impinging the buffer will be either a simple Fock state $|1\rangle$ in the case of the single spin detection or a coherent state $|\alpha\rangle$ with a very low number of photons for the detector characterization. To derive the value of $\eta_{4\mathrm{wm}}$ we place ourselves in the case where a weak coherent tone of amplitude b_{in} is sent on the buffer. The number of photons arriving on the cavity per unit of time is defining as $|b_{\mathrm{in}}|^2$. Assuming that the drive illuminates the buffer for a time t, the resonator will be in a coherent state α where $|\alpha|^2 = |b_{\mathrm{in}}|^2 t$ is the number of photon in the incoming wave-packet. Like $|\alpha| \ll 1$, one can developed the state as $|\alpha\rangle \approx (1 - |\alpha|^2/2)(|0\rangle + \alpha\,|1\rangle)$. Then we can write the statistical mixture: $\hat{\rho} \approx (1 - |\alpha|^2)\,|0\rangle\,\langle 0| + |\alpha^2|\,|1\rangle\,\langle 1|$. Considering this input state, the 4-wave mixing will promote the qubit in its excited state with the probability $p_{\mathrm{e}} = \eta_{4\mathrm{wm}}|\alpha|^2$.

The idea of the derivation is to solve Equation 4.26 and write the evolution of the qubit excited state p_{e} as a function of the number of photons in the incoming field . The drive amplitude will be defined such as $\epsilon_{\mathrm{d}} = \sqrt{\kappa_{\mathrm{b}}} b_{\mathrm{in}}$.

We rewrite the Equation 4.26 for $\Delta_{\mathrm{nl}} = 0$, $\delta_{\mathrm{b}} = 0$ and in the limit where $\chi_{\mathrm{qb}}, \chi_{\mathrm{bb}} \ll \kappa_{\mathrm{nl}}, \kappa_{\mathrm{b}}$:

$$\frac{d}{dt}\hat{\rho}_{\mathrm{qb}} \quad = \quad \kappa_{\mathrm{nl}}\mathcal{D}_{\hat{b}\hat{\sigma}^\dagger}(\hat{\rho}_{\mathrm{qb}}) + \kappa_{\mathrm{b}}\mathcal{D}_{\hat{b}}(\hat{\rho}_{\mathrm{qb}}) + \epsilon_{\mathrm{d}}[\hat{b} + \hat{b}^\dagger, \hat{\rho}_{\mathrm{qb}}] \tag{4.32}$$

We search for a solution of this equation in the form:

$$\hat{\rho}_{\mathrm{qb}} = \hat{\rho}_{\mathrm{gg}}\,|g\rangle\,\langle g| + \hat{\rho}_{\mathrm{eg}}\,|e\rangle\,\langle g| + \hat{\rho}_{\mathrm{ge}}\,|g\rangle\,\langle e| + \hat{\rho}_{\mathrm{ee}}\,|e\rangle\,\langle e|\,. \tag{4.33}$$

The reduced density matrix ρ_{kl} represents the buffer state for a qubit state $|k\rangle\,\langle l|$. The goal is to find the expression of the qubit excited state $p_{\mathrm{e}} = \mathrm{Tr}(\rho_{\mathrm{ee}})$ by tracing on the degree of freedom of the buffer resonator.

By injecting the Equation 4.33 in Equation 4.32 and projecting on $\langle e|\cdot|e\rangle$ and $\langle g|\cdot|g\rangle$, we obtain the equation leading the dynamic of ρ_{gg} and ρ_{ee}:

$$\dot{\rho}_{\mathrm{gg}}(t) = -\frac{\kappa_{\mathrm{nl}}}{2}(\hat{b}^\dagger\hat{b}\hat{\rho}_{\mathrm{gg}} + \hat{\rho}_{\mathrm{gg}}\hat{b}^\dagger\hat{b}) + \kappa_{\mathrm{b}}\mathcal{D}_{\hat{b}}(\hat{\rho}_{\mathrm{gg}}) + \epsilon_{\mathrm{d}}[\hat{b} + \hat{b}^\dagger, \hat{\rho}_{\mathrm{gg}}] \tag{4.34}$$

$$\dot{\rho}_{\mathrm{ee}}(t) = -\frac{\kappa_{\mathrm{nl}}}{2}\hat{b}\hat{\rho}_{\mathrm{gg}}\hat{b}^\dagger + \kappa_{\mathrm{b}}\mathcal{D}_{\hat{b}}(\hat{\rho}_{\mathrm{ee}}) + \epsilon_{\mathrm{d}}[\hat{b} + \hat{b}^\dagger, \hat{\rho}_{\mathrm{ee}}]. \tag{4.35}$$

From Equation 4.35 and with the trace properties, we can write the equation leading the dynamic of p_{e}:

$$\dot{p}_{\mathrm{e}} = -\frac{\kappa_{\mathrm{nl}}}{2} \operatorname{Tr}\left(\hat{b}\hat{\rho}_{\mathrm{gg}}\hat{b}^{\dagger}\right) \tag{4.36}$$

To finish the derivation, one needs an explicit solution for ρ_{gg} . The Equation 4.34 can be solved by assuming a solution of the form: $\rho_{\mathrm{gg}}(t) = A(t) \left|\beta\right\rangle \left\langle\beta\right|$, where $\left|\beta\right\rangle$ is a coherent state to determined and $A(t)$ a real function. One indeed finds a solution provided that:

$$\beta = \frac{-2\epsilon_{\mathrm{d}}}{\kappa_{\mathrm{b}} + \kappa_{\mathrm{nl}}} \tag{4.37}$$

$$A(t) = \exp\left(\kappa_{\mathrm{nl}} \frac{-4\epsilon_{\mathrm{d}}^2}{(\kappa_{\mathrm{b}} + \kappa_{\mathrm{nl}})^2} t\right). \tag{4.38}$$

This result allows us to rewrite Equation 4.36 in the form $\dot{p}_{\mathrm{e}} = |\beta|^2 A(t)$. Considering that the qubit is in its ground state at $t = 0$, one obtains the following result for its excited population:

$$p_{\mathrm{e}}(t) = 1 - \exp\left(-\eta_{4\mathrm{wm}}|b_{\mathrm{in}}|^2 t\right) \approx \eta_{4\mathrm{wm}} n_{\mathrm{in}} \tag{4.39}$$

Where we take $n_{\mathrm{in}} = |b_{\mathrm{in}}|^2 t$ as the mean number of photon contained in a pulse of length t at short times. This estimate gives the efficiency $\eta_{4\mathrm{wm}}$ for the 4-wave mixing process:

$$\boxed{\eta_{4\mathrm{wm}} = 4\frac{\kappa_{\mathrm{b}}\kappa_{\mathrm{nl}}}{(\kappa_{\mathrm{b}} + \kappa_{\mathrm{nl}})^2}} \tag{4.40}$$

We can define a last figure to fully characterize the conversion process. To convert efficiently a photon sent to the buffer resonator into a qubit excitation, the filling rate of the buffer resonator (equal to the coupling rate κ_{b}) has to be equal to the conversion rate. This criterion is contained in the cooperativity defined as follows:

$$\boxed{\mathcal{C} = \frac{\Gamma_{\mathrm{SMPD}}}{\kappa_{\mathrm{b}}} = 4|\xi_{\mathrm{p}}|^2 \frac{\chi_{\mathrm{qb}}\chi_{\mathrm{qw}}}{\kappa_{\mathrm{w}}\kappa_{\mathrm{b}}}} \tag{4.41}$$

The efficiency of the 4-wave mixing process can then be expressed as:

$$\boxed{\eta_{4\mathrm{wm}} = \frac{4\mathcal{C}}{(1 + \mathcal{C})^2}} \tag{4.42}$$

The process efficiency $\eta_{4\mathrm{wm}}$ is thus maximal for unit cooperativity. We can reach this regime by adjusting the pump strength so that $|\xi_{\mathrm{p}}|^2 = \kappa_{\mathrm{w}}\kappa_{\mathrm{b}}/(4\chi_{\mathrm{qb}}\chi_{\mathrm{qw}})$.

However, ξ_{p} cannot take arbitrary values, in fact, since the pump contributes to the phase across the junction, its maximum value must be much smaller than π. The circuit parameters must therefore satisfy the inequality:

$$\frac{\kappa_{\mathrm{b}}\kappa_{\mathrm{w}}}{\chi_{\mathrm{b}}\chi_{\mathrm{w}}} \ll 4\pi^2 \approx 40. \tag{4.43}$$

In addition, we have also to avoid the triggering of spurious and uncontrollable parametric processes, involving more than two photons. These processes that need a high pump energy can be mitigated by keeping the energy required to trigger the four-wave mixing as low as possible. A low pump energy also avoids to excite the phonon bath which could transfer its energy to the qubit and consequently create false positives.

It is therefore always better to have the lowest possible pump strength. As a consequence, the SMPD presented in the following will be designed such that $\chi_{\mathrm{b}}\chi_{\mathrm{w}} \gg \kappa_{\mathrm{b}}\kappa_{\mathrm{w}}$.

4.3 Two coupled cavities model

4.3.1 Input-output equations

The adiabatic elimination performed in the last section captures the system dynamics and extracts the efficiency of the four-wave mixing process, but it works only under restrictive assumptions. The waste dissipation rate κ_w has to be much larger than the rate Γ_SMPD of the SMPD dynamics. In addition, this derivation does not give us access to the detector bandwidth.

To simplify the model, we can use the input-output theory as outlined in Section 3.1.4.2. We write the input-output equations for the buffer operator $\hat{b}$ and the hybrid operator $\hat{\sigma}\hat{b}$, which captures the dynamics of both the qubit and the waste. We will use the Hamiltonian given by Equation 4.19 without the source term and by excluding the cross-Kerr terms χ_mn as they have a small effect compared to g_3 and are not important for the system dynamics.

With this assumption, the evolution of the operators reads:

$$\dot{\hat{b}} = -i\delta_\mathrm{b}\hat{b} - ig_3\hat{w}\hat{\sigma} - \frac{\kappa_\mathrm{b}}{2}\hat{b} + \sqrt{\kappa_\mathrm{bext}}\hat{b}_\mathrm{in} \tag{4.44}$$

$$\dot{\hat{\sigma}\hat{w}} = -i(\delta_\mathrm{b} - \delta_\mathrm{p})\hat{\sigma}\hat{w} - ig_3\hat{b}(\hat{\sigma}\hat{\sigma}^\dagger - \hat{w}^\dagger\hat{w}\hat{\sigma}_\mathrm{z}) - \frac{\kappa_\mathrm{w}}{2}\hat{\sigma}\hat{w} + \sqrt{\kappa_\mathrm{wext}}\hat{\sigma}\hat{w}_\mathrm{in} \tag{4.45}$$

In all generality, these equations have to be solved in the Hilbert space: $\mathcal{H}_\mathrm{SMPD} = \mathcal{H}_\mathrm{b} \otimes \mathcal{H}_\mathrm{w} \otimes \mathcal{H}_\sigma$ which have an infinite dimension. However, the 4-wave mixing process at the heart of the SMPD implies one-to-one photon conversion. We can therefore safely restrict ourselves to the subspace representing the 4-wave mixing generated by the states: $|0,g,0\rangle, |1,g,0\rangle, |0,e,1\rangle$ and $|0,e,0\rangle$. More precisely, $|0,g,0\rangle$ describe the system ready to detect a photon, $|1,g,0\rangle$ represents the photon impinging the buffer, then the four-wave mixing occurs with $|0,e,1\rangle$ and finally the waste photon is dissipated into the environment with $|0,e,0\rangle$.

The projection operator in the desired space is:

$$\hat{\Pi} = |0,g,0\rangle\langle 0,g,0| + |1,g,0\rangle\langle 1,g,0| + |0,e,1\rangle\langle 0,e,1| + |0,e,0\rangle\langle 0,e,0| \tag{4.46}$$

where $|i,j,k\rangle$ denotes the states containing i (resp j,k) photons in the buffer (resp qubit,waste). By using the redefinition $\hat{O} \leftarrow \hat{\Pi}\hat{O}\hat{\Pi}$, Equation 4.44 and Equation 4.45 become:

$$\dot{\hat{b}} = -i\delta_\mathrm{b}\hat{b} - ig_3\hat{w}\hat{\sigma} - \frac{\kappa_\mathrm{b}}{2}\hat{b} + \sqrt{\kappa_\mathrm{bext}}\hat{b}_\mathrm{in} \tag{4.47}$$

$$\dot{\hat{\sigma}\hat{w}} = -i(\delta_b - \delta_p)\hat{\sigma}\hat{w} - ig_3\hat{b} - \frac{\kappa_\mathrm{w}}{2}\hat{\sigma}\hat{w} + \sqrt{\kappa_\mathrm{wext}}\hat{\sigma}\hat{w}_\mathrm{in} \tag{4.48}$$

because, in the restricted subspace we cannot simultaneously have one photon in the buffer and in the waste, so $\hat{\Pi}\hat{b}\hat{w}^\dagger\hat{w}\hat{\Pi} = 0$ and one can verify that $\hat{\Pi}\hat{b}\hat{\sigma}\hat{\sigma}^\dagger\hat{\Pi} = \hat{\Pi}\hat{b}\hat{\Pi}$. This system is similar to the one describing the coupling between two cavities, with a coupling strength given by $g_3 = \xi_\mathrm{p}\sqrt{\chi_\mathrm{qb}\chi_\mathrm{qw}}$.

To extract the interesting parameters, we take the average values of the field: $\langle\hat{b}\rangle = \beta$, $\langle\hat{b}_\mathrm{in}\rangle = \beta_\mathrm{in}$ and $\langle\hat{\sigma}\hat{w}\rangle = v$. As no photons impact the output resonator, we will take $\langle\hat{\sigma}\hat{w}_\mathrm{in}\rangle = 0$. In addition, we define $v_\mathrm{out} = \langle\hat{\sigma}\hat{w}_\mathrm{out}\rangle = \sqrt{\kappa_\mathrm{w}}\langle\hat{\sigma}\hat{w}\rangle = \sqrt{\kappa_\mathrm{w}}v$. With these averaged values the system becomes:

$$\dot{\beta} = -i\delta_\mathrm{b}\beta - ig_3 v - \frac{\kappa_\mathrm{b}}{2}\beta + \sqrt{\kappa_\mathrm{bext}}\beta_\mathrm{in} \tag{4.49}$$

$$\dot{v} = -i(\delta_\mathrm{b} - \delta_\mathrm{p})v - ig_3\beta - \frac{\kappa_\mathrm{w}}{2}v. \tag{4.50}$$

We then Fourier transform these equations and redefine β and v as the Fourier components, yielding to the simple system:

$$-i\delta\beta = -i\delta_{\mathrm{b}}\beta - ig_3 v - \frac{\kappa_{\mathrm{b}}}{2}\beta + \sqrt{\kappa_{\mathrm{bext}}}\beta_{\mathrm{in}} \tag{4.51}$$

$$-i\delta v = -i(\delta_{\mathrm{b}} - \delta_{\mathrm{p}})v - ig_3\beta - \frac{\kappa_{\mathrm{w}}}{2}v \tag{4.52}$$

where δ represents the frequency detuning of the incoming photon compared to the frequency of the rotating frame.

4.3.2 Transmission coefficient and bandwidth

From the above input output equation, we can extract the frequency-dependent transmission coefficient $|S_{21}(\delta)|^2 = |v_{\mathrm{out}}/\beta_{\mathrm{in}}|^2$ which represents the transmission efficiency from a buffer photon to a waste photon as a function of the frequency. The full calculation well developed in [Alb21] gives:

$$|S_{21}(\delta)|^2 = \frac{4\mathcal{C}}{\left|1 + \mathcal{C} - 4\frac{\delta(\delta+\delta_{\mathrm{p}})}{\kappa_{\mathrm{b}}\kappa_{\mathrm{w}}} + 2i\frac{\delta}{\kappa_{\mathrm{b}}} + 2i\frac{(\delta+\delta_{\mathrm{p}})}{\kappa_{\mathrm{w}}}\right|^2}. \tag{4.53}$$

where $\mathcal{C} = 4|\xi_0|^2\frac{\chi_{\mathrm{b}}\chi_{\mathrm{w}}}{\kappa_{\mathrm{b}}\kappa_{\mathrm{w}}}$ is the cooperativity, δ is the detuning of the incoming photon with the $\hat{b}$ mode and δ_p the frequency detuning of the pump compared to its optimal frequency. The Figure 4.3a,b illustrate the evolution of this transmission coefficient as the function of the pump and photon frequency detuning. Two configurations of buffer and waste bandwidth are shown, corresponding to the situations encountered in the rest of this manuscript.

When the pump is optimally tuned and the incoming photon in resonance with the buffer, the transmission coefficient becomes simply:

$$|S_{21}(\delta)|^2 = \frac{4\mathcal{C}}{(1+\mathcal{C})^2} \tag{4.54}$$

equal to the result given by Equation 4.42.

An important advantage of this two coupled cavity model is to provide an analytical expression for the SMPD bandwidth. By taking a unit cooperativity and considering that the pump is optimally tuned, the full-width-half-maximum of $|S_{21}(\delta)|^2$ is:

$$\boxed{\kappa_{\mathrm{d}} = \sqrt{2}\sqrt{\sqrt{\kappa_{\mathrm{b}}^2\kappa_{\mathrm{w}}^2 + \left(\frac{\kappa_{\mathrm{b}} - \kappa_{\mathrm{w}}}{2}\right)^4} - \left(\frac{\kappa_{\mathrm{b}} - \kappa_{\mathrm{w}}}{2}\right)^2}.} \tag{4.55}$$

Let us to consider now a few particular cases. For $\kappa_{\mathrm{b}} \approx \kappa_{\mathrm{w}}$, one gets $\kappa_{\mathrm{d}} \approx \sqrt{2\kappa_{\mathrm{b}}\kappa_{\mathrm{w}}}$. This regime is shown on Figure 4.3b. For $\kappa_{\mathrm{b}} \ll \kappa_{\mathrm{w}}$, $\kappa_{\mathrm{d}} \approx 2\kappa_{\mathrm{b}}$ (Figure 4.3a) and reciprocally for $\kappa_{\mathrm{b}} \gg \kappa_{\mathrm{w}}$, $\kappa_{\mathrm{d}} \approx 2\kappa_{\mathrm{w}}$.

4.3.3 Cooperativity-dependent bandwidth

For the experiments that will be presented in the next chapters, it is also interesting to estimate the transmission coefficient when the incident photons are not frequency tuned with the detector, i.e when $\delta \neq 0$. we rewrite Equation 4.53 in these conditions keeping a well tuned pump frequency ($\delta_{\mathrm{p}} = 0$):

$$|S_{21}(\delta)|^2 = \frac{\mathcal{C}\kappa_{\mathrm{w}}^2\kappa_{\mathrm{b}}^2/4}{|\delta^2 - i(\frac{\kappa_{\mathrm{b}}+\kappa_{\mathrm{w}}}{2})\delta - \frac{\kappa_{\mathrm{b}}\kappa_{\mathrm{w}}}{4}(1+\mathcal{C})|^2} \tag{4.56}$$

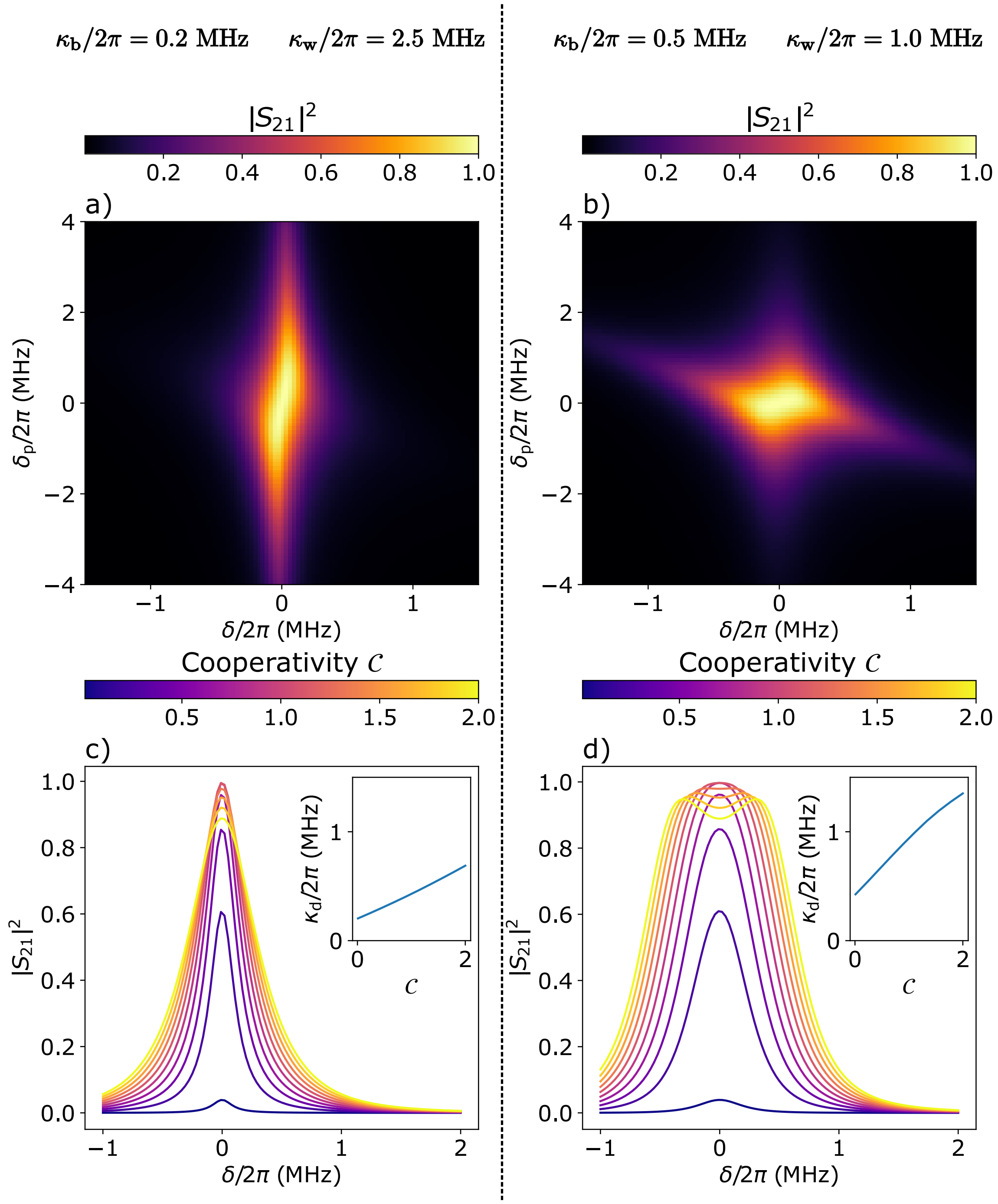

Figure 4.3: **SMPD $|S_{21}|^2$ in various configurations versus δ, δ_p and the cooperativity $\mathcal{C}$.** (a), (b) Transmission parameter $|S_{21}|^2$ represented versus the photon and pump frequency detuning (δ and δ_p) for two different configurations of waste and buffer linewidth. We set a unit cooperativity in both cases. (c), (d) $|S_{21}|^2$ as the function of the photon detuning plotted for various cooperativity $\mathcal{C}$ and for $\delta_\mathrm{p} = 0$. The detector bandwidth extracted from the transmission parameter is plotted in inset.

In order to factorize this expression, we determine the two roots of the denominator, ie the poles of $|S_{21}(\delta)|^2$:

$$\delta_{\pm} = i\frac{\kappa_{\mathrm{b}} + \kappa_{\mathrm{w}}}{4} \pm \frac{1}{2}\sqrt{\kappa_{\mathrm{b}}\kappa_{\mathrm{w}}(1+\mathcal{C}) - \frac{(\kappa_{\mathrm{b}} + \kappa_{\mathrm{w}})^2}{4}} \tag{4.57}$$

The photon counter studied in this part operate in a regime where $\kappa_{\mathrm{b}} \ll \kappa_{\mathrm{w}}$. In addition, we work in a regime where $\mathcal{C} \sim 1$ so we have the condition $4\kappa_{\mathrm{b}}\mathcal{C}/\kappa_{\mathrm{w}} \ll 1$. With these assumptions, we can perform a first order development of the poles yielding to:

$$\delta_{-} \approx i\frac{\kappa_{\mathrm{b}}}{2}(1+\mathcal{C}) \tag{4.58}$$

$$\delta_{+} \approx i\frac{\kappa_{\mathrm{w}}}{2} - i\frac{\kappa_{\mathrm{b}}\mathcal{C}}{2}. \tag{4.59}$$

The transmission coefficient can be rewritten using these expressions:

$$|S_{21}(\delta)|^2 \approx \frac{\mathcal{C}\kappa_{\mathrm{w}}^2\kappa_{\mathrm{b}}^2/4}{\left(\delta^2 + \frac{(\kappa_{\mathrm{w}} - \kappa_{\mathrm{b}}\mathcal{C})^2}{4}\right)^2\left(\delta^2 + \frac{\kappa_{\mathrm{b}}^2(1+\mathcal{C})^2}{4}\right)^2} \tag{4.60}$$

Then, considering only small detunings so that $\delta \ll \kappa_{\mathrm{w}}$, one obtains a simpler result:

$$|S_{21}(\delta)|^2 \approx \frac{4\mathcal{C}}{(1+\mathcal{C})^2}\frac{1}{1+(\frac{2\delta}{\kappa_{\mathrm{b}}(1+\mathcal{C})})^2} \tag{4.61}$$

As expected, taking the value $\delta = 0$, we recover the result given by Equation 4.54. Furthermore, with the assumptions detailed above, the reflection coefficient takes a Lorentzian form with bandwidth $\kappa_{\mathrm{d}} \approx \kappa_{\mathrm{b}}(1+\mathcal{C})$. For unit cooperativity, we find the condition $\kappa_{\mathrm{d}} \approx 2\kappa_{\mathrm{b}}$ already expressed above.

The evolution of the bandwidth in the regime where $\kappa_{\mathrm{b}} \ll \kappa_{\mathrm{w}}$ is shown on Figure 4.3c. The shape of the transmission coefficient versus the photon detuning is almost Lorentzian even at high cooperativity.

Figure 4.3d shows the evolution of the bandwidth in a regime slightly different with $\kappa_{\mathrm{b}} = \kappa_{\mathrm{w}}/2 = 0.5$ MHz. We encounters this regime in the second part of this manuscript for the spin detection. Here on the contrary, the shape of $|S_{21}|^2$ is rapidly moving away from a Lorentzian with the cooperativity. The resulting bandwidth is wider.

4.4 SMPD operation

4.4.1 SMPD cyclic operation

The SMPD operates in a cyclic manner decomposed in three parts (see Figure 4.4):

Detection (D): After initializing the qubit, the SMPD can be prepared for photon detection by applying a microwave tone at frequency ω_{p} to the pump line. The frequency is chosen in order to match the energy condition of the 4-wave mixing. During this detection window, if no photon enters the buffer, the qubit relaxes from its reset population p_{reset} to its equilibrium population p_{eq} with the characteristic time T_1 (see Figure 4.5a). If a detection event occurs, the qubit get excited and starts to relax from the excited state to the equilibrium (see Figure 4.5b). In both cases, the duration of the detection window T_{d} has to be shorter than the qubit relaxation time T_1 as will be described in the next section.

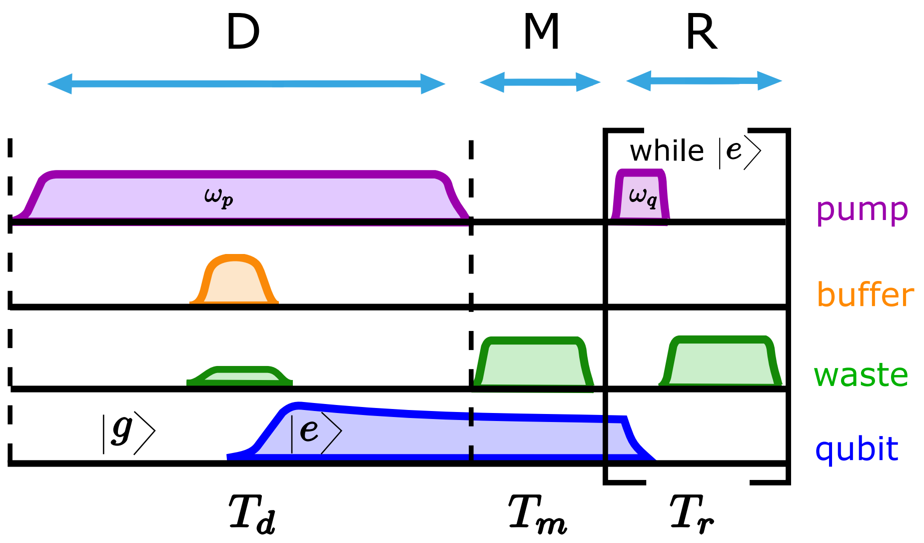

Figure 4.4: **SMPD cyclic operation** The SMPD cycle is composed of three windows, respectively the detection (D), the measurement (M) and the reset (R) window. During the detection a continuous tone at frequency ω_p is sent on the qubit trough the pump line (purple line). Once a photon impinges the buffer resonator (orange line) the four-wave mixing occurs. The qubit gets excited (blue line) while a photon is created in the waste resonator (green line). Due to the strong coupling to the environment, the waste photon is rapidly dissipated. After the initial excitation, the probability to find the qubit in the excited state $|e\rangle$ decreases with the characteristic time T_1 until the measurement window. The qubit state is dispersively readout thanks to the waste resonator. Finally, in the reset window, the qubit is put back in its ground state with a conditional sequence: while the qubit is in $|e\rangle$ a resonant pulse at frequency ω_q is applied trough the pump line and a measurement is performed to check the state. The duration of each window is denoted T_d (resp T_m,T_r) for the detection window (resp measurement and reset)

Measurement (M): The qubit is then dispersively readout using to the waste resonator. A detector "click" corresponds to the measurement of the excited state. The measurement duration T_m is chosen so that the separation between the states in the quadrature phase plane is well sufficient to resolve the reset population of the qubit. The measurement has to be non-destructive as described in Section 3.4.2.

Reset (R): In this part of the cycle, we prepare the qubit in a state where the probability to measure an excited state p_reset is less than the equilibrium population p_eq. In other words, The qubit is almost certainly initialized in its ground state. For this purpose, we apply a conditional sequence. We use the pump line to send resonant pulse at frequency ω_q on the qubit which triggers a Rabi oscillation. The duration of the pulse is chosen so that it inverts the qubit population (π-pulse). The conditional reset begins with a qubit measurement, if the result is $|e\rangle$, a while loop starts, else, the qubit is already is in ground state. The while loop consists in a π-pulse followed by a measurement. The exit condition is to measure the qubit in the ground state. The duration T_r of this window is thus not constant since the number of iterations of the while loop varies between cycles.

4.4.2 SMPD efficiency

In this section we explicit the total detector efficiency η_d defined as the click probability when a photon impinges the detector. This overall efficiency can be broken down into several contributions.

Duty cycle η_D: The duty cycle η_D is the ratio of the detection time to the total cycle time. It accounts for the fact that incident photons arriving during the qubit read-out and reset are not detected. It is written as : $\eta_\mathrm{D} = T_\mathrm{d}/T_\mathrm{cycle}$ where $T_\mathrm{cycle} = T_\mathrm{d} + T_\mathrm{m} + T_\mathrm{r}$.

Qubit efficiency η_qubit: As shown of the Figure 4.5a, due to the relaxation time T_1 of the qubit, information is lost between the arrival of the photon and the qubit readout. Considering that a photon arrives on the resonator at time t and excites the qubit with an unit probability, the loss of information is simply given by: $\eta_\mathrm{qubit}(t) = e^{-(T_\mathrm{d}-t)/T_1}$. Here we assume that the equilibrium population $p_\mathrm{eq} \ll 1$, so we do not include it in the calculation. By averaging this quantity over the detection window:

$$\eta_\mathrm{qubit} = \frac{1}{T_\mathrm{d}} \int_0^{\mathrm{T_d}} e^{-(T_\mathrm{d}-t)/T_1} dt \tag{4.62}$$

we can extract the value of η_qubit:

$$\boxed{\eta_\mathrm{qubit} = \frac{T_1}{T_\mathrm{d}}(1 - e^{-T_\mathrm{d}/T_1})} \tag{4.63}$$

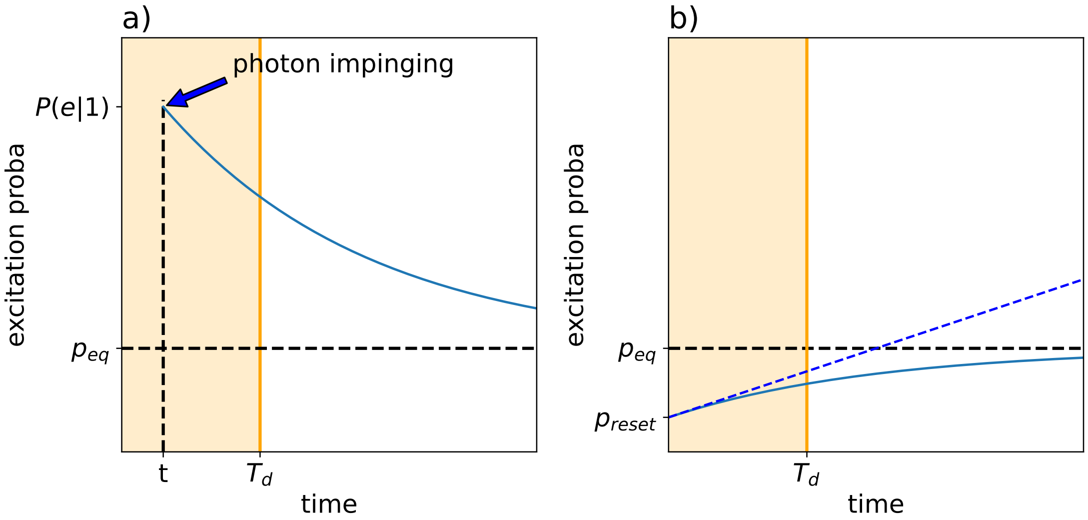

Figure 4.5: **SMPD cyclic operation** (a) Evolution of the qubit excitation probability $P(e)$ as the function of the time when a photon impinges the SMPD at time t. The qubit relaxes exponentially with the characteristic time T_1 from its excited state until the end of the detection window (yellow zone). (b) Evolution of the qubit when no photons enter the buffer resonator. The qubit population increases from the reset population p_reset with the same characteristic time T_1. The dashed blue line represents the linear approximation of the population evolution.

This expression suggests that one can make η_qubit arbitrarily close to one by reducing the duration of the detection window to reduce the ratio T_d/T_1. However, such a reduction of T_d would also imply a large decrease of the duty cycle η_D. One has thus to find a trade-off between these two quantities for maximizing the product:

$$\eta_\mathrm{D}\eta_\mathrm{qubit} = \frac{T_1}{T_\mathrm{m}+T_\mathrm{r}+T_\mathrm{d}}(1-e^{-T_\mathrm{d}/T_1}). \tag{4.64}$$

The variations of of $\eta_\mathrm{D}\eta_\mathrm{qubit}$ with the duration of the detection window T_d is shown in Figure 4.6a.

In the limit where $T_\mathrm{m}+T_\mathrm{r} \ll T_\mathrm{d} \ll T_1$, the product $\eta_\mathrm{D}\eta_\mathrm{qubit}$ takes the simple form:

$$\eta_\mathrm{D}\eta_\mathrm{qubit} \approx \left(1-\frac{T_\mathrm{m}}{T_\mathrm{d}}\right)\left(1-\frac{T_\mathrm{d}}{2T_1}\right). \tag{4.65}$$

The optimal detection window is then equal to :

$$T_\mathrm{d} \approx \sqrt{2T_\mathrm{m}T_1} \tag{4.66}$$

4-wave mixing efficiency η_4wm: The four-wave mixing efficiency η_4wm is equal to the transmission coefficient $|S_{21}|^2$ for $\delta = 0$ and $\delta_\mathrm{p} = 0$ (see Section 4.3). Here, we take into account the internal losses of the buffer resonator κ_bint, yielding to:

$$\boxed{\eta_\mathrm{4wm} = \frac{4\mathcal{C}}{(\frac{\kappa_\mathrm{bint}}{\kappa_\mathrm{bext}}+1+\mathcal{C})^2}}. \tag{4.67}$$

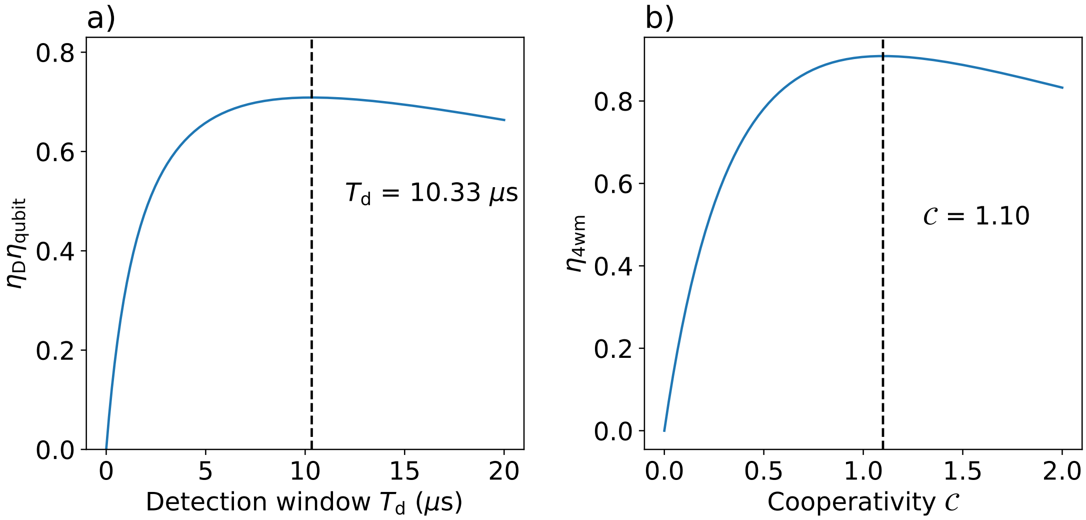

Figure 4.6: $\boldsymbol{\eta_\mathrm{D}\eta_\mathrm{qubit}}$ **and** $\boldsymbol{\eta_\mathrm{4wm}}$ (a) efficiency product $\eta_\mathrm{D}\eta_\mathrm{qubit}$ as the function of the detection window time T_d for $T_1 = 30$ μs and $T_\mathrm{r}+T_\mathrm{m} = 2$ μs. The dashed line showed the optimal detection window. (b) η_4wm as the function of the cooperativity $\mathcal{C}$ for $\kappa_\mathrm{int}/\kappa_\mathrm{ext} = 0.1$. The optimal cooperativity is shown in dashed line.

This expression implies that the optimal efficiency is not anymore given for a unit cooperativity. Indeed, by maximizing Equation 4.67 as the function of C, the new optimal cooperativity is given by $C = 1+\kappa_\mathrm{bint}/\kappa_\mathrm{bext}$. A graphical representation of η_4wm is shown in Figure 4.6b as the function of the cooperativity. Injecting this cooperativity in Equation 4.67 we find that the optimal 4-wave mixing efficiency in presence of internal losses is now given by:

$$\eta_\mathrm{4wm} \leq \frac{1}{1+\kappa_\mathrm{bint}/\kappa_\mathrm{bext}}. \tag{4.68}$$

Measurement efficiency η_m: The measurement efficiency η_m is the excited state fidelity $P(e|e)$. This parameter depends on distance between the coherent states associated to the qubit state in the phase plan (see Figure 3.10) and on the threshold chosen to separate the states. The use of a quantum amplifier (TWPA, JPA) is mandatory in order to achieve single shot readout. In addition, the distance between states can be optimized by adjusting the number of photons sent into the cavity and the readout time.

Eventually, the total SMPD efficiency is the product of all these contributions: $\eta_\mathrm{d} = \eta_\mathrm{4wm}\eta_\mathrm{qubit}\eta_\mathrm{D}\eta_\mathrm{m}$

4.4.3 SMPD Darkcount

Another imperfection of a photon detector is its dark count rate α_d defined as the false positive rate in $\mathrm{click}\cdot\mathrm{s}^{-1}$. As for the efficiency, the dark count rate reduces the detector sensitivity. Once again, it can be broken down into several contributions.

Measurement dark count rate α_m: This contribution, due to a measurement error when the qubit is its ground state, is defined as the conditional probability $P(e|g)$. It depends on the distance between the coherent states in Figure 3.10 obtained during the measurement, on the threshold selected, and on the readout noise.

Qubit dark count rate α_qubit: This contribution is due to the non-zero qubit population at the end of the detection window despite the fact that no photon has arrived in the buffer resonator. This spurious excitation probability, shown on Figure 4.5b, takes the value $P(e) = (p_\mathrm{reset} - p_\mathrm{eq})e^{-T_\mathrm{d}/T_1} + p_\mathrm{eq}$ at the end of the detection window. In the operative case where $T_1 \gg T_\mathrm{d}$ one can make the approximation $P(e) \approx (p_\mathrm{eq} - p_\mathrm{reset})T_\mathrm{d}/T_1 + p_\mathrm{reset}$. This probability represents the average number of extra clicks per cycle, which can be translated into a dark count rate:

$$\boxed{\alpha_\mathrm{qubit} \approx \frac{(p_\mathrm{eq} - p_\mathrm{reset})\eta_\mathrm{D}}{T_1} + \frac{p_\mathrm{reset}}{T_\mathrm{cycle}}} \tag{4.69}$$

Pump dark count rate α_pump: This contribution depends on the spurious heating of the qubit by the pump tone due to higher non-linear terms and the heating of the microwave environment.

Thermal dark count rate α_th: This dark count contribution is due to the presence of residual thermal photons $\bar{n}_\mathrm{b}$ in the buffer transmission lines. These photons are due to the non-zero temperature of these lines, and to insufficient attenuation in their low temperature sections of thermal radiation coming from higher temperature sections.

This thermal photon source can be described by a Johnson-Nyquist noise source [Joh28], [Nyq28]. In the classical framework, the noise power is expressed as a function of the detector bandwidth Δf and the temperature of the experiment as: $P_\mathrm{th} = k_\mathrm{b}T\Delta f$. In the quantum regime relevant for our experiment performed at low temperature 10 mK ($k_\mathrm{b}T \ll \hbar\omega_\mathrm{b}$), the average energy provided by the modes is given by Bose-Einsten statistics such as: $k_\mathrm{b}T \to \hbar\omega\bar{n}_\mathrm{b}$ with $\bar{n}_\mathrm{b} = 1/(e^{\hbar\omega/k_\mathrm{b}T} - 1)$ the number of photons per mode. The expression describing the flux of thermal photons per second is then:

$$\frac{P_\mathrm{th}}{\hbar\omega_\mathrm{b}} = \bar{n}_\mathrm{b}\Delta f \tag{4.70}$$

Given the small frequency interval relevant for qubit excitation, the frequency dependence of the mode occupation $\bar{n}_\mathrm{b}$ can be neglected.

To extract the extra number of clicks α_{th} induced by this photon flux, we must take into account its conversion efficiency, which depends on the total detector frequency η_{d}, but also on its frequency detuning with the buffer resonator. In the limit where $\kappa_{\text{b}} \ll \kappa_{\text{w}}$, from Section 4.3.3, we can consider that the conversion efficiency $|S_{21}|^2(f)$ is given by a Lorentzian function centered around $f_{\text{b}} = \omega_{\text{b}}/2\pi$ with a FWHM $\kappa_{\text{d}}/2\pi$. This assumption yields the total number of extra clicks during a detection window:

$$\alpha_{\text{th}} = \int_{-\infty}^{+\infty} \frac{\bar{n}_{\text{b}}\eta_{\text{d}}}{1 + (\frac{f - f_{\text{b}}}{\kappa_{\text{d}}/(4\pi)})^2} df \tag{4.71}$$

$$\boxed{\alpha_{\text{th}} = \frac{\bar{n}_{\text{b}}\eta_{\text{d}}\kappa_{\text{d}}}{4}} \tag{4.72}$$

It is interesting to relate this contribution to the dark count to the cooperativity $\mathcal{C}$ and the buffer resonator bandwidth κ_{b} by writing explicitly the expression of η_{4wm} (taken with $\kappa_{\text{bint}} = 0$) and κ_{d} (for $\kappa_{\text{b}} \ll \kappa_{\text{w}}$):

$$\boxed{\alpha_{\text{th}} \approx \frac{\bar{n}_{\text{b}}\mathcal{C}\kappa_{\text{b}}}{(1 + \mathcal{C})} \eta_{\text{qubit}}\eta_{\text{m}}\eta_{\text{D}}} \tag{4.73}$$

From this expression, one sees that when $\mathcal{C} \ll 1$, α_{th} increases linearly with $\mathcal{C}$, due to the increase of the bandwidth with the cooperativity. This spurious buffer heating mechanism is important insofar it dominates the total dark count rate in our experiment.

The final dark count rate is the sum of all these contributions: $\alpha_{\text{d}} = \alpha_{\text{th}} + \alpha_{\text{qubit}} + \alpha_{\text{pump}} + \alpha_{\text{m}}$, dominated by α_{th}

4.5 Noise equivalent power (NEP)

4.5.1 General case

In this section, we describe the performances of the detector in terms of a quantity known as the noise equivalent power (NEP). The NEP is defined as the minimum detectable power with an signal-to-noise ratio (SNR) of 1 for a certain integration time t. This quantity provides a good representation of the absolute sensitivity of the SMDP. It is expressed in $\text{W}/\sqrt{\text{Hz}}$.

We will first write the signal-to-noise ratio considering that the detected signal is provided by a continuous tone of power P, at resonance with the buffer resonator and with a Poissonian noise.

When the microwave tone is turning ON, the number of photon impinges the detector for a time t is $Pt/\hbar\omega_{\text{b}}$. Due to the dark count rate, the number of clicks given by the detector is $S_{\text{ON}} = \eta_{\text{d}}Pt/\hbar\omega_{\text{b}} + \alpha_{\text{d}}t$. On the contrary, when the microwave tone is OFF, the signal integrated by the detector for a time t is $S_{\text{OFF}} = \alpha_{\text{d}}t$.

The signal of interest is $S_{\text{int}} = S_{\text{ON}} - S_{\text{OFF}} = \eta_{\text{d}}Pt/\hbar\omega_{\text{b}}$. As all the distributions are Poissonian, the associated noise is $N_{\text{int}} = \sqrt{S_{\text{ON}} + S_{\text{OFF}}}$. Assuming that the dark count is perfectly known we can reduce the expression of the noise to $N_{\text{int}} = \sqrt{S_{\text{ON}}}$

We can then express the SNR of the detection:

$$\text{SNR} = \frac{\eta_{\text{d}}Pt/\hbar\omega_{\text{b}}}{\sqrt{Pt/\hbar\omega_{\text{b}} + \alpha_{\text{d}}t}} \tag{4.74}$$

The power P corresponding to $\text{SNR} = 1$ gives the NEP :

$$\text{NEP} = \frac{\hbar\omega_{\text{b}}(1 + \sqrt{1 + 4t\alpha_{\text{d}}})}{2t\eta_{\text{d}}}. \tag{4.75}$$

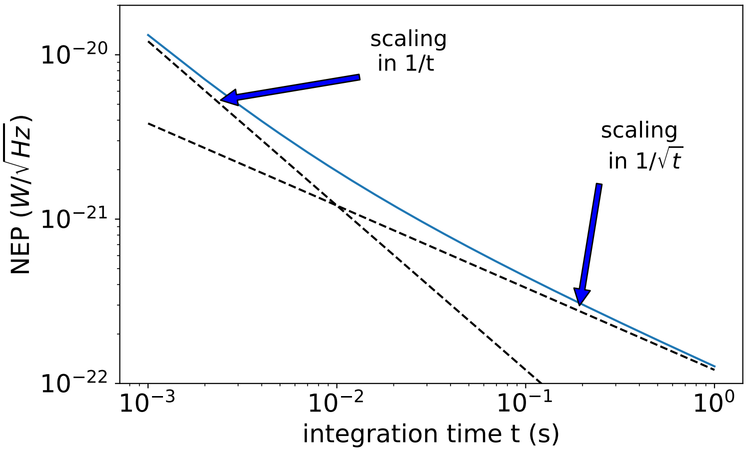

Figure 4.7: **SMPD Noise equivalent power**. NEP (blue) as the function of the integration time t for the parameters: $\alpha_\mathrm{d} = 100\mathrm{s}^{-1}$, $\eta_\mathrm{d} = 0,4$, $\omega_\mathrm{b}/2\pi = 7.3$ GHz. The two scaling laws in $1/t$ and $1/\sqrt{t}$ are shown in dashed black lines.

Here, two different regimes depending on the integration time t of the dark count rate α_d (see Figure 4.7) can be distinguished. For $\sqrt{\alpha_\mathrm{d} t} \ll 1$, we obtain NEP $= \hbar\omega_\mathrm{b}/\eta_\mathrm{d} t$, the sensitivity is limited by the shot noise of the source itself, which means that the detector is not used at its maximum capability. The minimal power detectable scales as like $1/t$, and does not depend on the dark count rate α_d. On the contrary, when the integration is correctly extended so that $\sqrt{\alpha_\mathrm{d} t} \gg 1$ we obtain :

$$\boxed{\mathrm{NEP} = \hbar\omega_\mathrm{b}\frac{\sqrt{\alpha_\mathrm{d}}}{\eta_\mathrm{d}\sqrt{t}}}. \tag{4.76}$$

The dark count rate is the main limitation for the NEP which scales as $1/\sqrt{t}$. The detector is used at its full potential and this regime is the relevant for our experiments.

From Equation 4.76, we can define the absolute sensitivity of the SMPD for and integration time of 1 s:

$$\mathcal{S} = \hbar\omega_\mathrm{b}\frac{\sqrt{\alpha_\mathrm{d}}}{\eta_\mathrm{d}} \tag{4.77}$$

which will give us a point of comparison between the signal we wish to detect and the performance of the counter for a reasonable integration time.

4.5.2 NEP for $\alpha_\mathrm{d} = \alpha_\mathrm{th}$

As stated in the previous section, the total dark count rate in our experiments is dominated by the spurious thermal noise. In this case, we can replace α_d by the expression of the thermal noise $\alpha_\mathrm{th} = \frac{\bar{n}_\mathrm{b}\mathcal{C}\kappa_\mathrm{b}}{(1+\mathcal{C})}\eta_\mathrm{qubit}\eta_\mathrm{m}\eta_\mathrm{D}$. In this case, the noise equivalent power expression becomes:

$$\mathrm{NEP}_\mathrm{th} = \frac{\hbar\omega_\mathrm{b}}{4}\sqrt{\frac{\bar{n}_\mathrm{b}\kappa_\mathrm{b}(1+\mathcal{C})^3}{A\mathcal{C}t}} \tag{4.78}$$

with $A = \eta_\mathrm{qubit}\eta_\mathrm{m}\eta_\mathrm{D}$. The dependence of the NEP_th with the integration time t and the cooperativity $\mathcal{C}$ is shown in Figure 4.8 .

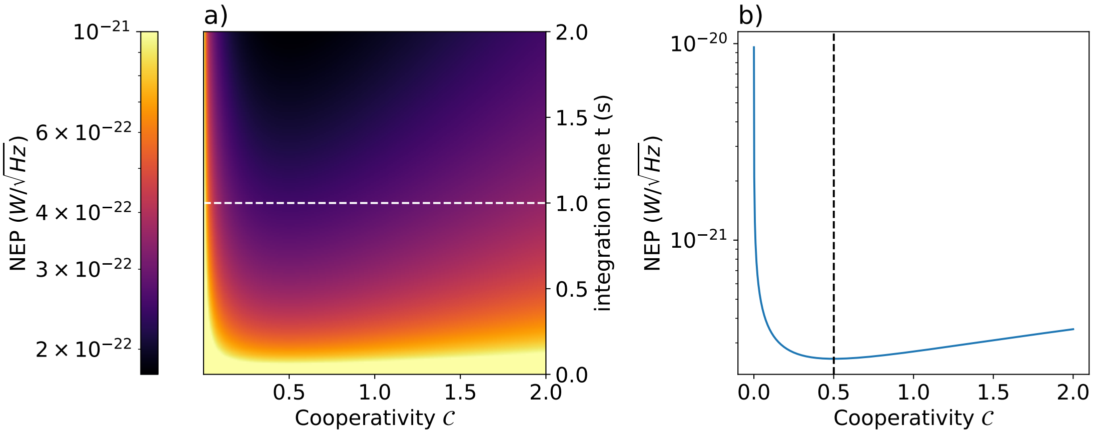

Figure 4.8: **SMPD Noise equivalent power when $\alpha_{\rm d}=\alpha_{\rm th}$.** (a) Colormap of $\rm NEP_{th}$ as the function of the integration time t and the cooperativity $\mathcal{C}$ for $\kappa_{\rm b}/2\pi=0.5$ MHz, $\bar{n}_{\rm b}=10^{-3}$ and $A=\eta_{\rm qubit}\eta_{\rm m}=0.5$. (b) Cross section taken for $t=1$ s corresponding to the white dashed line in (a). The black dashed line shows the minimum NEP reachable in this configuration corresponding to $\mathcal{C}=1/2$.

The search of an optimal sensitivity as a function of cooperativity yields $\mathcal{C}=1/2$, which is smaller than the optimal cooperativity ($\mathcal{C}=1$) in the generic case where the dark count is not dominated by spurious thermal photons. Indeed, as the detector bandwidth increases with cooperativity, the thermal dark count rate increases, which reduces the sensitivity. The value of $\mathcal{C}=1/2$ results from a compromise between the detector efficiency, which grown linearly with the cooperativity, and the thermal dark count rate.

Chapter 5

Device and experimental setup

The core task during this thesis was to improve the SMPD developed in Quantronics in order to reach single spin sensitivity, i.e. to detect a single microwave photon emitted by a single spin in a microwave resonator. The state of the art of SMPDs at the beginning of my research work was the device made by Emanuele Albertinale [Alb21] during his PhD research. This SMPD allowed to perform paramagnetic resonance experiments on small spin ensembles containing about 10^3 spins. Given the present PhD objective was to reach single spin sensitivity, improvements were clearly needed.

In this chapter we first briefly present the state of the art SMPDs prior to this thesis and the guidelines of the improvements needed to address the single spin detection challenge. I detail afterwards the design and fabrication process modifications that I made, and the new setup that I built.

5.0.1 State of the art of SMPDs prior to this thesis work

The succesful operation of a SMPD based on the irreversible excitation of a qubit by an itinerant microwave photon was first demonstrated by Raphaël Lescanne in 2020 [Les+20]. This result triggered in Quantronics the project to use such a SMPD for detecting the photons emitted by electronic spins strongly coupled to a small microwave resonator.

The first SMPD developed by Emanuele Albertinale defined the new state of the art in term of robustness against the dark count and sensitivity. Indeed, the most advanced alternative SMPD architectures, based on a lambda system [Ino+16] or Ramsey interferometry [Bes+18], had an order of magnitude higher dark rate. It was also the only one to be continuously operated and frequency tunable.

These two reasons have enabled the detection of photons emitted by a small set of 10^3 spins constituted by bismuth donors in silicon [Alb+21]. This measurement was the first proof of principle of the value of a SMPD for quantum detection. Moreover, as discussed in Section 4.5, the absolute sensitivity of a SMPD can be defined as $\mathcal{S} = \hbar\omega_\mathrm{b}\sqrt{\alpha_\mathrm{d}}/\eta_\mathrm{d}$, the NEP for and integrating time $t = 1$ s. This quantity is not theoretically limited and can be null for a zero dark count rate. As the consequence the prospect of performing ESR spectroscopy of a single spin has become credible.

However, the SMPD used in this first work was not sensitive enough to envision such a detection. With an efficiency $\eta_\mathrm{d,old} = 0.23$, and dark count rate $\alpha_\mathrm{d,old} = 1500\ \mathrm{s}^{-1}$, the SMPD had a sensitivity $\mathcal{S}_\mathrm{old} \approx 10^{-21}\ \mathrm{W}/\sqrt{\mathrm{Hz}}$. This quantity has to be compared to the typical radiative power of a single bismuth donor. In the experimental condition of [Alb+21], the radiative relaxation rate of donors is found to be $\Gamma_\mathrm{P}^{-1} \sim 300$ ms. At the typical detection frequency of the detector $\omega_\mathrm{d}/2\pi = 7$ GHz, this gives a radiative power $P = 1.5 \cdot 10^{-23}$ W two orders of magnitude below the SMPD sensitivity making impossible the single spin detection due to the incompatibility between the experiment stability and the long integration time.

The main objective of my thesis was to improve the SMPD by modifying its design and fabrication process in order to reach the required sensitivity specification for single spin detection. In the next section I will details the different guidelines for the improvements.

5.0.2 Analysis of SMPD sensitivity

As discussed above, the quantity to optimize to improve the SMPD is the absolute sensitivity given by $\mathcal{S} = \hbar\omega_{\mathrm{b}}\sqrt{\alpha}/\eta_{\mathrm{d}}$.

To reach the single-spin sensitivity, it is needed to work on the chip design and fabrication, but we also know that the setup is important since it determines the effective noise temperature of all the transmission lines connected to the SMPD

On the chip side, we aimed at improving the qubit relaxation time T_1 since it affects both the dark count rate and the detection efficiency. Because developing better transmons is a major goal in superconducting qubit research, we have benefited from the progress recently achieved in 2021 by [Pla+21], with the use of a thin layer of tantalum for the ground plane, deposited on a sapphire substrate. The improvement on qubit coherence time is link to the reduced interface losses in the tantalum layer [Cro+23], [McL+23] as well as the very low bulk loss tangent of the sapphire [Rea+22].

We have thus decided to follow this new fabrication process for our new SMPD generation which has represented many design and fabrication modifications compared to the previous version of the SMPD.

For improving the microwave setup, we first aimed at reducing the false positive rate α_{th} due the spurious excitation of the qubit by the electromagnetic bath by increasing the attenuation and the filtering of the lines. For the same goal, we improved the shielding of the chip in order to avoid spurious qubit excitation induced by high energy photons.

In the following, we firstly present the new design and the different upgrades compare to [Alb+21], then we describe the fabrication process and finally the measurement setup.

5.1 Design and simulation

5.1.1 SMPD design

In this section, the choices made for the design of the different elements of the circuit will be detailed step by step. The circuit is fabricated on a 0.33 mm thick sapphire substrate, polished on both sides and oriented along the C-axis. This substrate is first coated with a 60 nm tantalum superconductor film. The CPW resonators made on the chip share the same gap (20 μm) and the same track width (33.6 μm), as shown on Figure 5.1a). These parameters are chosen in order to reach a resonator impedance close to 50 Ω.

Purcell filters: Compared to the last SMPD generation, Purcell filters are designed both on the waste and buffer side and not only on the waste side. They consist of $\lambda/2$ CPW resonators, which reduce the spontaneous emission of the qubit due to the reduced density of states at the qubit frequency (see Section 3.5.1). Their frequency, controlled by their line length as explained in Section 3.1.3.1, matches that of their respective resonator (buffer or waste). The inductive coupling to the line is obtained through a stub. The coupling quality factors are determined by the asymmetry between the two arms, the target bandwidth being $\kappa_{\mathrm{Pb}}/2\pi = 290$ MHz for the Purcell filter on the buffer side, and $\kappa_{\mathrm{Pw}}/2\pi = 230$ MHz on the waste side.

Buffer resonator: the buffer is a $\lambda/2$ CPW resonator (orange in Figure 5.1) with a symmetric SQUID in its center where the current is maximum. The targeted resonance frequency for $\Phi_{\mathrm{tot}} = 0$ is 7.3 GHz with a participation ratio of the junction (see Section 3.2.2) of $p \sim 0.15$. In theory, we could tune the frequency of the resonator from its maximal value corresponding to $\Phi_{\mathrm{tot}} = 0$ to almost zero for $\Phi_{\mathrm{tot}} = \pi/2$. However, the tunability is limited by the Purcell filter bandwidth (~ 290 MHz). In addition, limiting the tunability range in a few hundred MHz mitigates the effect of the flux noise due to current instabilities. The current line generating the magnetic flux in the SQUID loop is depicted in red in Figure 5.1(b). It is symmetrical in order to distribute the current in the two ground half planes on either side of the flux line. This avoids potentially creating a voltage difference between the half ground planes. The targeted area for the SQUID junctions is $0.5 \cdot 2\mu\mathrm{m}^2$.

The coupling to the Purcell filter is both inductive and capacitive, with the strength of the coupling determined by the distance between the lines (see Figure 5.1a). We target a bandwidth $\kappa_{\mathrm{b}}/2\pi = 1.5$ MHz when the buffer is perfectly aligned with its Purcell filter. As shown in Section 4.3 in the regime $\kappa_{\mathrm{b}} \ll \kappa_{\mathrm{w}}$, the SMPD bandwith is then $\kappa_{\mathrm{d}} \approx 2\kappa_{\mathrm{b}} = 3$ MHz. By changing the frequency of the buffer, we detune it from its Purcell filter, which further reduces its bandwidth. For a 150 MHz detuning, the bandwidth given by the Purcell formula Equation 7.28 is $\kappa_{\mathrm{b}}/2\pi = 0.72$ MHz. The coupling to the qubit is capacitive, made by a facing electrode.

Waste resonator: Unlike other chip resonators, the waste resonator is a $\lambda/4$ CPW resonator (green in Figure 5.1), with a second mode frequency three times higher, which avoids coupling to the qubit. The coupling to the Purcell is realized in a similar to that of the buffer but with a larger coupling strength in order to reach a bandwidth $\kappa_{\mathrm{w}}/2\pi = 3$ MHz. The interest of this large bandwidth is double. Firstly, it allows to quickly release photons into the environment in order to create the dissipator Equation 4.1. Secondly, as this resonator will be used to readout the state of the qubit, a high bandwidth will speed up the readout, increasing the overall efficiency of the detector.

The coupling to the qubit is done with an electrode at the end of the resonator. We target a resonance frequency $\omega_{\mathrm{w}/}/2\pi = 8$ GHz.

Transmon qubit: It is interesting to design the qubit frequency $\omega_{\mathrm{q}}/2\pi$ so that it is far detuned from the buffer and waste resonator frequency in order to reduce its relaxation by spontaneous emission in these resonators. In addition, the pump frequency determined by the resonance condition $\omega_{\mathrm{b}} + \omega_{\mathrm{p}} = \omega_{\mathrm{w}} + \omega_{\mathrm{q}}$ should not be close to a characteristic frequency of the circuit elements. With these considerations in mind, we set $\omega_{\mathrm{q}}/2\pi = 5.7$ GHz, which yields $\omega_{\mathrm{p}}/2\pi = 6.5$ GHz. The coupling to the waste and the buffer resonators, given by their terminal electrode, determines the cross-Kerr rates χ_{qb} and χ_{qw}. The coupling strength depends both on the electrode geometry and on the distance to the transmon capacitor (blue in Figure 5.1). As demonstrated in Section 4.2.2, the efficiency of the four-wave mixing can be adjusted by the pump amplitude. However, in order to reduce the heating due to a too large pump power, it is interesting to ensure that $\chi_{\mathrm{qb}}\chi_{\mathrm{qw}} \gg \kappa_{\mathrm{b}}\kappa_{\mathrm{w}}$. The coupling strength is thus set to have $\chi_{\mathrm{qw}} = 11$ MHz and $\chi_{\mathrm{qb}} = 2.5$ MHz. These large cross Kerr couplings are not detrimental for our experiment with only one photon at a time.

From the work done by E. Albertinale in the old SMPD design, we know that we can reproducibly make a Josephson junction with typically $L_{\mathrm{j}} \approx 10$ nH. We set the charge energy E_{c} by adjusting the size of the capacitor pad (see Figure 5.1) in order to reach the transmon regime with $E_{\mathrm{J}}/E_{\mathrm{c}} = 70$. The resulting anharmonicity is $\alpha = E_{\mathrm{c}}/\hbar \approx 240$ MHz

The mask of the Josephson junction shown in Figure 5.1 has a bottle opener shape in order to increase fabrication reproducibility and decrease mask failure. The targeted area for the junction is $150 \cdot 160\ \mathrm{nm}^2$.

Pump line: The pump line (purple in Figure 5.1) is capacitively coupled to the qubit.

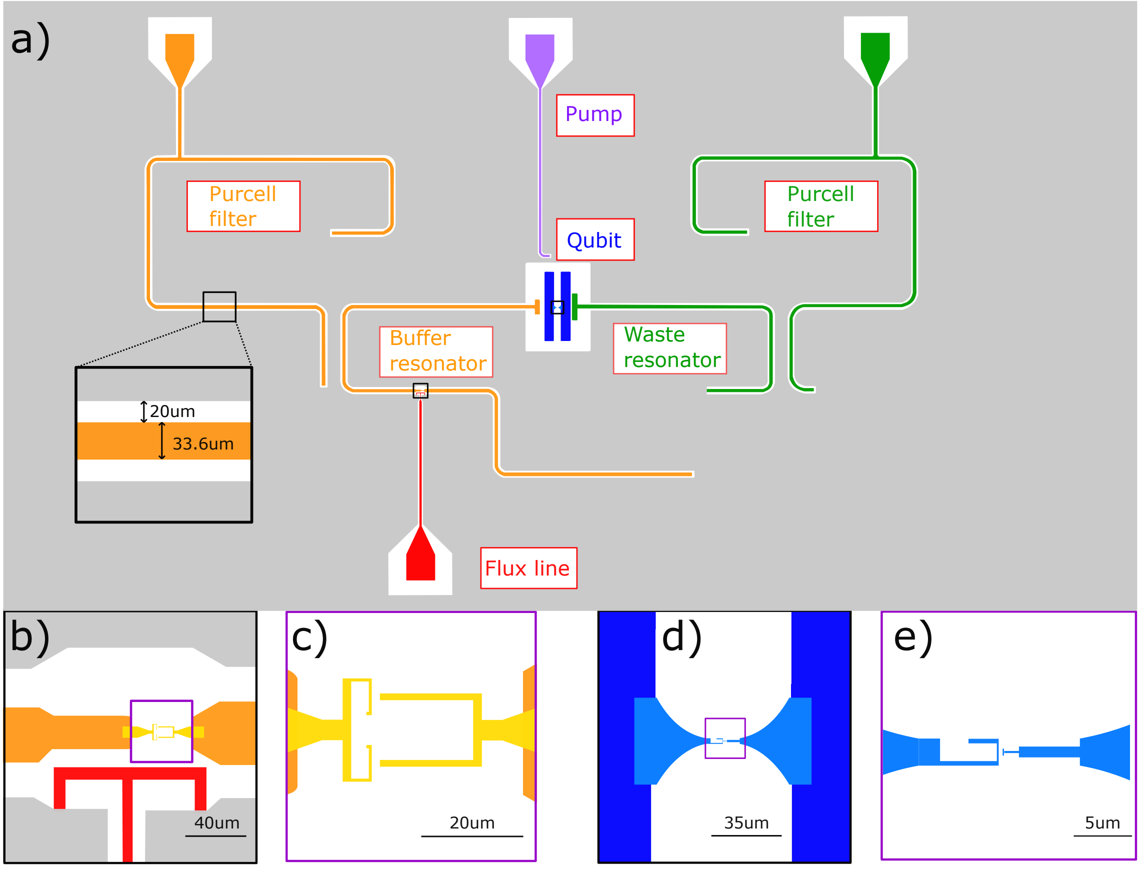

Figure 5.1: **SMPD design** (a) Schematic of the mask used to fabricate the SMPD. The two Purcell filters in orange (resp. green) for the buffer (resp. waste) are CPW $\lambda/2$ resonators. They are coupled to the measurement line to a stub. The buffer resonator (also a CPW $\lambda/2$ resonator) incorporates the SQUID controlled with the flux line (red). The waste resonator (green) is a $\lambda/4$ CPW resonator. (b) Zoom in on the SQUID embedded at the current anti-node of the buffer resonator. (c) Mask of the SQUID for the 2 angles evaporation. (d) Zoom of the transmon qubit at the chip center. (e) Mask of the transmon for the 2-angle evaporation

Compared to the previous design in [Alb+21], the coupling has been reduced in order to decrease this qubit loss channel.

5.1.2 Electromagnetic simulation

We set the values of the physical parameters of the chip design shown in Figure 5.1 by using electromagnetic simulation. We use the Electromagnetic Simulation Software ANSYS HFSS to simulate the linear resonators and extract their frequency and damping rate. Additionally, parameters related to the non-linearity of the Josephson junction, known as the dispersive couplings, are obtained through the Energy Participation Ratio (EPR) method [Min+21].

5.1.2.1 Linear simulation

The simulation of the chip begins by identifying the frequency and damping rates of the modes with the lowest frequency, utilizing the HFSS frequency eigenmode solver. We replace the non-linear elements (SQUID and transmon junctions) by the linear part of

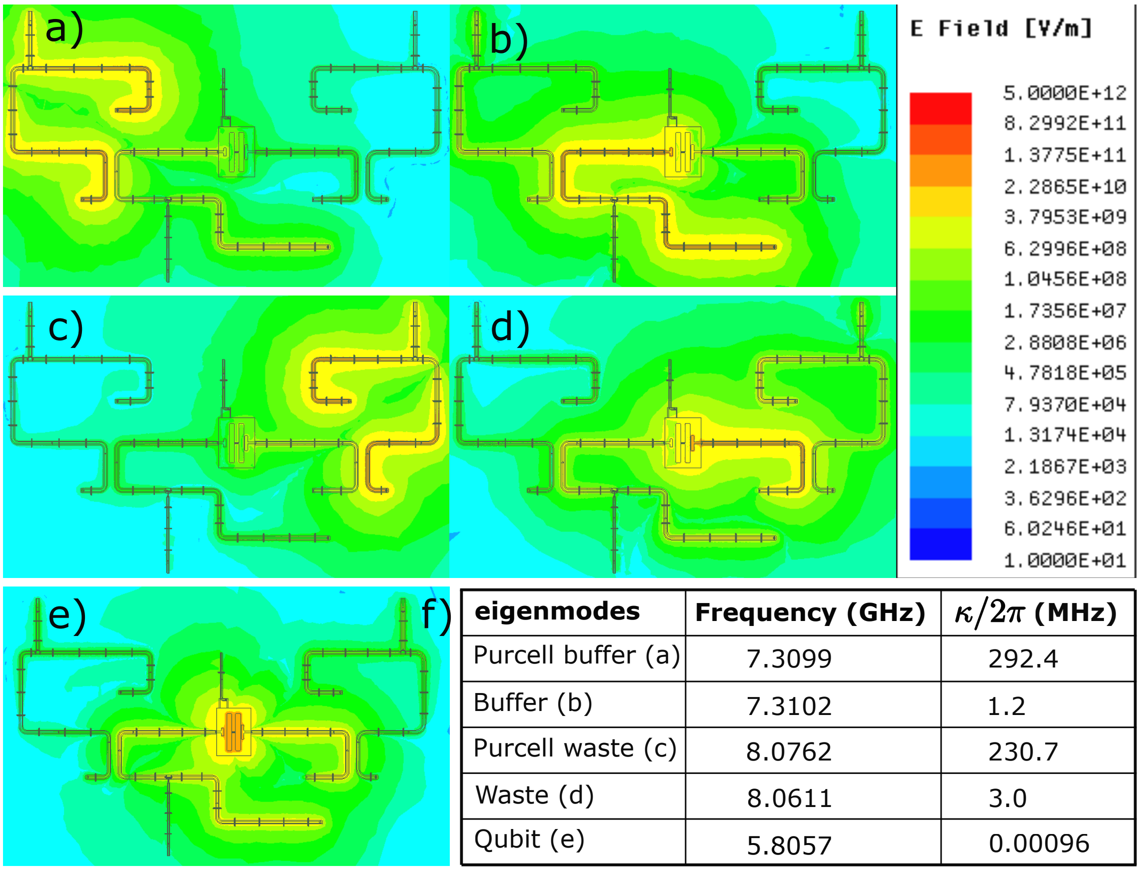

eigenmodes	**Frequency (GHz)**	**$\kappa/2\pi$ (MHz)**
Purcell buffer (a)	7.3099	292.4
Buffer (b)	7.3102	1.2
Purcell waste (c)	8.0762	230.7
Waste (d)	8.0611	3.0
Qubit (e)	5.8057	0.00096

Figure 5.2: **SMPD electromagnetic simulations** Finite element electromagnetic simulation using ANSYS HFFS. The electric field amplitude, obtained by setting 1J in the resonant mode, is plotted in log-scale for the different five different modes, respectively (a) Purcell buffer mode, (b) buffer mode, (c) Purcell waste mode, (d) waste mode and (e) transmon mode. The frequencies and energy decay rates for the first five eigen-modes of the circuit are reported in table (f).

their Josephson inductance. The table presented in Figure 5.2f summarizes the simulation results.

The buffer resonator frequency is aligned with its Purcell filter frequency for zero flux in the SQUID loop, corresponding to its maximum frequency. Its bandwidth, set at 1.2 MHz under these conditions, will evolve as a function of its detuning from the filter according to the Purcell formula Equation 3.98. The choice of the bandwidth of the Purcell filter is a trade-off between minimizing the spontaneous emission of the qubit and preserving the frequency control range of the detector. We have therefore chosen to set it at $\kappa_{\mathrm{Pb}}/2\pi = 290$ MHz, which offers a sufficient range to adapt to the frequency of an incident photon. The qubit frequency being simulated at $\omega_{\mathrm{q}}/2\pi = 5.8$ GHz, the frequency difference with the Purcell frequency is $\sim 5\kappa_{\mathrm{Pb}}/2\pi$, which ensures a small enough qubit relaxation rate due to this channel. All decoherence sources combined, the predicted qubit energy decay rate is $\kappa_{\mathrm{q}}/2\pi \approx 1$ kHz, which would correspond to a qubit relaxation time $T_1 = \kappa_{\mathrm{q}}^{-1} = 160\mu$s. These values of course only correspond to the maximum T_1 achievable for our design. Compared to [Alb21], the addition of the buffer-side filter and the decoupling of the pump line increase this limit by a factor of 6. This improvement was necessary to benefit from the progress made possible by the new fabrication process developed in [Pla+21], with relaxation times T_1 longer than a hundred microseconds.

5.1.2.2 Non-linear simulation with the EPR method

The dispersive couplings are simulated using the Energy Participation Ratio method [Min+21] briefly described here. This method applies when several microwave modes are non-resonantly coupled to a Josephson junction, as is the case in our design. The energy participation ratio p_i of mode i into the junction is defined as the ratio between the electromagnetic energy stored into the junction when mode i is excited and the total energy stored in the mode. This quantity is interesting because it is directly accessible from the linear simulations performed in HFSS, and because it then allows us to calculate non-linear effects induced by the junction, namely the non-linear dispersive couplings.

The EPR method can be conveniently implemented by using the Python library *pyEPR* provided and maintained by Z. Minev, Z. Leghtas and P.Reinhold.

The simulated parameters are summarized in Table 5.1 for both the linear and the dispersive coupling terms. The term χ_{qq} is the anharmonicity of the qubit. Its value of 240 MHz is typical for a transmon qubit. The values of the cross-Kerr term χ_{qb} and χ_{qw} respect well the condition $\chi_{\mathrm{qb}}\chi_{\mathrm{qw}} \ll \kappa_{\mathrm{b}}\kappa_{\mathrm{w}}$.

Qubit	
$\omega_{\mathrm{q}}/2\pi$	5.81 GHz
$\chi_{\mathrm{qq}}/2\pi$	240 MHz
$\chi_{\mathrm{qb}}/2\pi$	3 MHz
$\chi_{\mathrm{qw}}/2\pi$	11 MHz
T_1	160 µs
Buffer mode and filter	
$\omega_{\mathrm{b}}/2\pi$	7.31 GHz
$\kappa_{\mathrm{b}}/2\pi$	1.2 MHz
$\omega_{\mathrm{Pb}}/2\pi$	7.31 GHz
$\kappa_{\mathrm{Pb}}/2\pi$	290 MHz
Waste mode and filter	
$\omega_{\mathrm{w}}/2\pi$	8.06 GHz
$\kappa_{\mathrm{w}}/2\pi$	3 MHz
$\omega_{\mathrm{Pw}}/2\pi$	8.08 GHz
$\kappa_{\mathrm{Pw}}/2\pi$	230 MHz

Table 5.1: Table of the simulated parameters.

5.2 Fabrication process

In this section, we describe the SMPD fabrication process, with the guiding principle of obtaining the longest possible relaxation time T_1 for the transmon.

In the previous section, electromagnetic simulations showed us that the T_1 value is limited by design to 160us. However, till recently, it was impossible to obtain such a long lifetime for 2D transmons. Indeed, T_1 times did not improve much between 2012 when T_1's around 100us were first reported [DS13], and 2020 when the best known T1 was 114us [Ner+19].

A major fabrication innovation that occured in 2021 [Pla+21] allowed these authors and their followers to obtain 2D transmons with a lifetime longer than 300 μs. These results were obtained by using tantalum, grown in the α-phase, to form the ground plane in which the resonators and capacitance of the transmon are made.

The authors of [Pla+21] state that this improvement results from the reduction of the losses that take place at the metal-air interface of tantalum compared to those for other traditionally used metals (aluminium and niobium). It seems indeed plausible that there are fewer defects in the tantalum oxide, compared to other metal oxides, that could couple with the qubit and induce decoherence. This explanation is in agreement with the work of [Wan+22] that compares the T_1 of transmons made on tantalum, aluminium and niobium. Without surface treatment for removing the native oxide on the metal layers, tantalum devices are consistently better. The value of 500 us obtained for T_1 furthermore shows that the limit of the material had not been reached in [Pla+21]. More recent works [Cro+23], [McL+23] have carefully analyzed the loss channels and shown that although tantalum's performance is better, losses are still dominated by two-level-systems at interfaces.

Given these significant improvements, we decided to switch from an aluminum-on-silicon fabrication process to a tantalum-on-sapphire one. This new fabrication process is broken down into four steps: preparing the substrate, patterning the circuit, depositing the junction, and reconnecting the aluminum junctions and the tantalum circuit using bandage techniques [Dun+17].

As discuss above, the losses that limits transmon T_1 are mainly due to the interfaces. Therefore we pay particular attention to the cleanliness of surfaces by using aggressive cleaning methods before each deposition step.

Substrate preparation and tantalum deposition: We start from a 2inch sapphire wafer. Before metal deposition, the sapphire substrate is cleaned by dipping it in a 2:1 mixture of H_2S0_4 and H_2O_2 during 20 min. The substrate is then loaded in a sputtering machine. The tantalum is deposed on the sapphire at 600°C in order to favor growth in the α-phase. The thickness of the final tantalum layer is 60 nm. The wafer is then cut into rectangular chips of $10 \cdot 11\text{mm}^2$.

Circuit fabrication: Patterning of the circuit, shown in Figure 5.1, is achieved by etching tantalum using a commercial tantalum etchant (Transene 111) through an optically patterned AZ1518 resist mask. Given the etchant used is a mixture of of HF (33%) HNO_3 (33%) and H_2O (33%) is particularly aggressive for the mask [Pla+21], the choice of the resist is critical. The chip is then cleaned by immersing it in successive baths: IPA, acetone and 2:1 mixture of H_2S0_4 and H_2O_2.

Junction deposition: The junctions are made of aluminum using the Dolan bridge technique described in Figure 5.3. The mask is patterned using electron beam lithography (at 30 kV) of a double layer PMMA (110 nm) - MAA (1100 nm) resist. The sapphire being an insulator, using electron beam lithography requires the deposition of a conductive layer (7 nm of aluminum here) at the top of the mask for evacuating charges.

After the exposure, this layer is first removed by immersing the chip in a KOH solution ($10\text{g} \cdot \text{L}^{-1}$). The resist is then developed in a standard 1:3 MIBK/IPA mixture.

The MAA resist being more electron-sensitive than PMMA, the large undercuts needed for suspending the Dolan bridge are obtained, as shown in (Figure 5.3a).

The chip is then loaded in an electron beam evaporator. The Dolan technique consists of two depositions at opposite incidence angles (28° and −28°). The two layers created overlap over a well-defined area, controlled by the mask geometry. The overlap point between the two layers defines the junction (final result shown in Figure 5.5d). The first

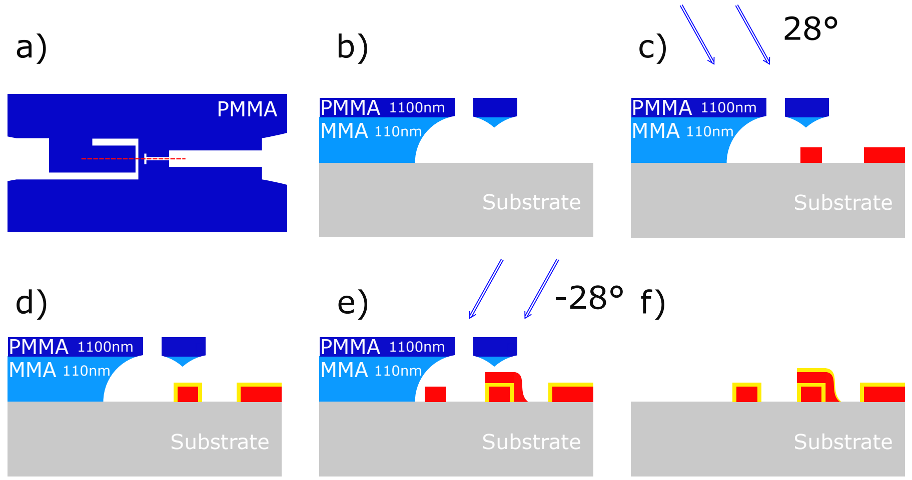

Figure 5.3: **Junction deposition with Dolan bridges** (a) Top view of the junction mask patterned in a double MAA/PMMA layer by using electron beam lithography. (b) Cross section of a) according the dashed red line. The MMA being more sensitive, undercuts appear below the PMMA layer. (c) First deposition of aluminum with an angle (28°). (d) Oxydation of the aluminum layer (yellow layer). (e) second evaporation with the reverse angle (−28°). (f) Lift-of the resist and oxydation caused by caused by the venting of the sample.

aluminum layer is 35 nm thick and the second 65 nm thick (to step on the first layer). Between the two deposition steps, the aluminum is oxidized during 5 min by injecting an argon-oxygen gas mixture into the deposition chamber at a pressure of 10 mbar. Finally, the resist mask is lifted-off by immersing the chip in an acetone bath.

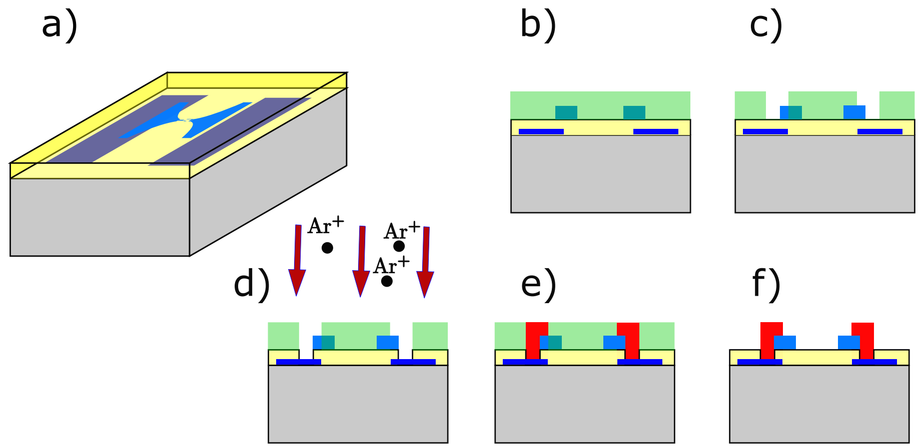

Figure 5.4: **Recontacting the junctions.** (a) The junctions (blue) are separated of the capacitor by a tantalum oxyde layer (yellow). (b) cross section of a), The green layer represents photo-resist. (c) opening of windows in the resist overlapping the junction and the capacitor. (d) Etching of the oxide with Ar^+ flux. (e) evaporation of aluminum patches (red) to connected the junction and the capacitor. (f) Lift-off of the resist.

Reconnecting the aluminum junctions: As depicted in Figure 5.4a, the junctions deposited in the previous step are separated from the rest of the circuit by tantalum oxide (TaO_5). We now recontact the two layers with aluminum patches. This technique reduces the capacitive losses induced by the insulating oxide layer [Dun+17] without damaging the substrate in the junction vicinity. After coating the chip with an optical resist (Microposit S1805), windows overlapping the junctions and the ground plane areas to be recontacted are opened using optical lithography. The chip is then loaded in an electron-beam evaporator. Tantalum oxide (covering the circuit) and aluminium oxide (covering the junctions) are first etched by a an argon ion beam accelerated by a 500V voltage difference (ion milling technique). A 100 nm aluminium layer is then deposited on the chip, without venting the sample, covering the areas etched by the ion milling step (see Figure 5.4).

An example of device obtained following our process is shown in Figure 5.5. The chip is then glued to a Printed-Circuit-Boarded (PCB), and all lines are connected using aluminum wire bonding. This PCB is then placed in a sample holder designed by Marius Villiers (collaboration between ENS Paris, ENS Lyon and CEA Saclay, see Figure 5.13). During the course of this thesis, two SMPDs were produced. The first one, called SMPD1, was used for the first demonstrations of sensitivity enhancement as well as for an ESR experiment on a small spin ensemble[Bil+22]. It will be the subject of the next chapter. The second,called SMPD2, was used for the detection of single spins [Wan+23].

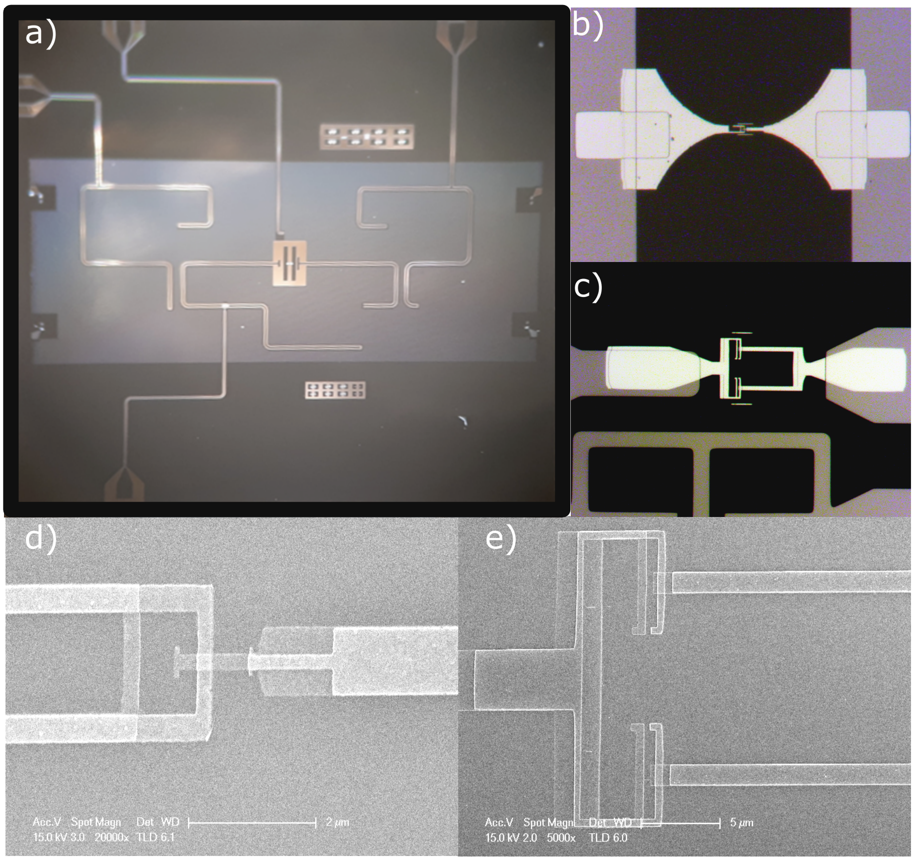

Figure 5.5: **SMPD chip and junctions** (a) Optical microscope image of the SMPD chip. (b) Optical microscope image of the aluminium transmon qubit (bright structure) with bandage patches on top of the tantalum capacitor (dark pink). (c) Optical microscope image of the SQUID. (d) SEM image of the Josephson junction of the transmon qubit. (e) SEM image of the SQUID Josephson junction.

5.3 Fabrication issues encountered

The development of the fabrication recipe presented in the previous section has been a long process that requested the first two years of my thesis research. Developing a cleanroom process is an extremely demanding task that requires a lot of work done with rigor and a good dose of resilience.

These two years taught me a lot about the different nanofabrication techniques (lithography, thin film deposition, etching, etc.) as well as how to identify a problem in the process and how to solve it. I would not have succeeded without the support of Pief Orfila and Sébastien Delprat, our cleanroom engineers, who trained me in the use of all the machines and gave me a lot of advice on technical choices. I also want to thank Denis Vion who got me out of more than one complicated situation thanks to his methodical and rational approach of fabrication problems.

The first part of my thesis was a continuation of the work done by Emanuele Albertinale on the Al/Si platform. I developed this fabrication over a period of 6 months, starting with the implementation of the design modifications discussed in the section on Section 5.1.1. However, after the publication of [Pla+21], we branched out to a Ta/Sapphire platform, which implied a complete revision of the fabrication process.

In this section, I outline some of the difficulties I encountered in implementing this new process and the solutions I found.

5.3.1 Circuit

The first part of the work consisted in redefining a functional recipe to design the SMPD circuit in the new platform.

Circuit wet etching

The first difficulty was to find a resist that was sufficiently resistant to the Transene 111 used for the wet etching of tantalum.

At first I designed my masks in Microposit S1805 resist, (a common resist that forms a 500 nm thick layer) by optical lithography. Despite the very short immersion time in Transene 111 (20 s), the mask was often damaged, thus making the fabrication process too unreliable. Some of these problems are shown in Figure 5.6. Recurrently, pieces of the central track of the CPW lines were torn off. These tracks are the most fragile elements of the mask because of their narrow width. The Transene made them fragile enough to break from time to time (see Figure 5.6a,b).

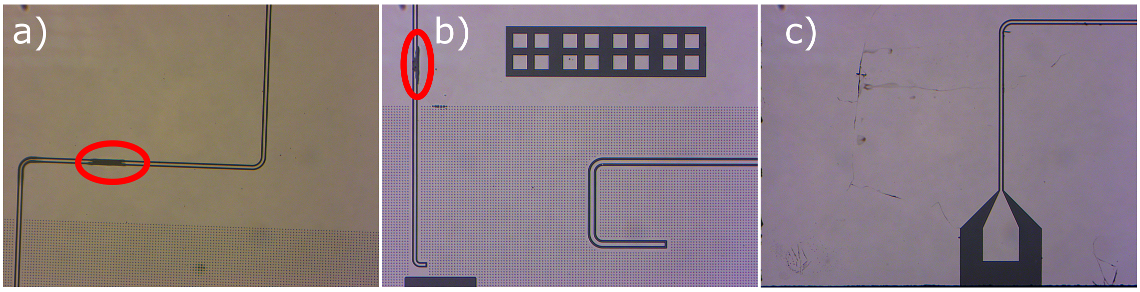

Figure 5.6: **Wet etching issue** (a) and (b), Removal of a track part of the line (red circle) due to the destruction of the S1805 protective resist layer during the wet etching with transene 111. Black part represents sapphire (c) Damaged tantalum layer (light pink) due to the degradation of the resist.

The ground plane of the circuit was also sometimes damaged as shown in Figure 5.6c.

To solve these issues, we change the resist to the one used in [Pla+21], the Merck AZ1518 resist. This resist is thicker than S1805 resist (1.8 μm vs 0.5 μm), which will better protect the ground plane from possible transene infiltration. In addition, its adhesion is better, which limits the risk of detachment.

The implementation of this new resist required a recalibration of the doses used to pattern the mask. The energy sent by the optical lithography machine was increased from 40 $\mathrm{mJ \cdot cm^{-2}}$ to 145 $\mathrm{mJ \cdot cm^{-2}}$. These new masks proved to be much more robust, and the problems experienced on the Figure 5.6 were no longer observed.

Inhomogeneity of the resist layer

Another issue encountered during this phase of circuit fabrication was the non homogeneity of the resist layer. The resist layer being spin coated on a rather small chip, the edges of the sample have a much greater resist thickness than the center. Because of the fluid back-flow imposed by the edge conditions of the chip, the edges thickness can be 2 or 3 times larger than to the nominal one. An overview of this inhomogeneity can be seen in Figure 5.7b. In this optical picture of a resist-coated connecting line, the fringes visible at the edges are due to a sharp increase in resist thickness.

This inhomogeneity is an important issue for the lithography process. Indeed, using a similar dose on the whole chip would make patterns at the edge of the chip largely under-exposed. This problem would affect the 4 lines used to connect the chip to the PCB. The consequence of this under-exposure is shown on Figure 5.7. After development, a block of resist that can remain on the chip protects the tantalum layer during the wet etching step. The protected tantalum is not be etched and is present on the final circuit.

To overcome this limitation, we make a second optical exposure of the edges after circuit exposure. An extra dose of 1000 $\mathrm{mJ \cdot cm^{-2}}$ is applied on the connectors. This additional step does suppress the poor etching of the connectors encountered before, which made our fabrication significantly more reproducible.

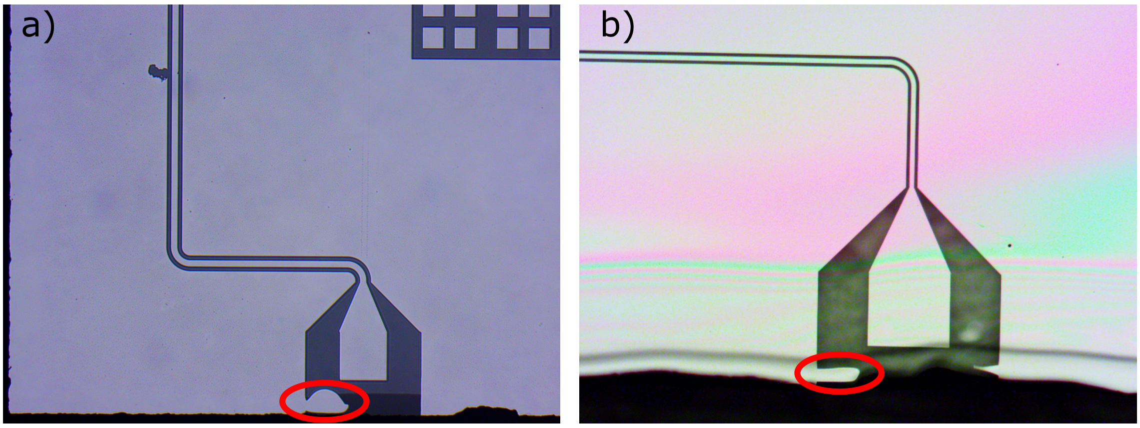

Figure 5.7: **Poor etching of connectors**. (a) Connector with un-etched area (red circle) due to ineffective optical lithography. Black parts are sapphire, bright parts tantalum (b) Connector with un-etched area under resist layer. The fringes near the edges show that the resist is much thicker in this area, which explains the lithography problems.

5.3.2 Junctions

The second part of the development of the SMPD fabrication recipe was to develop a reliable Josephson junction fabrication process on Sapphire.

The junctions are patterned by electron lithography in a PMMA/MAA double layer. As the sapphire is an insulator, it is necessary, as already mentioned, to deposit a conductive layer on top of the resist to evacuate the charges (in our case 7 nm of aluminum), which makes the procedure slightly more complex but does not create any particular difficulty. The real problem with the insulating nature of sapphire is that it is difficult to take Scanning Electron Microscope micrographs of structures made on a sapphire chip. Indeed, the charges accumulate during the observation and end up deflecting the beam, which blurs the picture. To overcome this problem, a thin conductive coating (gold, aluminum, etc.) could be deposited on top of the chip, as in electron lithography. However, this technique has the double disadvantage of rendering the chip unusable for further testing (for example, electrical testing of the junctions) and artificially increasing the size of the observed structures.

This is why we first chose to refine our fabrication procedure on a SiO_2 substrate with properties rather similar to those of sapphire, but which allow us to make images and lithography with an electron microscope without adding a discharge layer.

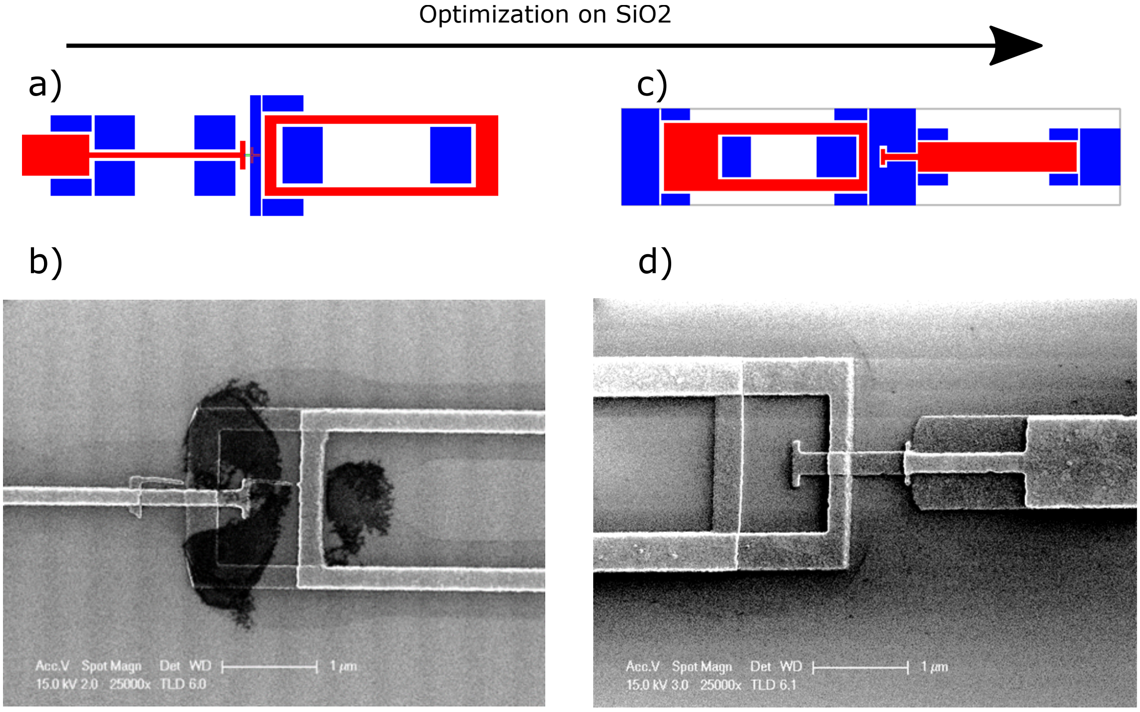

Figure 5.8: **Optimization on SiO2 substrate**. (a) Initial design of the transmon junction and doses for the electron lithography. Blue rectangles represent the low exposure areas ($50\mu C \cdot cm^2$) needed to increase the undercut. Red rectangles show the high exposed zone ($400\mu C \cdot cm^2$) (b) SEM image of the result obtain after development and evaporation under angles ($\pm 29.6°$). the black haze is caused by the evaporation of the aluminium on the resin walls. The undercut is not sufficient. (c) corrections to the design. The undercut is increased near the junction,the drawing is rotated 180 degrees and the length of the junction arm is reduced. (d) SEM image of the result obtains after evaporation.

Optimization on SiO2 substrate

The qubit junction which is the smallest element of the device presented the most difficulties in fabrication. We use it here to illustrate the problems encountered and the solutions found. These solutions are directly applicable to the SQUID junction.

The design (as well as the recipe) of the transmon junction presented in Figure 5.8a is inherited from the work carried out by Emanuele Albertinale. The red parts of the scheme correspond to the highly exposed areas used to cut the PMMA chains. The blue parts correspond to less exposed areas that that increase the undercut region defined in the MAA under the PMMA (see Figure 5.3). The bottle opener shape and the T-shape have been chosen during Emanuele Albertinale thesis work in order to improve the fabrication reliability.

The first junction made on $Si0_2$ is shown in figure Figure 5.8b, and two problems already appear. First, the undercut under the PMMA is insufficient, and the aluminium depositied at an angle touches systematically the resist and causes the black veil visible on the SEM micrograph. Another difficulty shown on the photo is the short-circuiting of the junction by the thin aluminium wire starting from the top of the T. This defect appears more randomly.

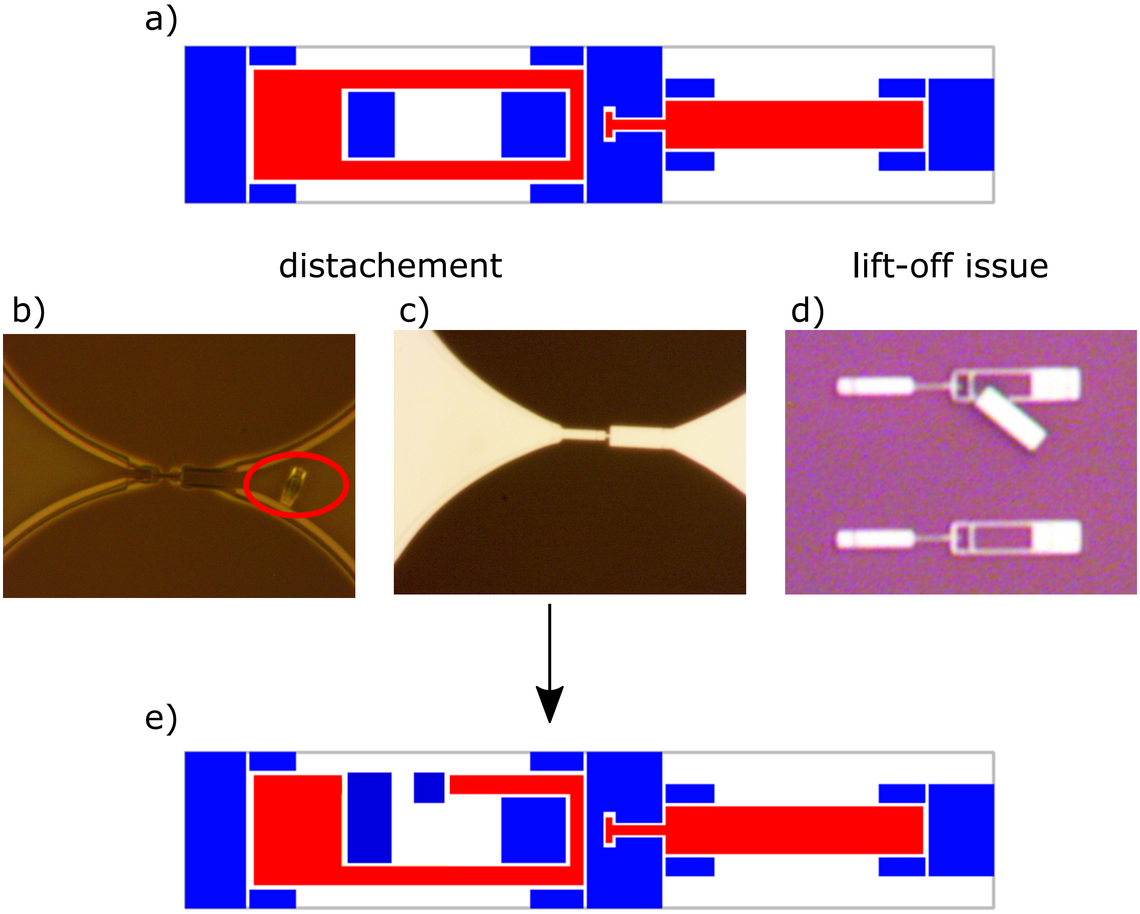

Figure 5.9: **Optimization of the junctions design** (a) Design after undercut optimisaition. colors correspond to the same dose as Figure 5.8. (b) optical image of the resist mask. The red circle shows the resist rectangle forming the bottle opener torn from the structure. (c) result after the evaporation whith the damaged mask b). (d) lift-off issue for non-damaged mask. (e) Improvement made on the design. The bottle-opener shaped structure is open to make it more resistant and easier to lift-off.

To solve the undercut problem, we increased the voltage of the electron gun from 25kV to 30kV for enlarging the undercut, and we reduced slightly the deposition angle from 29.6° to 28°. In addition, we added more undercut areas (in blue on the figure Figure 5.8c).

We also made some changes on the design in order to make the fabrication process more reliable. The arm carrying the T has been shortened and thickened to reduce the risk of line interruption. The side arms of the bottle opener have also been thickened for the same reason. Finally, the size of the T-bar was reduced, which reduced the probability of short-circuiting.

The final result after these optimizations is shown on Figure 5.8d.

Another recurring problem was the fragility of the resist mask. As shown on Figure 5.9a the rectangle of resist making up the center of the bottle-opener may pull away, which then results in an unusable junction (Figure 5.9b). After our actions to increase the size of the undercut, this part of the resist mask became too weakly attached to the substrate. In addition, even in the case when this rectangle sticked to the chip, the lift-off step after evaporation under angle was problematic as shown on Figure 5.9c.

The solution was to open the bottle-opener as shown on Figure 5.9d. This new design makes the structure more robust by connecting it to a large resist plane. In addition, the lift-off is also simplified since the structure is no longer independent and lifts off with the rest of the mask.

Junction fabrication on Sapphire

The design from the previous paragraph was then transferred to sapphire. The exposure doses had however to be increased compared to those on SiO_2 (Figure 5.10, red: $400\mu C \cdot cm^2$ $\rightarrow$ orange: $570\mu C \cdot cm^2$).

The major difficulty encountered was the systematic occurrence of short circuits caused by aluminum wire connecting the two sides of the junctions (see Figure 5.10h).

In order to understand what the problem was, we made SEM micrographs of the MAA/PMMA mask by depositing a thin gold layer on the resist (Figure 5.10e). it appeared that the mask was torn. The shape of the tear suggested that the mask had been stretched on both sides of the junction until it broke.

We first tried to strengthen the bridge by stopping to expose the gap between the T and the bottle opener (removing of the blue box dosed at $50\mu C \cdot cm^2$). This forced us to reduce the gap from 500 nm to 350 nm in order to still have a suspended bridge without additionnal exposure. This made the fabrication a little more reliable, but short circuits still occurred randomly.

The decisive change was to relax the stresses on the junction mask by piercing the resist on both sides. This is the purpose of the the bars added to the design on Figure 5.10b. As shown on Figure 5.10f, this modification solved the problem of the mask cracking in the vicinity of the junction but added another fragility between the bar and the structure (red circle). This additional issue was resolved by removing the useless low exposure zone (blue box) between the bar and the structure.

The junctions of the SQUID have benefited from all these innovations. A schematic of the SQUID design with the undercut boxes is shown in Figure 5.11a. SEM micrographs of the resist mask are shown on Figure 5.11b,c. This optimization process carried out initially on SiO_2 and then on sapphire lasted 6 months but resulted in a stable process.

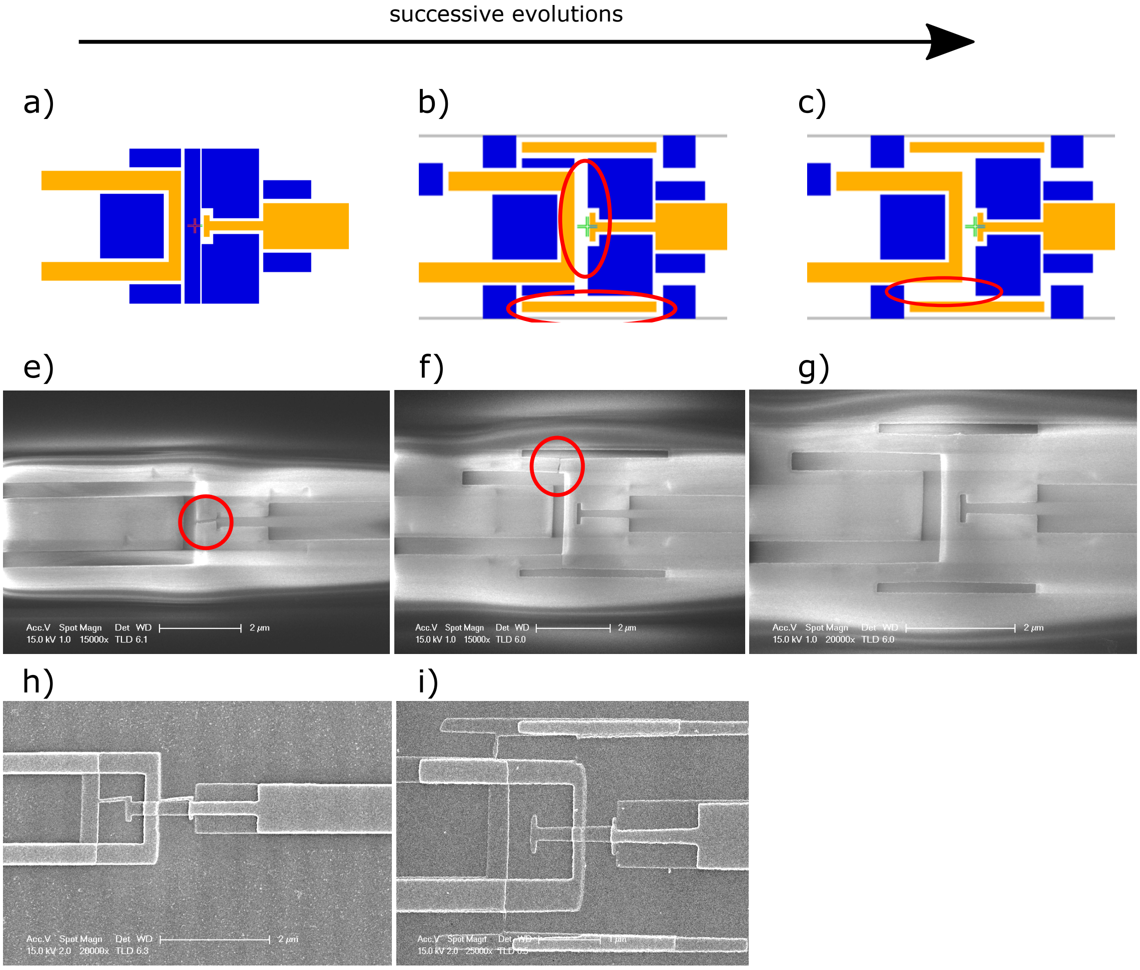

Figure 5.10: **Transmon junctions shorted on sapphire, identification and improvement**. (a),(b) and (c), successive improvement of the design. Orange rectangle correspond to a dose of ($570\mu\mathrm{C}\cdot\mathrm{cm}^2$). (d), (e) and (f), SEM image of the corresponding resist mask. Red circles show the tearing of the mask. (h) SEM image after evaporation under angles ±28°. (i) SEM image after evaporation under angles ±28°

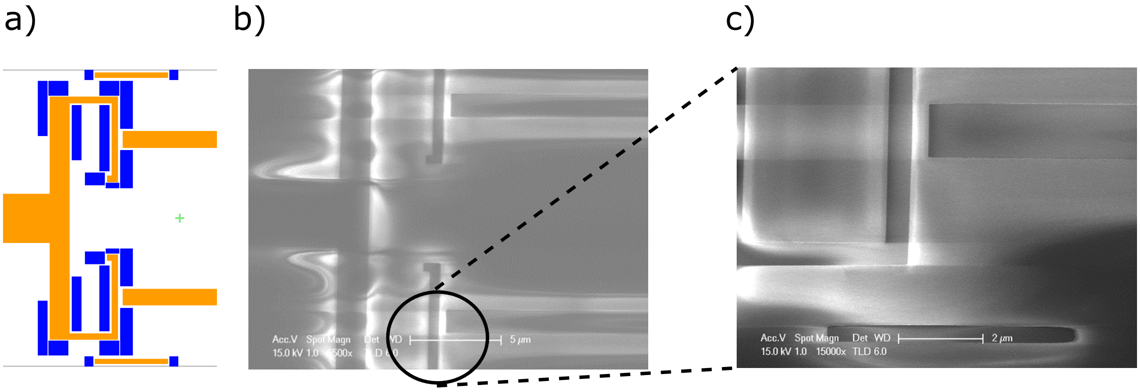

Figure 5.11: **SQUID junctions optimisation**. (a) Design of the SQUID and doses for the electron lithography. Dark orange rectangle correspond to $390\mu\mathrm{C}\cdot\mathrm{cm}^2$, blue rectangle correspond to $50\mu\mathrm{C}\cdot\mathrm{cm}^2$. (b) and (c), SEM micrographs of the mask resist, without visible cracks.

5.4 Setup

In this section we will describe the setup used for characterizing SMDPs. The measurements are performed by placing the sample in a dilution cryostat manufactured by the Finnish company Bluefors. The refrigerator consists of several stages at different temperatures and protected from radiation by a screen. The detector will be placed in the lowest stage at 10 mK. The microwave pulses are generated by commercial instruments at room temperature.

5.4.1 Microwave shield and Infra-red filters

The SMPD chip is glued and wire-bonded on a PCB integrated in a copper sample holder. This sample holder, called JAW and shown on Figure 5.13, has been designed by Marius Villiers. Once closed, the box modes of the formed cavity are well above 10 GHz, which avoids spurious couplings with the detector modes. The sample holder is then placed in a box consisting of a succession of three screens (copper, μ-metal, aluminum see Figure 5.12). The copper screen, in contact with the other screens, allows the aluminum to be uniformly thermalized and to form a low temperature superconducting Faraday cage. The μ-metal prevents vortex formation during the transition from the normal to the superconducting state of the aluminum screen. The sample holder is screwed onto a copper frame inside the box to ensure its thermalization. The red cylinders on Figure 5.13 are infra-red filters directly embedded in the box. Their role is to minimize the generation of out-of-equilibrium quasi-particles that contribute to the dark count rate.

The connection to the outside is ensured by SMA connectors. Four lines are used for the buffer, its SQUID, the waste and the qubit.

This device was designed entirely in our laboratory by Emmanuel Flurin, Miloc Rancic and Pascal for the new JAWS sample holders.

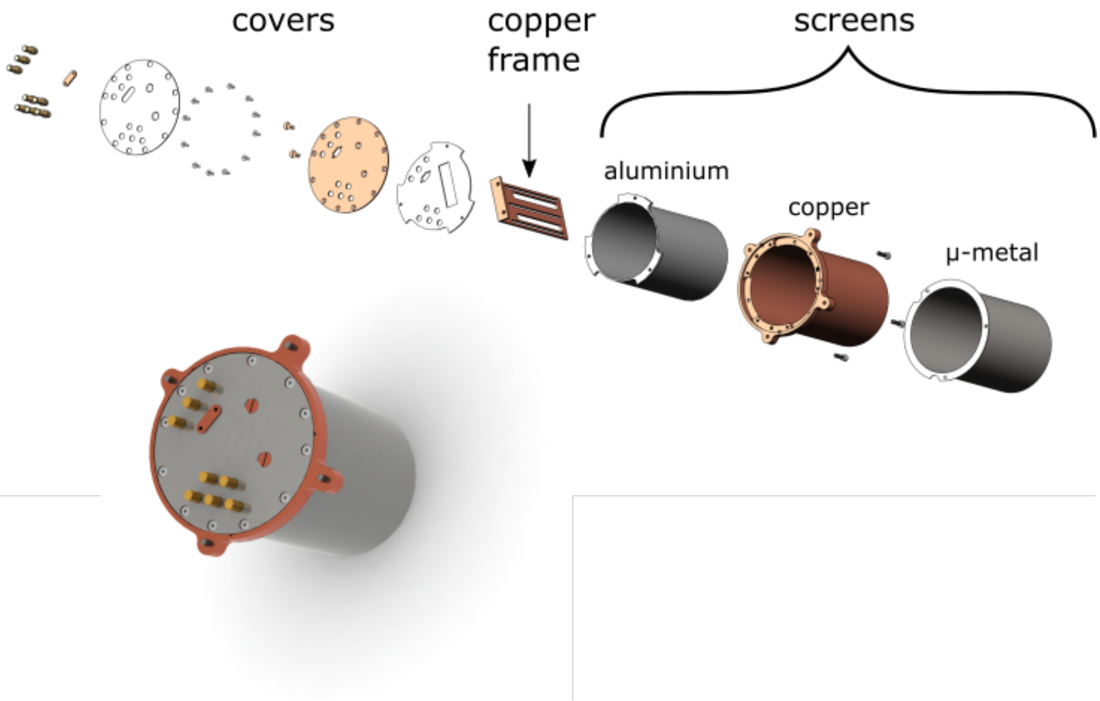

Figure 5.12: **Microwave shield** Explode view of the microwave shield used in the experiment. The sample holder is screwed on the copper chip-holder (copper frame)

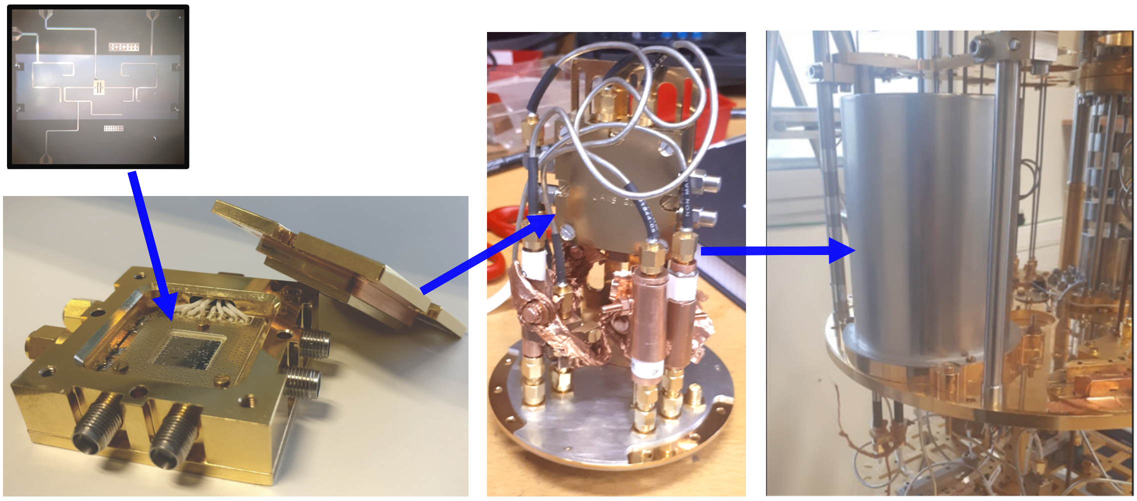

Figure 5.13: **Microwave packaging** The SMPD chip is glued and wire-bonded in the sample holder (called JAWS). The JAWS is screwed on a copper frame and put in a 3-screen shield (cooper, μ-metal, aluminium).

5.4.2 Microwave setup

The SMPD has four inputs (buffer, waste, SQUID, qubit), each one connected to a microwave line composed of a room temperature part and a low temperature part. The signal generation and acquisition is performed at room temperature, and filtering, attenuation or amplification is performed at low termperature. A complete description of the microwave setup is shown in Figure 5.14.

The electronic devices used to define the shape of our pulses (square envelope, Gaussian ...) convert analog signals into digital signals and vice versa. Given these devices rarely have a bandwidth higher than 200 MHz, we thus resort to heterodyning methods for reaching the operating frequency range. We modulate/demodulate signals from microwave local oscillators using IQ mixers, with I and Q the name of the two signals that will be mixed to the high frequency tone defined as ω_{LO}. We operate in an heterodyne mode, i.e. the modulation signals I and Q themselves oscillate with an intermediate frequency ω_{IF}. This gives rise to two side-bands at frequency $\omega_{\mathrm{LO}} - \omega_{\mathrm{IF}}$ and $\omega_{\mathrm{LO}} + \omega_{\mathrm{IF}}$ surrounding the initial local oscillator frequency ω_{LO}.

The modulation signals are deliverd by a Quantum Orchestration Platform (QOP see Figure 5.14) designed and manufactured by Quantum Machine which acts as a pulse generator of analog and digital signals. The signal acquisition is realized by the same device. The QOP is based on a Fast Programmable Gate Array (FPGA), fast enough for implementing short feedback time protocols.

5.4.2.1 Buffer line, SMPD input

Line 2 on the Figure 5.14 corresponds to the input of the detector. It is used both to characterize the parameters of the buffer resonator $(\omega_{\mathrm{b}}, \kappa_{\mathrm{b}})$ and to calibrate the detector efficiency by sending a well controlled number of photons.

The input signal is generated by IQ mixing of a Vaunix Labbrick source. The intermediate frequency chosen is $\omega_{\mathrm{IF}}/2\pi = 100$ MHz, which is sufficiently large compared to the bandwidth of the detector ($\sim \kappa_{\mathrm{b}}/2\pi$) to avoid the triggering of the dark count by photons at the frequency of the unwanted sidebands.

The signal is then routed into the fridge. The line is heavily attenuated at 10 mK (-60 dBm) in order to reduce as much as possible the number of thermal photons per mode as

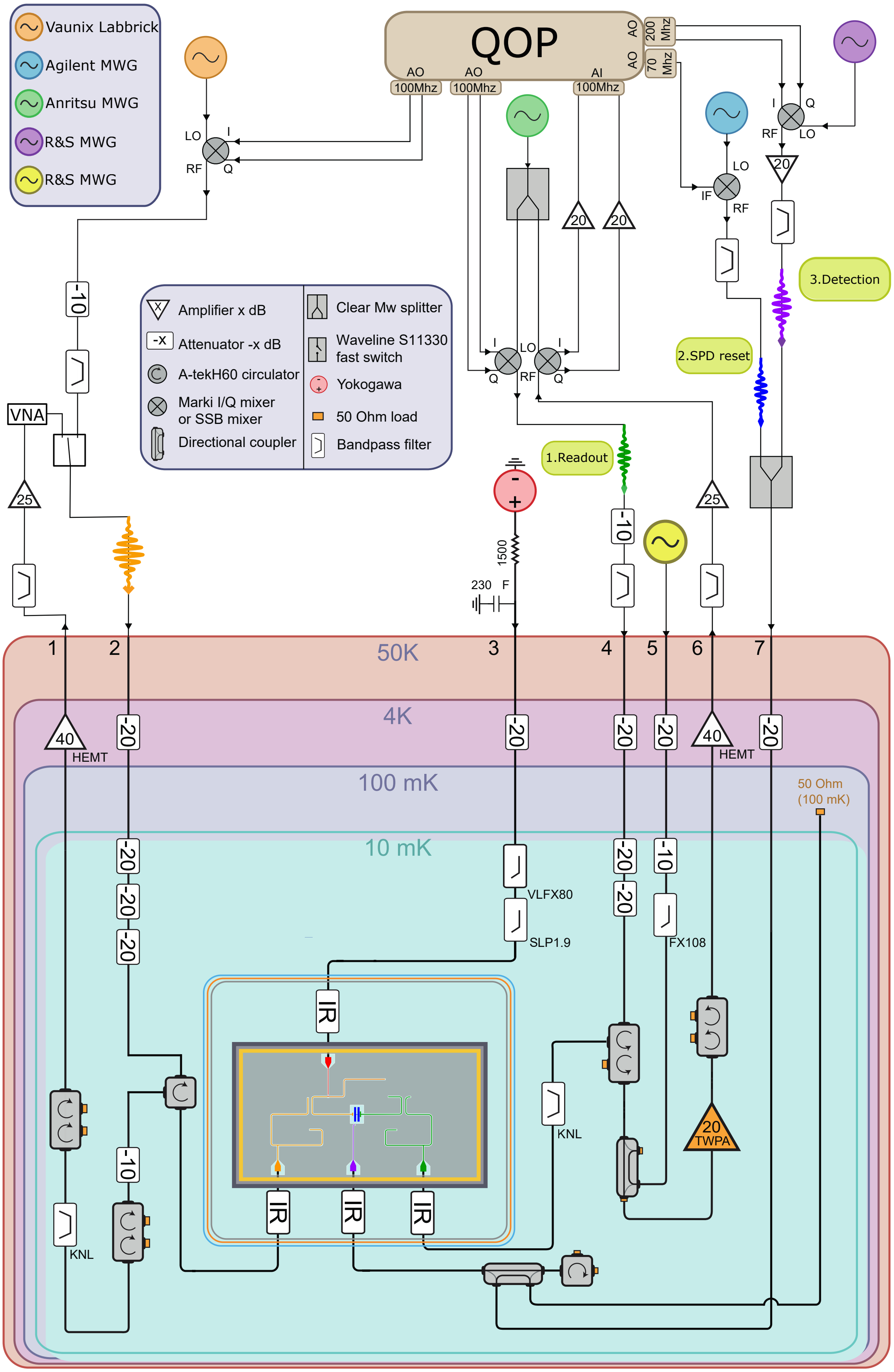

Figure 5.14: **SMPD1 setup**

discussed in Section 4.4.3. The remaining signal is routed to the SMPD with a circulator and will trigger a click if we operate the detector.

On the contrary, if we want to perform a reflective measurement of the buffer resonator, the reflected signal is routed to the line 1 through the circulator and amplified with a High Electron Mobility transistor (HEMT) thermally anchored at 4K. In this case, a VNA connected to the lines 1 and 2 measures the S_{11} parameter.

Under normal SMPD operating conditions, line 1 is closed with a 50Ω load and the HEMT is disconnected. The two doubles circulators and the KNL band-pass filter ensure that hypothetical thermal photons from the upper stages of the fridge are dissipated before causing a dark count.

5.4.2.2 Waste line, dispersive qubit readout

The waste resonator is used to dispersively readout the qubit state. The microwave tone coming from an Anritsu source is split to generate the readout pulses via IQ mixing, and to demodulate the signal reflected by the cavity.

The readout pulse is routed through the line 4 to the waste resonator via a double circulator. The reflected signal collected is first amplified with a Traveling Wave Parametric Amplifier (TWPA) provided by Will Oliver from MIT-Lincoln Labs. This kind of amplifier is intensively used in circuit QED experiments for their high gain and quantum-limited noise. The line 5 is used to send the microwave pump tone needed to trigger the amplification. An additional cryogenic amplification is realized with a commercial HEMT. Then the signal is routed through the line 6 to the demodulating mixer.

The I and Q quadrature are acquired by the QOP after a final amplification. I and Q are related to the field quadratures of the coherent pulse sent on the resonator, $\langle\hat{X}\rangle$ and $\langle\hat{Y}\rangle$ (defined in Section 3.4.2) through the relation: $I + iQ = \sqrt{G}(\langle\hat{X}\rangle + i\langle\hat{Y}\rangle)e^{i\phi}$ G being the amplification factor of the full chain.

5.4.2.3 Qubit line, pump and qubit control

Line 7 has two functions. One is to transmit the pump tone at frequency ω_p to trigger the four-wave mixing, and the other is to send resonance pulses to the qubit at frequency ω_q (e.g. to reset the qubit). Therefore, two mixers with two different microwave sources are used, with the two lines recombining just before the fridge input.

The pump signal is generated by IQ mixing on a Rohde&Schwarz source. A 20 dB amplifier is placed just after the mixer, because, since the pumping is non-resonant, the power level needed to trigger the four-wave mixing is high. The role of the 70MHz band-pass filter after the amplifier is crucial for preventing spurious side band resonances to generate unwanted mixing at other frequencies. The intermediate frequency is set at 200 MHz in order to push these side-band to 3 times the filter bandwidth for a decent attenuation.

The qubit control pulses (frequency ω_q) are generated by a single side-band mixer and routed to the fridge via a band pass filter.

In order to minimize heating of the low-temperature stage by the strong pump signal, the attenuation of the line needed at 10 mK is performed with a 30 dB directional coupler that routes most of the pump power towards the 100 mK stage where it gets easily dissipated.

5.4.2.4 SQUID line, adjustment of the buffer frequency

Line 3 is a dc flux bias line for tuning the SQUID inductance that controls the frequency ω_b of the buffer resonator. The current is delivered by a voltage source in series with a 1.5 kΩ resistor. A 230 μF capacitor in parallel filters the spurious high frequency parasitic signals. The different low temperature filters play the same role. The line is connected to the on-chip flux line providing the magnetic flux in the SQUID loop.

Chapter 6

SMPDs full characterisation

In this section, we characterize in detail the performances of the SMPD1 which was the first functional detector. We also briefly give the characteristics of the SMPD2.

The characterisation of the detector implies an accurate measurement of its components. The first part of this chapter aims at determining the different parameters of the resonators (resonance frequency, losses) and of the qubit (frequency, coherence time, etc.).

We then describe the four-wave mixing process obtained by applying a non-resonant pump tone to the qubit at frequency $\omega_{\mathrm{p}}/2\pi$. The cooperativity $\mathcal{C}$ is adjusted with the pump amplitude. The bandwidth of the detector is measured and compared to the two-coupled cavity model given by Equation 4.53.

We then introduce the cyclic operation of the detector. The precise characterization of the incoming flux of photons with Equation 3.92 allows us to extract the overall efficiency. The dark count study completes the analysis and gives access to the noise equivalent power of the detector.

Finally, we analyse the dark count more in detail by isolating the contribution α_{th} due to the finite temperature of the line. For this pirpose, we measure the dark count rate, the qubit T_1 and the equilibrium excited state population p_{eq} in function of the temperature. We show that the thermal dark count rate follows the Johnson–Nyquist relation $\alpha_{\mathrm{th}} = \frac{\bar{n}_{\mathrm{b}}\eta_{\mathrm{d}}\kappa_{\mathrm{d}}}{4}$ as detailed in Section 4.4.3.

6.1 Characterization of chip elements

6.1.1 Resonators SMPD1

In this section the waste resonator, the buffer resonators and their Purcell filters are characterised by reflectometry with a Virtual-Network-Analyser (VNA).

6.1.1.1 Waste resonator

The reflection coefficient $S_{11}(\omega)$ of the waste resonator is measured by connecting the VNA to inputs 4 and 6 of Figure 5.14.

The results of the measurement are shown on Figure 6.1. The $S_{11}(\omega)$ argument measured over a large frequency range (Figure 6.1a) shows a 2π-shift corresponding to the Purcell filter, and a narrower one narrower phase-shift around 7.7 GHz due to the waste resonator itself. A fit (orange line) of the data using the formula of the reflection coefficient Equation 3.48 allows us to extract the width $\kappa_{\mathrm{Pw}} \sim 180$ MHz and the resonance frequency $\omega_{\mathrm{Pw}}/2\pi = 7.62$ GHz. Note that the filter frequency is shifted from its simulated value by ~ 380 MHz. We attribute this shift to a slight difference between the estimated tantalum layer thickness and the actually deposited one, leading to a wrong estimation of the kinetic inductance. This issue has been corrected for the SMPD2.

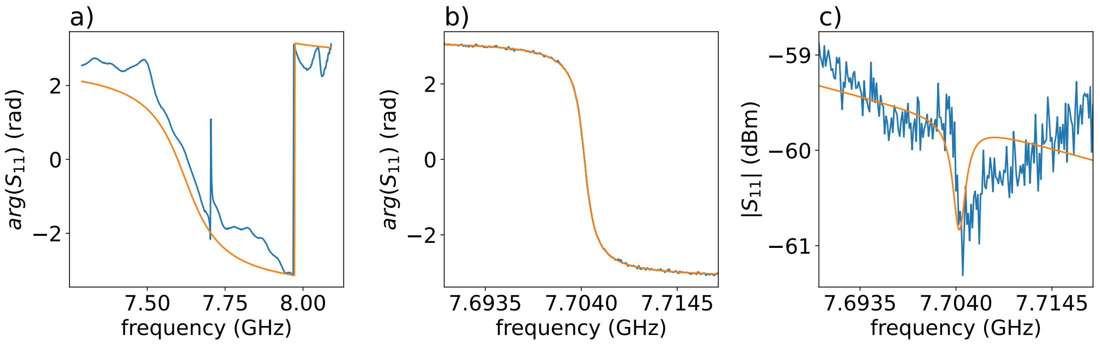

Figure 6.1: **Waste resonator characterization**. (a) Phase of the $S_{11}(\omega)$ reflection coefficient. The Purcell filter appear as the large 2π shift. The waste resonator appears as a much narrower resonance aligned with the filter. Phase (b) and amplitude (c) of the $S_{11}(\omega)$ reflection coefficient centered around the waste resonator.

The Figure 6.1b and Figure 6.1c show the amplitude and the argument of the reflection coefficient zoomed around the waste resonance frequency. A fit (orange line) allows to extract the resonance frequency $\omega_\mathrm{w} = 7.704$ GHz, shifted by 300 MHz compared to the simulation. The coupling losses $\kappa_\mathrm{wext}/2\pi = 1.72$ MHz and the internal losses $\kappa_\mathrm{wint}/2\pi = 0.11$ MHz are also obtained. The resonator is over-coupled, as required for the operation of the SMPD.

6.1.1.2 Buffer resonator

The reflection coefficient $S_{11}(\omega)$ of the buffer resonator is measured using the lines 1 and 2 shown on Figure 5.14.

As for the waste side, we first characterize the Purcell filter by measuring $S_{11}(\omega)$ over a large frequency range. The figure Figure 6.2a and Figure 6.2b show the phase of the reflection coefficient for two different fluxes applied in the SQUID loop, namely $\Phi = 0$ and $\Phi = 0.25 \cdot \Phi_0$. A fit allows to extract the value of the bandwidth $\kappa_\mathrm{Pb}/2\pi \sim 84$ MHz and the resonance frequency $\omega_\mathrm{Pb}/2\pi = 6.824$ GHz of the filter. Note that the resonance frequency is again shifted compared to the simulation, here by ~ 500 MHz . The Purcell filter coupling to the line is 3 times weaker than expected leading to a thinner bandwidth. This may be due to an impedance mismatch that could be due to a bad bonding wire between the chip and the PCB.

The two configurations of the buffer resonator corresponding to the reflection measurements shown in Figure 6.2a,b respectively correspond to $\omega_\mathrm{b}(0)/2\pi = 6.979$ GHz (no flux applied in the SQUID), and to the buffer resonator tuned with its Purcell filter, $\omega_\mathrm{b}(0.25\Phi_0) = 6.824$ GHz. The red and black stars depict these two configurations across the figure.

The Figure 6.2c,d show zooms around the two buffer resonator positions. The frequency range is fixed at 3 MHz in both cases, and a sizeable effect of the detuning with the Purcell filter is clearly visible. The parameters (frequency and bandwith) are extracted using the usual fitting procedure, yielding to the orange line best fits.

The Figure 6.2e shows the evolution of the buffer frequency as a function of the magnetic flux applied to the SQUID Φ, shifted by the initial flux present in the loop $\Phi_\mathrm{vortex} = -0.11\Phi_0$. The data are fitted with Equation 3.60 in order to extract the participation ratio $p = 0.13$ and the maximum frequency $\omega_\mathrm{b}(-\Phi_\mathrm{vortex})/2\pi = 7.005$ GHz.

The Figure 6.2 represents the coupling and the internal losses of the buffer resonator

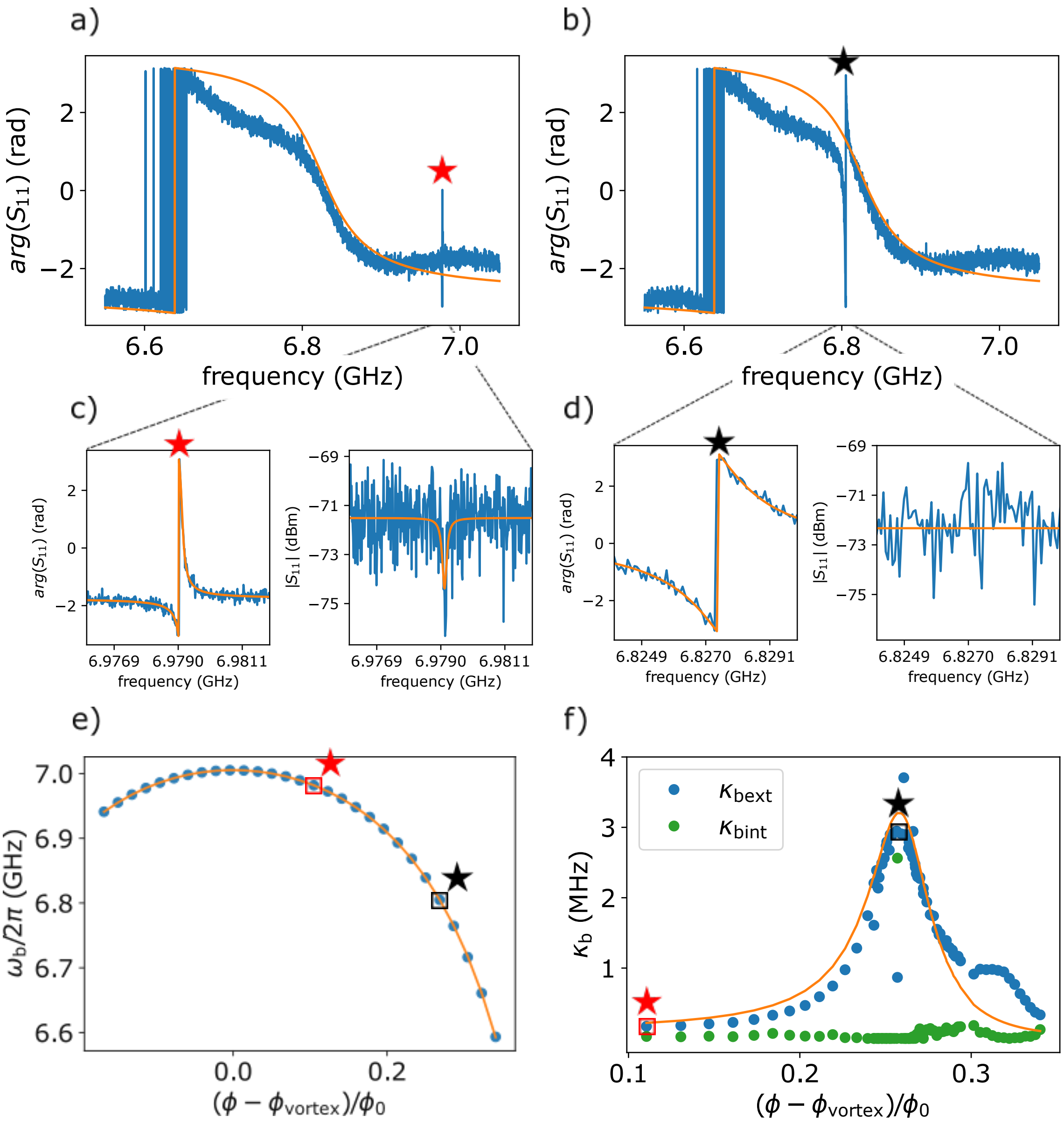

Figure 6.2: **Buffer resonator characterization**. (a) and (b) Phase of the S_{11} reflection coefficient. The Purcell filter appear as the large 2π shift. The buffer resonator appear at two different frequency $\omega_\mathrm{b}(\Phi)$ (red and black stars) according to the chosen value of the flux Φ. Red star represents the buffer aligned with its Purcell. Black star corresponds to the operating point chosen for the SMPD characterisation. (c) and (d), phase and amplitude of S_{11} according to the buffer position. The graphs are centred around the resonance frequencies. The frequency range is the same in both cases. (e) Resonance frequency of the buffer corresponding to the magnetic flux inside the loop shifted by the initial flux caused by the vortex trapped ($\Phi_\mathrm{vortex} = -0.11\Phi_0$). The red and black stars show the position of the resonance frequencies studied above. (f) Coupling and internal losses of the buffer resonator as the function of the magnetic flux. Outliers are due to fit errors. Solid line is a fit with Equation 7.28.

as the function of the shifted magnetic flux $\Phi_{\text{shift}} = (\Phi - \Phi_{\text{vortex}})/\Phi_0$. The coupling losses $\kappa_{\text{bext}}(\Phi_{\text{shift}})/2\pi$ reach a maximum (~ 3 MHz) when the frequency of the resonator is tuned with the Purcell filter. A fit realized with the Purcell formula Equation 7.28 allows us to confirm the bandwidth value extracted from the reflection coefficient and to estimate the coupling strength between the resonators at $g \approx 75$ MHz.

We can note from these data that the maximum value of $\kappa_{\text{b}}/2\pi$ is ~ 3 MHz which is larger than the simulated value. This is due to the finer width of the Purcell filter (84 MHz measured vs. 300 MHz simulated), which yields to a greater coupling between the line and the buffer resonator.

An important feature to bear in mind for what follows is that the bandwidth of the buffer resonator depends on its frequency. It will therefore be also the case for the SMPD bandwidth. All the resonator parameters are summarized in Table 6.1.

6.1.2 Qubit SMPD1

In this section we describe the different experiments allowing to extract the transmon qubit parameters (frequency, coherence time). Most of these experiments use the dispersive readout of the qubit described in Section 3.4.2. Contrary to previous work realised by Emanuele Albertinale [Alb+21], we use the waste resonator for this task. This is a logical choice as the strong coupling of the waste to the transmission line allows for short readout times. Furthermore, unlike the buffer resonator, the frequency and bandwidth of the waste resonator are fixed, which simplifies the readout characterization. Finally, using the buffer resonator could heat up the microwave line attenuator, which would generate unwanted spurious counts.

6.1.2.1 Two-tone spectroscopy

The first step in characterizing the transmon qubit is to measure its spectrum. The experiment realized, named "two-tone spectroscopy", is described in Figure 6.3a,b. The principle is to probe the resonator coupled to the qubit with a resonant fixed frequency tone. The reflection coefficient is continuously monitored.

A second tone at frequency $\omega/2\pi$ is sent to the qubit through the pump line, its frequency is swept around the qubit frequency. When the frequencies match ($\omega_{\text{q}} = \omega$), the qubit gets excited, and the resulting shift of the resonator frequency affects the reflection coefficient.

The result of a readout experiment performed on the waste side is shown on Figure 6.3c. The phase of $S_{11}(\omega_{\text{w}})$, is plotted as the function of the frequency of the tone applied on qubit. The main dip at $\omega/2\pi = 6.184$ GHz corresponds to the qubit frequency when no photons are present in the resonator. The secondary dip corresponds to the qubit frequency when 1 photon is presents on the resonator.

The frequency difference between the two peaks corresponds to the dispersive shift $\chi_{\text{qw}}/2\pi = 18.8$ MHz.

This experiment realized on the buffer side (Figure 6.3d) yields, as expected, a smaller dispersive shift $\chi_{\text{qb}}/2\pi = 5.2$ MHz. On these data, the qubit frequency with two photons in the resonator is also visible.

The measured qubit frequency is about 500 MHz higher than predicted in the simulation. This deviation is due to a poor determination of the junction area and of the critical current density, to be corrected for the SMPD2.

The frequency difference with the resonators is therefore smaller than expected, which increases the value of the dispersive coupling compared to the simulation. However, this is not detrimental to the performance of the detector since a stronger coupling between the resonators and the qubit allows us to reduce the pump signal needed for the four-wave

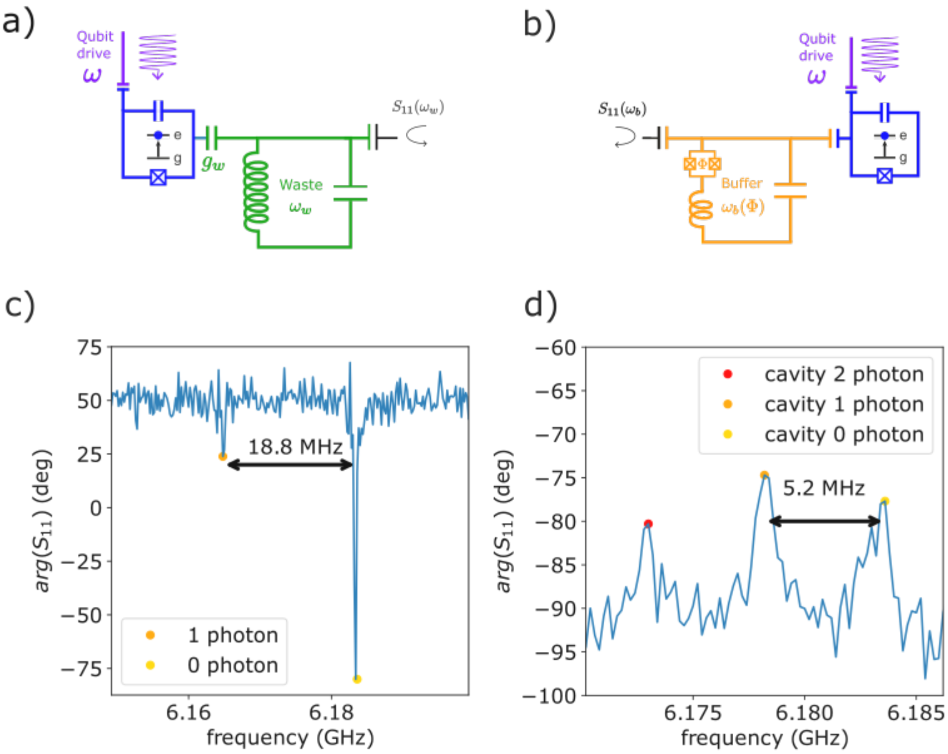

Figure 6.3: **Qubit two-tone spectroscopy**. (a) and (b), principle of a two-tone spectroscopy. A tone is shined on the qubit through the pump line, while the $S_{11}(\omega_\mathrm{r})$ of the coupled resonator is acquired continously. When the frequency of the qubit drive matches the qubit frequency, the frequency of the resonator is shifted which leads to a modification to $S_{11}(\omega_\mathrm{r})$. (c) Two-tone spectroscopy realized with the waste resonator. The frequency of the microwave tone sent to the qubit is plotted as the function of the phase of the reflection coefficient. The first peak corresponds to the qubit frequency with 0 photon in the waste resonator. The cross-Kerr $\chi_\mathrm{qw}/2\pi$ is the difference between the qubit frequency at 0 and 1 photon. (d) Two tone spectroscopy with the buffer resonator. $\chi_\mathrm{qb}/2\pi$ is measured in a similar way.

mixing. Moreover, the qubit frequency remains sufficiently distant from that of the buffer and the waste to consider that the dispersive regime approximation holds.

6.1.2.2 Qubit readout

In this section, we characterize the single-shot readout of the qubit performed with the waste resonator. As described in Section 3.4.2, a single-shot readout sequence detects the resonator frequency change controlled by the qubit state. A weak 500 ns long microwave pulse is sent to the waste resonator at the frequency $(\omega_\mathrm{w} - \chi_\mathrm{qw})/2\pi$. When the qubit is in its ground state $|g\rangle$, the pulse is reflected without phase shift. When the qubit is in its excited state, the pulse is resonant, and is therefore reflected with a π phase shift.

The microwave readout signal is generated via IQ mixing. After the reflection by the cavity, it is demodulated and represented in the IQ plan. The position of the signal in the

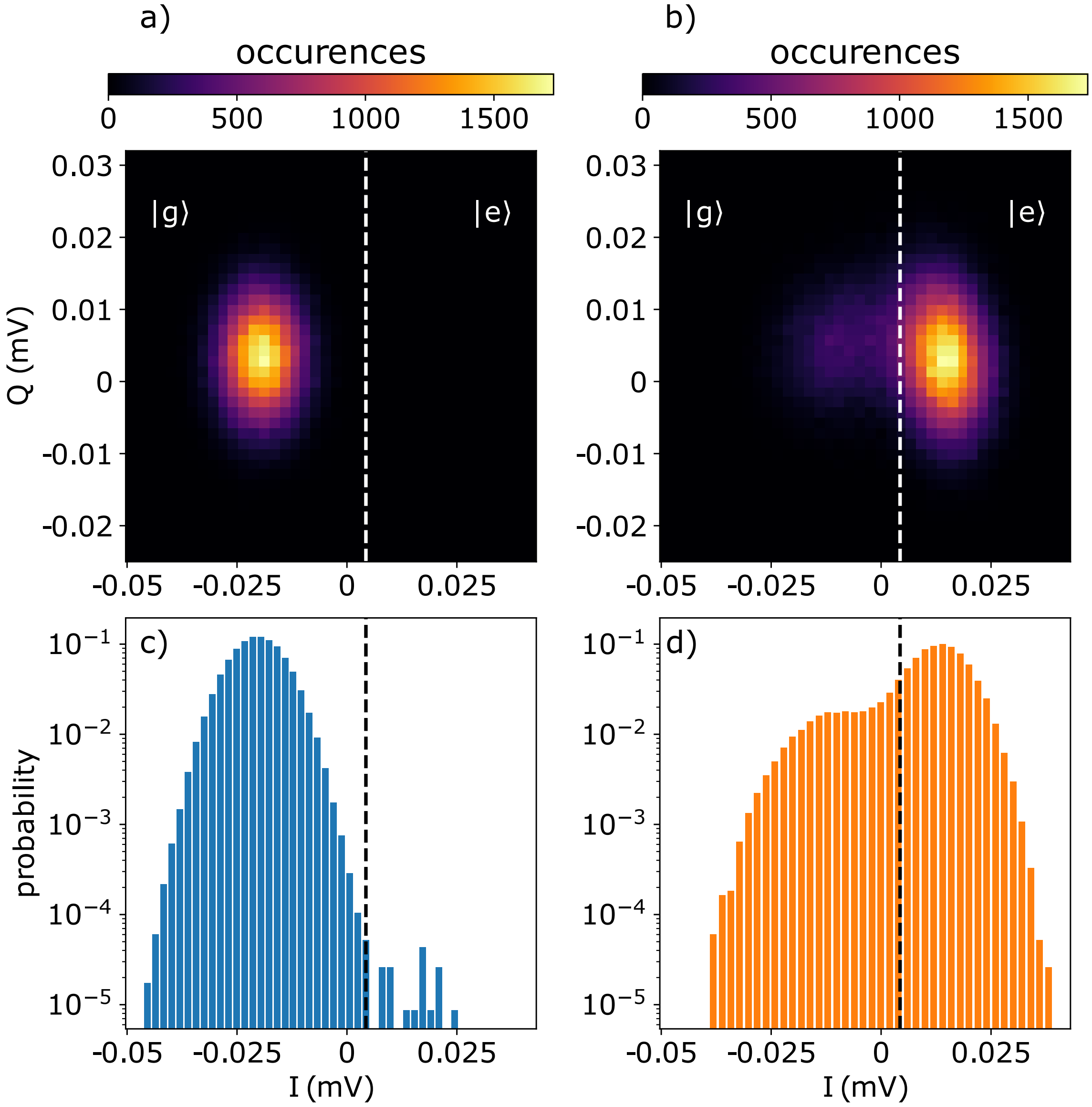

Figure 6.4: **Qubit readout**. (a) 2D Histogram showing the position on 10^5 qubit measurements in the I, Q plane. No pulses is applied to the qubit before the measurement. The dashed white line represents the threshold chosen to assign the result of the measure (ground or excited state). (b) same measurement with a pi-pulse applied on the qubit before the readout. (c) and (d) normalized histogram showing the projection of the above graphs on the I axis.

IQ plane gives the phase of the reflected signal difference, which allows us to identify the qubit state. A high fidelity single-shot readout is made possible by the use of a Traveling Parametric Wave Amplifier (TWPA) which amplifies the signal with a minimum of noise added.

Figure 6.4 shows the histograms of 10^5 measurements in the IQ plane when no control pulses are applied on the qubit (Figure 6.4a) and when a π-pulse is applied just before readout (Figure 6.4b). The distributions are centered around 2 values corresponding to the qubit states $|g\rangle$ and $|e\rangle$. The Figure 6.4c,d represents the projection of the 2D histograms on the I axis. One notices that, for the qubit at equilibrium without preparation pulse applied, a small fraction of the readout outcomes indicate the qubit in its excited state. This fraction is the equilibrium population of the qubit p_{eq}. On the contrary, when a π-pulse is applied the qubit is predominantly found in its excited state, but can also be found in its ground state due to pulse imperfections or qubit relaxation. These imperfections limit the efficiency η_m associated to the qubit measurement .

In order to assign a state to a measurement, one defines a threshold separating measurements corresponding to the two states (white dashed line on the figure). The choice of this threshold depends on the specific use of the qubit. In our case, the objective is to maximize the sensitivity of the detector proportional to $\sqrt{\alpha}/\eta$. In terms of readout, this means that the threshold should maximize the ratio $\sqrt{p_\mathrm{eq}}/\eta_\mathrm{m}$. This optimization yields the threshold shown on Figure 6.4 and corresponding to $\mathrm{I} = 4 \cdot 10^{-3}$ mV. With this setting, we obtain: $\eta_\mathrm{m} = 0.77$ and $p_\mathrm{eq} = 2 \cdot 10^{-4}$. This record equilibrium population is 2 orders of magnitude lower than the one of [Alb21]. We attribute this improvement to the new microwave shielding installed and to a more careful filtering of the lines, including the infrared filters. A lower p_eq yields a lower darkcount rate α_qubit, and thus a better sensitivity.

6.1.2.3 Qubit time domain characterization

In this section, we describe the various time-domain experiments needed to fully characterize the qubit coherence times.

The first experiment shown on Figure 6.5a is a measurement of Rabi oscillations. A microwave pulse of frequency $\omega_\mathrm{q}/2\pi$ is sent to the qubit via the pump line. The pulse duration is fixed at $T_\mathrm{rabi} = 500$ ns, and the pulse amplitude is swept. A dispersive readout of the qubit is then performed immediately after the Rabi pulse. The repetition of the experiment allows to extract the excited population p_e for each pulse amplitude.

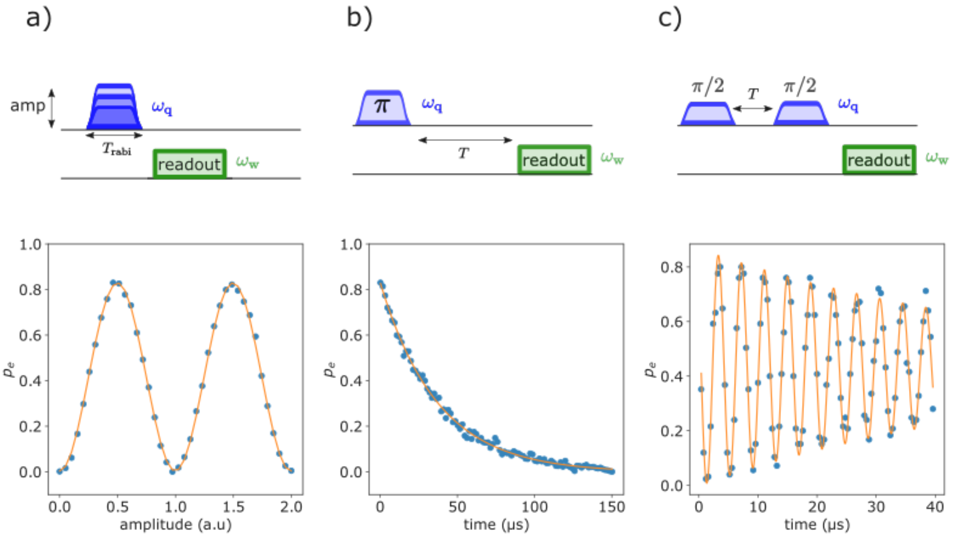

Figure 6.5: **Qubit characterization**. (a) Rabi oscillation. The pulse duration $T_\mathrm{rabi} = 500$ ns is fixed while the pulse amplitude is swept, resulting in an increase in the Rabi frequency. This sequence is used to calibrate the π-pulse. Blue dots are data, orange line corresponds to the fit used to extract the Rabi frequency (b) Relaxation time $T_1 = 37\mu$s of the qubit. A π-pulse is applied and the time before the readout is swept. (c) Ramsey experiment. Two $\pi/2$-pulses are applied with different time between them. The decay of the Ramsey fringes gives the qubit decoherence time $T_2^* = 56\mu$s

The data are then fitted with a cosine function in order to extract the value of the amplitude corresponding to a π-pulse.

Once the π-pulse is well calibrated, we measure the qubit relaxation time T_1. The corresponding sequence is shown on Figure 6.5. A π-pulse is applied on the qubit followed by a readout separated from the pulse with a variable time T. The excited population p_{e} decreases exponentially from its maximal value to its equilibrium p_{eq}. The characteristic time $T_1 = 37\mu$s is extracted from an exponential fit (orange line).

Another important figure of merit of a qubit is its coherence time T_2^*. Although the coherence time is important for qubit performance, it only weakly affects SMPD performances. It is measured thanks to a Ramsey sequence as shown in Figure 6.5c. A two $\pi/2$-pulse sequence with a slight detuning (200 kHz) and with a variable time delay T is applied to the qubit. A qubit readout is performed immediately after the second pulse. Between the two pulses, the qubit evolves freely on the Bloch sphere equator, and is subject to decoherence.

As shown on Figure 6.5, the excited state population p_{e} oscillates with T at the detuning frequency, and the envelope of the oscillations decays. An exponential fit of this decay yields the coherence time gives $T_2^* = 56\mu$s. Moreover, the measurement of the Ramsey detuning provides an accurate determination of the qubit frequency.

Qubit	
$\omega_{\mathrm{q}}/2\pi$	6.184 GHz
$\alpha/2\pi$	$\sim$ 240 MHz
$\chi_{\mathrm{qb}}/2\pi$	5.2 MHz
$\chi_{\mathrm{qw}}/2\pi$	18.8 MHz
T_1	$\sim 37\ \mu$s
T_2	$\sim 56\ \mu$s
p_{eq}	$\sim 2 \cdot 10^{-4}$

Buffer mode	top of arch	unbiased	at resonance
$\omega_{\mathrm{b}}/2\pi$	7.005 GHz	6.979 GHz	6.824 GHz
$\kappa_{\mathrm{bext}}/2\pi$	0.152 MHz	0.172 MHz	2.95 MHz
$\kappa_{\mathrm{bint}}/2\pi$	0.100 MHz	0.028 MHz	nc

Waste mode	
$\omega_{\mathrm{w}}/2\pi$	7.704 GHz
$\kappa_{\mathrm{wext}}/2\pi$	1.72 MHz
$\kappa_{\mathrm{wint}}/2\pi$	0.11 MHz

Purcell modes	
$\omega_{\mathrm{Pb}}/2\pi$	6.824 GHz
$\kappa_{\mathrm{Pb}}/2\pi$	84.2 MHz
$\omega_{\mathrm{Pw}}/2\pi$	7.620 GHz
$\kappa_{\mathrm{Pw}}/2\pi$	180 MHz

Table 6.1: Table of the experimental parameters SMPD1.

6.1.2.4 Qubit reset

As described in the Section 4.4.1, a key step of the SMPD cycle is the ability to quickly reset the qubit in its ground state. This allows the detector to be reset after the detection of a photon without waiting for the natural relaxation of the qubit, i.e. a few T_1. The qubit reset also plays a role in reducing the dark count rate by placing the excited state population below its equilibrium value.

Our reset protocol is described in Figure 6.6a. A qubit readout starts the sequence. If the qubit is in its excited state, a while loop starts, composed by a π-pulse (to put it back in its ground state) followed by a readout measurement. The exit condition of the loop is to measure the qubit in its ground state.

The experience presented in Figure 6.6a,c is a "reset and wait" measurement. The reset protocol is followed by a qubit readout after a variable time T. The results shown in Figure 6.6c confirm that the reset is functional. The qubit is placed out-of-equilibrium with an excited population $p_{\text{reset}} = 8 \cdot 10^{-5}$. Then, it relaxes through its equilibrium population with the characteristic time T_1.

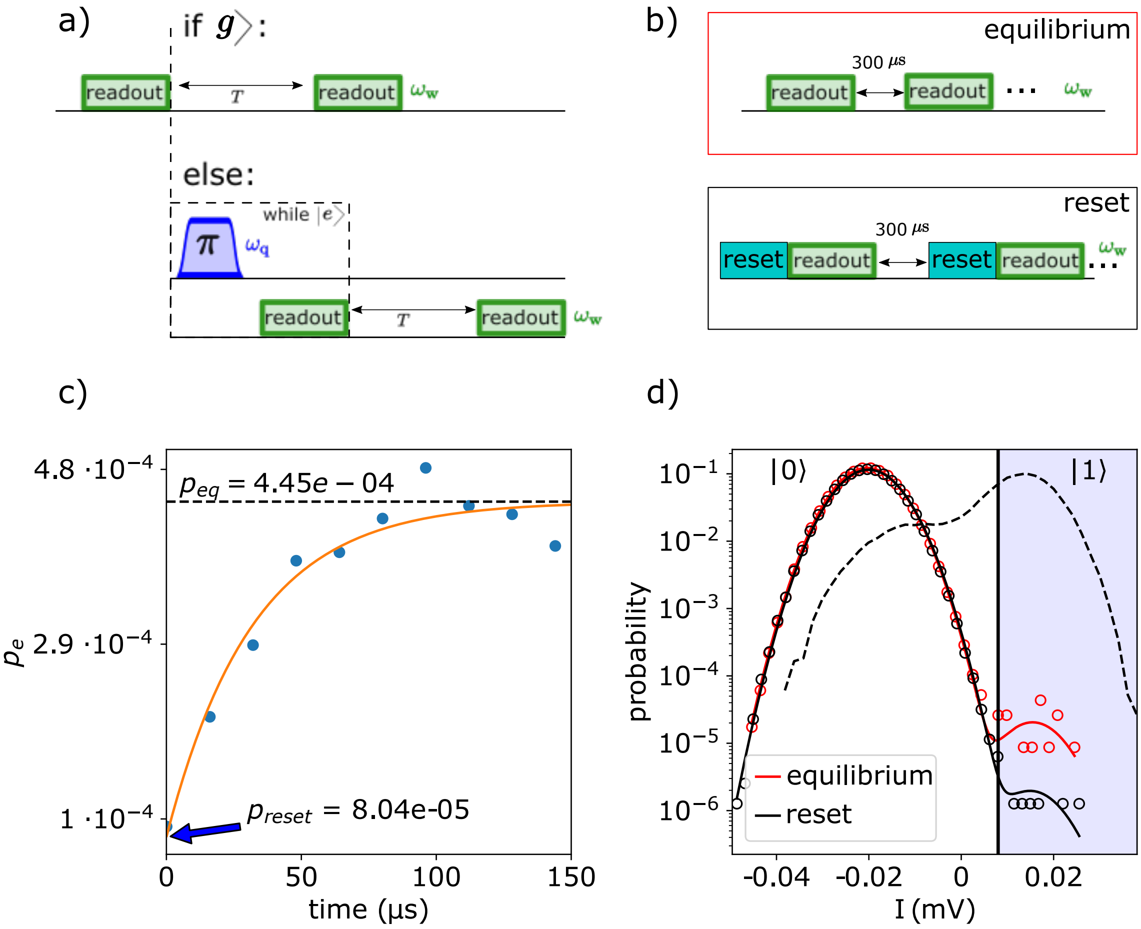

Figure 6.6: **Qubit reset** (a) Schematic of the reset and wait sequence. A qubit readout starts the sequence, if the qubit is in the excited state, π-pulses are applied until the qubit is measured in its ground state. A final readout of the qubit is realized after a time T. (c) Result of the reset and wait sequence. The qubit relaxes from its reset population p_{reset} to its equilibrium population p_{eq} with the characteristic time T_1. (b) Readout histogram measurement sequences with and without reset. (d) Histogram representing the qubit measurement in its natural qubit state (no pulses applied) and after a reset. The measurements give $p_{\text{eq}} = 2 \cdot 10^{-4}$ and $p_{\text{reset}} = 1 \cdot 10^{-5}$.

Another way to judge the quality of our reset is to directly compare the p_{reset} with p_{eq}. We first perform a succession of qubit measurements spaced by 300 μs (enough time for the qubit to be at equilibrium). In a second step, we perform the same experiment but with a reset just before the readout. The normalized histograms of these two measurements are presented in Figure 6.6d.

These data yield $p_{\mathrm{reset}} = 1 \cdot 10^{-5}$. Again, this value is lower than the previous SMPD version where $p_{\mathrm{reset,old}} = 1 \cdot 10^{-3}$.

6.2 Four-wave mixing

In this section, we describe the experiments required to set up the 4-wave mixing process. First, we adjust the cooperativity by varying the pump amplitude. Then we fine-tune the pump frequency to precisely meet the 4-wave mixing condition Equation 4.30. The bandwidth of the detector is then estimated using the two coupled cavity model.

6.2.1 Pump tuning

The first experiment consists in finding the conditions for triggering the 4-wave mixing. The sequence used is described in Figure 6.7a. A coherent tone at frequency $\omega_{\mathrm{b}}/2\pi$ illuminates the buffer resonator while a non-resonant pump tone is applied to the qubit. The microwaves are activated for 10 μs, then the qubit is measured. the blocks are separated by 500 μs. The incident photon flux on the buffer $P_{\mathrm{in}} = 0.075$ photon$\cdot\mu$s^{-1} is calibrated using the method described in Section 3.4.3. The details of this calibration are given in Section 6.3.1.

The frequency and the amplitude of the pump are swept in order to find the relevant parameters. The results of the experiment are shown in Figure 6.7b. The qubit excited population p_{e} is represented with a color map as the function of the pump amplitude and frequency. The bright zone, corresponding to a high p_{e}, indicates that a transfer occurred between a buffer photon and qubit excitation.

The four-wave mixing zone is not only depending on the pump frequency. Indeed, The higher the pump amplitude and the lower the frequency triggering the mixing. This is caused by the qubit Stark shift due to the pump. Quantitatively, this effect is represented by the term $2|\xi_{\mathrm{p}}|^2\chi_{\mathrm{qq}}$ in the four-wave mixing condition (see Equation 4.30).

A cross section of the color map along the dashed white line is shown in Figure 6.7c. This provides a representation of the conversion efficiency η_{4wm} as a function of the pump amplitude. The maximum of this curve corresponds to the optimal cooperativity. The black vertical line represents our choice for the rest of the experiment. We deliberately place ourselves slightly below the maximum in order to reduce the power sent to the chip, which mitigates the spurious false positive readouts due to chip heating or uncontrolled parametric conversion.

The fit represented by the orange line uses the expression of η_{4wm} in presence of losses given in Equation 4.67. Taking into account the values $\kappa_{\mathrm{bext}}/2\pi = 0.172$ MHz and $\kappa_{\mathrm{bint}}/2\pi = 0.028$ MHz (see Table 6.1), the cooperativity which maximizes the efficiency is $\mathcal{C} = 1.16$. The fit gives $\mathcal{C} = 0.9$ for the chosen pump amplitude (vertical black line). However, as can be seen on Figure 6.7d, our model does not adequately capture the behavior of the 4-wave mixing process at larger cooperativities, which suggests that our model is imperfect.

Several factors may contribute to this inadequacy. For instance, the qubit population can be excited by processes other than 4-wave mixing at large pump amplitude. In addition, our model for the efficiency is valid insofar as the pump frequency is perfectly tuned. In

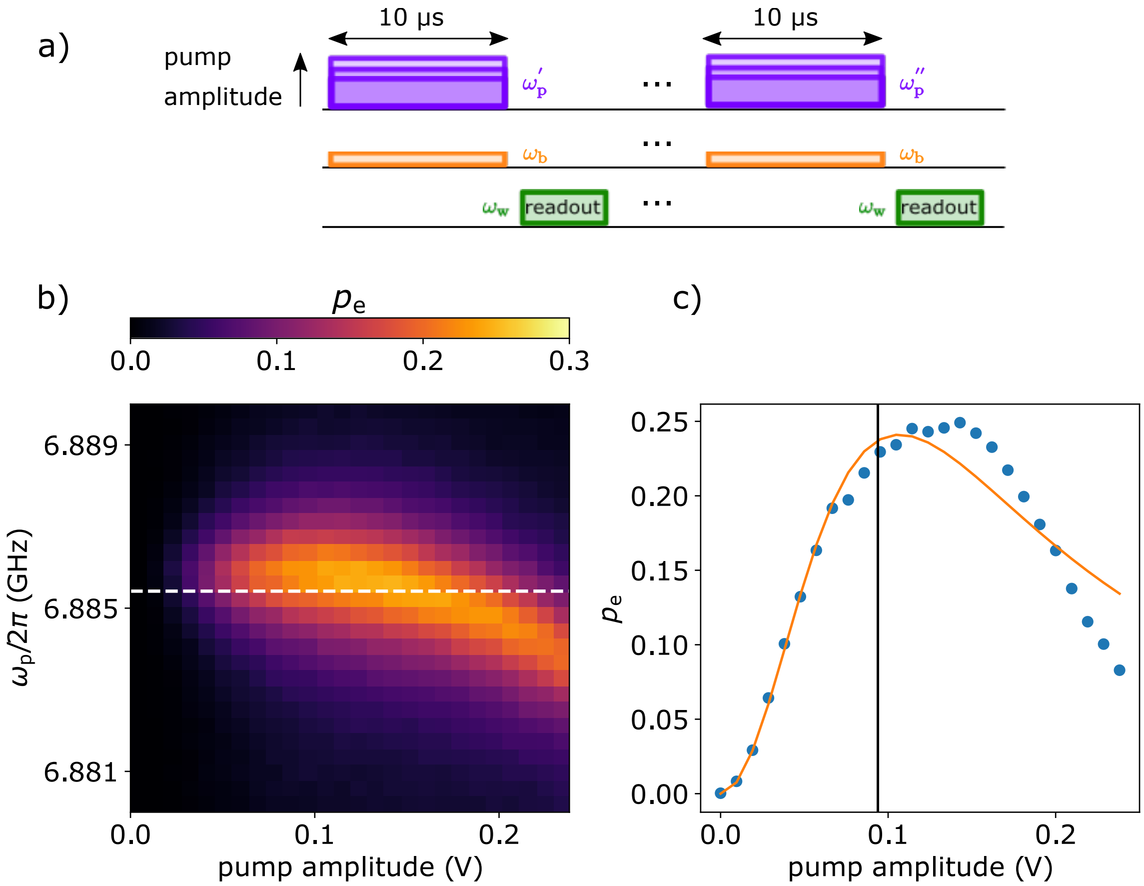

Figure 6.7: **Four-wave mixing** (a) Schematic of the four-wave mixing experiment. A pump tone is shined on the qubit while a weak coherent tone is applied on the buffer resonator. The frequency and the amplitude of the pump are swept. (b) Color plot of the qubit excitation probability p_e as the function of the pump frequency and amplitude. A high probability indicates that a buffer photon has been converted into an excited state of the qubit. (c) Cross section along the dashed white line ($\omega_p/2\pi = 6.8855$ GHz). Blue dots are the data, the orange line represents the fit using Equation 4.67. Solid black line is the chosen pump amplitude.

order to more precisely determine the cooperativity corresponding to the chosen pump amplitude, we use a model of two coupled cavities in the next section.

6.2.2 Detector bandwith

In this section, we use a coupled two-cavity model to extract the key parameters of the four-wave mixing (optimal pump frequency, cooperativity) as well as the detector bandwidth.

The experiment is schematically described in Figure 6.8a. The amplitude of the pump tone is now fixed (as set by the previous experiment), whereas the pump frequency $\omega_p/2\pi$ and the coherent tone frequency $\omega_b/2\pi$ are respectively swept around $\omega_b/2\pi = 6.982$ GHz and $\omega_p/2\pi = 6.885$. The incident flux of photons is similar to the one of Section 6.2.1. A qubit readout follows the four-wave mixing.

The variation of the qubit excited population p_e with the pump and photon frequency detuning is shown in Figure 6.8b using a color map. The brightest part, corresponding to the highest value of p_e, shows the frequency conditions for optimal conversion.

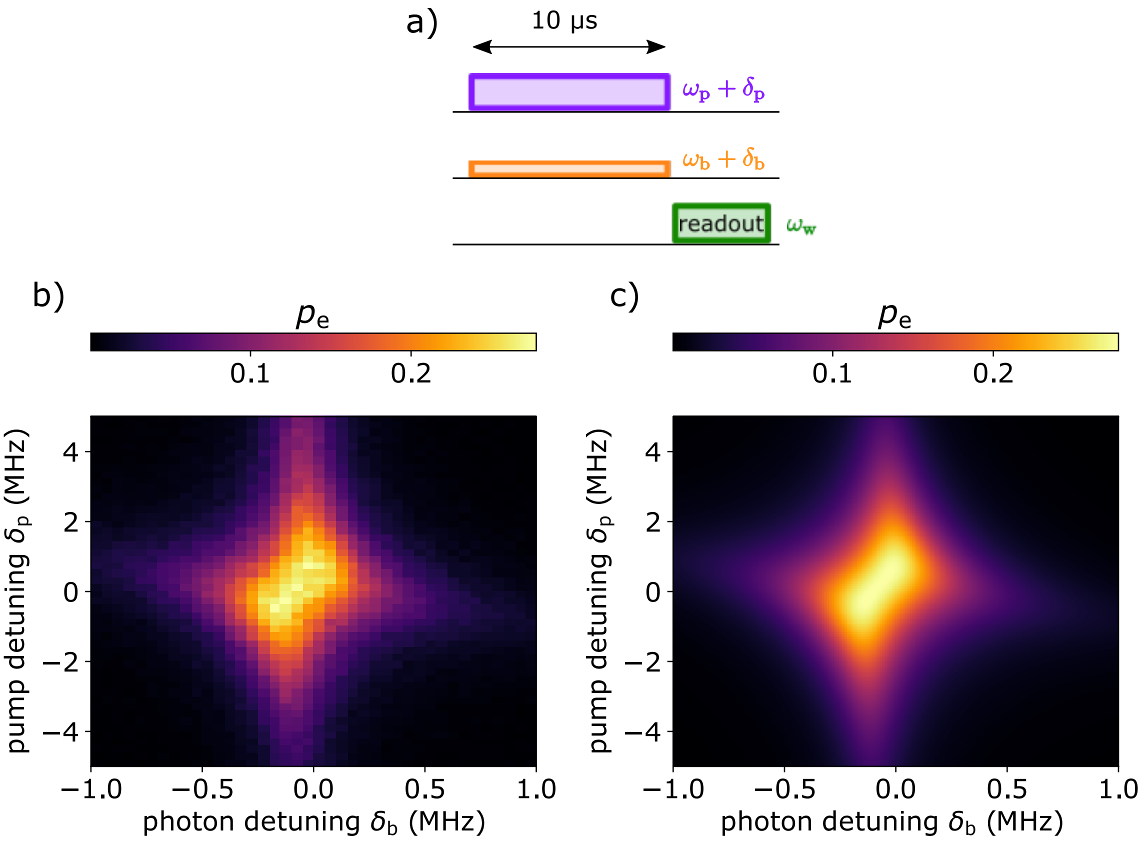

Figure 6.8: **Bandwidth and operating point from the coupled cavity model**. (a) Schematic of the experiment. For a given pump amplitude, the pump and the coherent tone frequencies are scanned. (b) Color plot of qubit excitation probability p_e as the function of the pump and coherent tone frequency. High probability indicates photon conversion. (c) Fit of the color plot with Equation 4.53. The extracted parameters are: the detector bandwidth $\kappa_d/2\pi = 0.59$ MHz and the operational cooperativity $\mathcal{C} = 1.12$.

A fit to these data using Equation 4.53 is plotted in Figure 6.8c. This fit allows us to precisely extract the different parameters. The best frequency shifts for tuning the conversion are $\delta_p = 0.140$ MHz and $\delta_b = 0.078$ MHz. The cooperativity found using the model is $\mathcal{C} = 1.12$, quite different from the value $\mathcal{C} = 0.9$ extracted in Section 6.2.1, but still less than the theoretical optimum cooperativity $\mathcal{C} = 1.16$. The corresponding four-wave mixing efficiency is $\eta_{4wm} = 0.86$.

In the limit where $\kappa_b \ll \kappa_w$, the theoretical detector bandwidth is given by $\kappa_d \approx 2\kappa_b(1+\kappa_b/\kappa_w) = 0.43$ MHz, to be compared to the bandwidth given by the fit $\kappa_d/2\pi = 0.59$ MHz. We attribute this discrepancy to the spectral broadening caused by the finite duration of the excitation pulses. It is also important to keep in mind that the bandwidth of the buffer resonator (and therefore of the detector) varies with frequency because on its Purcell filter. Note that this calibration must be performed again for detecting photons at a different frequency.

In the following section we use the different parameters set in the two last sections for operating the detector in cyclic mode.

6.3 SMPD cyclic operation

As explained in Section 4.4.1, the SMPD operates in a cyclic way. We first motivate the choice of cycle parameters and then measure the different figures of merit needed to determine the sensitivity of the detector.

6.3.1 Cycle parameters

The cycle consists of three different phases with durations to be set. The choice of the readout pulse duration $T_{\mathrm{m}} = 500$ ns (made in Section 6.1.2.2) sets the length of the readout window.

The duration of the reset sequence depends on the qubit state. However, when the microwave photon source to be detected emits a small number of photons per second compared to the cycle repetition rate, we can consider that in most cases the reset is not activated. We therefore do not consider this window in the following optimization.

Furthermore, between the reset and the new detection window, we place a waiting time of 1 μs in order to let the waste resonator return to its ground state. The total cycle duration is thus $T_{\mathrm{cycle}} = 1.5\mu\mathrm{s} + T_{\mathrm{d}}$.

To determine the optimal duration of the detection window T_{d}, we maximize the product of the duty cycle and the qubit relaxation efficiency $\eta_{\mathrm{d}}\eta_{\mathrm{qubit}} = T_1/T_{\mathrm{cycle}}(1 - e^{-T_{\mathrm{d}}/T_1})$. The resulting duration is $T_{\mathrm{d}} = 10$ μs.

The real average cycle time measured in the following experiment is $T_{\mathrm{cycle}} = 11.9$ μs. The duty cycle is thus $\eta_{\mathrm{D}} = 0.83$, almost the double of the value $\eta_{\mathrm{D,old}} = 0.43$ for the previous SMPD generation [Alb21].

6.3.2 Efficiency

Once the cycle parameters are fixed, the first figure of merit to characterize is the detector overall efficiency. The experiment consists in illuminating the buffer resonator with a well-calibrated photon flux, and to compare the number of clicks obtained with the number of incident photons.

6.3.2.1 Calibration of the photon number

In this section we calibrate the number of incoming photons per second thanks to the qubit coherence properties described in Section 3.4.3. We exploit the effect of photons in the buffer on the qubit frequency and coherence time T_2 to accurately measure the incident photon flux.

A schematic description of the pulse experiment performed is shown in Figure 6.9a. It consists in applying a Ramsey pulse sequence similar to the one described in Section 6.1.2.3, superimposed with a coherent tone sent to the buffer resonator (to calibrate). The frequency of the tone is swept, and, for each frequency point, a full Ramsey experiment is performed in order to extract the coherence time and the qubit frequency. When the microwave tone is resonant with the buffer, the latter is populated and the qubit coherence time is reduced.

Ramsey oscillations measured at photon frequency $\omega_{\mathrm{b}}/2\pi - \delta$ for two values of the frequency detuning δ are shown in Figure 6.9b. For $\delta = 0$ (red curve), the tone is resonant with the buffer cavity and the qubit coherence time is significantly reduced. One also notes,as expected, a slight change in the oscillation frequency indicating a qubit frequency shift. The fits that allow us to extract the two figures searched for in this experiment are represented by solid lines.

The variations of the decoherence rate $\gamma_2 = 1/T_2^*$ with the frequency detuning δ are shown in Figure 6.9c. As expected, the decoherence rate dramatically increases at $\delta = 0$ because of the shot noise induced by the photons in the cavity. Another peak appears for

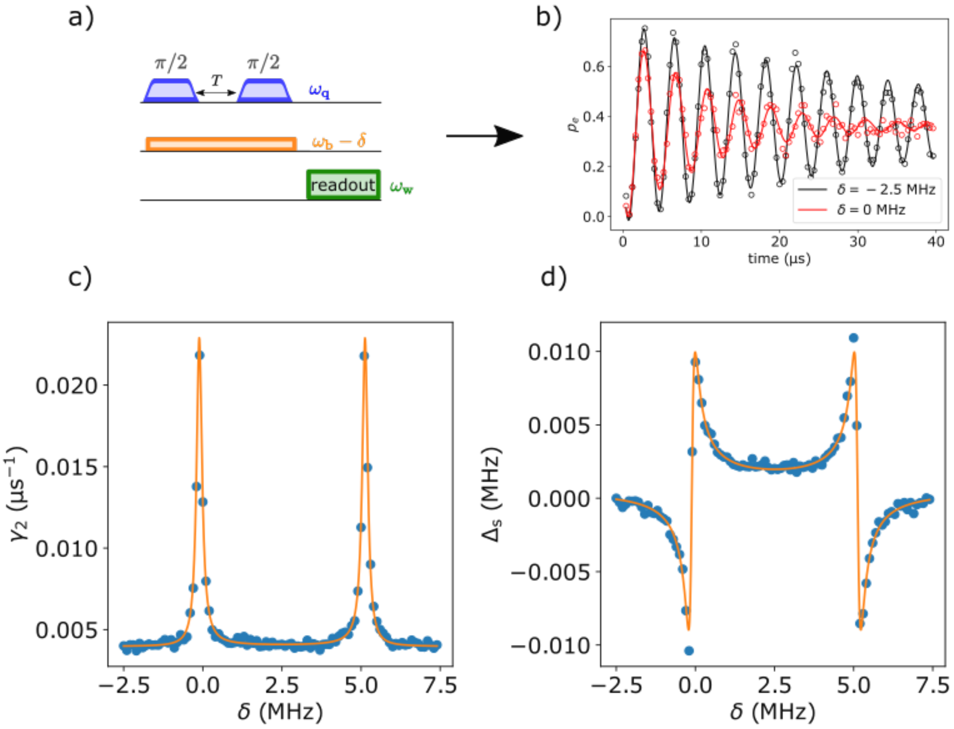

Figure 6.9: **Photon number calibration** (a) Pulse sequence applied on the system. A Ramsey sequence is sent on the qubit while a weak coherent tone is shined on the buffer resonator. (b) Ramsey oscillation for two different frequencies of the coherent tone sent on the buffer. When the buffer is populated (red curve), T_2 decrease and the qubit frequency is shifted. (c,d) $\gamma_2 = 1/T_2^*$ and Qubit frequency detuning as the function of the tone frequency. Blue dots are the data, the solid orange curve a fit based on Equation 3.92 allowing to extract the average number of photon populating the buffer resonator.

$\delta = 5.2$ MHz. It corresponds to the second cavity mode frequency $(\omega_b - \chi_{qb})/2\pi$ due to its coupling with the qubit. This experiment provides an accurate determination of the dispersive shift $\chi_{qb} = 5.2$ MHz, in perfect agreement with the previously estimated one.

The variations of the qubit detuning Δ_s with the detuning frequency detuning δ are shown in Figure 6.9d. The value of Δ_s is maximal for $\delta = 0$ and $\delta = \chi_{qb}/2\pi$, i.e. at resonance with the buffer.

The fits (orange line) in Figure 6.9c,d are based on Equation 3.92. They allow us to extract the average photon number $\bar{n}$ in the resonator for the steady state when the microwave tone is resonant with the cavity. From this average population we can calculate the incident power impinging the resonator using Equation 3.93. The obtained photon flux is $P_{in} = 7.5 \cdot 10^4$ photon$\cdot s^{-1}$. This figure allows us to determine the overall efficiency.

6.3.2.2 Operational efficiency

Once the incoming flux of photon is calibrated for a given amplitude, it is easy to choose the photon flux that we want to send to the cavity given that $P_{in} \propto A^2$ where A is the microwave tone amplitude.

The response of the detector over 1 second ($\sim$ 80000 cycles) for five different values of

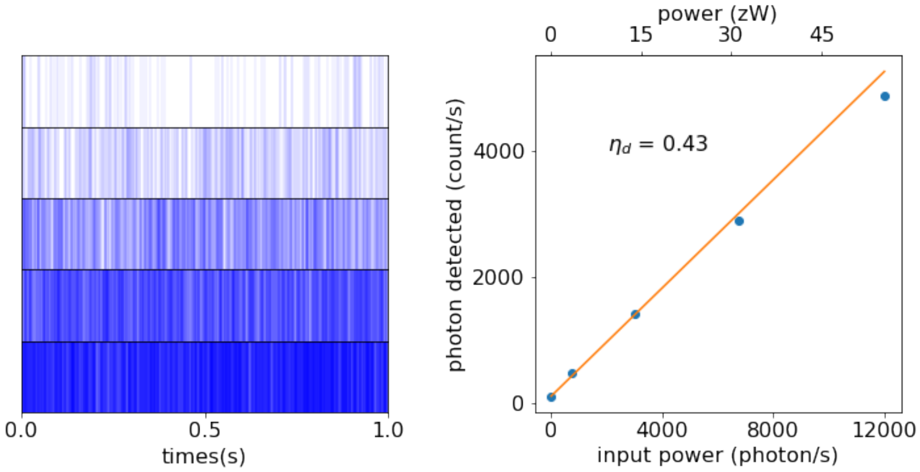

Figure 6.10: **SMPD1 operational efficiency** Right panel, time traces representing one second of detection ($\sim$ 80000 cycles) for different powers applied to the buffer. Each blue line represents a click. Left panel, number of clicks per second as the function of the number of incoming photons. The fit (orange line) allows to extract the overall efficiency $\eta_\mathrm{d} = 0.43$.

the photon flux (0, 750, 300, 6750 and 12000 photon-s^{-1}) is shown in Figure 6.10a. Each blue bar represents a detection event. As expected, the number of detections increases with the intensity of the photon flux.

The variations of the detector click rate with the input power are shown in Figure 6.10b. The input power is given in photons $\cdot \mathrm{s}^{-1}$ and in zW (10^{-21} W, top scale). A simple linear fit allows us to extract the overall efficiency $\eta_\mathrm{d} = 0.43$.

The SMPD is a fast saturating detector: once the qubit is excited during one cycle, the detector is blind until it is reset. Typically for a 12 μs cycle, assuming uniform photon arrival, the maximum detectable power is thus $P_\mathrm{in} \sim 8 \cdot 10^4$ photon$\cdot$s^{-1}. In real measurements, the photons are not evenly distributed, and saturation gradually occurs as the incident power is increased. This saturation is visible for the two last points in Figure 6.10b.

The measured efficiency $\eta_\mathrm{d} = 0.43$ compares rather well with the theoretically estimated one $\eta_\mathrm{d} = \eta_\mathrm{D}\eta_\mathrm{qubit}\eta_\mathrm{4wm}\eta_\mathrm{m} = 0.83 \cdot 0.88 \cdot 0.85 \cdot 0.77 = 0.48$.

6.3.3 Dark count

The second experimental characteristic important for the sensitivity of the detector is the overall dark count rate α_d.

Its characterization consists in repeating the cycle a large number of times without sending photons to the detector. The cycles are collected in groups of 10^6 sequences (12 s of measurement) from which an average dark count rate is extracted.

The results of such dark count measurements performed during 10 hours are shown on Figure 6.11. At the beginning the dark count rate increases from 60s^{-1} to about 85s^{-1}. This transient regime is attributed to the heating of the cold stage of the refrigerator due to the continuous power delivered by the qubit pump. A steady state is reached after about 1 hour with an average dark count rate $\alpha_\mathrm{d} = 84$ s^{-1}.

This experimental evidence for a small dark count rate is the main progress achieved by our new version of the SMPD. This present value $\alpha_\mathrm{d} = 84$ s^{-1} is indeed more than one order of magnitude smaller than achieved by the previous version where $\alpha_\mathrm{d,old} = 1500$ s^{-1}

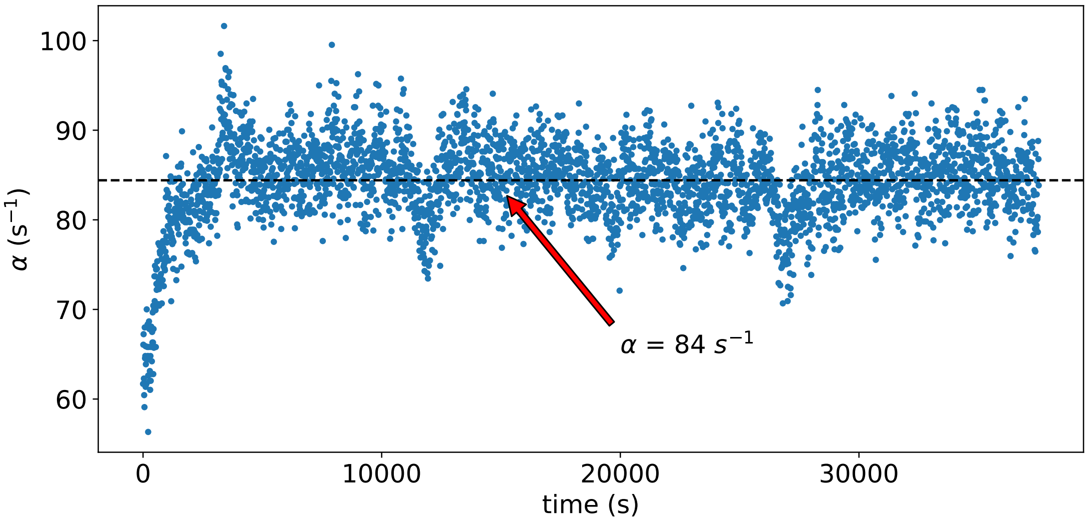

Figure 6.11: **Dark count measurement** Acquisition of the dark count rate α_d as the function of the time. Each point correspond to the average false positive rate over $\sim$ 12s (10^6 cycles). α_d increases due to the heating induced by the repetition of the detection cycle and saturates around 84 click·s^{-1}.

[Alb21]. I attribute this sizeable improvement mainly to the lower excited qubit population at equilibrium, and to the longer qubit relaxation time T_1.

6.3.4 Noise equivalent power

In the last two sections we measured the efficiency of the detector η_d as well as its false positive rate α_d. Here we combine these two values to estimate the absolute sensitivity of the detector based on the NEP.

Based on Section 4.5, we define the sensitivity $\mathcal{S}$ of the detector as the minimum detectable power for a 1 second integration time. Since we are in the regime where $\sqrt{\alpha_\mathrm{d}} \gg 1$, we can express this sensitivity as $\mathcal{S} = \hbar\omega_\mathrm{b}\sqrt{\alpha_\mathrm{d}}/\eta_\mathrm{d}$. Given $\alpha_\mathrm{d} = 84$ s^{-1}, $\eta_\mathrm{d} = 0.43$ and $\omega_\mathrm{b}/2\pi = 6.982$ GHz, one obtains the NEP $\mathcal{S} = 10^{-22}$ W/$\sqrt{\mathrm{Hz}}$.

This sensitivity is almost one order of magnitude better than the one of the previous SMPD $\mathcal{S}_\mathrm{old} = 8 \cdot 10^{-22}$ W/$\sqrt{\mathrm{Hz}}$. In practical terms, this means that the integration time required to detect a microwave photon source (typically a spin) with a sufficient signal-to-noise ratio a is divided by $\sim$64. In terms of detection, this is a real breakthrough because it allows the detection of a single spin, as we show in Chapter 8 and in [Wan+23].

6.4 Temperature measurements

In this section, we demonstrate that the thermal contribution to dark counts α_th follows the Johnson-Nyquist law introduced in Section 4.4.3. For this purpose, we measure the variations of the dark count rate with the temperature. We also record the different SMPD parameters in order to ascertain the origin of false positives.

These measurements, called run 2, were made 6 months after the measurements presented in the previous sections, called run 1. For some unknown reason, after several cool-down cycles, the qubit frequency increased from 6.184 GHz to 6.3 GHz . Its relaxation time T_1 was also greatly reduced from 37 μs to 20 μs and its equilibrium population increases from 10^{-4} to $2 \cdot 10^{-3}$ these parameters are summurazid in Table 6.2. Both of

Qubit	run 1	run 2
$\omega_q/2\pi$	6.184 GHz	6.3 GHz
T_1	$\sim 37\,\mu$s	$\sim 23\,\mu$s
p_{eq}	$\sim 2 \cdot 10^{-4}$	$\sim 2 \cdot 10^{-3}$

Buffer mode	run 1	run 2
$\omega_b/2\pi$	6.979 GHz	7.011 GHz
$\kappa_{bext}/2\pi$	0.172 MHz	2.95 MHz
$\kappa_{bint}/2\pi$	0.028 MHz	nc

Table 6.2: Parameters modifications between the run 1 and run 2.

these changes could have been caused by the frequency change of the qubit which would have coupled it resonantly with a two-level system (TLS). In any case, these modifications are highly detrimental to the performance of the SMPD and required adjustments of the detection parameters.

6.4.1 Operating point

In this section we describe the adjustments made to the SMPD parameters to account for the new qubit constants. We also detail the impacts of these modifications on the performance of the detector.

Detection window

The first adjustment concerns the detection window. With T_1 of $\approx 23\ \mu$s (see Figure 6.12a), the optimisation procedure presented in Section 6.3.1 gives a new detection window with length $T_d = 8\ \mu$s. . The new duty cycle is $\eta_D = 0.8$.

Buffer resonator

The increase of the qubit frequency is more problematic for the operation of the detector. Indeed, the 4-wave mixing condition Equation 4.30 implies that a rise of the qubit frequency requests a rise of the the pump frequency. With a qubit at 6.3 GHz, the pump frequency then starts to be close enough to the buffer frequency for populating it it with photons, as can be seen in Figure 6.12c. On this plot that represents the qubit excited population as the function of the frequency and amplitude of the pump, the saturated color on the top right corner, denoting a large qubit population, is due to the pump. In order to avoid this collision, we decided to operate the circuit at the largest possible buffer frequency (and no longer at zero flux applied in the SQUID) $\omega_b/2\pi = 7.0114$ GHz. One furthermore notes that this frequency has also slightly increased compared to the measurements presented in Table 6.1. Since the resonator is further away from its Purcell filter, its bandwidth is narrower $\kappa_b/2\pi = 0.152$ MHz.

This adjustment allowed us to place the pump at 32 MHZ of the cavity, which proved to be sufficient to perform the experiments.

Dark counts

The larger qubit population p_{eq} shown in Figure 6.12b leads to an increase in the dark count rate (200 s^{-1} vs 84 s^{-1}).

Efficiency and SMPD bandwith

The efficiency and bandwidth of the SMPD were here determined in the same experiment. We applied the same protocol as described in Figure 6.10 to extract the efficiency, but applied it to several frequencies of the coherent tone sent to the buffer resonator. The results are shown in Figure 6.12d. The efficiency at resonance is found to be $\eta_{\mathrm{d}} = 0.29$, and the detector bandwidth is $\kappa_{\mathrm{d}}/2\pi = 0.278$ MHz.

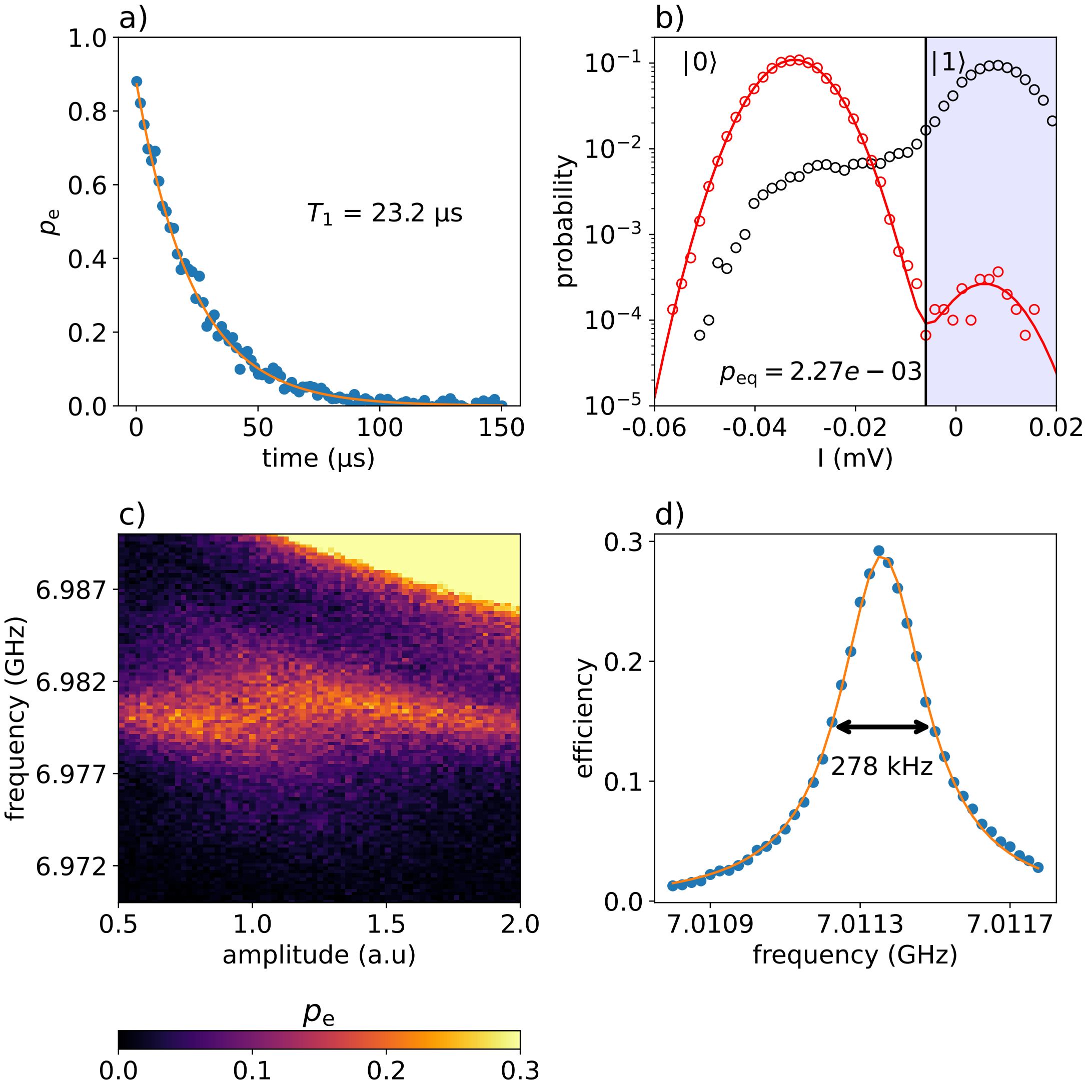

Figure 6.12: **Operating point for temperature measurements**. (a) Measurement of qubit relaxation time T_1. (b) Qubit readout, the equilibrium population is $p_{\mathrm{eq}} = 2.27 \cdot 10^{-3}$ while the measurement efficiency is $\eta_{\mathrm{m}} = 0.88$. (c) Four wave mixing experiment. Color map represents the qubit excited population p_{e} as the function of the pump amplitude and the pump frequency. (d) Overall efficiency and bandwidth measurement. Each efficiency point is acquired in the same way as Figure 6.10 but for a different photon frequency.

It is interesting to note that with this measurement, The measured SMPD bandwidth is in better agreement with the theoretical one $\kappa_\mathrm{d} = 2 \cdot \kappa_\mathrm{b}$. This is due to the fact that, unlike in the experiment measuring the bandwidth in Figure 6.8, the coherent tone sent to the buffer is one second long, and therefore much better defined spectrally.

Furthermore, since the efficiency depends on the frequency of the incident photon flux, this measurement is more reliable than the one presented in Figure 6.10 performed at a fixed frequency.

6.4.2 SMPD and refrigerator temperature

The experiments performed in this section consist in tracking α_d, T_1 and p_eq as the function of the fridge cold stage temperature. A resistor thermally anchored to the stage enables us to heat it up to typically 1 K by passing a small dc current.

The dark count rate is acquired by group of 10^5 cycles (one point per second). The qubit T_1 and p_eq are recorded every 60 α_d points ($\sim$ 1 minute).

The evolution of these quantities are shown in Figure 6.13. Eleven temperature values were investigated from 10 mK to 100 mK. We have limited ourselves the temperature to 100 mK in order to avoid saturating too much the detector.

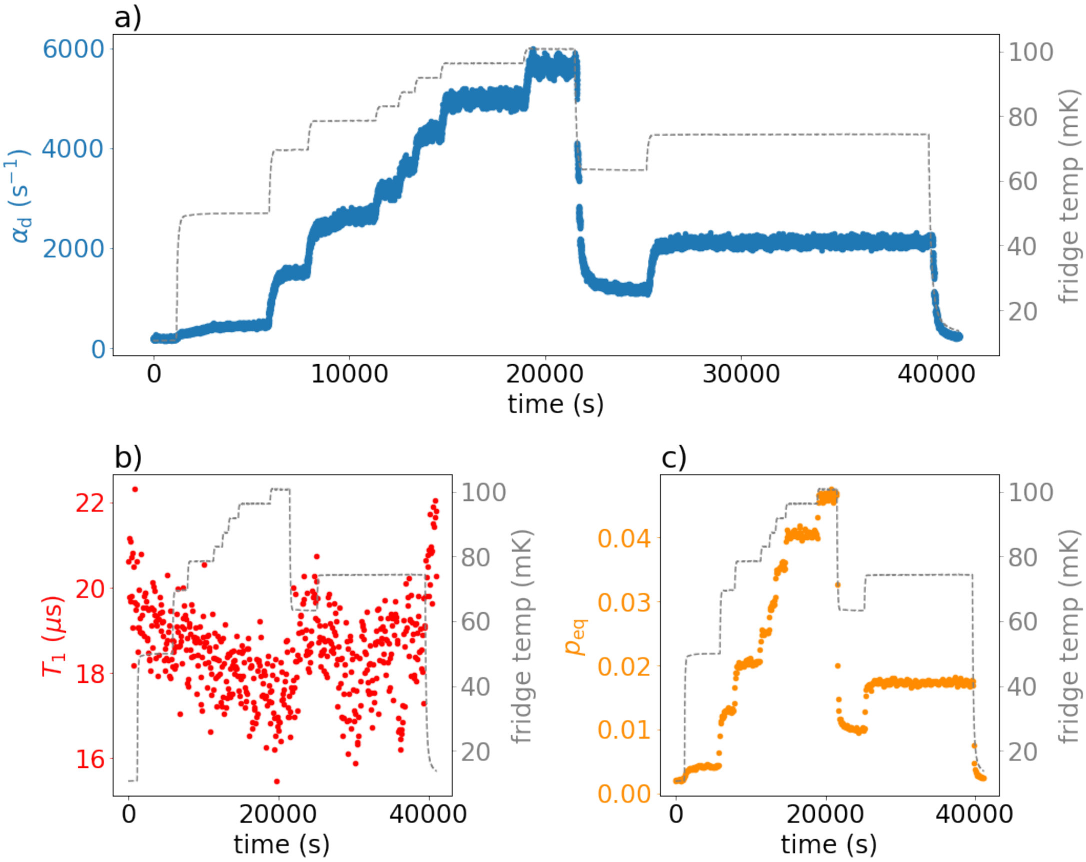

Figure 6.13: **Temperature measurements raw data** (a) Dark count rate α_d (blue dots) and fridge temperature (dashed grey line) as the function of the time. Each dark count points correspond to a the average rate over 10^5 cycles ($\sim$ 1 s) (b) qubit T_1 (red dots) acquired every minutes and fridge temperature. (c) Qubit equilibrium population (dark orange dots) acquired every minutes and fridge temperature.

One first notices that α_d and p_eq strongly increase with the temperature. This is expected since these two quantities follow the Bose-Einstein statistics: the higher the temperature, the higher the occupation number $\bar{n}$. Monitoring the thermal population of the qubit allows us to remove its contribution to the total dark count in order to extract α_{th}.

Similarly, the relaxation rate increases with temperature, and thus T_1 decreases with temperature. This behaviour, also expected from previous work [Pal+09], is detrimental to detector efficiency and must be taken into account.

6.4.3 Johnson Nyquist law

In this section, we show how to dissociate the false positives linked to the qubit from those linked to thermal photons. We will also take into account the efficiency decrease by applying a corrective factor to the dark count as a function of temperature. Finally, we demonstrate that the thermal noise obtained follows the Johnson Nyquist law.

Efficiency evolution

The estimated evolution of the efficiency is plotted in Figure 6.14a. Each T_1 point allows us to estimate the efficiency η_{qubit} related to the qubit. Furthermore, for each group of 10^5 cycles, we estimate the duty cycle η_{d} by calculating the average cycle time. From these two values, we derive a correction factor C_{cor} to be applied to the nominal efficiency $\eta_{\mathrm{d}} = 0.29$. C_{cor} is calculated for each group of 60 α_{d} points.

False positives due to the qubit

The evolution of α_{qubit} is shown in Figure 6.14a. This parameter is simply extracted from the T_1 and p_{eq} measurements with the formula given in Section 4.4.3 (considering $p_{\mathrm{reset}} = 0$): $\alpha_{\mathrm{qubit}} = \eta_{\mathrm{D}} p_{\mathrm{eq}}/T_1$.

Calculation of α_{th}

The dark count rate due to the thermal photons is represented in Figure 6.14c. The contribution of the qubit to the total dark count is removed, and the correction factor C_{cor} is applied to the result to account for the decrease in efficiency. We have thus the relation, $\alpha_{\mathrm{th}} = (\alpha_{\mathrm{d}} - \alpha_{\mathrm{qubit}}) \cdot C_{\mathrm{cor}}$. The values α_{qubit} and C_{cor} are updated every 60 points (every minute).

The blue and green areas on Figure 6.14 correspond to the points selected to extract the average value of α_{th} for each temperature. These areas are selected away from transient temperature changes.

Dark count and Johnson Nyquist law

The 11 average values of α_{th} extracted from Figure 6.14c are shown in Figure 6.14d. The inset shows an example of the α_{th} distribution for the green area. The purple points are the distribution average values, and the error bars correspond to a standard 2σ deviation.

These values are plotted as the function of the average number of photon $\bar{n}$ (see Figure 6.14e) calculated from the Bose Einstein formula for the different experimental temperatures. The solid black line in Figure 6.14e corresponds to the Johnson Nyquist relation $\alpha_{\mathrm{th}} = \eta_{\mathrm{d}} \kappa_{\mathrm{d}} \bar{n}/4$ where $\eta_{\mathrm{d}} = 0.29$ is the nominal efficiency.

The data and the theoretical predictions are found in good agreement. We attribute the deviation observed for the for the three highest temperature points to the saturation of the SMPD.

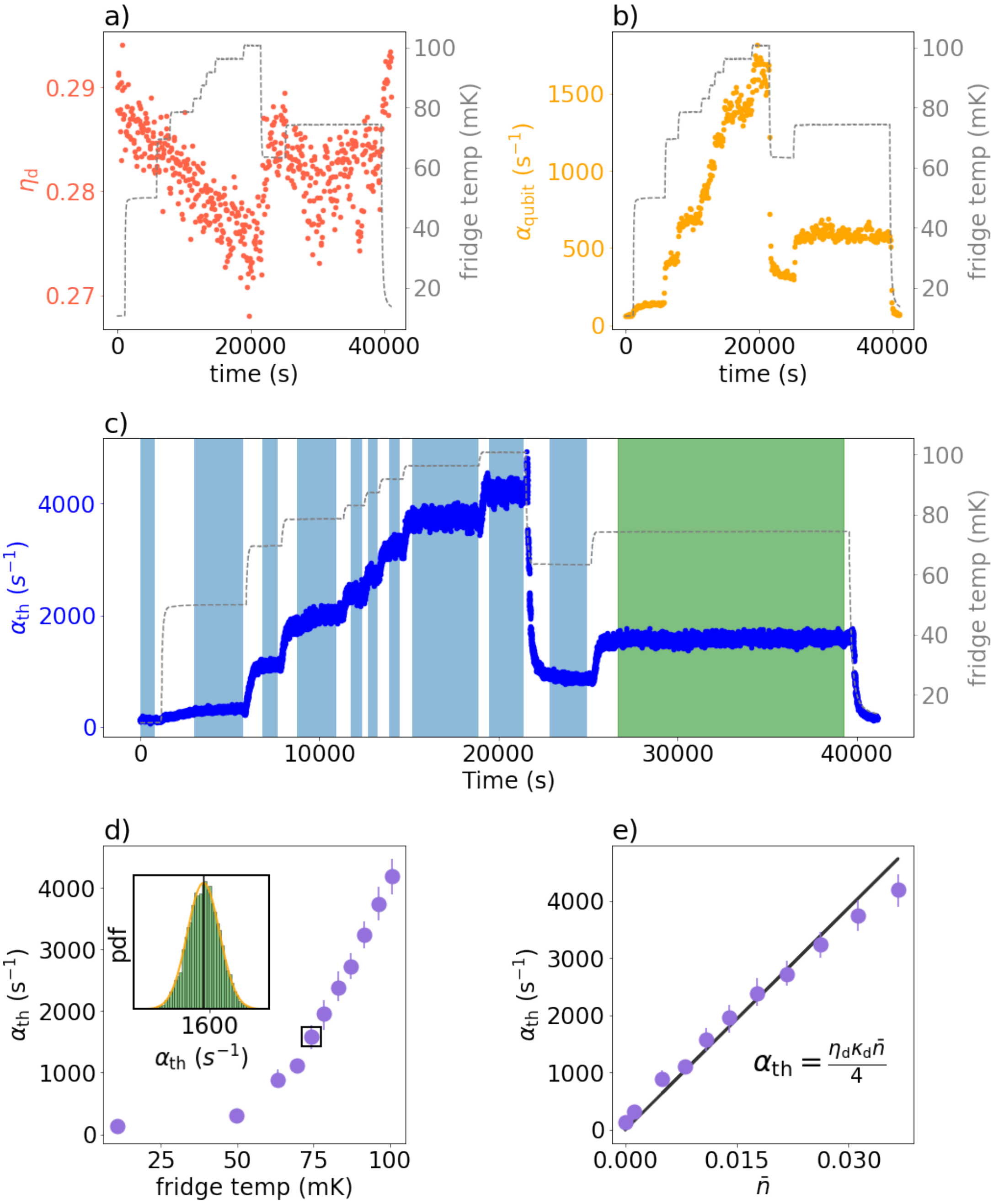

Figure 6.14: **Johnson Nyquist law** (a) SMPD efficiency η_d (red dots) calculated from Equation 4.63, taking into account the effect of the temperature on the qubit T_1 and on the duty cycle. The 10 mK efficiency is $\eta_d = 0.29$. (b) Dark count rate due to the qubit α_{qubit} as the function of the time calculated with Equation 4.69. (c) Thermal dark count rate α_{th} calculated by removing the contribution of the qubit to the overall dark count rate and re-scaling the result to account for the efficiency drop. The blue and green areas represent the data selected to extract an average thermal dark count rate at given temperature. (d) Average of each α_{th} distribution contained in the blue and green area versus temperature. An example of distribution is given in inset for the green area. (e) Average thermal dark count α_{th} as the function of the number of photon per modes $\bar{n}$ (Bose-Einstein formula evaluated for the buffer frequency and the fridge temperature). Purple dots are data, solid black line correspond to the theoretical Johnson Nyquist noise.

Conclusion

We have shown in this section that a dark count rate given by the SMPD can be directly converted to temperature via the Johnson Nyquist relation. Several interesting consequences follow from this.

First, we can accurately estimate the effective electromagnetic temperature of our lines by expressing the average occupation number as a function of the dark count. For example, for the first temperature point (refrigerator at 10 mK), we measured $\alpha_{\mathrm{th}} = 133\mathrm{s}^{-1}$ which corresponds to $\bar{n} = 2.5 \cdot 10^{-4}$ and $T = 40.6$ mK.

Second, if we consider the first operating point with better SMPD characteristics, the overall dark count is dominated by the thermal dark count. Indeed, for $T_1 = 37$ μs and $p_{\mathrm{eq}} = 2 \cdot 10^{-4}$, we obtain $\alpha_{\mathrm{qubit}} = 4.5$ s^{-1} much smaller than the overall dark count rate $\alpha_{\mathrm{d}} = 84$ s^{-1}. This means that when our system is operated under the right conditions, its false positive rate and therefore its sensitivity is not limited by internal defects but by our inability to properly attenuate the background microwave field reaching the experiment.

The electromagnetic temperature corresponding to the small thermal false positive rate $\alpha_{\mathrm{th}} = 80$ s^{-1} associated with this operating point is $T = 35.0$ mK and corresponds to an average photon number $\bar{n} = 6.9 \cdot 10^{-5}$.

6.5 SMPD2

6.5.1 Characterisation SMPD2

During my thesis I built a second photon detector called SMPD2. Given the characterization presented in the previous sections, adjustments were necessary in the simulations and fabrication. The kinetic inductance of the tantalum was adjusted in the simulations so that the simulated frequencies matched the measured frequencies. The size of the resonators was then reduced to increase their frequency.

Furthermore, since we had established that the main source of noise is due to thermal photons, we decided to reduce the detector bandwidth. We therefore reduced the coupling between the buffer resonator and its Purcell filter. The simulated coupling loss rate decreased from 1.2 MHz to 0.5 MHz.

The qubit frequency of the SMPD1 was too high. Therefore, we modified the the junction design for reducing the junction area and increase the inductance.

The results of the SMPD2 characterisation are shown in Table 6.3. The resonator frequencies have been readjusted, but for some unknown reason the qubit frequency is similar to that of SMPD1. This shows that the junction fabrication is not fully under control. Furthermore, the relaxation time T_1 of the qubit is now shorter than that of the SMPD1 (15 μs vs 37 μs), which limits the detector efficiency. However, the equilibrium population of the qubit is still extremely low (comparable to that of the SMPD1), which makes this detector fully functional and with similar performances to the SMPD1 in terms of sensitivity.

Qubit	
$\omega_\mathrm{q}/2\pi$	6.193 GHz
$\alpha/2\pi$	~ 240 MHz
$\chi_\mathrm{qb}/2\pi$	3.3 MHz
$\chi_\mathrm{qw}/2\pi$	15.0 MHz
T_1	$\sim 15\,\mu$s
T_2^*	$\sim 28\,\mu$s
p_eq	$\sim 2 \cdot 10^{-4}$

Buffer mode	unbiased	operational
$\omega_\mathrm{b}/2\pi$	7.459 GHz	7.347 GHz
$\kappa_\mathrm{bext}/2\pi$	0.09 MHz	0.41 MHz
$\kappa_\mathrm{bint}/2\pi$	0.13 MHz	0.18 MHz

Waste mode	
$\omega_\mathrm{w}/2\pi$	8.004 GHz
$\kappa_\mathrm{wext}/2\pi$	1.002 MHz
$\kappa_\mathrm{wint}/2\pi$	0.146 MHz

Purcell modes	
$\omega_\mathrm{Pb}/2\pi$	7.303 GHz
$\kappa_\mathrm{Pb}/2\pi$	100 MHz
$\omega_\mathrm{Pw}/2\pi$	7.857 GHz
$\kappa_\mathrm{Pw}/2\pi$	212 MHz

Dark count and efficiency	
α_d	130 s^{-1}
α_qubit	10 s^{-1}
η_d	0.32

Table 6.3: Table of the experimental parameters SMPD2.

Part II

Detection of a single electronic spin of Er^{3+} in CaWO_4 crystal and interaction with the nuclear spin bath

Chapter 7

Overview and theoretical background

Electron spin resonance (ESR) spectroscopy is a magnetic resonance method in which transitions between Zeeman levels of an unpaired electron in a material placed in a magnetic field are detected electromagnetically [SJ01a; Abo+22]. The most common ESR technique is the inductive detection of the signal emitted by electronic spins magnetically coupled to a resonator, often a microwave cavity. The resonance frequency is set by the g factor or tensor of the electron(s), and the resonance line provides information on the local electric field felt by the electron and on its contact or dipolar interactions with nuclear spins in the neighborhood. ESR is a powerful investigation method of transition metal ions in solids, and of free radicals in organic chemistry. The introduction of spin labelling in biological materials has also made ESR a powerful investigative technique in biology. A typical ESR spectrometer in the X band (10 GHz) has a cm-size cavity containing a large number of spins. The inductive detection of ESR is thus not a very sensitive detection method, and gives access to ensemble averaged quantities. Higher detection sensitivities, in the $\mathcal{S} = 10$ spins/$\sqrt{\mathrm{Hz}}$ range, have recently been achieved [Ran+20] using superconducting microwave nanoresonators, in which electronic spins more strongly coupled to the cavity are measured using microwave amplifiers with the minimal noise imposed by quantum mechanics.

Reaching single-spin sensitivity was then a very clear goal in ESR. Achieving this goal by further improving the inductive detection technique developed in our team is certainly possible, but we had also realized that the spin fluorescence detection method we demonstrated in [Alb+21] could offer a better solution, with an equally broad scope of applications on numerous spins. Indeed, although our first spin-fluorescence experiment had only achieved a sensitivity in the $\mathcal{S} = 10^3$ spins/$\sqrt{\mathrm{Hz}}$ range, we thought that its progress margin both on the SMPD side and on the coupling of the spins to a microwave resonator was large enough to justify following this new route.

In this research, my task has been to make a higher sensitivity SMPD, as described in the first part of this thesis. Increasing the radiative emission rate of spins in a resonator beyond the value achieved in our first work [Alb+21], namely $\sim 3.3\ \mathrm{s}^{-1}$, has been the research work of Zhiren Wang during his PhD research. The demonstration of magnetic resonance on a single electronic spin using a method with a broad application range, as is spin fluorescence, is the object of the second part of this thesis. For our proof of concept experiment on single spin ESR, we have chose a particular spin platform, erbium spins in calcium tungstate ($\mathrm{CaWO_4}$), described below.

Let us nevertheless mention here that magnetic resonance on a single electronic spin has already been performed using specific methods. The Optically detected Magnetic Resonance (ODMR) technique has achieved major successes on numerous spins, NV centres being the most famous ones [Wra+93; Gru+97; Rah+20]. In this method, optical transitions are used to perform optical pumping and to determine the spin state of a paramagnetic impurity. Transport measurements [Elz+04; Vin+12; Pla+12; Thi+14] and scanning-probe techniques have also reached single-spin sensitivity. It is nevertheless fair to state that these methods are system specific and do not apply to a broad range of electronic spins. Optical transitions are in particular requested for ODMR. On the contrary, our method has the potential to apply to arbitrary paramagnetic species with long enough non-radiative relaxation time. In addition, the volume of detection given the resonator magnetic mode volume can be several orders of magnitude larger than other specific single-spin detection techniques.

7.1 An appealing spin platform: erbium ions in Scheelite

The choice of erbium spins in Scheelite is based on several criteria. The first is related to the high g-factor that can be achieved for erbium ions in this matrix, which increases the radiative emission rate in a superconducting resonator coupled to the spins. Furthermore, the $CaWO_4$ matrix has a low level of internal magnetic noise. The main source of fluctuation comes from the tungsten atoms with the isotope ^{183}W (0.145 natural abundance) which has a nuclear spin 1/2. Due to this low abundance combined with a relatively small gyromagnetic ratio $\gamma_W/2\pi = 1.78$ kHz/mT, $CaWO_4$ is one of the most magnetically-silent materials that can be found and is therefore well-suited to host long-coherence times electron spins [Kan+22]. This platform was indeed recently considered as well suited for applications in quantum information [Sag+15] .

Erbium, a lanthadide atom, forms a spins tripositive ion when incorporated in a solid such as scheelite. Its electronic structure: $1s^2 2s^2 2p^6 3s^2 3p^6 4s^2 3d^{10} 4p^6 5s^2 4d^{10} 5p^6 4f^{N_e}$ where $N_e \in [0, 14]$ is the number of electron in the $4f$ electronic layer ($N_e = 11$ for the erbium). The radial probability distribution of the Er^{3+} shells from the 1s to the 6s is shown in Figure 7.1, where the colored curves correspond to populated orbitals. The $4f$ orbital being spatially closer to the nucleus than the $5s$ and $5p$ orbitals, the electrons in this layer are shielded and do not participate in the chemistry. They are thus not very sensitive to electromagnetic disturbances due to sources out of the atom, noticeably the crystal field.

For this reason, the electronic level structure of the erbium ion can be first approximated by the free-ion energy levels. The interactions in the scheelite crystal will be then treated as a perturbation.

7.1.1 Free erbium ion energy level

To describe the free erbium ion Hamiltonian, we use the central field approximation [Wei83]. In this framework, the Hamiltonian can be decomposed into 3 terms:

$$H_{\mathrm{FI}} = H_0 + H_{\mathrm{NC}} + H_{\mathrm{SO}}, \tag{7.1}$$

which we will detail:

$$H_0 = -\sum_{i=1}^{11} \left[\frac{\hbar^2}{2m} \nabla_i^2 + U(r_i) \right] \tag{7.2}$$

is the sum of the kinetic energy of the electrons with a potential energy function $U(r_{\mathrm{i}})$. This function approximates the potential energy of the electron i in the field generated by the nucleus and the 10 other electrons such that:

$$\sum_{i=1}^{11} U(r_i) = -\sum_{i=1}^{N} \frac{Ze^2}{r_i} + \langle \sum_{i<j}^{N} \frac{e^2}{r_{ij}} \rangle, \tag{7.3}$$

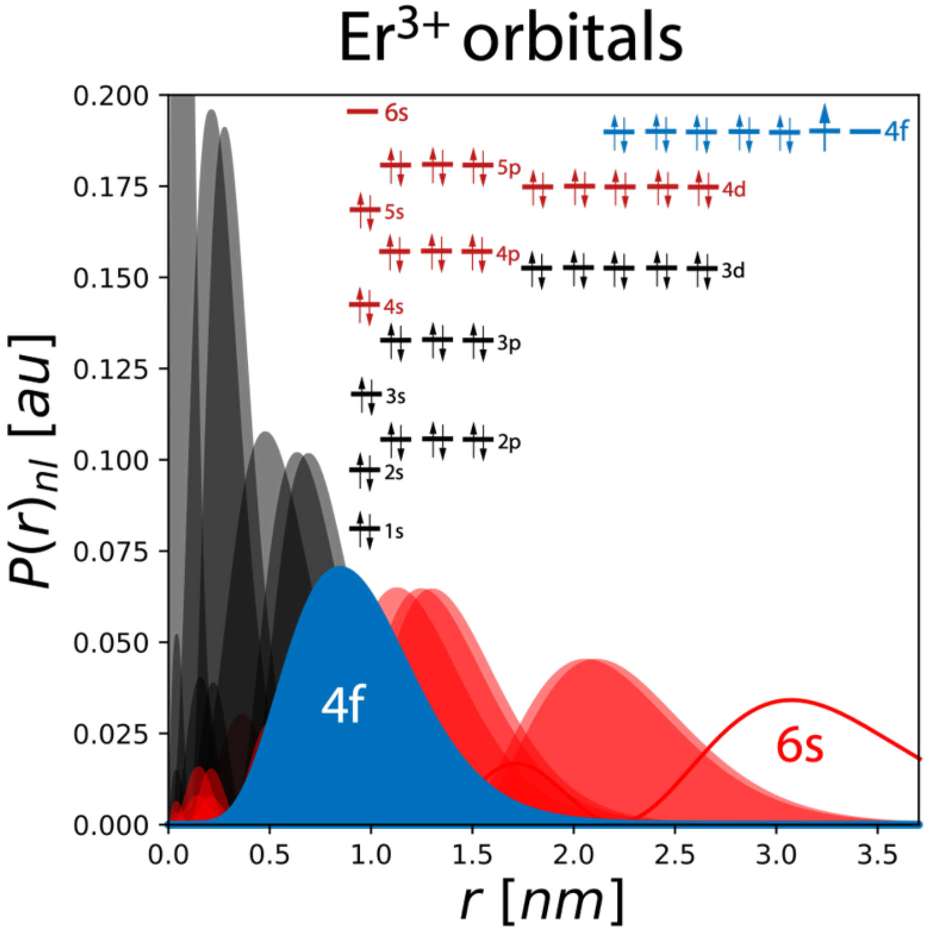

Figure 7.1: **Electronic shell distribution for** Er^{3+}. Electron probability of presence as the function of the radial distance r to the nucleus.

where the right term represents the spherical averaged coulomb term and includes most of the inter electron repulsion.

Therefore, the term H_0 describes the independent motion of the 11 electrons. The Schrödinger equation can be solved independently for each of them. Furthermore, as $U(r_\mathrm{i})$ has spherical symmetry, each electron can be described in the same way as the hydrogen atom, the electron state being described by the usual 4 quantum numbers. The principal quantum number n which represents the electron shell, the angular momentum l $(0 \leq l < n-1)$, the magnetic quantum number m_l $(-l \leq m_\mathrm{l} \leq l)$ and finally the spin quantum number $m_\mathrm{s} \pm 1/2$. In the following, we will focus on the $n = 4$, $l = 3$ configuration which corresponds to the $4f$ layer.

The second term of the free ion Hamiltonian:

$$H_\mathrm{NC} = \sum_{i<j}^{11} \frac{e^2}{r_{ij}} - \langle \sum_{i<j}^{11} \frac{e^2}{r_{ij}} \rangle \tag{7.4}$$

is the remaining part of the Coulomb potential and represents the electron-electron interaction not taken into account in $U(r_\mathrm{i})$.

Finally, the last term is the spin-orbit interaction:

$$H_{\mathrm{SO}} = \sum_{i=1}^{11} \xi(r_{\mathrm{i}}) \boldsymbol{l}_{\mathbf{i}} . \boldsymbol{s}_{\mathbf{i}} \tag{7.5}$$

In the case of the erbium ion, the two Hamiltonian H_{NC} and H_{SO} are typically of same magnitude. They can be treated together as a perturbation of H_0 using the so-called intermediate coupling scheme [JL05]. This model introduces the operator $\boldsymbol{J} = \boldsymbol{L} + \boldsymbol{S}$ with $\boldsymbol{L} = \sum_i^{11} \boldsymbol{l_i}$ and $\boldsymbol{S} = \sum_i^{11} \boldsymbol{s_i}$. It defines another good quantum number J such that $\hbar J(J+1)$ is an eigenvalue of $\boldsymbol{J}^2$. The energy levels end up being $(2J+1)$ degenerate multiplets. The ground state of the free erbium ion corresponds to $J = 15/2$ with $L = 6$ and $S = 3/2$ yielding to a 16 times degenerate level. The fist excited state is defined by $J = 13/2$ and $L = 5$, the transition between the two states is an optical transition at 1.5 μm. As the sample is placed in a dilution fridge at 10 mK, the ground state is fully polarized.

7.1.2 Crystal field and effective spin 1/2

When the ion is embedded in the crystal, it is subjected to an electric field produced by its surroundings which breaks the spherical symmetry of the electronic structure described in the previous section. However, as the electrons of the 4f layer interact little with the environment, the crystal-field can be considered as a perturbation which lifts the $(2J+1)$ degeneracy of the multiplets.

The Kramers theorem [Kra30] based on the time reversal symmetry states that the degeneracy is fully or partially lifted in function of the number of electrons considered. In the case on an odd number, the multiplet splits into the so-called "Kramers doublet" twice degenerated. For the erbium ground state, the level splits into 8 doublets (labeled $Z_1 ... Z_8$). The energy scale between Z_1 and Z_2 is 0.57 THz for erbium in $\mathrm{CaWO_4}$ crystal [Enr71]. The ground state Z_1 is thus fully polarized at 10 mK.

The last degeneracy can be lifted by applying a magnetic field $\mathbf{B}_0$ to the system. The doublet is then split by the Zeeman Hamiltonian:

$$H_Z = \mu_{\mathrm{B}} \boldsymbol{B_0} \cdot (\boldsymbol{L} + \mathrm{g}_s \boldsymbol{S}) = \mathrm{g}_J \mu_{\mathrm{B}} \boldsymbol{B_0} \cdot \boldsymbol{J}, \tag{7.6}$$

where μ_{B} is the Bohr magneton, $\mathrm{g}_s = 2$, and g_J is the Landé g-factor. For the erbium ion ground state doublet, the Landé g-factor is $\mathrm{g}_J = 6/5$.

This Zeeman interaction can be interpreted as the interaction between a magnetic field $\boldsymbol{B_0}$ and a spin 1/2 with an anisotropic g-factor. This approximation remains valid in the limit when the Zeeman splitting is small compared to the gap between Kramers levels. In this case the Zeeman interaction can be expressed as:

$$\hat{H}_{\mathrm{Z}} = \mu_B \boldsymbol{B_0} \cdot \mathbf{g} \cdot \hat{\boldsymbol{S}} = \mu_B \begin{pmatrix} B_x & B_y & B_z \end{pmatrix} \begin{pmatrix} \mathrm{g}_{xx} & \mathrm{g}_{xy} & \mathrm{g}_{xz} \\ \mathrm{g}_{yx} & \mathrm{g}_{yy} & \mathrm{g}_{yz} \\ \mathrm{g}_{zx} & \mathrm{g}_{zy} & \mathrm{g}_{zz} \end{pmatrix} \begin{pmatrix} \hat{S}_x \\ \hat{S}_y \\ \hat{S}_z \end{pmatrix} \tag{7.7}$$

where $\hat{S}_{\mathrm{i}} = 1/2 \hat{\sigma}_{\mathrm{i}}$ are the effective spin operators defined from the Pauli matrix (see Section 3.3).

The sequence of the different mechanisms that lift level degeneracy is shown in Figure 7.2.

In this thesis we will only consider erbium isotopes that do not possess a nuclear spin ($^{164}\mathrm{Er}$,$^{166}\mathrm{Er}$,$^{168}\mathrm{Er}$,$^{170}\mathrm{Er}$). They represent 77% of the natural erbium. We will therefore remain at this level of description for the interaction Hamiltonian between the magnetic field and the ion. The reader can find a more precise account of the general properties of erbium in [Dan22].

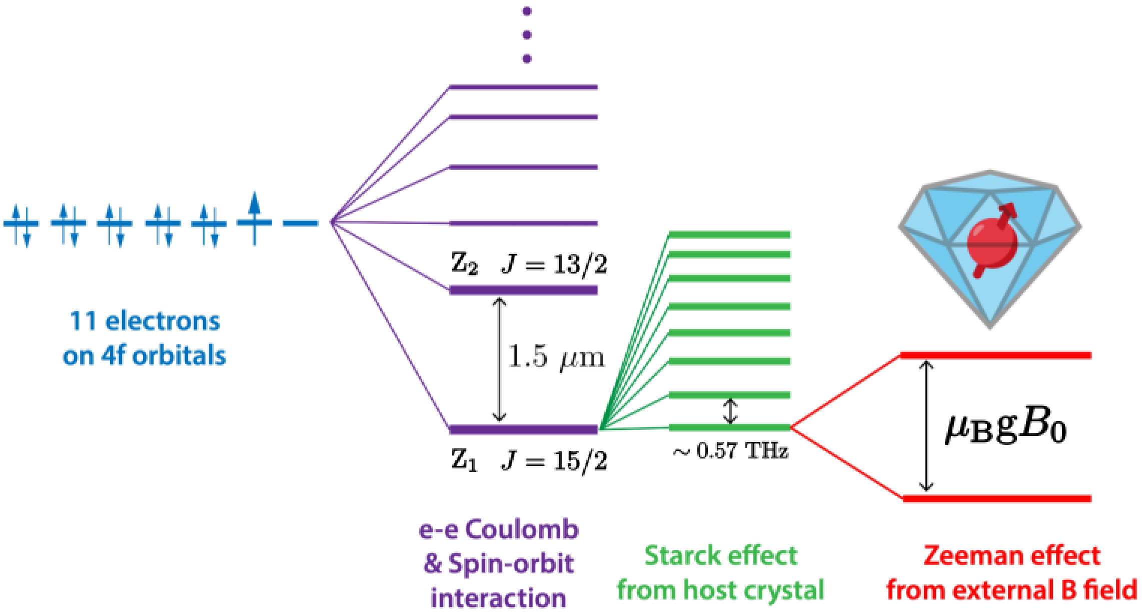

Figure 7.2: **Energy levels of** Er^{3+} **embedded in** $\mathrm{CaWO_4}$ **crystal**. The 11 electrons of the $4f$ orbital form $2J + 1$ degenerate multiplets in the intermediate coupling scheme (purple levels). The crystal field lifts the degeneracy of the ground state multiplet into 8 doubly degenerate Kramers levels (green levels). These levels behave as effective spin 1/2 whose degeneracy can be lifted by a magnetic field (red levels). The energy difference $\mu_{\mathrm{b}} \mathrm{g} B_0$ depend on the magnetic field orientation.

7.1.3 Effective Hamiltonian of $\mathrm{Er}^{3+}(\mathrm{I} = 0)$ in $\mathrm{CaWO_4}$

In this section we focus on the $\mathrm{CaWO_4}$ properties and the description of the effective spin Hamiltonian.

7.1.3.1 $\mathrm{CaWO_4}$ crystal properties

The calcium tungstate crystal, represented in Figure 7.3, has a tetragonal structure with lattice parameters $a = b = 0.524$ nm and $c = 1.138$ nm. In this crystalline structure, impurity erbium ions Er^{3+} substitute to calcium ions Ca^{2+}. This substitution implies a modification of the charge from a 2+ to a 3+. A charge compensation therefore inevitably takes place during the growth of the crystal, for example by the appearance of calcium vacancies [MG67]. This rebalancing phenomenon is random and can occur at any point in the crystal, which generates a random inhomogeneous electric field. The local electromagnetic environment of each ion is therefore slightly different, which has consequences on its properties (frequency, coherence...).

If we consider a calcium site in the lattice as shown in Figure 7.3, we can observe that the composition of a 90° rotation along the c-axis and a reflection in the (a,b) plane leaves the site unchanged. This symmetry, called S4, will shape the crystal-field. As a consequence, the **g**-tensor of the erbium ion involved in Equation 7.7 also respects this symmetry. It is diagonal in the (a, b, c) basis, with identical components is the (a, b) plane ($\mathrm{g_a} = \mathrm{g_b} = \mathrm{g_\perp} = 8.38$), and a different value along the c-axis ($\mathrm{g_c} = \mathrm{g_{||}} = 1.247$) [WB64]. The **g**-tensor takes remarkably large values in the (a, b) plane, 4 times larger than the

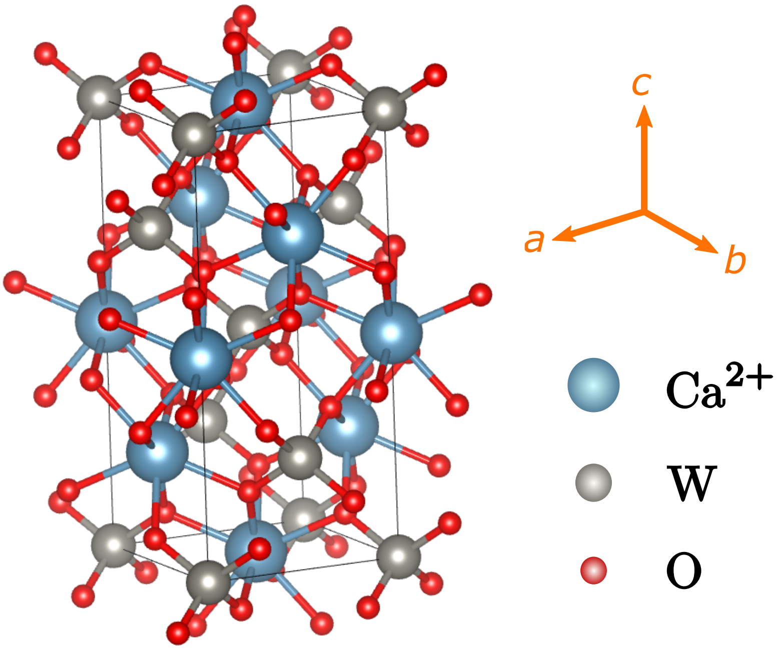

Figure 7.3: $CaWO_4$ **crystal structure**. Schematic of the $CaWO_4$ lattice showing a tetragonal structure, with a rotational symmetry around the c-axis

g-factor of the free electron $g_e = 2$.

7.1.3.2 Er^{3+} spin Hamiltonian

Following the previous discussion, the **g**-tensor of erbium in calcium tungstate is diagonal in the (a, b, c) base. Its expression is given by:

$$\mathbf{g} = \begin{pmatrix} g_\perp & 0 & 0 \\ 0 & g_\perp & 0 \\ 0 & 0 & g_\parallel \end{pmatrix}_{(a,b,c)} = \begin{pmatrix} 8.38 & 0 & 0 \\ 0 & 8.38 & 0 \\ 0 & 0 & 1.247 \end{pmatrix}_{(a,b,c)} . \tag{7.8}$$

The Hamiltonian Equation 7.7 can be write with this **g**-tensor for a given magnetic field $\boldsymbol{B_0}$ expressed in spherical coordinates. The expansion of the scalar product gives:

$$\hat{H}_s = \mu_B B_0 (g_\perp \sin\theta \cos\varphi \hat{S}_x + g_\perp \sin\theta \sin\varphi \hat{S}_y + g_\parallel \cos\theta \hat{S}_z), \tag{7.9}$$

where θ and φ characterize the magnetic field orientation. Because of the axial symmetry around the c-axis, we can take $\varphi = 0$ without loss of generality. By rearranging the terms, the spin Hamiltonian reads:

$$\hat{H}_s = g_{\text{eff}} \mu_B B_0 \hat{S}'_z \tag{7.10}$$

with:

$$\begin{aligned} g_{\text{eff}} &= \sqrt{(g_\perp \sin\theta)^2 + (g_\parallel \cos\theta)^2} \\ \hat{S}'_z &= \hat{S}_z \cos\theta' + \hat{S}_x \sin\theta' \\ \sin\theta' &= \sin\theta \times g_\perp / g_{\text{eff}} \\ \cos\theta' &= \cos\theta \times g_\parallel / g_{\text{eff}} \end{aligned} \tag{7.11}$$

The eigenstates of the spin Hamiltonian are the eigenstates of the operator $\hat{S}'_z$ with quantization axis along θ'. Note that contrarily to the case with an isotropic g-factor, the quantification axis is not along the direction of $\boldsymbol{B_0}$. Nevertheless, except for this subtlety, we can consider that an ion Er^{3+} in $\mathrm{CaWO_4}$ simply behaves as a spin 1/2 .

7.1.4 Magnetic dipole-dipole interaction with $^{183}\mathrm{W}$

As already stated earlier, the nuclear spin bath in the $\mathrm{CaWO_4}$ is dominated by the contribution of the nuclear spins $I = 1/2$ of the $^{183}\mathrm{W}$ nuclei. These weak magnetic dipoles create a fluctuating magnetic field that induces dephasing of the electronic spins. On the other hand, this coupling could allow us to control the quantum state of nuclear spins, as demonstrated for NV centers in diamond [Tam+12].

Let us detail the magnetic dipole-dipole interaction between the electronic spin of a Er^{3+} ion and the $^{183}\mathrm{W}$ nuclear spins in its neighborhood.

The coupling Hamiltonian is given by [AB12]:

$$\hat{H}_{\mathrm{dd}} = \frac{\mu_0}{4\pi} r^{-3} [\hat{\boldsymbol{\mu}}_{\mathbf{S}} \cdot \hat{\boldsymbol{\mu}}_{\mathbf{I}} - 3r^{-2} (\hat{\boldsymbol{\mu}}_{\mathbf{S}} \cdot \boldsymbol{r})(\hat{\boldsymbol{\mu}}_{\mathbf{I}} \cdot \boldsymbol{r})] \tag{7.12}$$

where $\hat{\boldsymbol{\mu}}_{\mathbf{S}} = \mu_{\mathrm{B}} \mathbf{g} \cdot \hat{\boldsymbol{S}}$ is the magnetic moment operator of the electronic spin and $\hat{\boldsymbol{\mu}}_{\mathbf{I}} = \mu_{\mathrm{N}} \mathrm{g_W} \hat{\boldsymbol{I}}$ that of the nuclear spin. μ_{N} is the nuclear magneton and $\mathrm{g_W}$ the g-tensor of the tungsten. Note that unlike erbium, this tungsten g-tensor is isotropic. Finally, $\mathbf{r} = (r_{\mathrm{x}}, r_{\mathrm{y}}, r_{\mathrm{z}})$ is the distance vector between the spins.

In all generality, this expression is complicated, however, like the magnetic moment of the nuclear spin is $\sim 4-5$ orders of magnitude (depending on the field orientation) lower than that of the electronic spin, it changes little the quantization axis of the latter. We can thus perform the so-called secular approximation and consider that only $\hat{S}'_{\mathrm{z}}$ has to be considered in the coupling Hamiltonian. The expression of $\hat{H}_{\mathrm{dd}}$ reduces to:

$$\hat{H}_{\mathrm{dd}} = A\hat{S}'_z\hat{I}''_z + B\hat{S}'_z\hat{I}''_x + C\hat{S}'_z\hat{I}''_y \tag{7.13}$$

where A, B and C are constant depending of the $\mathbf{g}$-tensor and the distance $\mathbf{r}$ between the spins. The signs $'$ and $''$ stress the fact that for an arbitrary orientation of the magnetic field, the spins do not share the same quantization axis.

In the following, we assume for simplicity that the magnetic field and therefore the electron spin are aligned along the c-axis corresponding to the z-axis of the frame. In this case, Equation 7.13 becomes:

$$\hat{H}_{\mathrm{dd}} = \frac{\mu_0 \mu_{\mathrm{B}} \mu_{\mathrm{N}}}{4\pi r^3} \hat{S}_{\mathrm{z}} \mathrm{g}_{\|} \mathrm{g_W} \left(3\frac{r_{\mathrm{z}}}{r^2} [\hat{I}_{\mathrm{x}} r_{\mathrm{x}} + \hat{I}_{\mathrm{y}} r_{\mathrm{y}}] + \hat{I}_{\mathrm{z}} [3\frac{r_{\mathrm{z}}^2}{r^2} - 1] \right) \tag{7.14}$$

that we can write:

$$\hat{H}_{\mathrm{dd}} = \hat{S}_{\mathrm{z}} \boldsymbol{A}_{\mathrm{hyp}} \cdot \hat{\boldsymbol{I}} \tag{7.15}$$

with:

$$\boldsymbol{h} = \frac{1}{r\sqrt{3r_{\mathrm{z}}^2 + r^2}} (3r_{\mathrm{x}} r_{\mathrm{z}}, 3r_{\mathrm{y}} r_{\mathrm{z}}, 3r_{\mathrm{z}}^2 - r^2) \tag{7.16}$$

$$\boldsymbol{A}_{\mathrm{hyp}} = \frac{\mu_0 \mu_{\mathrm{B}} \mu_{\mathrm{N}} \mathrm{g}_{\|} \mathrm{g_W}}{4\pi r^3} \cdot \frac{1}{r} \sqrt{r_{\mathrm{z}}^2 - r^2} \cdot \boldsymbol{h} \tag{7.17}$$

In order to get a clearer idea of the behaviour of Equation 7.15, we can perform a change of reference frame. We keep the same z-axis which is the direction of the magnetic

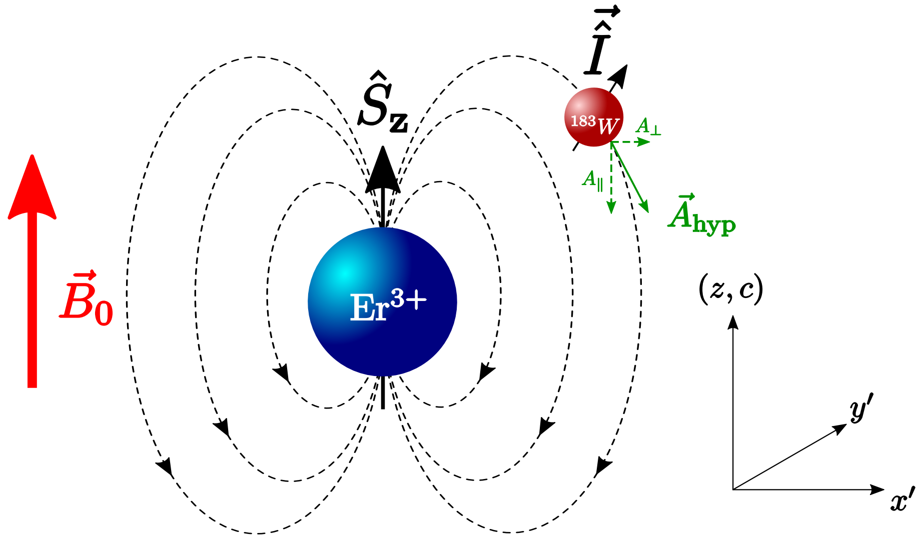

Figure 7.4: **Magnetic dipole-dipole interaction between an** Er^{3+} **spin and a** $^{183}\mathrm{W}$ **nuclear spin**. The magnetic field $\boldsymbol{B}_0$ is directed along the z-axis corresponding to the crystallographic axis c. The magnetic moment Er^{3+} is thus also along z. The $^{183}\mathrm{W}$ nuclear spin is perturbed by the field generated by the electronic spin (dotted lines). Its magnetic moment is no longer oriented along the z-axis, but is deflected by the dipole-dipole interaction represented by $\boldsymbol{A}_{\mathbf{hyp}}$. The frame is defined such that $\boldsymbol{A}_{\mathbf{hyp}}$ is in the $(z, x^{'})$ plane.

field. We then define $y^{'}$-axis perpendicular to $\boldsymbol{A}_{\mathbf{hyp}}$ and we complete the orthonormal frame with the $x^{'}$-axis (see Figure 7.4).

In this new frame $\boldsymbol{A}_{\mathrm{hyp}}$ only has two components : $\boldsymbol{A}_{\mathrm{hyp}} = (\hbar A_\perp, 0, \hbar A_\parallel)$. The expressions of $A_\perp$ and $A_\parallel$ can be easily calculated from Equation 7.17. The secular part of the dipolar Hamiltonian takes the simple form:

$$\hat{H}_{\mathrm{dd}}/\hbar = \hat{S}_{\mathrm{z}}(A_\perp \hat{I}_{\mathrm{x}} + A_\parallel \hat{I}_{\mathrm{z}}). \tag{7.18}$$

In the case where the magnetic field is not aligned with the c-axis, the form of the dipolar Hamiltonian expressed in Equation 7.18 remains valid. We can always define a reference frame from the hyperfine vector $\boldsymbol{A}_{\mathbf{hyp}}$ and the magnetic field so that $\boldsymbol{A}_{\mathbf{hyp}}$ is in the (z,x) plane and can be expressed as $\boldsymbol{A}_{\mathrm{hyp}} = (\hbar A_\perp, 0, \hbar A_\parallel)$.

7.1.5 Resonance linewidth

Each spin in the crystal has its own environment, notably due to charge compensation. This leads to both an inhomogeneous broadening of the ESR line due to the distributed static part of the crystal field, and to an homogeneous broadening due to the dynamical part.

homogenous broadening

The dynamics of the nuclear spin bath also produces a fluctuating field that contributes to homogeneous broadening of the ESR line, i.e. to dephasing of the erbium spins at a rate Γ_{h} given by the spectral density of the fluctuating field at low frequency.

inhomogenous broadening

In a crystal, the inhomogeneous broadening Γ_{inh} of the spin line is generally much larger than the homogeneous one given by Γ_{h}.

The local perturbation of the spin environment can be related to the dipole interaction with nuclear spins or paramagnetic impurities. These magnetic dipoles disturb the $\boldsymbol{B_0}$ field felt by the electron spin and thus shift its frequency. However, as we consider a very dilute crystal, the density of impurities is low, and it can be shown that the broadening due to dipole coupling is of the order of 100 kHz.

The other broadening mechanism is due to the electric field inhomogeneity caused by the charge compensation. In principle, due to the time reversal symetry of Kramers doublet, electric field do not induce Stark shift. However, when a magnetic field is applied, this symmetry is broken and the electric field can modify the **g**-tensor [Kie66] causing a static frequency shift. This effect was measured by Mims and Gillen [Mim65] and is the dominant source of inhomogeneous broadening. Indeed, the measured inhomogenous bandwith is $\Gamma_{\text{inh}} \approx 8$ MHz which is much larger than the contribution due to the magnetic dipole interaction.

7.2 Single Er^{3+} coupled to a cavity

In this section we describe the coupling between a lumped element resonator (see Section 3.1.2) called the "spin resonator" and a single spin.

We first describe theoretically the spin-resonator system in all generality. Then we discuss the characteristics of the crystal used in the experiment and the resonator geometry. This geometry determines the magnetic field $\boldsymbol{B_1}(\boldsymbol{r})$ produced by the current flowing in the resonator wire-inductor, and thus the spin-resonator coupling. Finally we describe the interaction between the environment and the system.

7.2.1 System Hamiltonian

The Hamiltonian of system is:

$$\hat{H} = \hat{H}_{\text{r}} + \hat{H}_{\text{s}} + \hat{H}_{\text{int}} = \hbar\omega_0(\hat{a}^\dagger\hat{a} + \frac{1}{2}) - \mu_{\text{B}}\mathbf{g}\cdot\hat{\boldsymbol{S}}\cdot\boldsymbol{B_0} + \hat{H}_{\text{int}} \tag{7.19}$$

with ω_0 the spin resonator frequency. The spin Hamiltonian $\hat{H}_{\text{s}} = -\mu_{\text{B}}\mathbf{g}\cdot\hat{\boldsymbol{S}}\cdot\boldsymbol{B_0}$ can be expressed as the function of the energy difference between the two spin level such as $\hat{H}_{\text{s}} = \hbar\omega_{\text{s}}/2\hat{\sigma}_{\text{z}}$ with $\omega_{\text{s}}/2\pi$ the spin frequency and z the direction of quantization (not necessary aligned with $\boldsymbol{B_0}$).

The interaction Hamiltonian $\hat{H}_{\text{int}}$ involves the magnetic field $\hat{\boldsymbol{B}}_{\boldsymbol{1}}(\boldsymbol{r})$ generated by the resonator. As described in Section 3.1.1, one can express $\boldsymbol{B_1}(\boldsymbol{r})$ in function of the magnetic field vacuum fluctuations such as $\hat{\boldsymbol{B}}_{\boldsymbol{1}}(\boldsymbol{r}) = \boldsymbol{\delta B}(\boldsymbol{r})(\hat{a}^\dagger + \hat{a})$. With this expression, $\hat{H}_{\text{int}}$ reads:

$$\hat{H}_{\text{int}} = \mu_B\hat{\boldsymbol{B}}_{\boldsymbol{1}}\cdot\mathbf{g}\cdot\hat{\boldsymbol{S}} = \mu_B\boldsymbol{\delta B}\cdot\mathbf{g}\cdot\hat{\boldsymbol{S}}(\hat{a} + \hat{a}^\dagger) \tag{7.20}$$

where we have omitted the spatial dependent for readability. This expression can be developed in the $|g\rangle, |e\rangle$ basis as:

$$\hat{H}_{\text{int}} = \hbar(\hat{a} + \hat{a}^\dagger)[\alpha_e |e\rangle\langle e| + \alpha_g |g\rangle\langle g| + g_0\hat{\sigma}^\dagger + g_0^*\hat{\sigma}] \tag{7.21}$$

where

$$\begin{aligned} \alpha_e &= \frac{\mu_B}{\hbar}\boldsymbol{\delta B}\cdot\mathbf{g}\cdot\langle e|\hat{\boldsymbol{S}}|e\rangle, &\qquad \alpha_g &= \frac{\mu_B}{\hbar}\boldsymbol{\delta B}\cdot\mathbf{g}\cdot\langle g|\hat{\boldsymbol{S}}|g\rangle \\ g_0 &= \frac{\mu_B}{\hbar}\boldsymbol{\delta B}\cdot\mathbf{g}\cdot\langle e|\hat{\boldsymbol{S}}|g\rangle, &\qquad g_0^* &= \frac{\mu_B}{\hbar}\boldsymbol{\delta B}\cdot\mathbf{g}\cdot\langle g|\hat{\boldsymbol{S}}|e\rangle \end{aligned} \tag{7.22}$$

By writing Equation 7.21 in the interaction picture with respect to $\hat{H}_0 = \hat{H}_\mathrm{s} + \hat{H}_\mathrm{r}$, we can apply the rotating wave approximation which only preserves the term of the form $\hat{a}\hat{\sigma}^\dagger$ and $\hat{a}^\dagger\hat{\sigma}$. By assuming for simplicity that $g_0 = g_0^*$, the expression of the interaction Hamiltonian is:

$$\hat{H}_\mathrm{int} = g_0(\hat{a}\hat{\sigma}^\dagger + \hat{a}^\dagger\hat{\sigma}) \tag{7.23}$$

This term describe the exchange between a resonator photon and a spin excitation controlled by coupling strength:

$$\boxed{g_0 = \frac{\mu_B}{\hbar}\boldsymbol{\delta B}\cdot\mathbf{g}\cdot\langle e|\,\hat{\boldsymbol{S}}\,|g\rangle} \tag{7.24}$$

7.2.2 Spin-resonator sample

7.2.2.1 Host crystal

The $CaWO_4$ crystal used in experiment originates from a boule grown by the Czochralski method from $CaCO_3$ (99.95% purity) and WO_3 (99.9 % purity). The sample we use was cut from the boule into parallelepipedic pieces (7 mm × 4 mm × 0.5 mm). The surface (4 mm × 0.5 mm) of the parallelepiped is approximately in the (ac) crystallographic plane, and the c-axis is parallel to its great length Figure 7.5a.

This sample has already been characterized by ESR during the PhD research of Marianne Le Dantec [Dan22]. Its erbium ion concentration is 3.1 ± 0.2 ppb. Given the lattice parameters, this yields an average distance of ~ 300 nm between neighboring erbium ions.

7.2.2.2 Superconducting resonator

The resonator described here is patterned in a niobium layer deposited at the surface of the $CaWO_4$ crystal piece. It was made by Zhiren Wang, and more information about its fabrication procedure can be found in his PhD thesis.

The resonator is designed for strongly coupling hundreds of spins to it. As discussed in Section 7.2.1, the spin-resonator coupling g_0 scales as the magnetic fluctuations $\boldsymbol{\delta B}$ generated by the current fluctuation in the resonator $\delta I = \omega_0\sqrt{\hbar/(2Z_\mathrm{c})}$ with $Z_\mathrm{c} = \sqrt{L/C}$ the characteristic impedance of the circuit. A low impedance resonator is needed for maximizing the zero point fluctuations $\boldsymbol{\delta B}$ and the spin resonator coupling.

This is achieved by placing an interdigitated capacitor C, as sketched in Figure 7.5b, in parallel with an inductive nanowire, as sketched in Figure 7.5c. This nanowire, placed at the center of the resonator, is 600 nm-wide and 94 μm-long and parallel to the c-axis of the crystal. Figure 7.6 shows optical and SEM micrographs of the resonator used in our experiments.

7.2.2.3 Coupling strength estimation

In this section we give some orders of magnitude for the value g_0. To simplify the discussion, we consider the nanowire as a cylinder of radius $a = 300$ nm and length $L = 94$ μm (see Figure 7.7a). Since the nanowire is approximately aligned along the crystal c-axis (see Figure 7.5), its current generates a magnetic field in the (ab) plane. The Biot-Savard gives $\boldsymbol{B}_\perp = \mu_0\frac{I}{2\pi r} < \mu_0\frac{I}{2\pi a}$ assuming a homogeneous current in the wire.

The magnetic fluctuation can then be write as the function of the resonator parameters for $r > a$:

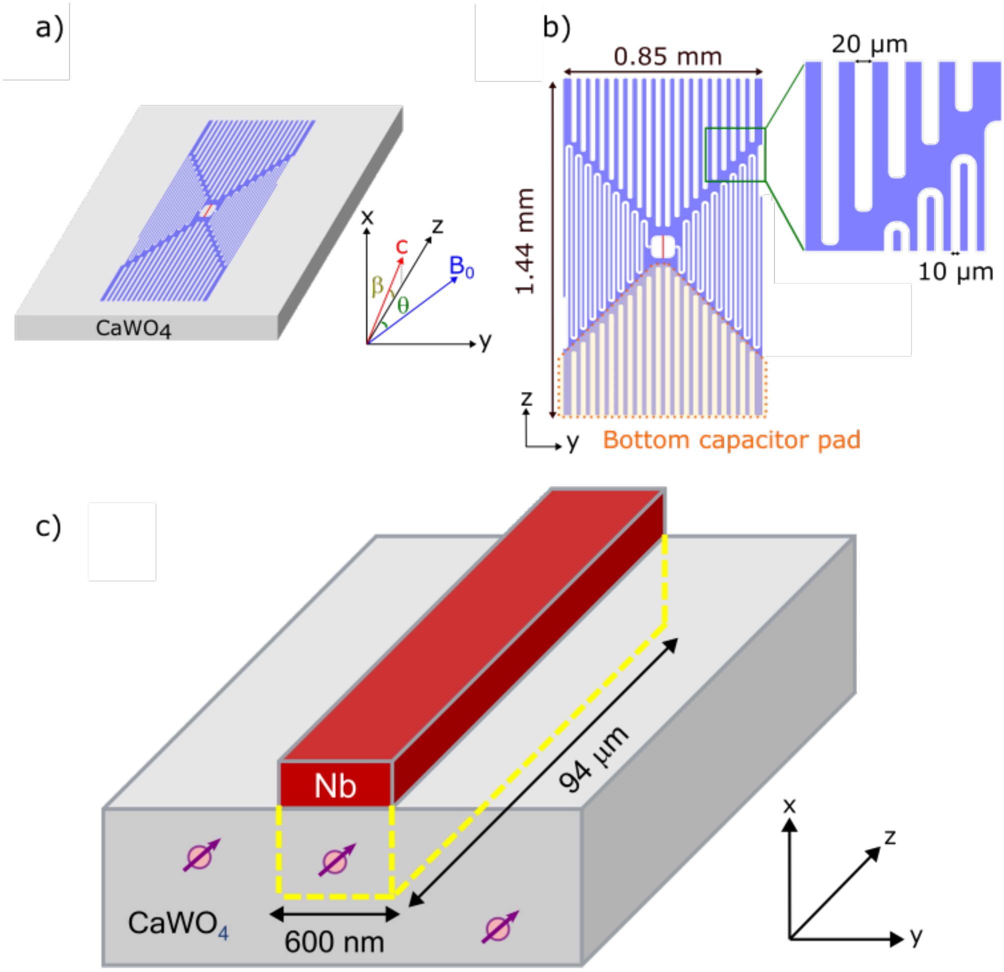

Figure 7.5: **Spin resonator design**. (a) $CaWO_4$ parallepided (grey) with the superconducting resonator patterned in a niobium layer on top. The *c*-axis is approximately along the z-direction (parallel to the wire) while the (*ab*) crystallographic plane corresponds to the (x, y) plane. (b) Resonator design, the wire is surrounding by two symmetric interdigitated capacitors on the left and right. The top and bottom capacitor pads are antennas used to maximize the coupling with the output line. (c) Schematic of the nanowire (red). The zone delimited by the dashed yellow line correspond to the addressable spins.

$$|\boldsymbol{\delta B}(\boldsymbol{r})| = \mu_0 \frac{\delta I}{2\pi r} = \mu_0 \frac{\omega_0}{2\pi r}\sqrt{\frac{\hbar}{2\mathrm{Z}_0}}. \tag{7.25}$$

which yields to the following expression of the spin-resonator coupling :

$$g_0(r) = \frac{\mathrm{g}_\perp \mu_B}{\hbar}\delta B_1(r)\,\langle e|\,\hat{S}\,|g\rangle = \frac{\mathrm{g}_\perp \mu_B}{\hbar}\mu_0 \frac{\omega_0}{2\pi r}\sqrt{\frac{\hbar}{2\mathrm{Z}_0}}0.5. \tag{7.26}$$

We then fill this expression with the parameters of our experience. The resonator frequency is $\omega_0/2\pi \approx 7$GHz, its impedance $Z_0 \approx 17.5\,\Omega$ and the perpendicular Landé factor is $\mathrm{g}_\perp \approx 8$.

In the case of a spin located just next to the wire ie with $r = 300$ nm we obtain $g_{0,\max}/2\pi = 2.8$ kHz. This value has to be compared with the typical damping rate of our

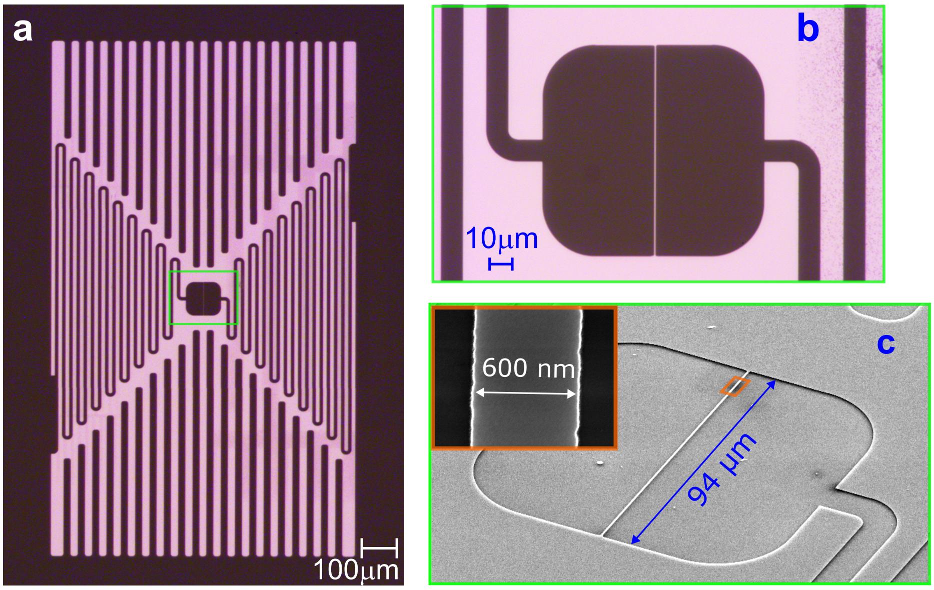

Figure 7.6: **Fabrication images of the spin-resonator**. (a) and (b) optical images of the resonator. The nanowire is visible on (b). (c) Picture of the nanowire taken with a SEM.

microwave resonator: $\kappa_t/2\pi \sim 500$ kHz. As $g_{0,\mathrm{max}} \ll \kappa_t$ we will work in the weak coupling regime (see Section 3.5.1).

7.2.2.4 Distribution of spin as a function of coupling

In this section, we estimate the distribution of spins as a function of their coupling.

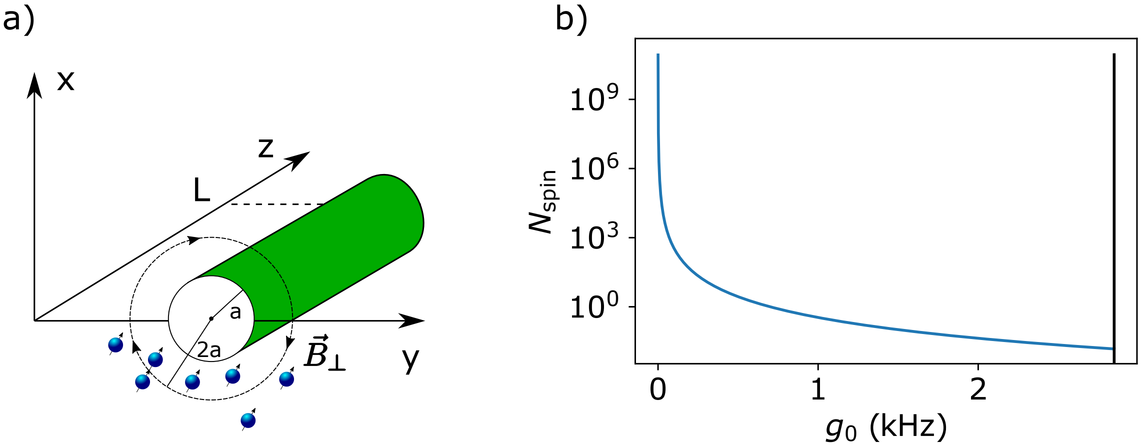

Figure 7.7: **Detectable spins and coupling strengt simulation**.(a) Simplified wire model for estimating the number of addressable spins contained in the half-shell bounded by a and $2a$. (b) Density of spin N_{spin} as the function of the coupling constant g_0. Vertical black line represents $g_{0,\mathrm{max}} = 2.8$ kHz

The number of spins whose coupling is within the range: $g_{0,\mathrm{max}} > g > g_0$ can be written as:

$$N_{\mathrm{spin}}(g_{0,\max} > g > g_0) = \frac{\rho L \pi}{2}\left(r(g=g_0)^2 - a^2\right) \tag{7.27}$$

with $\rho = 1 \cdot 10^{19}$ m^{-3} the concentration of erbium ion in the crystal. Here we only consider the spins in the half-shell below the (zy) plan (see: Figure 7.7a).

The density of spin $N_{\mathrm{spin}}(g_0)$ is obtained by deriving Equation 7.27 as the function of g_0. As shown on Figure 7.7b, $N_{\mathrm{spin}}(g_0) \propto 1/g_0^3$. This scaling involves that the number of spin well coupled is negligible compare to the total number of spin. Typically, we can estimate that the number of spins with a coupling greater than $g_{0,\max}/2$ is ≈ 400. These spins are located in the half-shell bounded by a and $2a$, which corresponds to a detection volume $V = 40$ μm^3.

The main advantage of this configuration is that, in principle, the signal of the strongly coupled spins will not be polluted by the electron spin bath.

7.2.3 Spin-resonator system coupled to a microwave line

The coupled spin-resonator system is connected to the environment via the transmission line. This allows us to both control the spin by sending microwave pulses and to collect the emitted photons due to its relaxation.

7.2.3.1 Purcell effect

The weak coupling regime involves that the radiative relaxation rate of the spin is enhanced by the resonator. The situation is comparable to the four-wave irreversible mixing process described in Chapter 4. When a photon emitted by the spin enters the resonator, it is immediately dissipated into the environment.

A direct calculation, or an adiabatic elimination of the degree of freedom of the resonator according to the procedure described in Section 3.5, yield the well known expression of the Purcell relaxation rate :

$$\Gamma_{\mathrm{p}}(\Delta, g_0) = \frac{g_0^2 \kappa_{\mathrm{t}}}{\frac{\kappa_{\mathrm{t}}^2}{4} + \Delta^2} \tag{7.28}$$

where $\Delta = \omega_0 - \omega_{\mathrm{s}}$ is the frequency difference between the spin and the resonator, κ_{t} the total resonator linewidth, and g_0 the spin-resonator coupling.

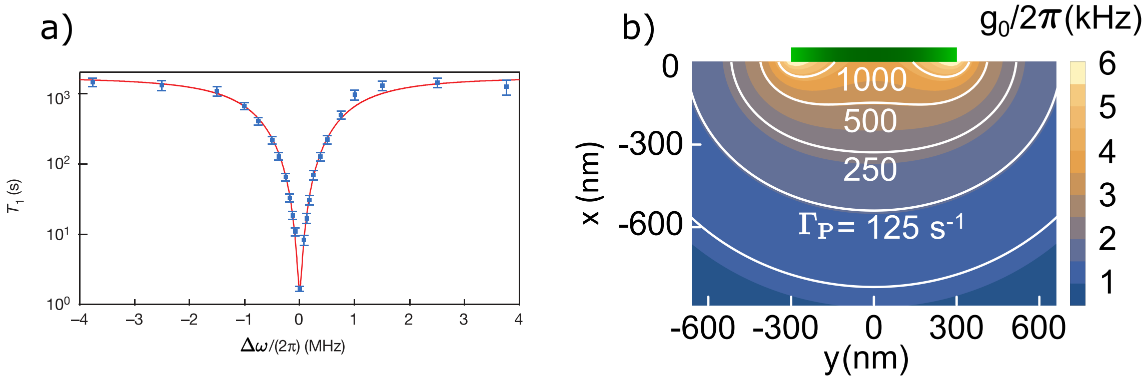

Figure 7.8: **Purcell effect** Illustration of the Purcell effect from [Bie+16]. a) Radiative relaxation time T_1 of spins ensemble provided by bismuth donor in silicon as the function of the frequency detuning Δ between the spins and the resonator. b) Simulation of the spin-resonator coupling constant g_0 and the associated Purcell effect in the case of the superconducting resonator described in Section 7.2.2.

The measurement by Audrey Bienfait from Quantronics of the relaxation time of bismuth spins in silicon[Bie+16], see Figure 7.8a, provided a first illustration of the Purcell effect for a spin ensemble coupled to a microwave resonator.

In the case of our resonator coupled to the Er^{3+} electron spins, a simulation taking into account the real geometry of the wire and a more realistic distribution of current is done in [Bil23] to calculate the coupling distribution. The Purcell rate is then deducted from Equation 7.28 where we fix the resonator frequency at $\omega_0/2\pi = 7$ GHz. An illustration of this simulation is shown in Figure 7.8b.

7.2.3.2 Bloch equations

Another consequence of the weak coupling regime is that the spin and resonator modes do not hybridize. Therefore, the spin dynamics can be computed using only the mean field value α of the cavity ladder operator $\hat{a}$. In our experiment, α is created by a coherent tone sent to the resonator for driving the spin (see Figure 7.9).

The Hamiltonian of the coupled spin-resonator system Equation 7.19 written in the rotation frame of the resonator takes the form:

$$\hat{H}/\hbar = -\frac{\Delta}{2}\hat{\sigma}_\mathrm{z} + g_0(\hat{\sigma}^\dagger \alpha + \hat{\sigma}\alpha^*). \tag{7.29}$$

The spin dynamics is then computed using the master equation introduced in Equation 3.69:

$$\frac{\partial \hat{\rho}_\mathrm{s}}{\partial t} = \frac{-i}{\hbar}[\hat{H}, \hat{\rho}_\mathrm{s}] + \sum_{\hat{L}} \mathcal{D}_{\hat{L}}(\hat{\rho}_\mathrm{s}) \tag{7.30}$$

where the different Linblad operators $\hat{L}$, quite similar to the one described in Section 3.3.2, can be decomposed in the following list:

- **Radiative relaxation**: the radiative relaxation rate, dominated by the Purcell rate with $L_\mathrm{p} = \sqrt{\Gamma_\mathrm{p}}\hat{\sigma}$.
- **Non radiative relaxation**: the spins can also loose energy in a non-radiative way, for instance in the lattice phonon bath, at a rate Γ_NR with $L_\mathrm{NR} = \sqrt{\Gamma_\mathrm{NR}}\hat{\sigma}$.
- **Pure dephasing**: Fluctuation of the spin frequency, due for instance to the magnetic environment, dephase the spin at a rate Γ_Φ with $L_\Phi = \sqrt{\Gamma_\Phi/2}\hat{\sigma}_z$.

In the experiment presented in the following, we are in a regime where the relaxation rate is dominated by the radiative process: $\Gamma_\mathrm{p} \gg \Gamma_\mathrm{NR}$. Therefore from now we neglect the non radiative contribution to relaxation.

The spin density matrix, expressed using the Pauli matrices and the Identity, takes the form:

$$\hat{\rho}_\mathrm{s} = \frac{1}{2}(\mathbb{1} + \hat{\boldsymbol{S}}.\hat{\boldsymbol{\sigma}}). \tag{7.31}$$

where $\hat{\boldsymbol{S}}$ is the average of the spin operator:

$$S_\mathrm{i} = \mathrm{Tr}[\hat{\rho}_\mathrm{s}\hat{S}_\mathrm{i}] = \langle \hat{S}_\mathrm{i} \rangle. \tag{7.32}$$

We can now inject this expression into the master equation in order to obtain equations for the mean value of the spin vector :

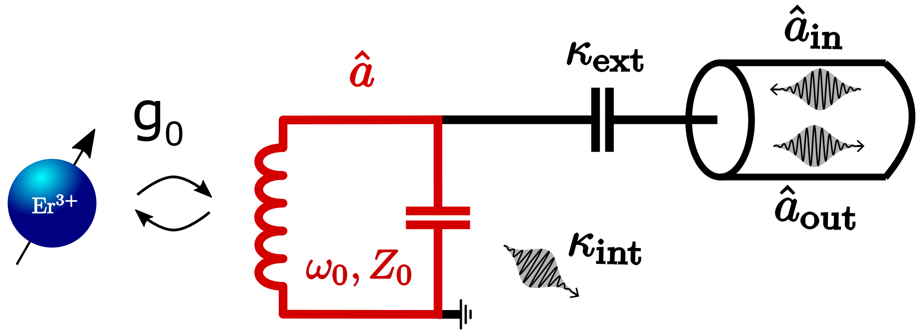

Figure 7.9: **schematic of the spin resonator system coupled to an external line.** Figure inspired from [Bil23]. A resonator of frequency $\omega_0/2\pi$ and impedance Z_0 is coupled to a spin with the coupling strength g_0. It is coupled to the lines at the rate κ_{ext} and has internal losses κ_{int}. The travelling microwave modes $\hat{a}_{\text{in}}$ and $\hat{a}_{\text{out}}$ enter or exit the system

$$\dot{\boldsymbol{S}} = \begin{pmatrix} \langle \dot{\hat{S}}_X \rangle \\ \langle \dot{\hat{S}}_Y \rangle \\ \langle \dot{\hat{S}}_Z \rangle \end{pmatrix} = \begin{pmatrix} 0 & \Delta & -2g_0 \, \mathrm{Im}[\alpha] \\ -\Delta & 0 & -2g_0 \, \mathrm{Re}[\alpha] \\ 2g_0 \, \mathrm{Im}[\alpha] & 2g_0 \, \mathrm{Re}[\alpha] & 0 \end{pmatrix} \boldsymbol{S} - \begin{pmatrix} \Gamma_2 \\ \Gamma_2 \\ \Gamma_{\mathrm{p}} \end{pmatrix} \boldsymbol{S} \tag{7.33}$$

where $\Gamma_{\mathrm{p}} = 1/T_1$ is the spin longitudinal relaxation rate and $\Gamma_2 = 1/T_2 = \Gamma_\phi + \Gamma_1/2$ is the spin transversal relaxation rate.

Assuming for simplicity that $\alpha = \alpha^*$, the first term of the equation describe a rotation around the axis $\boldsymbol{n} = -2g_0\alpha\boldsymbol{e}_{\mathbf{x}} + \Delta\boldsymbol{e}_{\mathbf{z}}$ at the Rabi frequency:

$$\Omega_{\mathrm{R}} = \sqrt{\Delta^2 + (2g_0\alpha)^2}. \tag{7.34}$$

These Rabi oscillations are caused by the coherent tone that we have sent to the cavity. From there, we can control the spin by defining control pulses (π-pulse ...).

7.2.4 Fluorescence signal and photon detection

In this section, we establish the link between the field $\hat{a}_{\text{out}}$ coming out of the resonator, and the photons emitted by the spin.

We write the input-output equation (Section 3.1.4.2) for both $\hat{a}$ and $\hat{a}^\dagger$ using the Hamiltonian Equation 7.19 and considering that we do not inject power on the resonator, i.e. $\langle \hat{a}_{\text{in}} \rangle = 0$. The combination of the two equations allows us to write the evolution of the intra-cavity photon number operator:

$$\frac{d}{dt}\langle \hat{a}^\dagger \hat{a} \rangle = i g_0 \langle \hat{a}\hat{\sigma}_+ - \hat{a}^\dagger \hat{\sigma}_- \rangle - \kappa_{\mathrm{t}} \langle \hat{a}^\dagger \hat{a} \rangle. \tag{7.35}$$

On the other hand, the Heisenberg evolution equation of the spin operator is then:

$$\frac{d}{dt}\langle \hat{\sigma}_z \rangle = -2 i g_0 \langle \hat{a}\hat{\sigma}_+ - \hat{a}^\dagger \hat{\sigma} - \rangle. \tag{7.36}$$

By injecting Equation 7.36 in Equation 7.35, we find the relation linking the average intra-cavity photon number and the spin operator:

$$\frac{d}{dt}\langle \hat{a}^\dagger \hat{a} \rangle = -\frac{d}{dt}\langle \frac{\hat{\sigma}_z}{2} \rangle - \kappa_{\mathrm{t}} \langle \hat{a}^\dagger \hat{a} \rangle. \tag{7.37}$$

In the weak coupling regime and for $\Delta = 0$, one has $\kappa_{\mathrm{t}} \gg \Gamma_{\mathrm{p}} = 4g_0^2/\kappa_{\mathrm{t}}$. We can thus consider that the resonator always is in its steady state with a small number of intra-cavity photons. The link between the outgoing field operator and the intra-cavity field: $\hat{a}_{\mathrm{out}} = \sqrt{\kappa_{\mathrm{ext}}}\hat{a}$ then gives the signal detected by the SMPD between two times t_0 and t_1 :

$$\int_{t_0}^{t_1} \langle \hat{a}^{\dagger}_{\mathrm{out}} \hat{a}_{\mathrm{out}} \rangle dt = \frac{\kappa_{\mathrm{ext}}}{\kappa_{\mathrm{t}}} \frac{\langle \hat{\sigma}_{\mathrm{z}} \rangle (t_0) - \langle \hat{\sigma}_{\mathrm{z}} \rangle (t_1)}{2}. \tag{7.38}$$

Eventually, the signal detectable by the SMPD coming from the resonator is directly proportional to the variation of $\langle \hat{\sigma}_{\mathrm{z}} \rangle$ through the ratio $\kappa_{\mathrm{ext}}/\kappa_{\mathrm{t}}$.

7.3 Single Er^{3+} spin fluorescense detection

The full understanding of spin fluorescence detection requests to link the photon emission by spins in the transmission line and the photon detection by the SMPD.

In this section we first describe the full detection sequence and the spin-to-click efficiency. We then move to the calculation of the signal-to-noise ratio of the experiment.

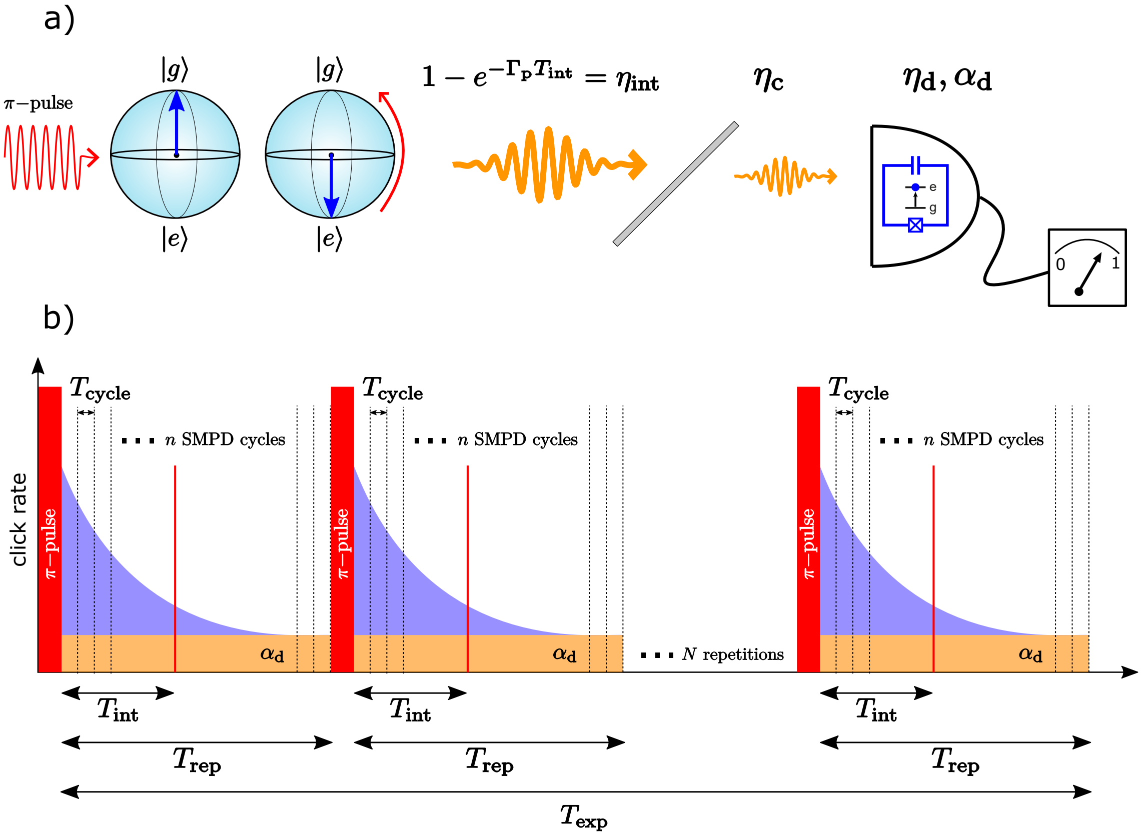

Figure 7.10: **Principle of spin detection with the SMPD**. (a) A single spin sketched with a Bloch sphere initialy in the ground state is excited with a π-pulse. It then emits randomly a photon with the probability η_{int} depending on the integration time T_{int} chosen. The photon is collected with and efficiency η_{c} and sent to the SMPD. (b) Following the π-pulse applied on the spin, the SMPD cycle is repeated n time during a repetition time T_{rep}. The signal is integrated over T_{int} adjusted as the function of the relaxation time Γ_{p}^{-1}. The experiment is repeated N times in order to average the signal. The total experimenet duration is T_{exp}.

7.3.1 Signal collected from the spin relaxation

7.3.1.1 Signal acquisition

As indicated in Figure 7.10a, the detection experiment consists of exciting a single spin initially in its ground state with a π pulse. It then relaxes by emitting a photon in the transmission line as described in Section 7.2.4. The emission probability depends on the radiative relaxation rate Γ_{p}. The signal is acquired by repeating the SMPD cycle n times defining the repetition time $T_{\mathrm{rep}} = nT_{\mathrm{cycle}}$ (see Figure 7.10b). Usually $T_{\mathrm{rep}} \sim 5T_1$ in order to let the spin return completely in its ground state. The signal obtained is integrated during a time T_{int} chosen to maximize the signal to noise ratio.

As the spin can only emit a single photon, the experiment must be repeated several times to extract the emission rate Γ_{p}. We define the total experiment time $T_{\mathrm{exp}} = NT_{\mathrm{rep}}$ where N is the number of experiment repetition.

7.3.1.2 Total detection efficiency

In this section we define the overall spin-to-click efficiency. In addition to the detector efficiency measured in Section 6.3.2.2, two other loss channels play a role in spin detection.

The first is due to the relaxation dynamics itself. After the integration time T_{int}, the spin may still be in its excited state, resulting in detection inefficiency. We define the integration efficiency as $\eta_{\mathrm{int}} = 1 - e^{-\Gamma_{\mathrm{p}} T_{\mathrm{int}}}$. The second source of loss is due to the routing of the photon from the resonator to the SMPD, yielding to an additional collection efficiency η_{c}.

In the following we will defined the spin-to-click efficiency as:

$$\eta_{\mathrm{tot}} = \eta_{\mathrm{d}} \eta_{\mathrm{c}} \eta_{\mathrm{int}}. \tag{7.39}$$

7.3.2 Signal-to-Noise ration of the detection

7.3.2.1 SMPD signal

The overall signal given by the SMPD during the experiement is $S_{\mathrm{ON}} = \alpha_{\mathrm{d}} T_{\mathrm{int}} N + \eta_{\mathrm{tot}} N$. In a similar way to the discussion in the Section 4.5, we define the background signal as $S_{\mathrm{OFF}} = \alpha_{\mathrm{d}} T_{\mathrm{int}} N$ as the signal when no pulse is applied on the system.

The signal of interest is thus $S_{\mathrm{int}} = S_{\mathrm{ON}} - S_{\mathrm{OFF}}$.

7.3.2.2 Noise of the detection

We can then describe the noise associated to the detection which has two contributions:

Dark count rate: The dark count rate depicted in Section 4.4.3 creates false positive detections, which degrades the signal to noise ratio of the measurement. The appearance of these false clicks is a memoryless process whose fluctuations can be described by a Poissonian law $\delta_{\mathrm{DC}}^2 = \alpha_{\mathrm{d}} T_{\mathrm{int}} \mathrm{N}$.

Partition noise: The presence of a photon-to-click efficiency lower than one involves that the detection process is subject to a binomial distribution with parameter η_{tot}. The fluctuation introduced in the signal is $\delta_\eta^2 = \eta_{\mathrm{tot}}(1 - \eta_{\mathrm{tot}})N$.

The sources of noise being independent the total fluctuation is simply the sum of the two contributions:

$$\delta_{\mathrm{tot}}^2 = \delta_\eta^2 + \delta_{\mathrm{DC}}^2 = \alpha_{\mathrm{d}} T_{\mathrm{int}} N + (1 - \eta_{\mathrm{tot}}) \eta_{\mathrm{tot}} N \tag{7.40}$$

7.3.2.3 Signal-to-noise ratio and discussion

From the two last sections, we can write the signal to noise ratio of the detection:

$$\mathrm{SNR} = \frac{S_{\mathrm{int}}}{\sqrt{\delta^2_{\mathrm{tot}}}} = \frac{\eta_{\mathrm{tot}}\sqrt{N}}{\sqrt{\alpha_{\mathrm{d}}T_{\mathrm{int}} + (1-\eta_{\mathrm{tot}})\eta_{\mathrm{tot}}}} = \mathrm{SNR}^{\mathrm{SS}}\sqrt{N} \tag{7.41}$$

Where $\mathrm{SNR}^{\mathrm{SS}}$ is the single shot signal-to noise ratio corresponding to one repetition. Its evolution as the function of the integration time T_{int} is shown on Figure 7.11a and exhibits a maximum for $T_{\mathrm{int}} = 1.62 \cdot T_1$. For the typical parameters of our experiment ($\alpha_{\mathrm{d}} = 100\ \mathrm{s}^{-1}$, $\eta_{\mathrm{c}} = 0.5$, $\eta_{\mathrm{d}} = 0.4$), the maximum single shot SNR is $\mathrm{SNR}^{\mathrm{SS}} = 0.237$.

The figure Figure 7.11b is a theoretic simulation of S_{OFF} and S_{ON} from a Poissonian law. We set the experiment times to $T_{\mathrm{exp}} = 100 \cdot T_{\mathrm{rep}} = 1$ s. The spin considered as a relaxation time $T_1 = 2$ ms and we fix T_{int} at its optimum value. These parameters yield to a total $\mathrm{SNR} = \mathrm{SNR}^{\mathrm{SS}}\sqrt{100} = 0.237 \cdot 10 = 2.37$.

This signal-to-noise ratio involves that with the SMPD describe in the last chapter and a spin with a relaxation time less than or equal to 2 ms, the single spin detection is perfectly feasible as long as our setup remains stable on time scales of the order of a second.

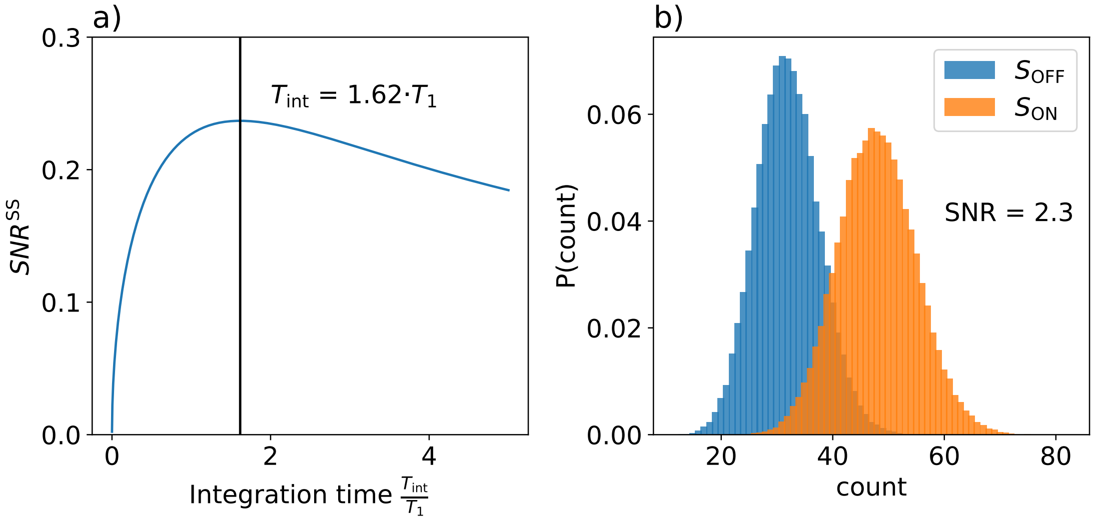

Figure 7.11: **Principle of spin detection with the SMPD.**(a) Single shot signal-to-noise ratio SNR^{SS} as the function of the normalised integration time T_{int}/T_1. We set $\alpha_{\mathrm{d}} = 100$ s^{-1}, $\eta_{\mathrm{c}} = 0.5$ and $\eta_{\mathrm{d}} = 0.4$. The maximal $\mathrm{SNR}^{\mathrm{SS}} = 0.237$ is reached for $T_{\mathrm{int}} = 1.62 \cdot T_1$. (b) Histogram of S_{ON} and S_{OFF} generated from a Poissonian law for $T_{\mathrm{exp}} = 1$ s, $T_{\mathrm{rep}} = 10$ ms, $T_1 = 2$ ms and $T_{\mathrm{int}} = 1.62 \cdot T_1$. The final SNR is found to be 2.3.

Chapter 8

Detection and characterization of single Er^{3+} electronic spins

In this chapter, we combine the Single Microwave Photon Detector SMPD2 (properties given in Table 6.3), and the spin sample described in Section 7.2.2 to perform the detection of individual Er^{3+} electron spins embedded in a $\mathrm{CaWO_4}$ crystal. The spins are controlled by pulses applied via the resonator fabricated on the crystal surface, and the photons emitted by their Purcell relaxation are detected by the SMPD. We first describe the experimental setup and the various adjustments needed for achieving an efficient detection.

We then perform the ESR spectroscopy of the sample by varying the magnetic field $\boldsymbol{B_0}$. We show that the erbium ESR main line is composed of several individual narrow lines, visible at low microwave drive amplitude. By measuring the photon statistics of the fluorescence signal of individual lines, we prove that each individual spectroscopic line can be attributed to a single Er^{3+} electronic spin. Interestingly, each identified spin has its own **g**-tensor which varies slightly from the average tensor introduced in the previous chapter. This deviation is the mark of the uniqueness of the spin environment making this experiment the first measurement of the spin local environment by ESR techniques.

In a third part, we choose a particular spin to probe our ability to control it through the microwave resonator. The spin is treated there as a two level system for which the framework developed in the previous chapters for analyzing the transmon qubit can be applied. We determine its different coherence times with the usual control sequences (2Pulse Ramsey, Hanh echo, ...). Here again the dispersion of the measured values is the mark of a different electromagnetic environment for each spin.

This experiment constitutes the first manipulation of an individual spin by electron paramagnetic resonance techniques.

8.1 Experimental setup and adjustment of the experiment

In this section we describe the experimental setup and the different adjustments needed for its operation. Three different resonance frequencies are involved in the detection chain, that of the spins, the spin resonator and SMPD detection. These three frequencies must be precisely tuned. The spin frequency is controlled by the Zeeman effect via a static magnetic field $\boldsymbol{B_0}$, whereas the SMPD buffer frequency can be adjusted using a tuning SQUID.

8.1.1 Microwave setup and 3-axis magnet

For this experiment, we apply a magnetic field on the spin sample. For this purpose, we install the setup in a fridge different from the one used in Chapter 6, and which is fitted with a 3-axis magnet.

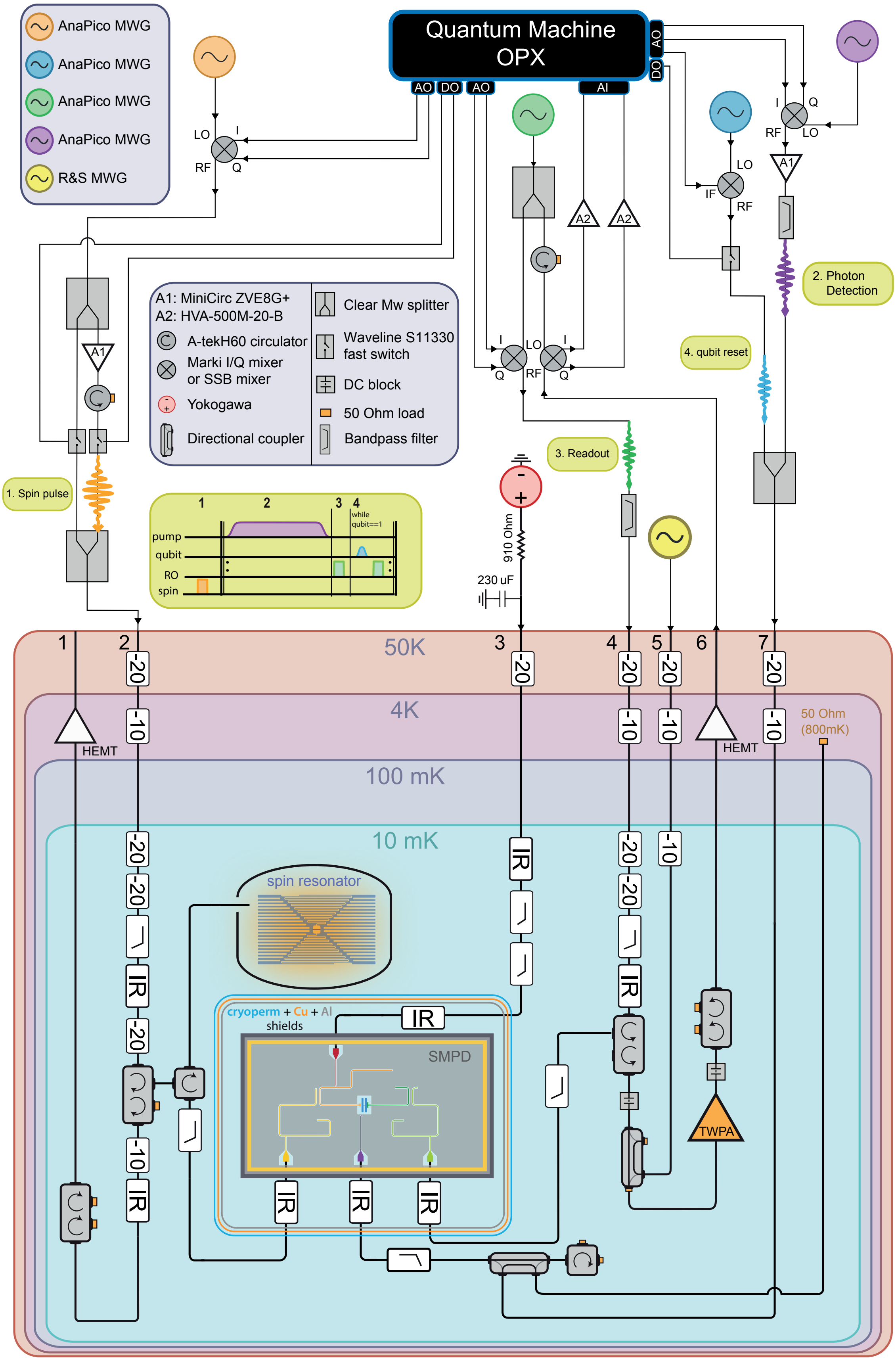

Figure 8.1: **Microwave setup of spin detection.**

Microwave setup: The full microwave setup of the experiment is shown in Figure 8.1. It is similar to the one of SMPD1 shown in Figure 5.14. At low temperature, the main concern is always to reduce thermal population of the lines by installing adequate attenuation and filtering. The room temperature electronics used to control the SMPD2 is similar to the one used for operating the SMPD1. The Quantum Machines OPX allows us to implement sequences involving dc pulses, microwave pulses, demodulation pulses, ADC fast measurements, and intermediate calculations.

The spin sample is connected to the buffer resonator of the SMPD via a circulator. The incoming signal from the line 2 on Figure 8.1 is first routed to the spin sample, then reflected and guided to the SMPD. The connections between the different elements are made by SMA cables.

Spin sample packaging: The spin sample described in Section 7.2.2 is glued into a copper cavity into which we insert a pin. This pin is simply the end of the central conductor of a SMA cable connected to the rest of the circuit. The electric field generated by this antenna in the copper cavity provides the coupling between the resonator and the line. The top and bottom pad present on Figure 7.5b contribute to increase the coupling.

Once the sample is installed, the copper cavity is mounted at the center of the 3-axis magnet at the bottom of the fridge.

3-axis magnet: The 3-axis vector magnet consists of three superconducting coils capable of delivering up to 1T along the X, Y, and Z axes. We thus have a fully adjustable magnetic field $\boldsymbol{B_0} = (B_\mathrm{x}, B_\mathrm{y}, B_\mathrm{z})$.

Each coil is fed by a commercial current source (Four-Quadrant Power Supply Model 4Q06125PS from AMI) and is fitted with a parallel shunt that can be switched between a superconducting state and a normal state. These shunts allow us to operate each coil in two different modes:

- Current supply mode: The shunt is in the normal state, and the current source feeds the coil. This mode is suitable for spectroscopy experiments requiring to vary the magnetic field in amplitude or orientation. Its drawback is the the presence of magnetic field fluctuations due to the current noise of the current source.

- Persistent mode: Once the coil is loaded with an initial current, one can cool down the shunt for placing it in the superconducting state. One can then reduce the source current down to zero while maintaining the current in the coil. This is the so-called persistent mode. The current in the coil is then constant. The field stability time in this mode is longer than the duration of an experiment. Rare thermally assisted flux creep events induce a very slow decay of the magnetic field. This mode that ensures a stable spin frequency is well suited for quantum coherence measurements.

8.1.2 Spin resonator characterization by reflectometry

The spin resonator is characterized at zero magnetic field by reflectometry using the line 1 and 2 shown in Figure 8.1. The resonance frequency $\omega_0/2\pi = 7.3487$ GHz matches well the operating range of the SMPD2 with maximum detectable frequency $\omega_\mathrm{b}(0)/2\pi = 7.459$ GHz.

At zero field, the coupling and internal loss rates are respectively: $\kappa_\mathrm{ext}/2\pi = 200$ kHz and $\kappa_\mathrm{int}/2\pi = 121$ kHz.

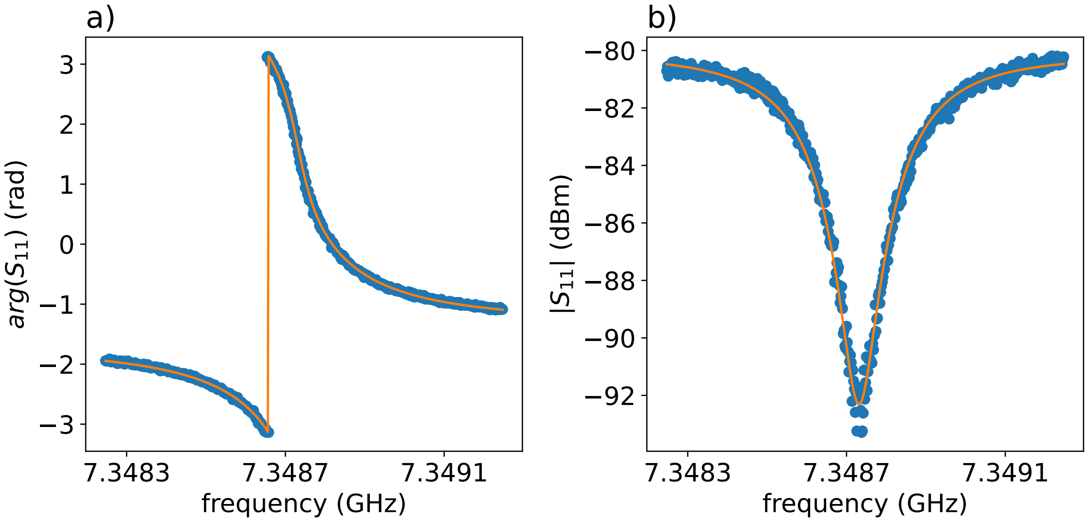

Figure 8.2: **Spin resonator characterization for $B_0 = 0$.** Phase (a) and amplitude (b) of the reflection coefficient $S_{11}(\omega)$. The solid orange lines represent the best fit with parameters $\kappa_{\text{ext}}/2\pi = 200$ kHz, $\kappa_{\text{int}}/2\pi = 121$ khZ.

8.1.3 Field alignment

The sample is mounted in the refrigerator so that the cristallographic (ac)-plane (sample plane in Figure 7.5a) is approximately in the YZ-plan of the 3-axis magnet, the c-axis being parallel to the Z-axis. This adjustment of the orientation by eye is not very accurate and the sample is always slightly misaligned at the beginning of the experiment.

As we work with superconducting thin films, placing the field in the sample plane is essential for avoiding the formation of vortices. Therefore, an alignment field procedure is needed at the beginning of an experiment.

This alignment procedure takes advantage of the weakening of the superconductivity in the thin film caused by the perpendicular field component. The consequence is the reduction of the superconducting gap, which yields a small decrease of the spin resonator frequency.

The full alignment procedure is depicted in Figure 8.3:

- We first applied 50 mT on the Y-axis with the Y coils, $\boldsymbol{B_0} = (0, 50, 0)$ mT.

- We rotate the magnetic field around the Z-axis by increasing the B_{x} component, $|\boldsymbol{B_0}| = |(B_{\text{x}}, B_{\text{y}}, 0)| = 50$ mT. For each value of $\varphi = \arctan(B_{\text{Y}}/B_{\text{Y}})$ (see **??**a) we measure the resonator frequency and find the angle φ_0 that maximises it. As the sample is mounted in the YZ-plan, this angle is small, within a range of $\pm 1°$. Figure 8.3d shows an example of this optimization. The field is reduced down to 0 mT, and the new frame is now $(\text{X}^{'}, \text{Y}^{''}, \text{Z})$.

- We applied 50 mT on the Z-axis with the Z coils, $\boldsymbol{B_0} = (0, 0, 50)$ mT.

- Similarly, we rotate the field in the $(\text{X}^{'}\text{Z})$-plane. For each value of $\psi = \arctan(B_{\text{Z}}/B_{\text{X}})$ (see Figure 8.3b), we measure the resonance frequency in order to find ψ_0 which maximizes it. The field is reduced down to 0 mT. The new frame $(\text{X}^{''}, \text{Y}^{''}, \text{Z}^{''})$ is now such as the $(\text{Y}^{''}, \text{Z}^{''})$-plane corresponds to the sample plane.

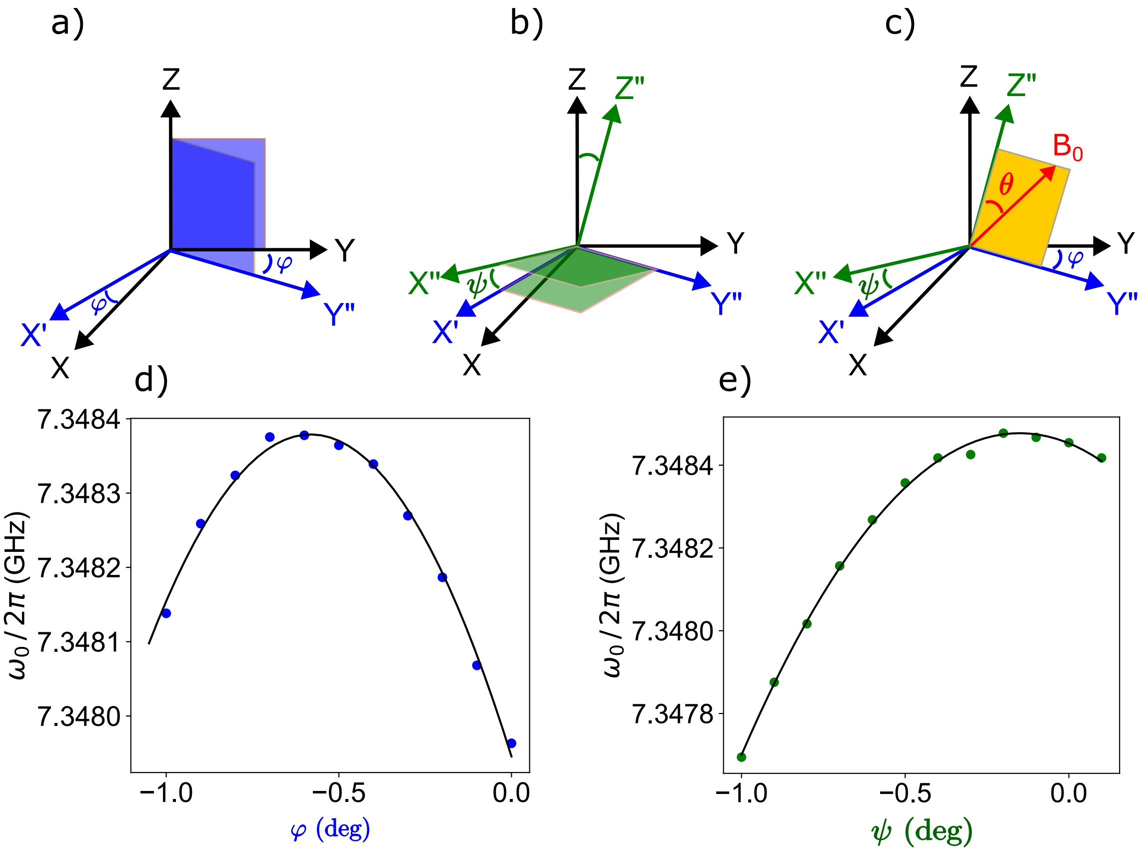

Figure 8.3: **Field alignment procedure**.(a) Definition of the φ angle with the respect to Y-axis, and of the plan $(\mathrm{X}', \mathrm{Y}'')$. (b) Definition of the ψ angle with the respect to the X$'$-axis, and of the $(\mathrm{X}'', \mathrm{Y}'', \mathrm{Z}'')$-frame. At this step, the $(\mathrm{Y}'', \mathrm{Z}'')$-plan matches the sample plan. (c) When the $(\mathrm{X}'', \mathrm{Y}'', \mathrm{Z}'')$-frame is defined, we can move the magnetic field freely in the $(\mathrm{Y}'', \mathrm{Z}'')$-plan, we define the angle θ with the respect to the Z$''$-axis. (d) resp (e) resonator frequency as the function of the angle φ and ψ

.

Now with the known correction angles φ_0 and ψ_0, an arbitrary field B_0 in the Y$''$-Z$''$ resonator plane, with an angle θ with respect to Z$''$ (see Figure 8.3c) is obtained by setting the (X,Y,Z) magnets as:

$$\boldsymbol{B_0} = \begin{pmatrix} B_X \\ B_Y \\ B_Z \end{pmatrix} = B_0 \begin{pmatrix} \sin\theta \sin\varphi_0 - \cos\theta \sin\psi_0 \sin\varphi_0 \\ \sin\theta \cos\varphi_0 + \sin\theta \sin\psi_0 \cos\varphi_0 \\ \cos\theta \cos\psi_0 \end{pmatrix}. \tag{8.1}$$

From now on, the B_0 fields we express will be considered as being in the plane of the sample. However, the frequency of the resonator is still slightly dependent on the magnetic field amplitude as shown on Figure 8.4a. This is due to a small residual perpendicular field component.

In addition, the evolution of the internal and coupling losses are shown in Figure 8.4b. In the following, we will take data around 420 mT, with $\kappa_{\mathrm{int}}/2\pi = 200$ kHz and $\kappa_{\mathrm{ext}}/2\pi = 270$ kHz. These parameters determine the contribution of the resonator to the detection efficiency: $\kappa_{\mathrm{ext}}/(\kappa_{\mathrm{ext}} + \kappa_{\mathrm{int}}) = 0.57$ (see Equation 7.38). Combined with the SMPD2 efficiency 0.32 , one obtains a maximum overall detection efficiency $\eta_{\mathrm{tot}} \leq 0.57 \cdot 0.32 = 0.18$.

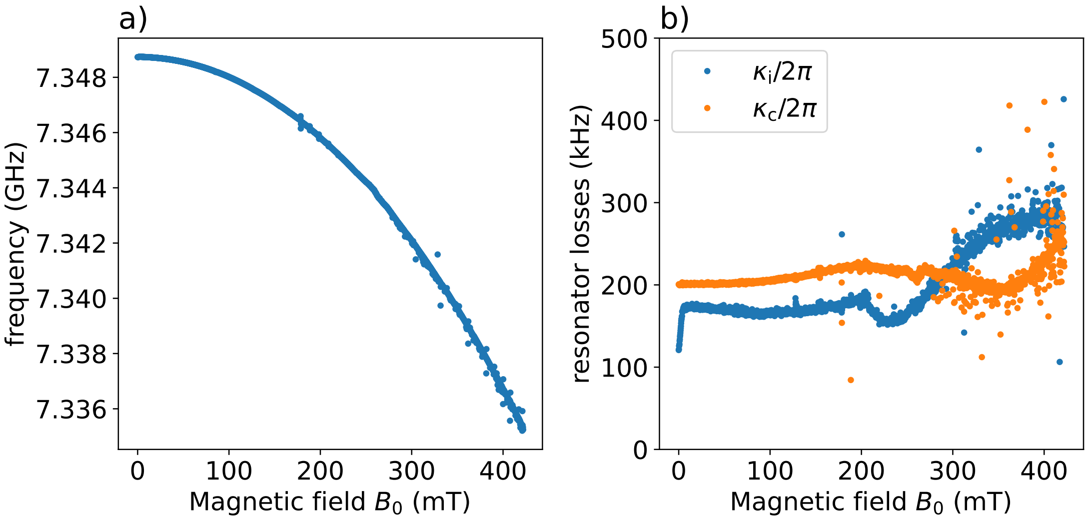

Figure 8.4: **Spin resonator characterization as the function of B_0** (a) Resonator frequency $\omega_0/2\pi$ and resonator losses (b) as the function of the magnetic field amplitude B_0.

8.1.4 Tuning the SMPD for spin detection

In this section, we briefly recap the SMPD2 operational parameters and we show how to align the detection frequency of the SMPD with that of the spin cavity.

As shown in Table 6.3 the overall dark count rate of the SMPD2 is $\alpha_d = 130\ \mathrm{s}^{-1}$. The qubit equilibrium population $p_e = 2 \cdot 10^{-4}$ is comparable to the one of SMPD1. The dark count rate contribution due to this intrinsic circuit imperfection is $\alpha_{\mathrm{qubit}} = 10\ \mathrm{s}^{-1}$, still negligible compared to the excess thermal dark count rate of the SMPD.

The overall efficiency of the detector is 0.32, slightly smaller than that of SMPD1 because of a shorter qubit relaxation time $T_1 \approx 15\ \mu\mathrm{s}$.

We chose the detection window time $T_d = 10\ \mu\mathrm{s}$ by performing the optimization depicted in Section 6.3.1. The cycle time is $T_{\mathrm{cycle}} \approx 12\ \mu\mathrm{s}$.

We now discuss the measurement of the detector bandwidth. A flux of 50 photons$\cdot$ms^{-1} is sent to the detector through the line 2. When the photon frequency is away from the spin resonator frequency, they are fully reflected and impinge the SMPD. The variations of the detector response with the frequency of the incoming photons is shown in Figure 8.5a for a 10 MHz detuning of the buffer resonator from the spin resonator.

Since the SMPD2 is in the regime where $\kappa_b \ll \kappa_w$ and $\kappa_d = 2\kappa_b$, we can fit the detector response with a Lorentzian function. The corresponding bandwidth is $\kappa_d/2\pi = 870$ kHz.

We now perform the same experiment but with the buffer frequency tuned with the spin cavity frequency. The detector response in this situation is shown in Figure 8.5b. The cavity resonance makes a sharp dip in the Lorentzian response of the detector because, at the spin resonator frequency, a large part of the incoming photon flux is absorbed in this resonator instead of being reflected towards the SMPD.

This procedure will be repeated regularly during our experiments to compensate for frequency drifts, due for example to the effect of the magnetic field on the spin resonator.

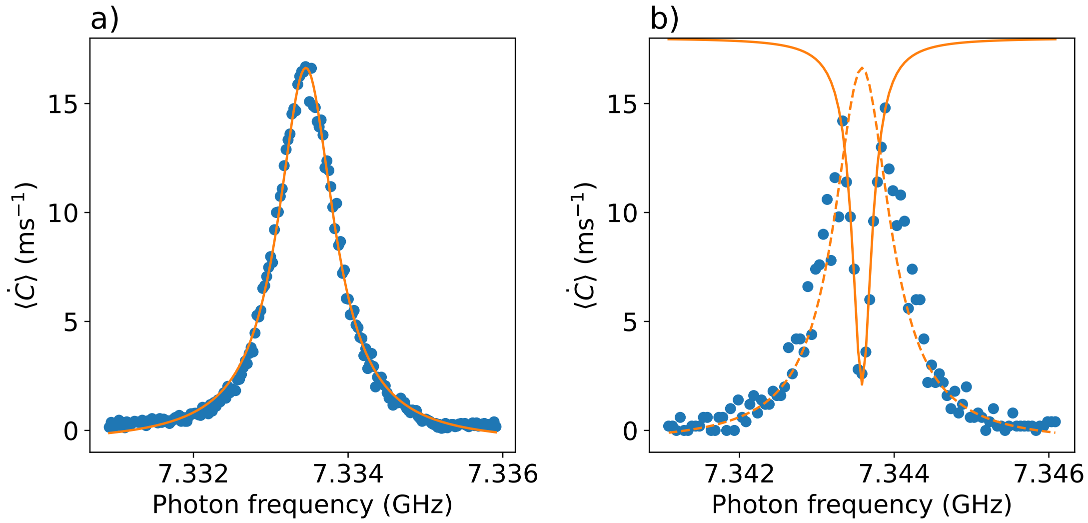

Figure 8.5: **SMPD2 bandwidth measurement and setting with the spin resonator**. (a) Number of detection per millisecond $\langle \dot{C} \rangle$ in function of the frequency of the incoming photons. The flux of incoming photons is set to be 50 ms^{-1} and is sent through the line 2 of the setup (see Figure 8.1). Here the buffer resonator is de-tuned by 10 Mhz from the spin resonator, which yields a full reflection of the photons by the spin cavity. Solid orange line represents a Lorentzian fit form which we we find $\kappa_{\mathrm{d}}/2\pi = 870$ kHz. (b) Same experiment with the buffer resonator tuned with the spin resonator. In contrast to (a), the incident photon flux is absorbed by the spin cavity before reaching the SMPD. The result is the appearance of a dip in $\langle \dot{C} \rangle$ with the shape of an inverted Lorentzian.

8.2 Spin fluorescence detection by photon counting

The raw data of one complete experiment consist in a (N, n)-matrix where each component is a Boolean variable $c_{\mathrm{i}}(t_{\mathrm{j}})$, representing the SMPD output for the i^{th} repetition and the j^{th} cycle (corresponding to the time t_{j}). The i and j index vary according to: $0 \leq i \leq N$ and $1 \leq j \leq n$.

N is the total number of the repetition while n is the total number of SMPD cycle in one repetition. As defined in Figure 7.10b, the duration of a repetition is: $T_{\mathrm{rep}} = nT_{\mathrm{cycle}}$ and the total experiment time is $T_{\mathrm{exp}} = NT_{\mathrm{rep}}$.

From the raw data we can define several quantities:

- **The total and average number of count**

$$\langle C \rangle = \frac{1}{N} \sum_{j=1}^{N} \sum_{t=0}^{T_{\mathrm{rep}}} c_j(t) \tag{8.2}$$

  An illustration of this quantity is given in Figure 8.6b for $N = 4000$.

- **The background-corrected average number of counts**

$$\langle \tilde{C} \rangle = \frac{1}{N} \sum_{j=1}^{N} \left[\sum_{t=0}^{T_{\mathrm{int}}} c_j(t) - \sum_{t=T_{\mathrm{bg}}}^{T_{\mathrm{rep}}} c_j(t) \right], \tag{8.3}$$

  T_{int} is the integration time (see Figure 8.6) while T_{bg} is the time from which the signal is considered to be solely due to the dark-count and not anymore to the spin relaxation.

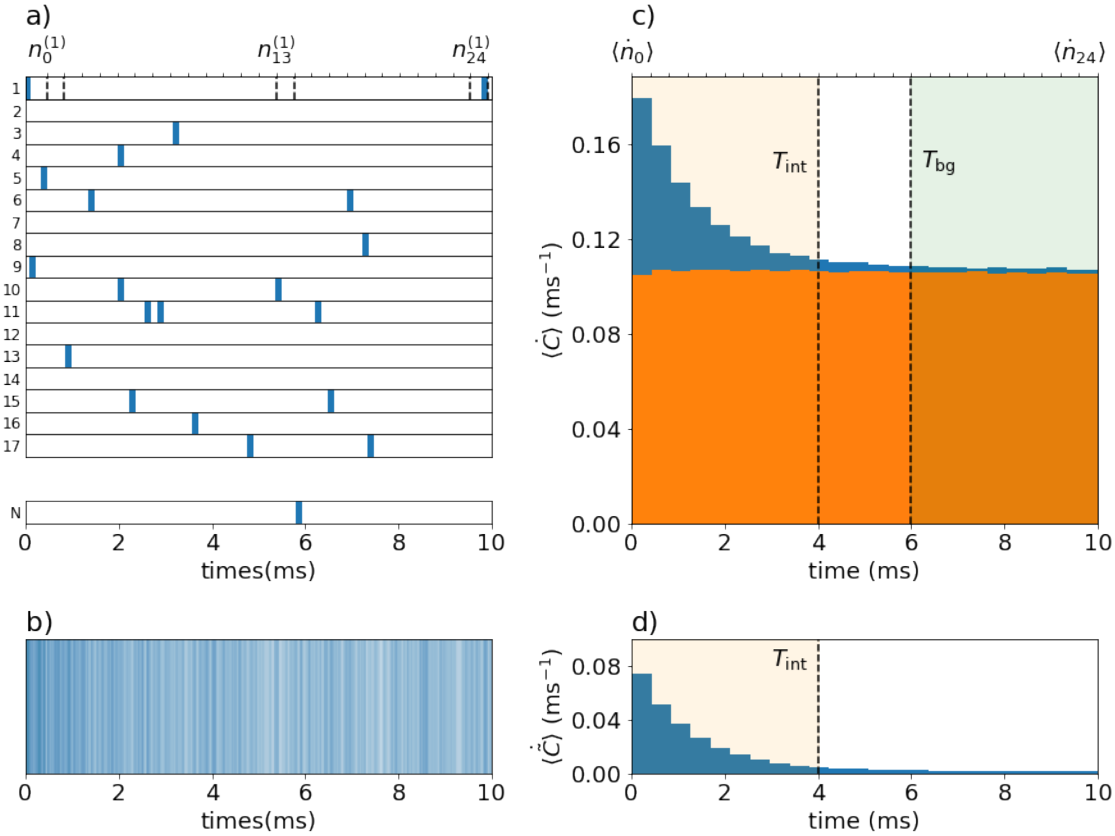

Figure 8.6: **Raw data and count rate**. (a) Time traces of the N repetition of a real single spin detection experiment. A π-pulse is applied to the spin before each measurement repetition. Here $T_{\mathrm{rep}} = 10$ ms which correspond to $\sim$800 SMPD cycle for $T_{\mathrm{cycle}} = 12.5\ \mu$s. The signal is coarse-grained in 25 bins represented on the first time trace by dashed lines. The $n_j^{(1)}$ correspond to the number of clicks in the j$^{\mathrm{th}}$ bin for the first experiment repetition. (b) representation of the total number of count C for $N = 4000$ by concatenating the different traces of a). The beginning of the trace has a denser concentration of count due to spin relaxation. (c) Representation of the average count rate $\langle \dot{C} \rangle$ calculated from the bins according to the detection time. The blue (resp. orange) histogram corresponds to a situation where a π-pulse (resp. no pulse) is applied to the spin. The integration time T_{int} defines the limits of the signal that will be taken into account (orange area). T_{bg} corresponds to the background signal. (d) Representation of the background-corrected average count rate $\langle \dot{\tilde{C}} \rangle$ calculated by removing the orange area of c) to the blue one.

- **The average count rate**

$$\langle \dot{C}(\tau_j) \rangle = \frac{1}{N} \sum_{i=1}^{N} \dot{n}_j^{(i)} \tag{8.4}$$

with

$$\dot{n}_j^{(i)} = \frac{1}{T_{\mathrm{b}}} \sum_{t=\tau_j - T_{\mathrm{b}}/2}^{\tau_j + T_{\mathrm{b}}/2} c_i(t) \tag{8.5}$$

the bin rate at time τ_j of the repetition i, obtained by coarse-graining the counts into bins of duration T_b with $T_\mathrm{b}/T_\mathrm{cycle}$ SMPD cycle (see Figure 8.6a).

- **The background-corrected average count rate**

$$\langle \dot{\tilde{C}}(t_d) \rangle = \langle \dot{C}(t_d) \rangle - \frac{1}{N_\mathrm{bg}} \sum_{\tau_j = T_\mathrm{bg}}^{T_\mathrm{rep}} \langle \dot{C}(\tau_j) \rangle, \tag{8.6}$$

where $N_\mathrm{bg} = (T_\mathrm{rep} - T_\mathrm{bg})/T_\mathrm{b}$ is the number of bins chosen to define the background to remove (see Figure 8.6d).

8.3 Spin spectroscopy measurements

In the section Section 7.2.3.2 we have shown how the spins can be manipulated and excited through the spin resonator. In this section we combine spin excitation and photon detection to perform the spectroscopy of the sample with respect to the magnetic field $\boldsymbol{B_0}$.

8.3.1 Experiment principle

8.3.1.1 Driving spins with Rabi oscillations

The number of spins contributing to the fluorescence signal depends on their Rabi frequency and the rotation axis $\boldsymbol{n}$ on the Bloch sphere. These two parameters are controlled by the product of the pulse amplitude with the spin-resonator coupling $g_0\alpha$, and by the frequency detuning Δ between the spin and the resonator (see Equation 7.34).

In practice, if the frequency of the spins is too different from that of the resonator, the rotation axis is the Z-axis, and the spins are not excited. At zero detuning $\Delta = 0$, the spins are driven by the microwave field and their final state is determined by the pulse characteristic (length and amplitude) as well as the spin-resonator coupling. At a given pulse length, the pulse amplitude allows to select the number of spins that participate to the fluorescence signal. The greater the amplitude, the greater this number of spins.

8.3.1.2 Spectroscopy in magnetic field $\boldsymbol{B_0}$

The spectroscopy experiment consists in scanning the magnetic field and, for each field value, to apply microwave pulses on the resonator and collect the fluorescence signal emitted by the spins.

The narrow band spin resonator can be seen as a fixed window behind which the entire ESR spectrum scrolls. To get an idea of the width of this window for an electron spin polarized along the c-axis, one can convert the resonator bandwidth into magnetic field. $\kappa_\mathrm{t} = \kappa_\mathrm{ext} + \kappa_\mathrm{int} = 2\pi \times 470$ kHz, which corresponds to $\delta B_\mathrm{t} = \kappa_\mathrm{t}/(\mu_\mathrm{B} g_\parallel) \approx 28\ \mu$T. Rather than a window, it is a thin slit through which we can scroll the whole spectrum.

This allows us to recover the different spectroscopic lines of the paramagnetic species present in the sample and in particular those of erbium. With the magnetic field almost aligned along the c-axis and with the resonator frequency $\omega_0/2\pi = 7.349$ GHz, we expect to find the erbium line at a magnetic field around $B_0 = (\omega_0\hbar)/(\mu_\mathrm{B} \mathrm{g}_\parallel) = 421$ mT.

8.3.2 High power spectroscopy

8.3.2.1 Scan along the Z-axis

In order to obtain the best field stability possible, we put the X and Y coils in persistent mode and we scan the magnetic field with the Z coil. Note that in this case, the angle θ is

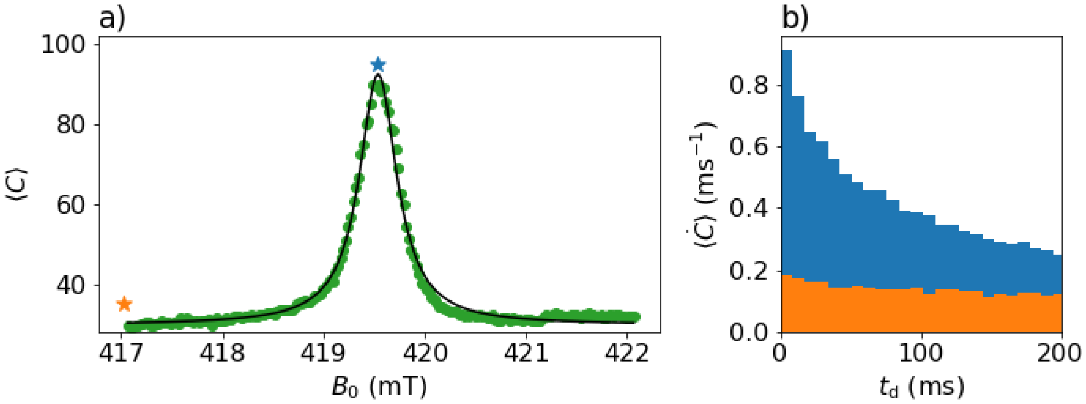

Figure 8.7: **High power spectroscopy of the** Er^{3+} **line**. (a) Microwave fluorescence spectroscopy at high power (~ -97 dBm). The average count rate $\langle C \rangle$ is represented for an integrating time of 200 ms as the function of the magnetic field amplitude B_0. Solid line represents a Lorentzian fit from which we can extract the FWHM = 0.45 mT. Note that the θ angle varies linearly between $-0.06°$ and $0.06°$ during the scan. (b) Average count rate $\langle \dot{C} \rangle$ as the function of the time showing the typical fluorescence signal over an integration window. The blue (orange) histogram corresponds to point represented by the blue (orange) star in a).

not constant during the spectroscopy but varies between $-0.06°$ and $0.06°$ for a B_0 scan between 417 and 422 mT.

We first record the spectrum of the Er^{3+} resonance with a high input power (~ -97 dBm) in order to excite many weakly coupled spins, away from the wire, with a small Γ_P. For each field amplitude B_0, we integrate the fluorescence signal over a window of 200 ms from which we extract an average number of photons $\langle C \rangle$. The average count $\langle C \rangle$ is plotted in Figure 8.7a as in function of the of the magnetic field amplitude. A smooth, approximately Lorentzian curve is obtained whose maximum is observed at $B_0 = 419.5$ mT close to the expected field value $B_0 = (\omega_0 \hbar)/(\mu_B g_{||})$ for the Er^{3+} spin resonance. The slight difference can be attributed to the misalignment of the c-axis with the sample. Indeed, the sample comes from a boule that was cut along a c-plane. The cutting method being imperfect, the presence of a residual angle β is expected.

A typical fluorescence signal is shown in Figure 8.7b. At the maximum of the Erbium line ($B_0 = 419.5$ mT) (blue histogram), the average count rate $\langle \dot{C} \rangle$ shows an excess compared to the dark count level and decays non-exponentially over a time scale of ~ 100 ms. This signal comes from the contribution of large ensemble of spins that have a large coupling inhomogeneity Γ_P as explained in Chapter 7.

One may notice that far from the erbium line, the count $\langle \dot{C} \rangle \sim 180$ s^{-1} is still above the dark count rate of the SMPD (~ 130 s^{-1}). This is attributed to the high amplitude microwave pulses which heat up the lines significantly. A complete investigation of this background increase due to the microwave pulses is carried out in [Wan+23].

8.3.2.2 Rotation pattern

As the CaWO$_4$ presents an asymmetric g-tensor, it is interesting to perform the measurement of the previous section for various θ angles in order to visualize the **g**-tensor.

The ESR spectra for 7 different angles θ is shown in Figure 8.8a. The magnetic field B_0^{peak} corresponding to the top of the erbium line in function of the angle θ is shown in

Figure 8.8b. The line center is maximum in magnetic field (and minimum in effective gyromagnetic ratio) at an angle defined as $\theta = 0°$ when B_0 is aligned with the projection of the crystallographic c-axis onto the crystal plane

This magnetic field can be expressed as a function of the θ and β angles: $B_0^{\text{peak}} = (\hbar\omega_0)/(\mu_{\text{B}} g_{\text{eff}}(\theta))$, with $\text{g}_{\text{eff}} = \sqrt{(\text{g}_\perp \sin\theta \sin(\beta))^2 + (\text{g}_\parallel \cos\theta \cos(\beta))^2}$ (Equation 7.11).

The fit with this formula allows us to extract the angle $\beta = 0.5°$.

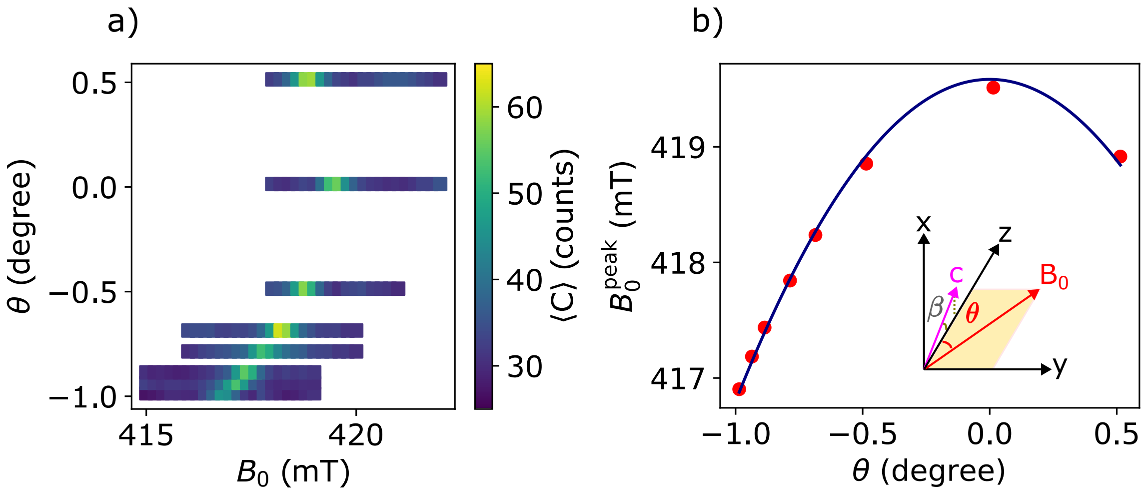

Figure 8.8: **Rotation pattern**. (a) Spectroscopy of the Er^{3+} line realize for different θ angle. The fluorescence signal is integrated over 200 ms. (b) Magnetic field B_0^{peak} corresponding to the maximum average count as the function of θ. The solid blue line is a fit according to the formula $B_0^{\text{peak}} = (\hbar\omega_0)/(\mu_{\text{B}} g_{\text{eff}}(\theta, \beta))$ which yields to $\beta = 0.5$ and a maximum field for $\theta = 0$

8.3.3 Low power spectroscopy

We now discuss the low power spectroscopy in order to probe a different spin population. The experiments of the previous section are repeated by attenuating the pulse power by 20 dB and reducing the integration time to 2 ms. We now detect the most strongly coupled and fastest relaxing spins.

8.3.3.1 Scan along the Z-axis

Figure 8.9a shows the variations of the integrated count $\langle C \rangle$ with the magnetic field amplitude B_0. The spectrum appears as a sum of narrow, unevenly distributed peaks, with typical amplitude ~ 0.1 excess count over the noise floor.

The Figure 8.9b is a zoomed part of the spectrum showing 7 different peaks (s0 ... s6). These narrow lines are stable and perfectly reproducible over days or weeks.

A typical fluorescence curve of one of these peaks, that of s0, is shown in (Figure 8.9c). One always observes a continuous decay with a characteristic time in the ms range. These features raise a question: does each peak correspond to the microwave fluorescence signal originating from a single Er^{3+} ion spin, similarly to the optical fluorescence spectrum of a collection of individual solid-state emitters ? [OB90; Kin+20; Dib+18] . Note that while we observe a large fluorescence signal at the centre of the inhomogeneous absorption line, some individual peaks are still found far from the centre; a common observation in low-density spectra of optical emitters, and a natural consequence of the random nature of inhomogeneous broadening. This is also possibly supplemented in our particular device

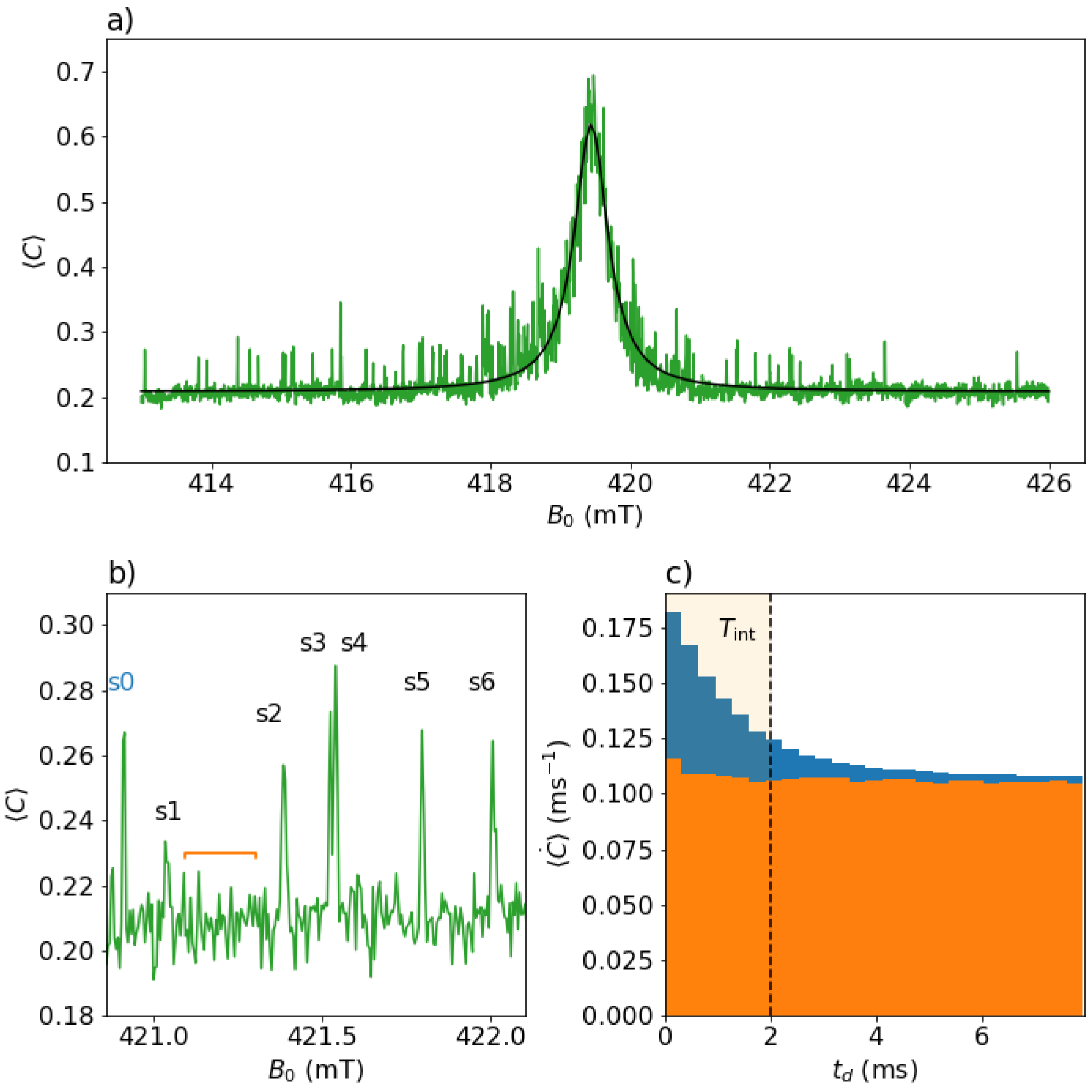

Figure 8.9: **Low power spectroscopy**. (a) Spin spectroscopy at low power (~ -107 dBm at sample input), with an integration window of 2 ms. Green line is measured data, black line is a Lorentzian fit. Note that the angle θ varies linearly between $-0.016°$ and $0.016°$ over the scan. (b) Zoom between 420.86 mT and 422.1 mT exhibiting 7 peaks (labelled s0 to s6). (c) Fluorescence histograms of spin s0 (blue) and background (orange) averaged over the range of B_0 shown in the zoom fig b). The light orange window is the integration window for the data in a) and b).

by the strain imparted by thermal contractions of the metallic wire on the substrate just below [Pla+18; Ran+21].

Note that now the dark count rate retrieve its nominal value (orange histogram in Figure 8.9c). The microwave pulse thus no longer increases the temperature of the microwave bath.

8.3.3.2 2D spectroscopy

For probing the stability and reproducibility of the peaks, we perform a two-dimensional magnetic field scan by recording the background-corrected average number of counts $\langle \tilde{C} \rangle$

as a function of B_0 and θ (see Figure 8.10). Since the seven different spin peaks we have chosen are well resolved, their spectrum is readily followed as a function of θ.

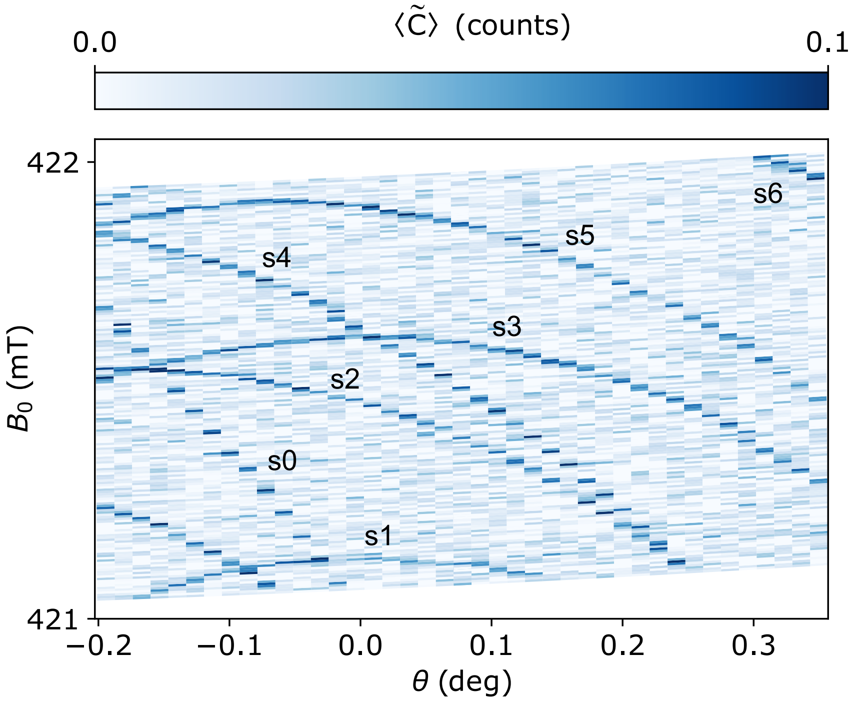

Figure 8.10: **2D low power spectroscopy**. Background-corrected average number of count $\langle\tilde{C}\rangle$ as the function of the magnetic field angle with the Z-axis θ and the magnetic field amplitude B_0. Each line in dark blue correspond to an individual peak observed in Figure 8.9.

The first observation is that each line has its own gyromagnetic tensor $\boldsymbol{\gamma} = \mu_{\mathrm{B}}\mathbf{g}$, close to the average one $\boldsymbol{\gamma_0}$ but with different values along the principal axes, and with a symmetry axis that can slightly deviate from the c-axis. The lines are so narrow that each ion gyromagnetic tensor could, in principle, be determined to better than 10^{-6} accuracy (using a suitably calibrated magnetic field). Because the deviation $\delta\boldsymbol{\gamma}$ of the gyromagnetic tensor from the ensemble-averaged $\boldsymbol{\gamma}_0$ is due to the local electrostatic and strain environment, its accurate measurement can also be turned into a sensitive way to probe this environment (as done with NV centres in diamond [Bro+19]). Note that our measurements also call for a better modeling of the response of rare-earth ion spins to applied electric or strain fields.

8.4 Single-spin time-domain measurements

In this section we further investigate the single spin nature of the different lines observed in the previous section. We show single spin control experiments on line s0, and we probe quantum coherence on the s6 line.

8.4.1 Characterization of the s0 line

8.4.1.1 Rabi oscillation

On this section, we focus on the s0 peak visible both on the low power spectroscopy curves Figure 8.9b and Figure 8.10. We first measure the average-background corrected number of clicks $\langle \tilde{C} \rangle$ as the function of the pulse duration for a fixed pulse amplitude. This experiment is the symmetric of the one shown in Section 6.1.2.3.

The signal is integrated over the first 2 ms as in the same way as done for the data in Figure 8.9c. We vary the pulse duration from 0 to 10 μs. As expected for a single emitter, we observe a sinusoidal oscillation corresponding to Rabi oscillations (see Figure 8.11). A gradual small increase in counts is observed, which we interpret as the progressive excitation of the spin background bath and the heating of the lines.

We then perform the same experiment but by also varying the amplitude of the microwave pulse. $\langle \tilde{C} \rangle$ is plotted in Figure 8.11a as the function of the pulse duration and amplitude. From this 2D plot we can observe that the Rabi frequency increase with the pulse amplitude. This effect clearly materializes in Figure 8.11b where the frequency is plotted as the function of the amplitude and increases linearly as expected from the Rabi frequency formula Equation 7.34.

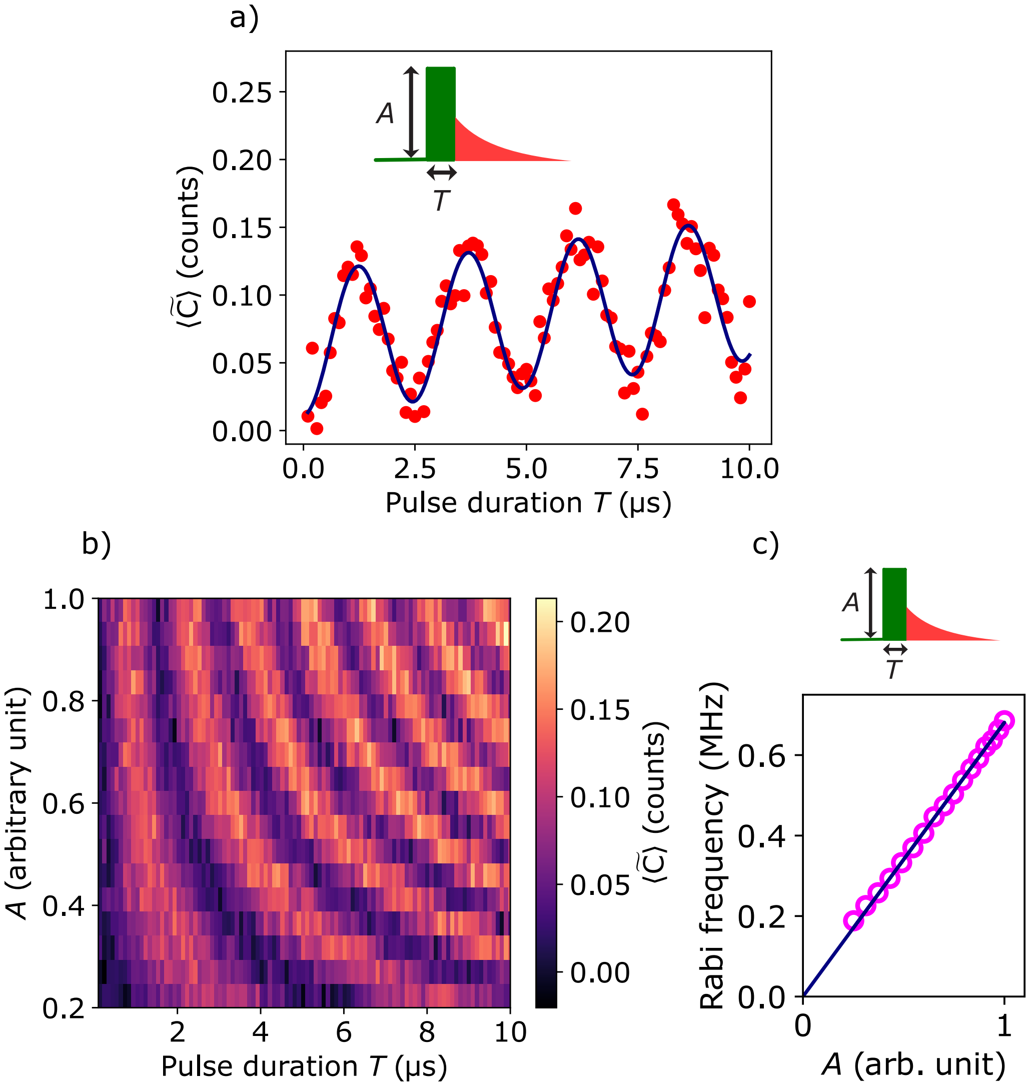

Figure 8.11: **Rabi oscillation,peak s0**. (a) Background-corrected average number of count $\langle \tilde{c} \rangle$ with the respect to the microwave pulse duration (see inset). red dots are data, solid blue line is a sinusoidal fit with a linearly increasing offset. (b) $\langle \tilde{C} \rangle$ with the respect to the pulse duration T and amplitude A. (c) Frequency of the oscillation as the function of the pulse amplitude A. Pink circles represent data while solid blue line is a linear fit.

This experiment gives us access to the (A,T) torque needed to achieve a controlled spin rotation on the Bloch sphere. This will be useful to define the implement pulse sequences with angle (π/n-pulse).

8.4.1.2 Intensity-intensity correlation function

As demonstrated for single emitters in optics, the best way to probe the single emitter nature of a source is to measure its intensity-intensity correlation function $g^{(2)}(\tau)$. For a single emitter, the probability of emitting a photon in the same wavepacket labeled n is zero i.e $\langle I^{(n)}(t)I^{(n)}(t+\tau)\rangle = 0$. However, the probability of emitting photon in separated wavepackets corresponding to distinct repetition is independent, therefore, $\langle I^{(n)}(t)I^{(m\neq n)}(t+\tau)\rangle = \langle I^{(n)}(t)\rangle\langle I^{(m\neq n)}(t+\tau)\rangle$. Moreover, the time resolution and the dead-time of the detector (~ 10 μs) are much smaller than the typical wavepacket duration (~ 1 ms). As the consequence, the intensity-intensity correlation function can be measured with a single detector only [Dib+18]. However, due to the dark-count, $g^{(2)}(\tau)$ is blurred. A simple correction can be performed assuming a Poissonian state for the dark-count.

$g^{(2)}$ dataset and definition:

Our protocol consists in acquiring a dataset corresponding to two interleaved series of 4363635 repetitions labelled from i=0 to i=4363634 repeated every $T_{\text{rep}} = 10.6\,\text{ms}$, where one series includes a π pulse at time $t = 0$ and the other has no excitation pulse. Time $t = 0$ is followed by 825 SMPD cycles.

The count data of the repetition are grouped in 350μs-long timebins indexed by j (with j running from 0 to 20), and centered at time $\tau_j = 100 + (2j+1) \times 350/2$ μs. The corresponding number of counts in the bin j of repetition i is $n_j^{(i)}$. The first bin is separated from the microwave pulse by 100 μs in order to avoid spurious heating effect.

We define the intensity-intensity correlation function in the same way as in [Dib+18] by comparing the number of counts in the two first bins of two repetitions. This yields to the definition of the inter-pulse $g^{(2)}$:

$$g^{(2)}(k) = \frac{\langle n_0^{(i)} n_1^{(i+k)} + n_1^{(i)} n_0^{(i+k)}\rangle_i/2}{\langle n_0^{(i)}\rangle_i \langle n_1^{(i+k)}\rangle_i}, \tag{8.7}$$

where we keep only the first and second bins of the two repetitions, symmetrize the function about k=0, and average over all pairs of repetitions with same separation $k \in \mathbb{Z}$. For N emitters, $g^{(2)}(0)$ should be equal to $(N-1)/N$; in particular, $g^{(2)}(0)$ should be equal to 0 for a single-emitter since it can emit only one photon per repetition.

Uncorrected $g^{(2)}$:

The $g^{(2)}(k)$ correlation function calculated from the dataset described above is shown in Figure 8.12a. For $k \neq 0$, $g^{(2)}(k \neq 0) = 1 \pm 0.006$ which is expected as there is no correlation between to different repetitions. On the contrary, the value of $g^{(2)}(0) = 0.906 \pm 0.007$ is slightly less than 1. This reduction is small, but this is not surprising given that dark counts sizeably contribute to false positives

.

Background-corrected $g^{(2)}$:

We now take into consideration the fact that the clicks from the detector have two independent origins: emission s_j from the spins, and Poissonian background noise d_j due to independent dark count events, such that $n_j = s_j + d_j$, $\langle n_j\rangle = \langle s_j\rangle + \langle d_j\rangle$, and

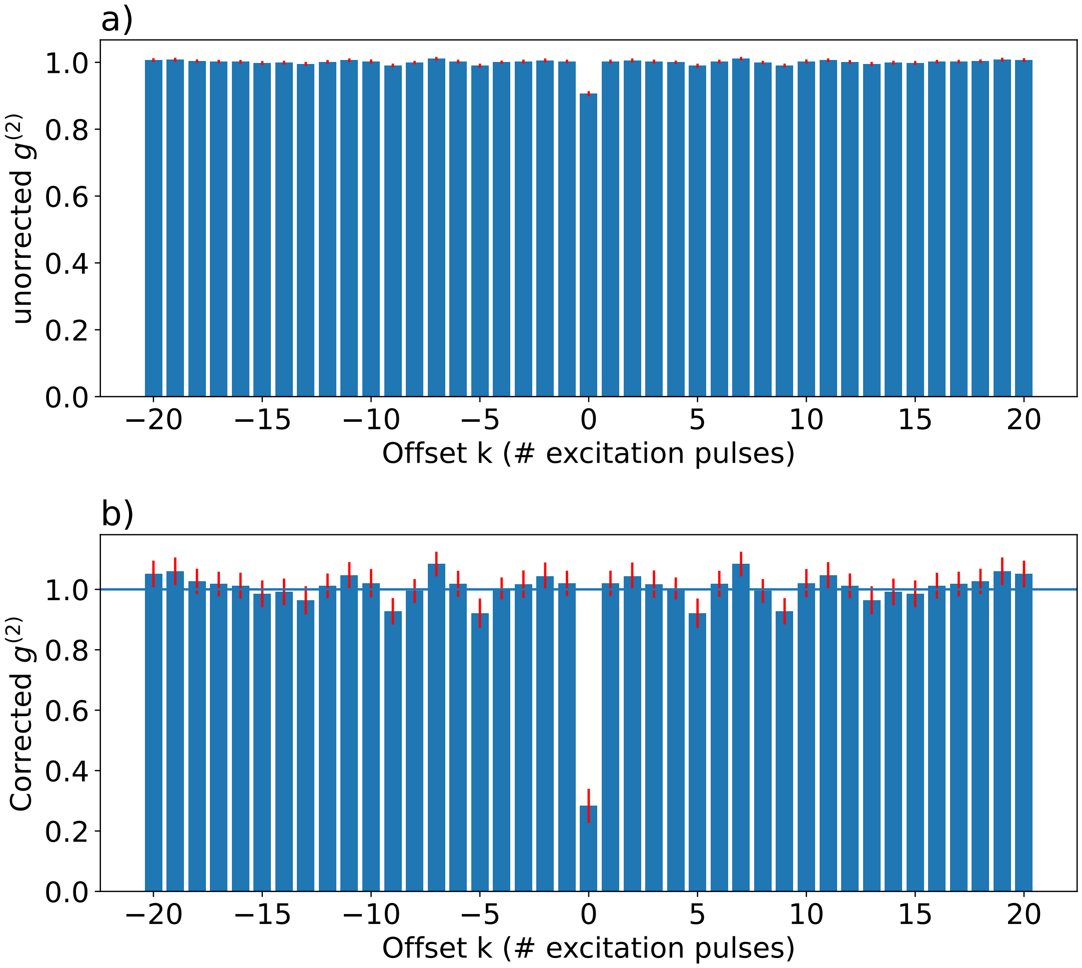

Figure 8.12: **Auto-correlation function, peak s0**. Raw data (a) and background-corrected (b) auto-correlation function $g^{(2)}$ (blue columns) and corresponding ±1-standard deviation error bars (red) measured as a function of the offset k between excitation pulses. Note that the function is exactly symmetric around 0 by definition.

$\langle s_j d_j \rangle = \langle s_j \rangle \langle d_j \rangle$. In addition, we assume that the instruments during the measurement time are stable enough so that the dark count rate is time-invariant: $\langle d_j \rangle = \langle d \rangle$.

We thus define the background-corrected autocorrelation function:

$$g^{(2)}_{\text{corr}}(k) = \frac{\langle s_0^{(i)} s_1^{(i+k)} + s_1^{(i)} s_0^{(i+k)} \rangle_i / 2}{\langle s_0^{(i)} \rangle_i \langle s_1^{(i+k)} \rangle_i} \tag{8.8}$$

and express it explicitly as a function of the uncorrected $g^{(2)}(k)$ of Eq. 8.7 and of the measurement outcomes $A_j \equiv (\langle n_j^{(i)} \rangle_i - \langle d \rangle)/\langle d \rangle$:

$$g^{(2)}_{\text{corr}}(k) = \frac{(1 + A_0)(1 + A_1) g^{(2)}(k) - A_0 - A_1 - 1}{A_0 A_1}. \tag{8.9}$$

The variations of the background corrected correlation function $g^{(2)}_{\text{corr}}$ with the offset between the repetitions are shown in Figure 8.12b. We find $g^{(2)}_{\text{corr}}(0) = 0.23 \pm 0.06$ and $g^{(2)}_{\text{corr}}(k \neq 0) = 1 \pm 0.04$. There is thus a very significant anti-bunching in each repetition, whereas the emission from different repetitions remains uncorrelated. The non-zero value of $g^{(2)}_{\mathrm{corr}}(0)$ may be due to heating by the excitation pulse. In any case, the fact that its value is well below 0.5 further strongly suggests that the spectral peak under investigation corresponds to a single microwave photon emitter, namely an individual Er^{3+} electron-spin.

8.4.1.3 Signal-to-noise ratio

Due to the presence of dark-count and inefficiency, we have to repeat the experiment a large number of time before being able to resolve the presence of a single spin. This can be quantified as the SNR of the spin detection.

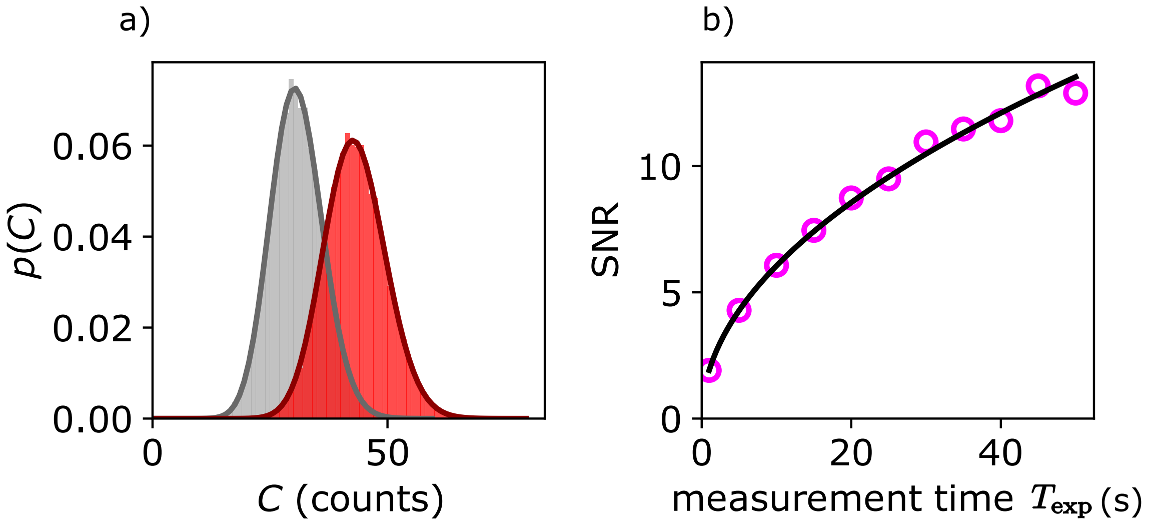

Figure 8.13: **Signal-to-noise ratio**. (a) Measured probability distribution $p(C)$ of the total count C integrated over the first 2 ms of 7.5 ms-long repetitions, either with no excitation pulse applied (grey) or with a π excitation pulse (red). Repetitions are repeated and counts are summed during an experiement time $T_{\mathrm{exp}} = 1\,\mathrm{s}$. Solid lines are Poissonian fits, yielding the spin signal $C_{spin} = 12.4$ (difference between the mean values of the two distributions) and the standard deviations $\delta C_0 = 5.5$ and $\delta C_\pi = 6.5$. This results in a single-spin SNR $C_{spin}/\delta C_\pi = 1.91$. (b) Measured signal-to noise ratio $C_{spin}/\delta C_\pi$ (magenta dots) as a function of the measurement time T_{exp}, and fit with the function $A\sqrt{T_{\mathrm{exp}}}$ (solid line). Data taken at $B_0 = 421.042$ mT and $\theta = -0.024°$.

From the same dataset as used for the intensity-intensity correlation function, we compute the sum C of the counts integrated over the first 2 ms following the excitation pulse, over repetitions played during T_{exp}.

The count probability histogram $p(C)$ for $T_{\mathrm{exp}} = 1\,\mathrm{s}$, with and without π pulses applied, is shown in Figure 8.13a. These date yield a single-spin detection SNR of 1.91.

A comparison with the expected SNR given in Equation 7.41 requires the knowledge of the overall efficiency η_{tot}, which we find to be equal to $\eta = 0.12 \pm 0.01$ by integrating the fluorescence signal after the π pulse with subtracted background. We then estimate an optimal theoretical SNR of ~ 2.5, quite close to the measured value. We also verify that the SNR scales as the square root of the measurement time T_{exp} up to at least 1 minute (see Figure 8.13b), which is indicative of good measurement stability.

Finally, in this experiment we achieve a sensitivity of 0.5 $\mathrm{spin}/\sqrt{\mathrm{Hz}}$, which is an improvement by a factor of ~ 20 compared to the previous state of the art [Ran+20; Alb+21].

8.4.2 Spin time domain measurements s6

The single-spin nature of the individual lines identified by spectroscopy (Figure 8.9) having been established, the next step is to manipulate the spin in the same way as done for the SMPD superconducting qubit Section 6.1.2.3. Our aim is to characterize the spin dynamics, and to determine its different quantum coherence times. In this section, we focus on the spin s6.

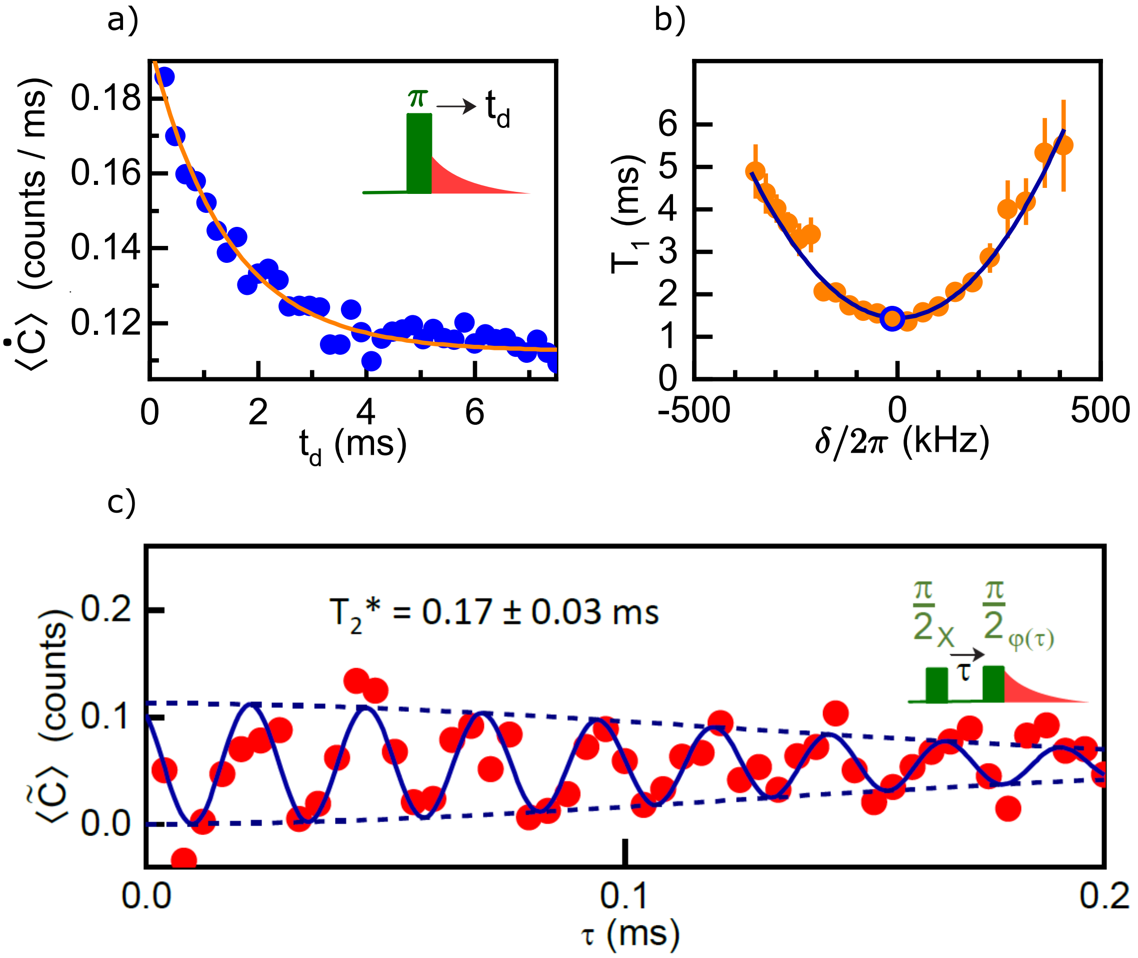

Figure 8.14: **Relaxation time and Purcell effect, spin** $s6$. (a)Energy relaxation: measured average count rate $\langle \dot{C} \rangle$ (blue dots) as a function of delay t_{d} after a resonant π excitation pulse. Exponential fit (solid orange line) yields the energy relaxation time $T_1(\delta = 0) = 1.42 \pm 0.07$ ms. (b) Purcell effect: measured T_1 as a function of spin-resonator frequency detuning δ (orange dots). A fit to $\Gamma_{\mathrm{P}}^{-1}(\delta)$ (solid black line) yields the spin-resonator coupling constant $g_0/2\pi = 3.59 \pm 0.15$ kHz. (c) Measured excess counts $\langle \widetilde{C} \rangle$ versus delay time τ between two resonant $\pi/2$ pulses with relative phase $\varphi(\tau) = 2\pi\Delta\tau$ and $\Delta = 0.025\,\mathrm{MHz}$ (dots). The corresponding fit (solid line) by a sine function with a Gaussian-decaying envelope (dash lines) yields a coherence time $T_2^* = 0.17 \pm 0.03\,\mathrm{ms}$.

8.4.2.1 Purcell effect an free-induction-decay time

Energy relaxation time T_1

We first measure the energy relaxation time T_1 of the spin s6 which is readily obtained from the fluorescence curve decay, as shown Figure 8.14a) . We find a relaxation time which is minimum at zero frequency detuning δ between the spin and the resonator, as expected for Purcell dominated relaxation, $T_1(\delta = 0) = 1.42 \pm 0.07$ ms.

Free-induction-decay (FID) time T_2^*

We then measure the free-induction-decay (FID) time using a Ramsey sequence $\pi/2_X - \tau - \pi/2_\varphi$, with the relative inter-pulse phase $\varphi = 2\pi\Delta\tau$, where $\Delta = 0.025\,\mathrm{MHz}$. As shown in Figure 8.14c, the excess count $\langle\tilde{C}\rangle$ shows oscillations at frequency $\Delta + \delta$, damped with an approximately Gaussian shape with a characteristic decay time $T_2^* = 170 \pm 33\,\mu\mathrm{s}$, which corresponds to a $\sim 2\,\mathrm{kHz}$ single-spin linewidth or $\approx 0.1\ \mu$T.

Spin-resonator detuning δ and Purcell rate Γ_p

The Ramsey sequence can be turned into a accurate way to measure the spin detuning δ with the respect to the pulse frequency centered on the resonator frequency. This allows us to probe quantitatively the dependence of the spin relaxation time T_1 on the detuning δ shown in Figure 8.14b, and to obtain an accurate determination of the spin-resonator coupling.

The spin detuning δ is controlled by changing the spin frequency using the magnetic field $\boldsymbol{B_0}$. We maintain the X and Z coils in in persistent mode, and use the Y coil (stabililized with homemade feedback loop) to fine-tune δ.

The relaxation time T_1 increases quadratically with δ , in agreement with the predicted dependence for Γ_P^{-1} given by Equation 7.28. We retrieve the results obtained by A.Bienfait [Bie+16], illustrated in Figure 7.8, but at the single spin level.

8.4.2.2 Hahn echo and dynamical decoupling

The spin Ramsey time T_2^* is limited by slow fluctuation of the environment such as the nuclear spins or static magnetic field fluctuation. In this section, we move on to a Hahn echo and then a dynamical decoupling experiment, which allow these slow fluctuations to be cancelled out by refocusing pulses.

The sequence applied is $\pi/2_X - \tau - \pi_X - \tau - \pi/2_\varphi$ [Bil+22],with the relative inter-pulse phase $\varphi = 2\pi\Delta\tau$, where and $\Delta = 1\,\mathrm{kHz}$. In contrast to the Ramsey sequence, the central refocusing π-pulse removes the slow frequency shift that occurs during acquisition. Therefore, the echo coherence time is longer, $T_2 > T_2$.

The results of a hahn echo sequence are shown in Figure 8.15a). The average count rate $\langle\tilde{C}\rangle$ shows an oscillatory pattern at frequency Δ , with an exponential decay with characteristic time $T_2 = 2.47 \pm 0.31\,\mathrm{ms}$. This value is close to the radiative decay limit $2T_1$, which allows us to determine a pure dephasing time is $\sim 16 \pm 5\,\mathrm{ms}$, in line with measurements on ensembles of $\mathrm{Er}^{3+}:\mathrm{CaWO}_4$ electron spins [Dan22]. This dephasing can be suppressed further by a 3-π-pulse Dynamical Decoupling sequence, yielding a transverse relaxation time $T_2^{\mathrm{DD}} = 2.99 \pm 0.33\,\mathrm{ms}$ (see Figure 8.15b), which is equal to $2T_1$ up to the accuracy of the measurements.

8.4.2.3 Coherence properties of different spins

These coherence times were also measured on a set of five Er^{3+} electron spins, and the results are listed in Table 8.1. One notices that T_2^* varies strongly among these spins (between 5μs and 300μs), whereas T_2 and T_2^{DD} are consistently close to $2T_1$. The variation of coherence time among different spins can be explained by the varying nuclear spin or paramagnetic environment of each ion, and also possibly their degree of exposure to surface magnetic noise given their approximate depth of $\sim 100 - 150\,\mathrm{nm}$ according to Figure 7.8b

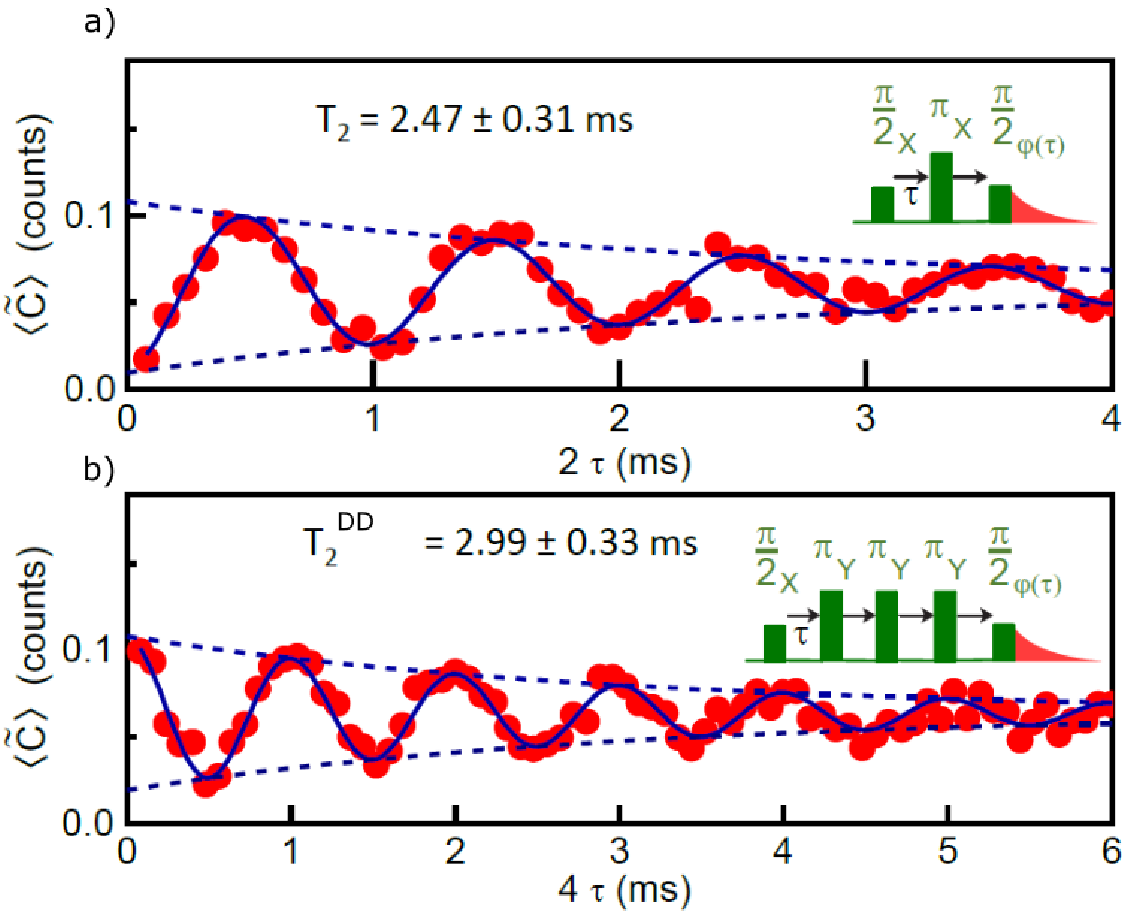

Figure 8.15: **Coherence time** . (a) Hahn-echo sequence (see inset): average background-corrected $\langle \tilde{C} \rangle$ versus delay τ between subsequent pulses with a linearly increasing phase $\varphi(\tau) = 2\pi\Delta\tau$ with $\Delta = 0.001\,\text{MHz}$ on the last pulse (red dots). The corresponding fit and its envelope (solid and dash lines) yield a coherence time $T_2 = 2.47 \pm 0.31\,\text{ms}$. (b) Dynamical Decoupling sequence (see inset): average background-corrected $\langle \tilde{C} \rangle$ versus inter-pulse delay time τ (red dots). A linearly increasing phase $\varphi(\tau) = 2\pi\Delta\tau$ with $\Delta = 0.001\,\text{MHz}$ is imparted on the last pulse. Corresponding fit and its envelope (solid and dash lines) are shown, yielding the coherence time $T_2^{\text{DD}} = 2.99 \pm 0.03\,\text{ms}$. Data taken at $B_0 = 422.085$ mT and $\theta = -0.003°$.

and [Mye+14; Ran+21]. It is also noteworthy that the coherence times measured here are on par with the longest reported for individual electron spins in solid-state [Muh+14], in a platform which gives access to several tens of these spin qubits by simply tuning the magnetic field.

Spin	T_1(ms)	$T_2^*(\mu s)$	T_2^{echo}(ms)
s0	1.26	79	1.38
s6	1.42	170	2.47
s7	2.21	7.5	2.1
s8	1.36	315	1.53

Table 8.1: Table of the various spins coherence time

8.4.3 Conclusion

In this section we have demonstrated the first measurement and control of a single electron spin by FD-ESR. The shift from ensemble measurement to single spin is an important paradigm modification for the field of magnetic resonance. It opens the way to many applications that were previously unattainable in quantum sensing and quantum computing.

For example, the record coherence times of erbium electron spins could be used to design hybrid spin-superconducting circuit quantum processors. As these coherence times are radiatively limited, they could also be increased by several orders of magnitude (up to one second) by reducing dynamically the Purcell effect until the relaxation limit imposed by phonons is reached.

In terms of quantum sensing, one can imagine creating a gradient with the static magnetic field $\boldsymbol{B_0}$ to resolve the position of the spins at the nanometre scale and to obtain precise 3D maps of the crystal. On a more local level, a single electron spin can be used as a probe of its environment, such as in recent studies carried out in NV center in diamond [Abo+19].

In the next chapter, we explore partially one of these possibilities by probing the ^{183}W nuclear spin bath surrounding an Er^{3+} ion.

Chapter 9

Probing the W183 nuclear spin bath with the electron spin

In the previous chapter, we succeeded in detecting and controlling individual electron spins from erbium ions in a $CaWO_4$ crystal. We have shown that their coherence times (FID time, echo ...) and their physical characteristics (Landé factor) are not identical. Their distribution arises from the different configurations of the electromagnetic environment surrounding each spin. Charge defects may indeed be present in the crystal and at different distances from a spin, as well as surface or interface defects. Tungsten being a constituent of CaWO4, the sites populated by the ^{183}W isotope (natural abundance 0.145) with a nuclear spin (I=½) furthermore yield a randomly distributed dipolar magnetic interaction that depends o the local environment of each erbium spin.

The coupling between a quantum system under control and the uncontrolled degrees of freedom of its environment is often mostly considered for the decoherence it induces. This is a particularly important issue in our era of the quantum computer race, and great efforts are thus made to isolate qubits.

However, one can also see this coupling not as a limitation but as a way to probe and control the environment of the quantum system, in our case the electron spins. This strategy has already been exploited for the NV centers in diamond [Tam+12; Kol+12; Lon+13] where the electron spin of the NV center is used to probe the ^{13}C nuclear spin bath. Individual detection and control of nuclear spin has even been demonstrated. This provides some appealing opportunities, such as the development of reliable quantum memories [Bra+19], or the development of NMR imaging with ultimate sensitivity [Abo+19].

The quantum control sequences that made possible to carry out these first experiments were derived from the dynamic decoupling concept developed for open quantum circuits. This concept, borrowed from nuclear magnetic resonance, was introduced in 1999 [VKL99]. It aims to free a quantum system from its interactions with the environment by introducing a suitable perturbation. The perturbation induces fast changes in the quantum system designed such that the effect of the coupling with the environment averages to zero in the evolution operator. In this chapter we transpose in our system some of the nuclear spin detection experiments carried out with NV centres.

We first briefly describe the hyperfine interaction between the Er^{3+} ion and the ^{183}W located on neighboring site in the crystal.

We then describe a pulsed dynamic decoupling experiment using a Carr-Purcell-Meiboom-Gill (CPMG) sequence on a particular Er^{3+} electron spin, following ref. [Tam+12; Kol+12]. We demonstrate the presence of a signal due to the surrounding ^{183}W nuclear spin bath. This work is the first local measurement of tungsten nuclear spins using magnetic resonance techniques.

We also perform a continuous dynamic decoupling experiment using a spin locking sequence [Lon+13]. These measurements allow us to make more accurate assumptions about the configuration of the surrounding nuclear spins. However, as the data is less clear than in the case of pulsed dynamic decoupling, these results are presented in the appendix.

9.1 Manipulating nuclear spins through electron spin

As shown in Chapter 7, the coupling between the nuclear spins of ^{183}W and the erbium electron spin is described by a magnetic dipole-dipole interaction (see Equation 7.12), it constitutes the hyperfine coupling.

The magnetic moment of the electron spin being 4-5 orders of magnitude larger than that of the nuclear spin, it strongly affects the dynamics of the nuclear spins, and this influence can be used as a means to manipulate nuclear spins coupled to it.

A crucial point for achieving this manipulation is to have a strong enough hyperfine coupling between the electron and the nuclear spin. This coupling depends linearly on the g-factor of the electron spin (see Equation 7.12). The anisotropy of the $CaWO_4$ crystal allows to tune this parameter by adjusting the θ angle between the crystal c-axis and the applied magnetic field $\boldsymbol{B_0}$ (see g_{eff} expression in Equation 7.11). We now evaluate how the hyperfine coupling evolves with the angle θ and explain the experimental situation configuration realized in our experiment.

9.1.1 Electron spin dependent quantization axis

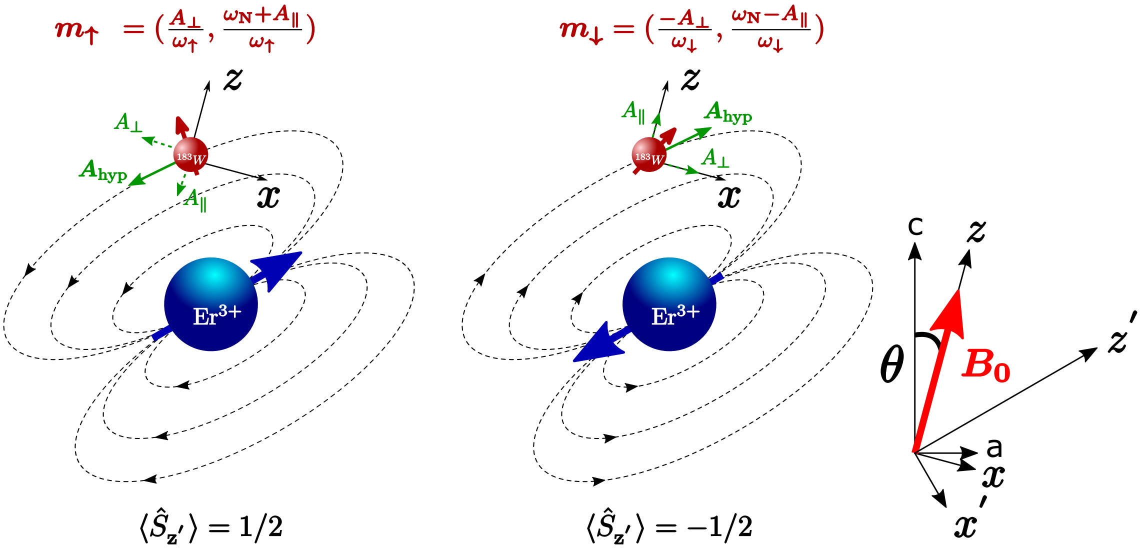

Figure 9.1: **Nuclear spin quantization axis evolution**. Evolution of the quantization axis $\boldsymbol{m}_{\uparrow\downarrow}$ of the ^{183}W nuclear spin with the respect to the state of Er^{3+} electron spin. The axis depends on the hyperfine parameters, bare Larmor frequency ω_L and the electron spin state dependent Larmor frequencies $\omega_{\uparrow\downarrow}$. The magnetic field being out of the c-axis the electron spin quantization axis is not aligned in the $\boldsymbol{B_0}$ direction. The (x, z) frame is defined such as $\boldsymbol{B_0} = B_0 \boldsymbol{u_z}$ and $\boldsymbol{A_{\text{hyp}}} \in (x, z)$. The (x', z') frame is defined such as the quantization axis of the electron spin is along z'. The crystallographic frame is noted (a, c).

In Section 7.1.4 we developed the expression of the dipolar Hamiltonian in the secular approximation framework when the magnetic field is aligned along the c-axis: $\hat{H}_{\text{dd}}/\hbar = \hat{S}_z(A_\perp \hat{I}_x + A_\parallel \hat{I}_z)$. When the magnetic field is at an angle θ, we redefine a basis of the Hilbert space such that the interaction keeps the same form: $H_{\text{dd}}/\hbar = \hat{S}_{z'}(A_\perp \hat{I}_x + A_\parallel \hat{I}_z)$, with the frame (x, z) and (x', z') defined in Figure 9.1. In the following we will remove the prime (') index on the quantization axes for the sake of readability. It is implicit that the bases of electron spin and nuclear spin are different.

The Hamiltonian of the electron-nuclear spin system can be expressed in the rotating frame of the electron spin as:

$$\hat{H}/\hbar = \omega_{\mathrm{L}}\hat{I}_{\mathrm{z}} + \hat{H}_{\mathrm{dd}}/\hbar \tag{9.1}$$

$$\hat{H}/\hbar = |\uparrow\rangle\langle\uparrow| \otimes \left([\omega_{\mathrm{L}} + A_{\|}]\hat{I}_{\mathrm{z}} + A_{\perp}\hat{I}_{\mathrm{x}}\right) + |\downarrow\rangle\langle\downarrow| \otimes \left(([\omega_{\mathrm{L}} - A_{\|}]\hat{I}_{\mathrm{z}} - A_{\perp}\hat{I}_{\mathrm{x}}\right) \tag{9.2}$$

where the kets $|\uparrow\rangle$ and $|\downarrow\rangle$ represent the electron spin state. The final form of this Hamiltonian is:

$$\hat{H}/\hbar = |\uparrow\rangle\langle\uparrow| \otimes \omega_{\uparrow}\hat{\boldsymbol{I}} \cdot \boldsymbol{m}_{\uparrow} + |\downarrow\rangle\langle\downarrow| \otimes \omega_{\downarrow}\hat{\boldsymbol{I}} \cdot \boldsymbol{m}_{\downarrow} \tag{9.3}$$

with:

$$\boldsymbol{m}_{\uparrow\downarrow} = \frac{(\omega_{\mathrm{L}} \pm A_{\|}/2)}{\omega_{\uparrow\downarrow}}\boldsymbol{e}_{\mathbf{z}} \pm \frac{A_{\perp}/2}{\omega_{\uparrow\downarrow}}\boldsymbol{e}_{\mathbf{x}} \tag{9.4}$$

$$\omega_{\uparrow\downarrow} = \sqrt{(\omega_{\mathrm{L}} \pm A_{\|}/2)^2 + (A_{\perp}/2)^2}. \tag{9.5}$$

From Equation 9.2, it is clear that both the Larmor frequency and the direction of the quantization axis of the nuclear spin depend on the electron spin state as illustrated in Figure 9.1. This dependence can be used to control the nuclear spin as done in [Tam+12; Kol+12; Lon+13] provided that the component $A_{\perp}$ is non zero. Indeed, in this case, the $\hat{S}_{\mathrm{z}}\hat{I}_{\mathrm{x}}$ term of the dipolar Hamiltonian is zero and the nuclear spin cannot be flipped.

As shown in Figure 9.1, the direction of the hyperfine interaction $\boldsymbol{A}_{\mathbf{hyp}}$ and thus the distribution between $A_{\perp}$ and $A_{\|}$ depends only on the direction of the magnetic field generated by the electron spin at the nuclear spin position. The strength of the interaction $|\boldsymbol{A}_{\mathbf{hyp}}|$ depends on the g-factor of the electron spin (Equation 7.17). A simple way to increase the hyperfine coupling is to shift the magnetic field $\boldsymbol{B}_{\mathbf{0}}$ away from the c-axis of the crystal by increasing the angle θ.

We now discuss the variations of the hyperfine coupling parameters with θ angle and the position of the tungsten site.

9.1.2 Increasing the electron-spin hyperfine interaction

9.1.2.1 Simulation of the hyperfine parameters

Since it involves the erbium anisotropic **g**-tensor, the dependence of the hyperfine parameters on θ is non-trivial and cumbersome to solve analytically. We rather perform a numerical calculation directly from the general form of the dipolar Hamiltonian in Equation 7.12. This calculation comports four steps:

- **Creation of the dipolar tensor $\bar{\bar{\boldsymbol{A}}}_{\mathbf{hyp}}$**: We create the $(3 \cdot 3)$ $\bar{\bar{\boldsymbol{A}}}_{\mathbf{hyp}}$ matrix from Equation 7.12. This tensor varies for each tungsten site as it is strongly depend on the relative position of the spins. The dipolar Hamiltonian reads now: $\hat{H}_{\mathrm{dd}} = \hat{\boldsymbol{S}}\bar{\bar{\boldsymbol{A}}}_{\mathbf{hyp}}\hat{\boldsymbol{I}}$.
- **Application of $\boldsymbol{B}_{\mathbf{0}}$**: A magnetic field $\boldsymbol{B}_{\mathbf{0}}$ is applied to the system creating the Zeeman Hamiltonian $\hat{H}_{\mathrm{Z}} = \mu_{\mathrm{B}}\boldsymbol{B}_{\mathbf{0}} \cdot \mathbf{g} \cdot \hat{\boldsymbol{S}} \otimes \mu_{\mathrm{N}}g_{\mathrm{N}}\boldsymbol{B}_{\mathbf{0}} \cdot \hat{\boldsymbol{I}}$. We numerically find a basis in which $\hat{H}_{\mathrm{Z}}$ is diagonal, ie a basis defined by the quantization axis of the two spins. The $(4 \cdot 4)$ change-of-basis matrix is noted $\hat{M}_{\mathrm{rot}}$.

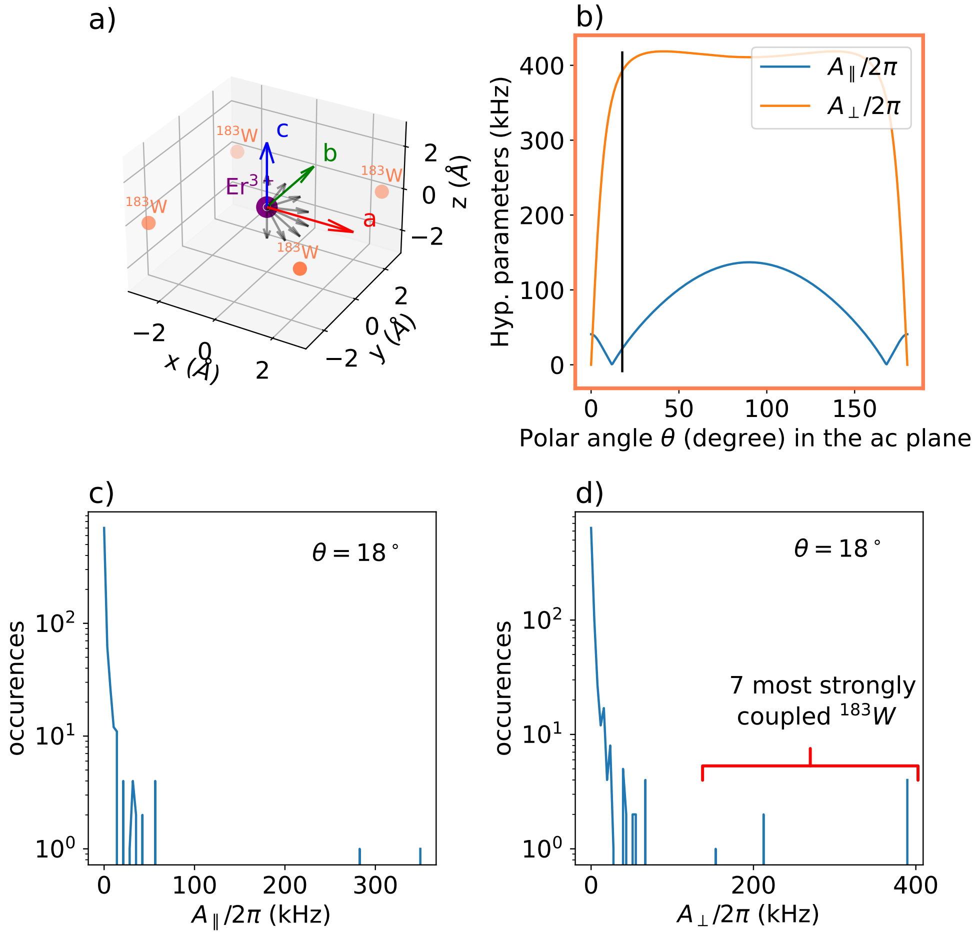

Figure 9.2: **Simulation of the hyperfine parameters with θ.** a) 3D scheme of a Er^{3+} ion surrounded by surrounded by its 4 closest tungsten neighbors. The crystalline axes are shown in blue (c-axis) red (a-axis) and green (b-axis). The magnetic field is sketched by the grey arrow for different configurations of θ, the angle between the c-axis and the a-axis. b) Simulation of the hyperfine parameters $A_{\perp}$ and $A_{\parallel}$ as the function of θ four the 4 closest neighbor. c) histogram of $A_{\parallel}$ the 800 closest W site for $\theta = 18°$. d) Same histogram for $A_{\perp}$, 7 ions are distinguished by a coupling > 170 kHz.

- **Basis change for $\hat{H}_{\mathrm{dd}}$**: We transform the dipolar Hamiltonian in $\hat{H}^{\mathrm{rot}}_{\mathrm{dd}} = \hat{M}^{\dagger}_{\mathrm{rot}} \hat{H}_{\mathrm{dd}} \hat{M}_{\mathrm{rot}}$
- **Application of the secular approximation**: We apply the secular approximation, ie we only consider the terms $\hat{S}_{\mathrm{z}}\hat{I}_{\mathrm{z}}$ and $\hat{S}_{\mathrm{z}}\hat{I}_{\mathrm{x}}$. The dipolar matrix element corresponding are $A_{\parallel} = \hat{H}^{\mathrm{rot}}_{\mathrm{dd,zz}}/\hbar$ and $A_{\perp} = \hat{H}^{\mathrm{rot}}_{\mathrm{dd,zx}}/\hbar$. The effective dipolar Hamiltonian then reads $\hat{H}_{\mathrm{dd}} = \hat{S}_{\mathrm{z}}\boldsymbol{A}_{\mathbf{hyp}} \cdot \hat{\boldsymbol{I}}$ where $\boldsymbol{A}_{\mathbf{hyp}}$ is the hyperfine vector described in Equation 7.15.

the result of this calculation is shown in Figure 9.2b for the 4 closest ^{183}W neighbors when angle θ varies from 0° to 180°.

The θ dependence of $A_{\perp}$ and $A_{\parallel}$ is mainly due to the evolution of the effective erbium g-factor, but it is also strongly dependent on the position of the ^{183}W with respect to the Er^{3+} ion. For example, the system composed of an erbium ion with four nearest ^{183}W neighbors in the same (ab) plane, as shown in Figure 9.2a, yields the hyperfine parameters shown in Figure 9.2b. When the $\boldsymbol{B_0}$ field is parallel to the c-axis, the field generated by the electron spin is parallel to the c-axis at the plane level. The perpendicular component $A_\perp$ vanishes, and the nuclear spins cannot be rotated by the electronic spin.

9.1.2.2 Experiment realized with $\theta = 18°$

We have chosen $\theta \approx 18°$ for the experiment in the next section. The effective g-factor corresponding to an angle $\theta = 18°$ is $\mathrm{g_{eff}} = 2.84 \sim 2.5 \cdot \mathrm{g}_{||}$. This choice is a trade-off between the maximization of the $A_\perp$ of the four nearest neighbors and the conservation of a large coupling g_0 between the electron spin and the resonator. Indeed, given the resonator nanowire which allows to couple the electron spin to the cavity is aligned along the c-axis (see Figure 7.5), the choice of a non-zero θ makes the spin quantization direction no longer perpendicular to the field generated by the wire, which yields a decrease of the coupling constant g_0 (see Equation 7.24). The reader can find more detail on this effect in [Dan22]. In the situation considered, the coupling is reduced by $\cos\theta \approx 0.95$.

Figure 9.2c,d shows the distribution of the hyperfine parameters (calculated for $\theta = 18°$) of 800 nuclear spins contained in a sphere of radius 2.5 nm centered on the Erbium ion. As shown on Figure 9.2d 7 ions are distinguished by their very strong coupling $A_\perp/2\pi > 170$ kHz.

9.1.3 Spectroscopy for $\theta = 18°$ and ion selection

In this section, we realize the high power spectroscopy of the erbium line around $\theta = 18°$. The protocol is similar to the one described in the previous chapter (see Section 8.3.2). We use the same experimental conditions with the Y and X coil in persistent mode. The scan will be realized with the Z coil.

As the effective g-factor $\mathrm{g_{eff}} = 2.84$, we expect to find the erbium line around $B_0 \approx 185$ mT, which corresponds to $B_\mathrm{Y} \approx 56$ mT and $B_\mathrm{Z} \approx 176$ mT.

The result of a "high" power spectroscopy is shown in Figure 9.3a. We represent the click rate $\langle \dot{C} \rangle$ as the function of the time after the pulse and the magnetic field $B_0 = \sqrt{B_\mathrm{Z}^2 + B_\mathrm{Y}^2}$. As expected, the erbium line is found around $B_0 = 184.1$ mT. The observed relaxation time is long and of the order of a few hundred ms, which is expected since we are probing the spin ensemble at high power and are therefore exciting weakly coupled spins with a long relaxation time [Bil23]. The integrated signal over 200 ms is shown in Figure 9.3c , with a Lorentzian fit with FWHM = 0.92 mT. This value is larger than the one found in the previous chapter. A full investigation of the dependence of the FWMH of the erbium inhomogeneous line with the θ angle can be found in [Dan22].

We then switch to a low power spectroscopic measurement at the edge of the line to find strongly coupled single spins. As shown on Figure 9.3b, the measurement time has been strongly reduced in order to select only spins with short T_1. The Figure 9.3d shows the integrated signal over 2.5 ms. Several lines appear, as in Section 8.3.3, corresponding to single spins. We select the spin indicated by the red star on the graph ($B_0 = 185.996$ mT) for the following experiment.

9.1.4 Quantum coherence of the selected spin

We then move on to time domain characterization of the selected spin. The nuclear spin detection techniques we will use in the following sections are intrinsically limited in their sensitivity by the coherence time of the electron spin. It is therefore necessary to know its exact value. Furthermore, the weakness of the couplings between the nuclear and electron spins requires a long integration time for reaching an acceptable signal-to-noise ratio. The

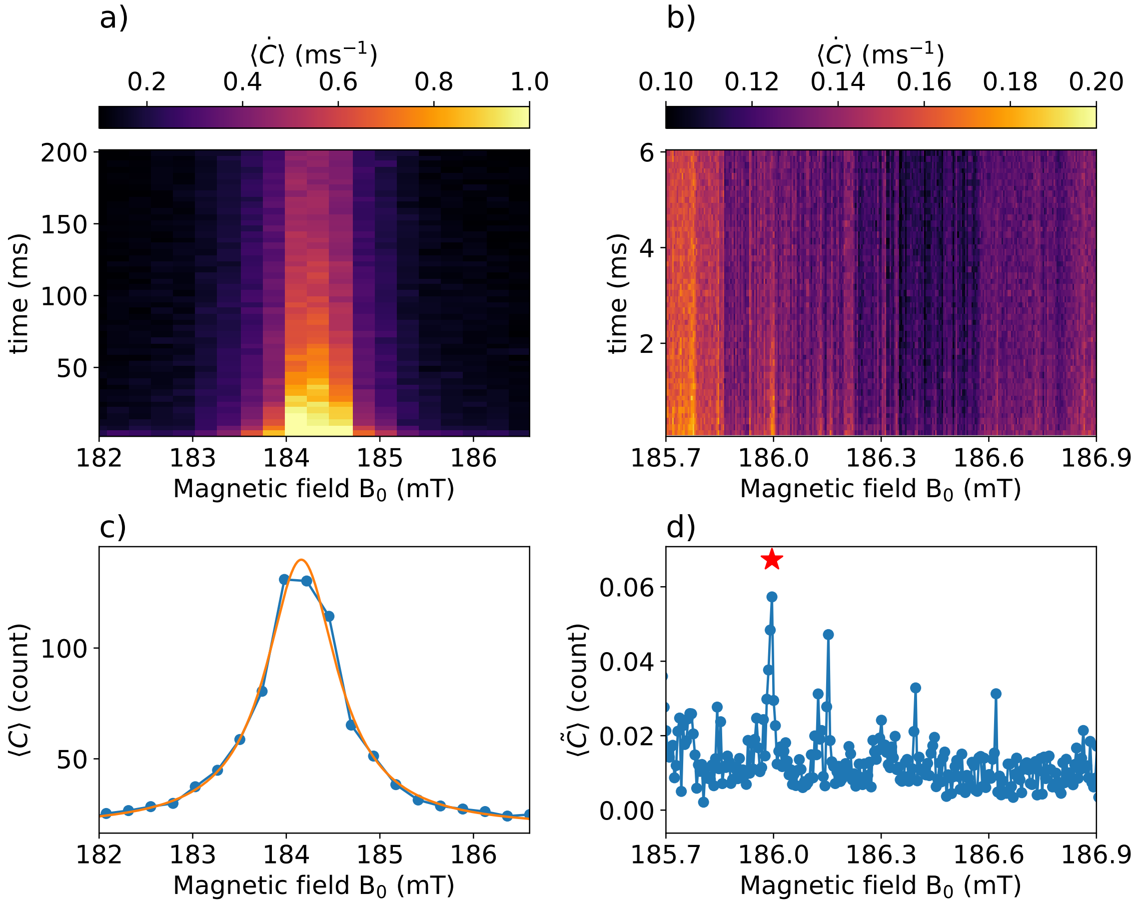

Figure 9.3: **High and Low power spectroscopy for $\theta = 18°$.** a) High power spectroscopy. The color map represents the SMPD click rate $\langle \dot{C} \rangle$ as the function of the magnetic field B_0 and the time. Note that the θ angle evolves from 17.93° to 17.46° during the spectroscopy b) Low power spectroscopy, same experiment realized at low power, θ evolves from 17.55° to 17.44°. c) Total number of count $\langle C \rangle$ integrated over 200 ms from (a) as the function of B_0. A Gaussian fit allows to extract the FWHM = 0.92 mT and the center of the erbium line: $B_0^{\text{center}} = 184.2$ mT. d) Total number of count integrated over 2.5 ms from (b). The peaks represent single ion. The red star shows the spin located at $B_0 = 185.996$ mT, selected for the following experiment.

electronic spin should therefore have as short a radiative lifetime as possible to reduce the acquisition time. The choice of spin was based on these two criteria.

9.1.4.1 Rabi oscillations

We first realize the calibration of the Rabi oscillations as in Section 8.4.1.1. The experiment consists in recording the average background corrected number of clicks $\langle \tilde{C} \rangle$ as the function pulse duration for different drive amplitudes. varying the drive amplitude and The integration time is fixed to $T_{\text{int}} = 1.9$ ms.

The results of the calibration are presented in Figure 9.4. We apply 5 different amplitudes expressed in arbitrary units (left panel). For each of them, we extract the frequency which increases linearly with the amplitude, as shown in the right panel. This linear relation allows us to calibrate precisely the amplitude-frequency transformation.

An interesting feature appears on Figure 9.4. The contrast of the Rabi oscillations associated with the third amplitude considered (amp=0.39) is greatly reduced, causing the

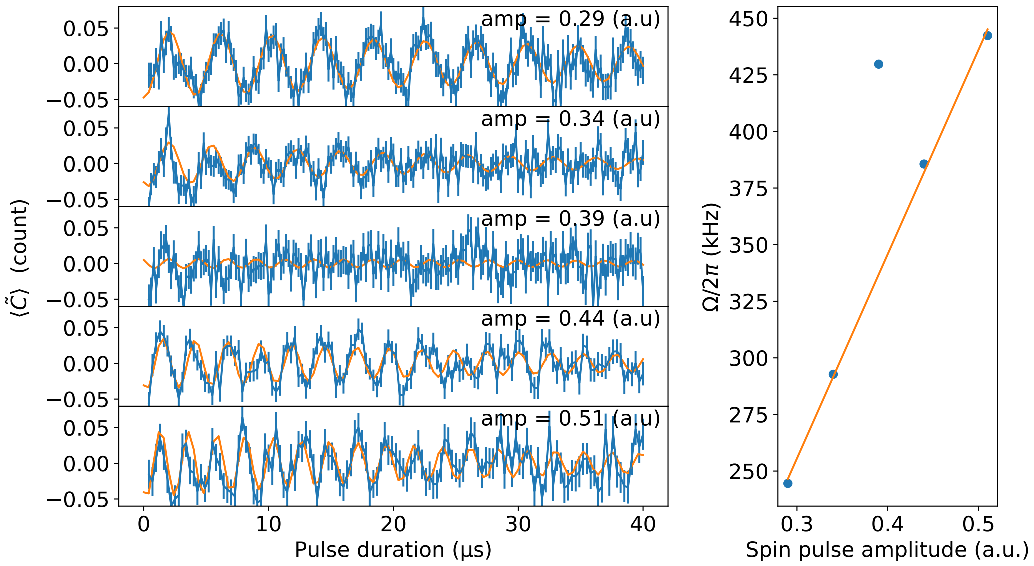

Figure 9.4: **Rabi oscillation for different drive amplitude**. Rabi experiment for different drive amplitude. Left panel, average background corrected number of clicks $\langle\tilde{C}\rangle$ as the function pulse duration for 5 amplitudes ranging from 0.29 a.u to 0.51 a.u. Blue lines are data, solid orange lines correspond to sinusoidal fit from which we extract the oscillation frequency. The contrast on the 0.39 amplitude is greatly reduced due to the interaction with the ^{183}W nuclear spins. Right panel, Rabi frequency as the function to the drive amplitude allowing to calibrate the amplitude-frequency relation. the outlier corresponding to the 0.39 amplitude is not taken into account.

fit to fail. According to the linear fit realized on the 4 valid point, this particular amplitude corresponds to a Rabi frequency $\Omega/2\pi = 336$ kHz which is very close to the nuclear spin Larmor frequency $\omega_{\mathrm{L}}/2\pi = 332$ kHz expected for $B_0 = 185.996$ mT.

This phenomena can be interpreted as the manifestation of the Hartman-Hahn double resonance which occurs between two spins with distinct energy separation when one spin is driven with a Rabi frequency equal to the energy scale of the other spin [HH62]. In our case, for the specific amplitude of 0.39 a.u, the Rabi frequency of the electron spin corresponds to the Larmor frequency of one or more ^{183}W nuclear spin of its immediate surroundings. Energy can therefore be exchanged during the sequence, which yields a collapse of the contrast of Rabi oscillations.

This is the first indication of the ability of our experiment to detect the ^{183}W nuclear spins surrounding a particular Er^{3+} ion.

9.1.4.2 Radiative relaxation and free induction decay time

The experiments realized to measure the different coherence times are similar to the one describe in Chapter 8.

From the last section, we define the π-pulse by using an amplitude of 1 a.u. In this condition, we avoid the double resonance effect thanks to a Rabi frequency $\Omega/2\pi = 890$ kHz.

Then we measure the radiative relaxation time of the spin $T_1 = 1.57$ ms (see Figure 9.5b. This value is comparable to the one found when $\boldsymbol{B_0}$ is aligned along the c-axis. We prospected several spins before finding this one with an acceptable T_1.

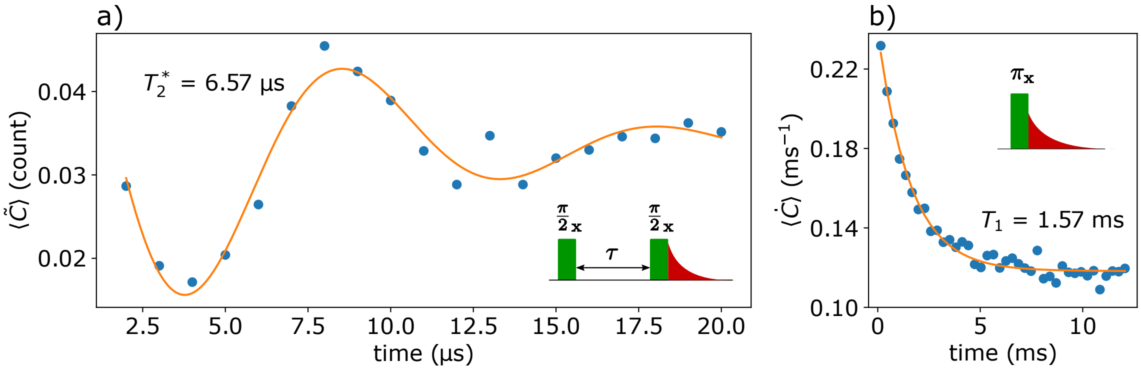

Figure 9.5: T_1 **and** T_2^*. a) Ramsey experiment. Background subtracted number of count $\langle\tilde{C}\rangle$ as the function of time τ (see inset). The exponentially damped sinusoidal fit allows to extract the free induction decay time $T_2^* = 6.57$ μs. b) Energy relaxation: measured average count rate $\langle\dot{C}\rangle$ as a function of delay after a resonant $\pi-$pulse yielding to $T_1 = 1.57$ ms.

We then measure the free induction decay (FID) time thanks to a Ramsey sequence. Figure 9.5a shows the result of the experiment yielding to $T_2^* = 6.6$ μs. This FID decay time is significantly lower than that observed in Chapter 8. This could be due to several causes such as the stronger coupling to the nuclear spin bath or the effect of a close interface. We discuss this point in the next sections.

9.1.4.3 Hahn echo and dynamical decoupling experiment

We now move to dynamical decoupling experiments in order to decouple the spin from its environment. We study the evolution of the coherence time as the function of the number N_π of refocusing pulses applied in a Carr-Purcell-Meiboom-Gill (CPMG) sequence described in Figure 9.6a.

When $N_\pi = 1$, we retrieve the Hahn-Echo sequence. Contrary to the Chapter 8 we alternate the phase of the last $\pi/2$-pulses in order to project the final state either on the ground or on the excited state. This phase-cycling technique makes the experiment less sensitive to the background noise fluctuations. A typical signal is sketched in Figure 9.6b for an echo sequence. The projection on the ground (resp. excited) state will be noted $\langle C\rangle_{|0\rangle}$ (resp. $\langle C\rangle_{|1\rangle}$). The contrast $\langle C\rangle_{|1\rangle} - \langle C\rangle_{|0\rangle}$ drops to zero when coherence is completely lost, as the state phase becomes less well defined with time.

Figure 9.6c shows the contrast as the function of the time for different number N_π of refocusing pulses. A Gaussian function multiplied by an exponential decay of the parameter $2T_1$ is used to extract the coherence time. As expected, the coherence time increases as a function of the number of pulses. For $N_\pi = 16$, the coherence time reaches 1.5 ms, which is well below the intrinsic limit fixed by $2T_1 = 3.14$ ms. However, we can show that the coherence time follows a scaling law in $N_\pi^{1/2}$ (see Figure 9.6d) which allows us to estimate that the limit $T_2 \approx 3$ ms could be reached around $N_\pi = 70$.

This scaling law carries information about the source of the noise. It has been shown that if the noise power spectrum $S(\omega)$ scales as $1/\omega^\alpha$ (generic model to describe the magnetic noise causes by surface spin), the coherence time should scale as N_π^γ with $\gamma = \alpha/(1+\alpha)$ [YSH11; ÁS11; Med+12].

Our measurement thus points to a $1/f$ noise spectrum. Such a spectrum has already been observed for NV centers close to the diamond surface (therefore, probing surface magnetic noise) [Mye+14] as well as in semiconducting quantum dots subjected to charge noise originating from the silicon/silicon oxide interface [Yon+18].

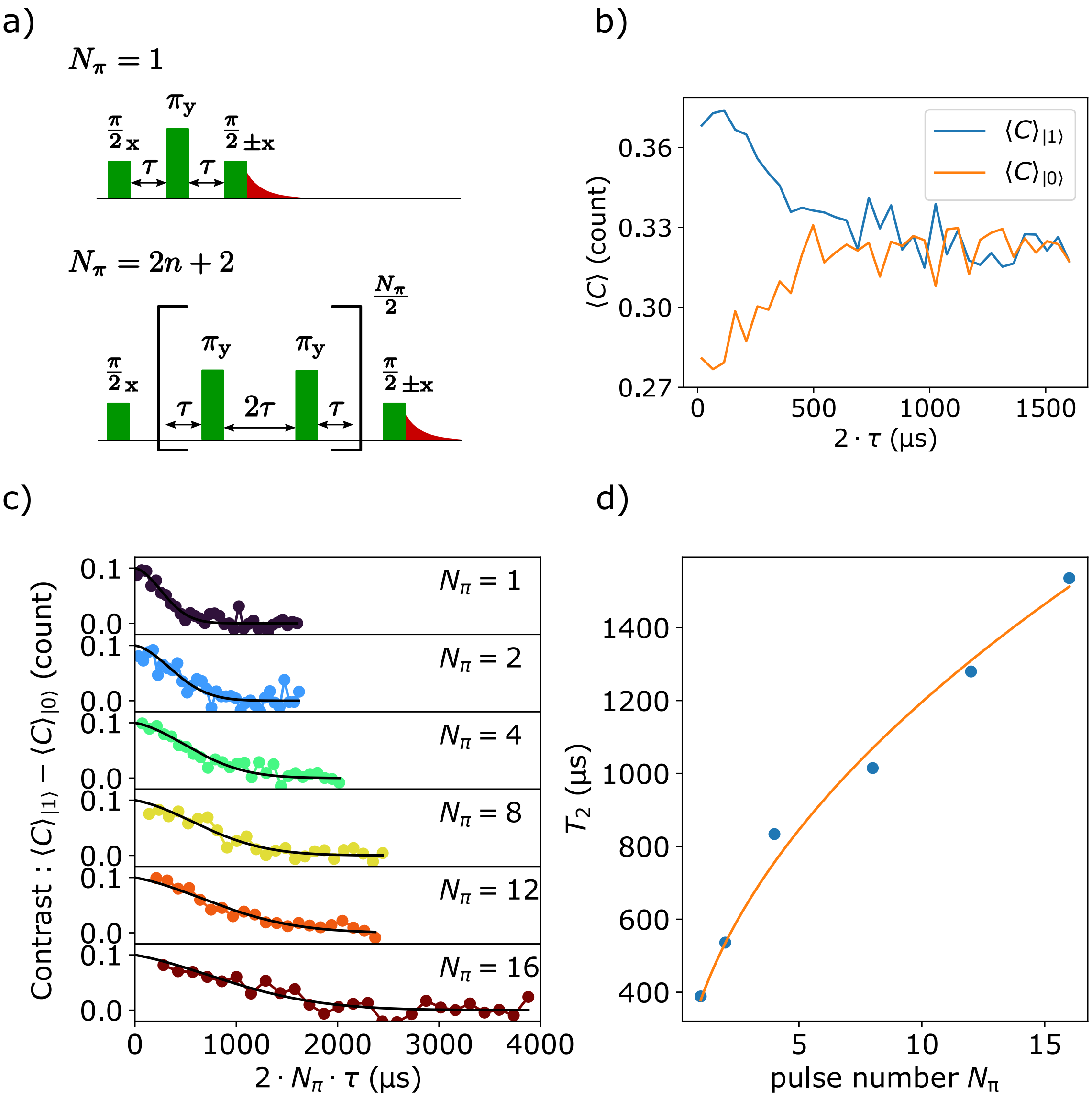

Figure 9.6: **Spin coherence with Dynamical Decoupling (DD) sequence**. a) Dynamical decoupling sequence for $N_\pi = 1$ (corresponding to an echo sequence) and $N_\pi = 2n+2$ with phase cycling. b) Raw data of an echo sequence applied on the selected spin. The two average number of counts coming from the phase cycle, $\langle C\rangle_{|1\rangle}$ (blue) and $\langle C\rangle_{|0\rangle}$ (orange) are shown as a function of the time 2τ. The coherence is lost when the two curves meet c) Contrast $\langle C\rangle_{|1\rangle} - \langle C\rangle_{|0\rangle}$ as the function of the time $2N_\pi\tau$ for different number N_π of refocusing pulses. We fit the data with the function $\exp(-t/T_1)\exp([-t/T_2]^2)$. d) T_2 as the function of N_π. The evolution of the coherence time follows a square root dynamic (orange line) of the pulse number.

This tends to indicate that the selected spin is close to the surface and that its free induction decay (FID) time could be intrinsically limited by fluctuators (electrical or magnetic) present at an interface (crystal/metal or crystal/air), which would explain its rather small value ($T_2^* = 6.6\ \mu$s see Section 9.1.4.2). However, another parameter limiting the FID time could also be the stronger coupling to the nuclear spin bath. It has indeed also been shown for NV centers that the nuclear spin bath can limit the FID time [Lon+13].

We will provide more details on the interaction between the electron spin and its nuclear ^{183}W spin environment in the next section as well as in Appendix A.

9.2 Nuclear spin detection with dynamical decoupling sequence

As stated in the introduction to this chapter, the ^{183}W nuclear spin detection experiments we will carry out are motivated by what has already been done on the diamond NV centers to detect the ^{13}C nuclear spins. In this section, we perform experiments based on a dynamical decoupling sequence conducted in 2012 by 3 different groups [Tam+12; Kol+12; Zha+12].

Initially we used a so-called XY-4 sequence as done in the references cited above (see Appendix B). However we realized [Lor+15] that this particular sequence could cause the appearance of an artifact. We therefore prefered to use a CPMG sequence without pulse phase change, the comparison between the sequences will be made in the last section.

9.2.1 Principle of the CPMG experiment and simulation

9.2.1.1 Unitary evolution of the system system during a CPMG sequence

The application of a dynamical sequence (see Figure 9.7a) such as the CPMG to the electron spin affects the state of the coupled nuclear spins by changing their quantization axes. Each time a refocusing pi pulse (assumed to be infinitely short in this section) is applied, the electron spin state changes and the nuclear spin quantization axis moves from $\boldsymbol{m}_{\uparrow\downarrow}$ to $\boldsymbol{m}_{\downarrow\uparrow}$ (see Figure 9.1 and Figure 9.7b). When its quantization axis is changed, the nuclear spin will suddenly starts rotating around the new axis, as shown in Figure 9.7b. The successive rotation sequences on the Bloch sphere around both axes is approximatively equivalent to a rotation around the median axis of $\boldsymbol{m}_{\downarrow}$ and $\boldsymbol{m}_{\uparrow}$.

To represent the nuclear spin evolution we rewrite the Hamiltonian of the system given in Equation 9.3 as:

$$\hat{H} = |\uparrow\rangle\langle\uparrow| \otimes \hat{H}_{\uparrow} + |\downarrow\rangle\langle\downarrow| \otimes \hat{H}_{\downarrow} \tag{9.6}$$

with $\hat{H}_{\uparrow} = \hbar\omega_{\uparrow}\boldsymbol{m}_{\uparrow} \cdot \hat{\boldsymbol{I}}$ and $\hat{H}_{\downarrow} = \hbar\omega_{\downarrow}\boldsymbol{m}_{\downarrow} \cdot \hat{\boldsymbol{I}}$, the Hamiltonian driving the evolution of the nuclear spin as a function of the electron spin state.

From this expression we can write the unitary evolution of the nuclear spin during the CPMG sequence, which is composed of $N_\pi/2$ basic decoupling unit $\tau - \pi_{\mathrm{y}} - 2\tau - \pi_{\mathrm{y}} - \tau$.

The evolution during the CPMG sequence considering instantaneous pulses consists in free evolution of the nuclear spin with alternating electron spin state. Therefore the nuclear spin evolution depending on the initial state of the electron spin $|\uparrow\rangle$ or $|\downarrow\rangle$ is given by

$$\hat{U}_{\uparrow} = \left[\exp\left(\frac{-i\hat{H}_{\uparrow}\tau}{\hbar}\right)\exp\left(\frac{-i\hat{H}_{\downarrow}2\tau}{\hbar}\right)\exp\left(\frac{-i\hat{H}_{\uparrow}\tau}{\hbar}\right)\right]^{N_\pi/2} \tag{9.7}$$

$$\hat{U}_{\downarrow} = \left[\exp\left(\frac{-i\hat{H}_{\downarrow}\tau}{\hbar}\right)\exp\left(\frac{-i\hat{H}_{\uparrow}2\tau}{\hbar}\right)\exp\left(\frac{-i\hat{H}_{\downarrow}\tau}{\hbar}\right)\right]^{N_\pi/2}. \tag{9.8}$$

We can then write the evolution of the full electron-nuclear spin system during the CPMG sequence:

$$\hat{U}_{\mathrm{CPMG}} = |\uparrow\rangle\langle\uparrow| \otimes \hat{U}_{\uparrow} + |\downarrow\rangle\langle\downarrow| \otimes \hat{U}_{\downarrow} \tag{9.9}$$

Those nuclear spin evolution operators correspond to the composition of 3 elementary rotations on the nuclear spin Bloch sphere repeated $N_\pi/2$ times (see Figure 9.7b for an illustration). Since any composition of multiple rotations can be reduced to a single equivalent rotation, we can write $\hat{U}_\uparrow$ and $\hat{U}_\downarrow$ as:

$$\hat{U}_\uparrow = \left[\exp\Big(-i\phi(\hat{\boldsymbol{I}} \cdot \boldsymbol{n}_\uparrow)\Big)\right]^{N_\pi/2} \tag{9.10}$$

$$\hat{U}_\downarrow = \left[\exp\Big(-i\phi(\hat{\boldsymbol{I}} \cdot \boldsymbol{n}_\downarrow)\Big)\right]^{N_\pi/2}. \tag{9.11}$$

where $\boldsymbol{n}_\downarrow$ and $\boldsymbol{n}_\uparrow$ are the equivalent axis of rotation depending on the electron spin state and ϕ is the angle of rotation during a basic decoupling unit (see Figure 9.7c). The expression of $\boldsymbol{n}_\downarrow$, $\boldsymbol{n}_\uparrow$ and ϕ can be calculated by composing the 3 elementary rotations. The reader can find the full derivation in the supplemental material of [Kol+12]. The resulting expression are:

$$\begin{aligned}\boldsymbol{n}_\uparrow = &- \boldsymbol{m}_\uparrow \sin(\omega_\uparrow\tau)\cos(\omega_\downarrow\tau) - \boldsymbol{m}_\downarrow \sin(\omega_\downarrow\tau)\cos(\omega_\uparrow\tau) \\ &+ 2\boldsymbol{m}_\uparrow \times (\boldsymbol{m}_\uparrow \times \boldsymbol{m}_\downarrow)\sin^2(\omega_\uparrow\tau/2)\sin(\omega_\downarrow\tau)\end{aligned} \tag{9.12}$$

$$\begin{aligned}\boldsymbol{n}_\downarrow = &- \boldsymbol{m}_\uparrow \sin(\omega_\uparrow\tau)\cos(\omega_\downarrow\tau) - \boldsymbol{m}_\downarrow \sin(\omega_\downarrow\tau)\cos(\omega_\uparrow\tau) \\ &+ 2\boldsymbol{m}_\downarrow \times (\boldsymbol{m}_\downarrow \times \boldsymbol{m}_\uparrow)\sin^2(\omega_\downarrow\tau/2)\sin(\omega_\uparrow\tau)\end{aligned} \tag{9.13}$$

$$\cos\phi = \cos(\omega_\uparrow\tau)\cos(\omega_\downarrow\tau) - \boldsymbol{m}_\downarrow \cdot \boldsymbol{m}_\uparrow \sin(\omega_\uparrow\tau)\sin(\omega_\downarrow\tau) \tag{9.14}$$

as expected, the angle ϕ is equivalent for both conditional operators due to the trace properties: $\mathrm{Tr}\hat{U}_\uparrow = \mathrm{Tr}\hat{U}_\downarrow = \cos N_\pi\phi/2$. The conditional nuclear Larmor frequencies $\omega_\downarrow$ and $\omega_\uparrow$ and the conditional quantization axis are given in Equation 9.5.

The interesting thing about these expressions is the dependence of τ on both the angle of rotation ϕ and the axis of rotation. We can modulate the impact of the CPMG sequence on the nuclear spins by changing the inter-pulse delay. From their point of view, the CPMG sequence consists of a rotation of the angle $N_\pi\phi/2$ around an axis ($\boldsymbol{n}_\uparrow$ or $\boldsymbol{n}_\downarrow$) that depends on the initial electron spin state. The Equation 9.9 can be rewritten as:

$$\hat{U}_{\mathrm{CPMG}} = |\uparrow\rangle\langle\uparrow| \otimes \exp\left(-i\frac{N_\pi}{2}\phi(\hat{\boldsymbol{I}} \cdot \boldsymbol{n}_\uparrow)\right) + |\downarrow\rangle\langle\downarrow| \otimes \exp\left(-i\frac{N_\pi}{2}\phi(\hat{\boldsymbol{I}} \cdot \boldsymbol{n}_\downarrow)\right) \tag{9.15}$$

In the next section, we show how to retrieve information about the nuclear spin evolution from the electron spin state.

9.2.1.2 Nuclear-electron spin entanglement

In the previous section, we showed that the application of a DD sequence on the electron spin allows us to drive the nuclear spin, and to apply rotations. However since the two spins are coupled, the electron spin is also impacted. This can be used to extract information about the nuclear spin state.

Concretely, in the absence of nuclear spin and assuming that there is no relaxation process, the electron spin will be in the state $|x\rangle = 1/\sqrt{2}(|\uparrow\rangle + |\downarrow\rangle)$ at the end of the DD sequence. On the contrary, if energy is exchanged during the sequence between the Er^{3+} ion and the ^{183}W nuclear spin bath the final state will be modified. This idea can be expressed mathematically by calculating the probability to find the electron spin in the $|x\rangle$ state at the end of the sequence.

The initial state of the electron-nuclear spin system is: $\hat{\rho}_{\mathrm{initial}} = |x\rangle\langle x| \otimes \hat{\rho}_{\mathrm{N}}$, where $\hat{\rho}_{\mathrm{N}} = 1/2 \cdot \mathbf{1}$ represents our lack of knowledge of the initial state of the nuclear spin. We are in a situation where the nuclear bath is unmonitored. The application of the evolution operator $\hat{U}_{\mathrm{CPMG}}$ to this state yields to:

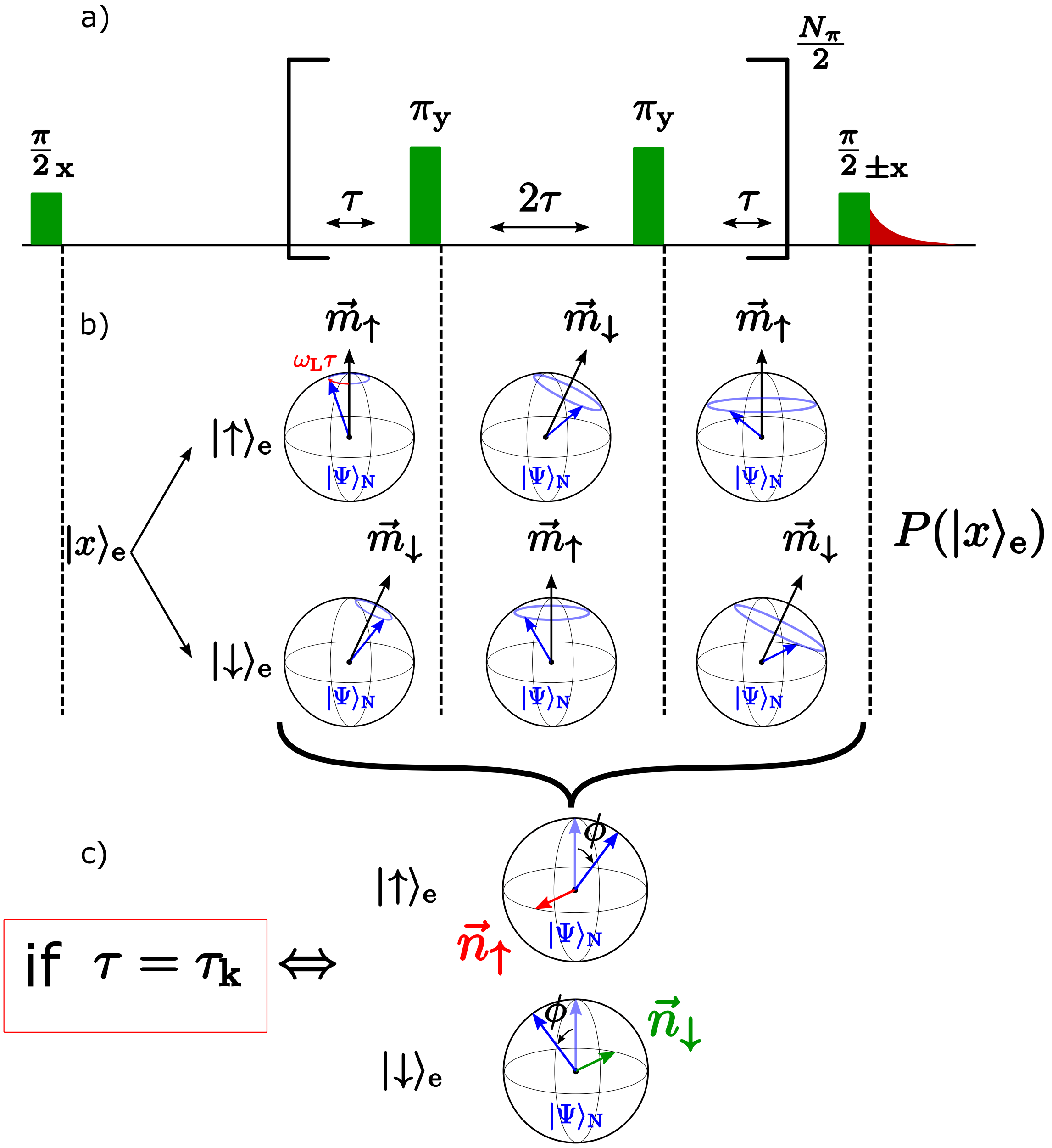

Figure 9.7: **Principle of a Dynamical Decoupling experiment**. a) Dynamical decoupling sequence applied on the electron spin. b) evolution of the nuclear spin during the dynamical decoupling sequence. The initial $|x\rangle$ state of the electron spin creates two different paths of for the evolution of the nuclear spin represented by the Bloch sphere. The successive π-pulse change the nuclear spin quantization axis ($\vec{m}_\uparrow$ or $\vec{m}_\downarrow$) which causes it to deviate from its course, this deviation depends on the time τ between the $\pi-$pulses. The information on the final state of the nuclear spin is recovered by the probability P_x of finding the electron in its initial state $|x\rangle$. c) For an optimal $\tau = \tau_k$, the effect of the pulses on the nuclear spin is optimal. The sequence corresponds to an unitary rotation of angle ϕ on the nuclear spin Bloch sphere with opposite rotation axis depending on the electron spin state

$$\hat{\rho}_{\text{final}} = \hat{U}_{\text{CPMG}} \left(|x\rangle \langle x| \otimes \hat{\rho}_{\text{N}}\right) \hat{U}^{\dagger}_{\text{CPMG}} \tag{9.16}$$

$$\hat{\rho}_{\text{final}} = \frac{1}{4}(\mathbf{1} \otimes \mathbf{1} + |\uparrow\rangle \langle\downarrow| \otimes \hat{U}_{\uparrow}\hat{U}^{\dagger}_{\downarrow} + |\downarrow\rangle \langle\uparrow| \otimes \hat{U}_{\downarrow}\hat{U}^{\dagger}_{\uparrow}). \tag{9.17}$$

The probability to find the electron spin in the $|x\rangle$ state is calculated by tracing on the nuclear spin degree of freedom:

$$P_{\text{x}} = \langle x| \operatorname{Tr}_{\text{N}}(\rho_{\text{final}}) |x\rangle . \tag{9.18}$$

As the partial trace deals only with the nuclear degree of freedom, one can commute the operation $\langle x| \cdot |x\rangle$ and $\operatorname{Tr}_{\text{N}}$. We obtain the following expression of P_{x} :

$$P_{\text{x}} = \frac{1}{2} + \frac{1}{4}\operatorname{Tr}\left(\operatorname{Re}[\hat{\mathrm{U}}_{\uparrow}\hat{\mathrm{U}}_{\downarrow}]\right). \tag{9.19}$$

From the expressions of $\hat{U}_{\uparrow}$ and $\hat{U}_{\downarrow}$, one can calculate the expression of $\operatorname{Re}[\hat{U}_{\uparrow}\hat{U}_{\downarrow}]$, which yields to:

$$\boxed{P_{\text{x}} = 1 - \frac{1 - \boldsymbol{n}_{\uparrow} \cdot \boldsymbol{n}_{\downarrow}}{2} \sin\frac{N_{\pi}\phi}{2}.} \tag{9.20}$$

To get an idea of the behavior of this quantity, it is interesting to consider the simple case where the hyperfine interactions are very small compared to the Larmor frequency i.e. $\omega_{\text{L}} \gg A_{\perp}, A_{\parallel}$. In this high field approximation, the quantization axis simplify as $\boldsymbol{m}_{\uparrow\downarrow} \approx \pm A_{\perp}\omega_{\text{L}}\boldsymbol{e}_{\mathbf{x}} + \boldsymbol{e}_{\mathbf{z}}$ while the conditional Larmor frequencies simply reduce to the bare Larmor frequency: $\omega_{\uparrow\downarrow} \approx \omega_{\text{L}}$. With these values we can simplify the expression of the effective rotation axis $\boldsymbol{n}_{\uparrow}$ and $\boldsymbol{n}_{\downarrow}$ given in Equation 9.13 as:

$$\boldsymbol{n}_{\uparrow} = -2\sin(\omega_{\text{L}}\tau)\cos(\omega_{\text{L}}\tau)\boldsymbol{e}_{\mathbf{z}} + 4\frac{A_{\perp}}{\omega_{\text{L}}}\sin^{2}(\omega_{\text{L}}\tau/2)\sin(\omega_{\text{L}}\tau)\boldsymbol{e}_{\mathbf{x}} \tag{9.21}$$

$$\boldsymbol{n}_{\downarrow} = -2\sin(\omega_{\text{L}}\tau)\cos(\omega_{\text{L}}\tau)\boldsymbol{e}_{\mathbf{z}} - 4\frac{A_{\perp}}{\omega_{\text{L}}}\sin^{2}(\omega_{\text{L}}\tau/2)\sin(\omega_{\text{L}}\tau)\boldsymbol{e}_{\mathbf{x}} \tag{9.22}$$

With these new expressions, it straightforward to see that for most τ values, $\boldsymbol{n}_{\uparrow}$ and $\boldsymbol{n}_{\downarrow}$ are parallel, since $A_{\perp}/\omega_{\text{L}} \ll 1$. In this case, $\boldsymbol{n}_{\uparrow} \cdot \boldsymbol{n}_{\downarrow} \approx 1$ and therefore, $P_{\text{x}} \approx 1$. There is no modification of the probability to find the spin elsewhere than in its original position, the electron-nuclear spins interaction causes by the sequence is negligible.

However, for a set of τ values such as:

$$\boxed{2\tau_{k} = \frac{(2k+1)\pi}{\omega_{\text{L}}}} \tag{9.23}$$

where $k = 0, 1, 2...$ is the order of the resonance, the $\boldsymbol{e}_{\mathbf{z}}$ component of $\boldsymbol{n}_{\uparrow}$ and $\boldsymbol{n}_{\downarrow}$ cancel. In this case, the rotation axes are anti-parallel (see Figure 9.7c.), $\boldsymbol{n}_{\uparrow} \cdot \boldsymbol{n}_{\downarrow} = -1$ and $P_{\text{x}} = 1 - \sin(N_{\pi}\phi/2)$. This means that each $\pi-$pulse optimally changes the final state of the electron spin, and causes the nuclear spin to undergo the greatest possible rotation allowed by the perpendicular hyperfine parameter $A_{\perp}$. This phenomenon can be seen as an energy transfer, which causes an entanglement between the spins of which P_{x} is the witness. This entanglement varies as the function of the number N_{π} of refocusing pulses.

Intermediate conclusion:

To summarize these introductory sections, this experiment has two interesting features: it allows both the detection of nuclear spins through the τ_k resonance condition and their manipulation by varying the number of π-pulses N_π.

In a real crystal the electron spin is surrounding by a multitude of nuclear spins, their overlapping signal tends to yield $P_\mathrm{x} = 0.5$ for resonant τ. In the experiment carried out with the NV centers in diamond, it was possible to separate individual nuclear spins from this bath. Indeed, the NV center magnetic quantum number $m_\mathrm{s} \in [0, 1]$ breaks the symmetry of spin operators, which results in a dependence of τ_k on the hyperfine interaction.

On the contrary, the Er^{3+} ion has a spin 1/2, and τ_k is independent on the coupling (see Equation 9.23). Therefore, we do not expect to be able to dissociate individual spins from the bath.

9.2.1.3 Simulation of P_x

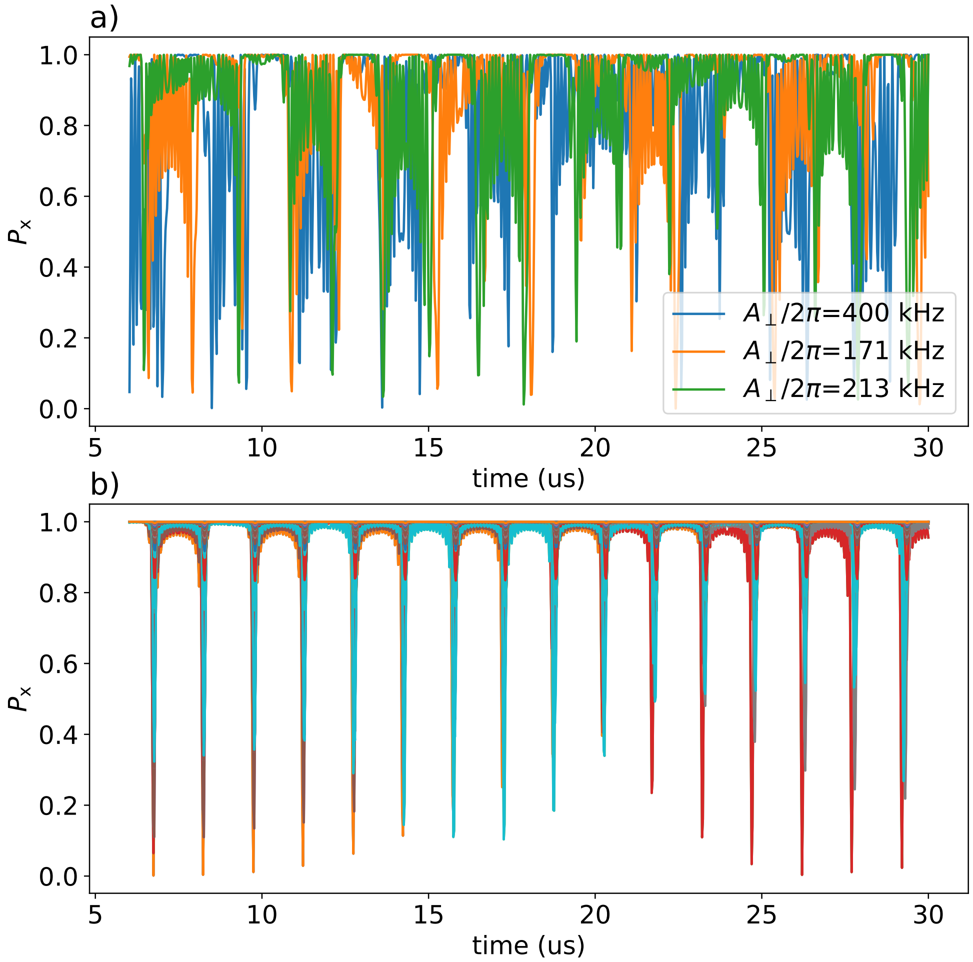

Figure 9.8: **Dynamical decoupling simulation**. a) Simulation of the probability P_x to find the electron spin in the $|x\rangle$ state after a Dynamical decoupling sequence when one W site is occupied by a ^{183}W atom. Only the 3 strongest perpendicular coupling $A_\perp$ are represented. b) Same simulation representing the 300 next stronger $A_\perp$.

From the calculation realized on the two previous sections, we can perform simulations of the probability to retrieve the electron spin in the $|x\rangle$ state at the end of the sequence.

We simply consider the interaction with a nuclear spin, which we place on the different possible W sites. In the real crystal, each W site has a probability of 0.145 (the natural abundance) to be occupied by a nuclear spin. The hyperfine coupling parameters associated with these sites have been simulated in Section 9.1.2.1.

As shown on Section 9.1.2.1d, 7 of the 8 closest sites will produce strongly coupled nuclear spin ($A_\perp/2\pi > 170$ kHz) if they are populated. On the other hand, from the spectroscopies realized in Section 9.1.3, we know that the magnetic working field at $\theta = 18°$ is $B_0 = 185$ mT which corresponds to $\omega_\mathrm{L}/2\pi = 332$ kHz. This involves that in particular for this 7 sites the resonant time is not well defined because the high field assumption is not satisfied. The simulation indeed confirms this result as shown on Figure 9.8a where we simulate the DD signal produced for $N_\pi = 16$ by the spins with the 3 highest $A_\perp$.

On the contrary, the high field regime applies to all the other sites where the coupling does not exceed $A_\perp/2\pi = 70$ kHz. The Figure 9.8b represents the simulated signal produced by the 300 next nuclear spins. The dips are located precisely at τ_k following Equation 9.23.

The consequence of this simulation is that it should be possible to detect immediately whether one of the 7 sites producing highly coupled nuclear spins is occupied or not by a nuclear spin. The behavior of the nuclear spin population will be well separated into two categories.

On the other hand, as expected, we do not see any individual nuclear spin dissociation from the bath due to the Er^{3+} spin one half. All the nuclear spins share the same resonance condition Equation 9.23

9.2.2 First detection of ^{183}W nuclear spin

In this section, we detail the dynamic decoupling (DD) measurement performed with the Er^{3+} ion characterized in the last section. A clear signal from the nuclear spin ^{183}W is observed. We then carry out a study of the variation of P_x as a function of the number of $\pi-$pulses at resonance.

9.2.2.1 Non adiabatic transformation of the quantization axis

A necessary condition for successfully changing the nuclear spin state by alternating its quantization axis between two situations is that the rate of evolution of the axis is large compared to its Larmor frequency $\omega_\mathrm{L}/2\pi = \mu_\mathrm{N} g_\mathrm{W} B_0 = 332$ kHz for $B_0 = 185.996$ mT [RHM65]. Otherwise, the evolution is adiabatic and the nuclear spin simply follows the tilt of the axis as it moves, remaining in its ground state. To change the state we need a non-adiabatic modification. the duration of the π-pulse applied on the electron spin must noticeably be shorter than a Larmor period $T_\mathrm{L} = 2\pi/\omega_\mathrm{L} = 3$ μs.

Alternatively, we can consider this problem from a frequency point of view base on the energy diagram presented in Figure 9.9a,b. To induce a flip-flop between the spins, the frequency broadening of the π-pulse must be sufficient to reach the forbidden transition (in red in Figure 9.9b). In the high field limits $\omega_\mathrm{L} \gg A_\perp, A_\parallel$, these transitions are shifted by ω_L from the electron spin frequency. The π-pulse has therefore to be broader than the Larmor frequency ω_L.

From this point of view it is interesting to use a non zero θ angle. Indeed, by increasing the effective Landé factor $\mathrm{g_{eff}}$, the magnetic field required to bring the electron spin into resonance with the superconducting cavity is reduced. The Larmor frequency of the nuclear spin follows linearly with this reduction, relaxing the experimental constraints.

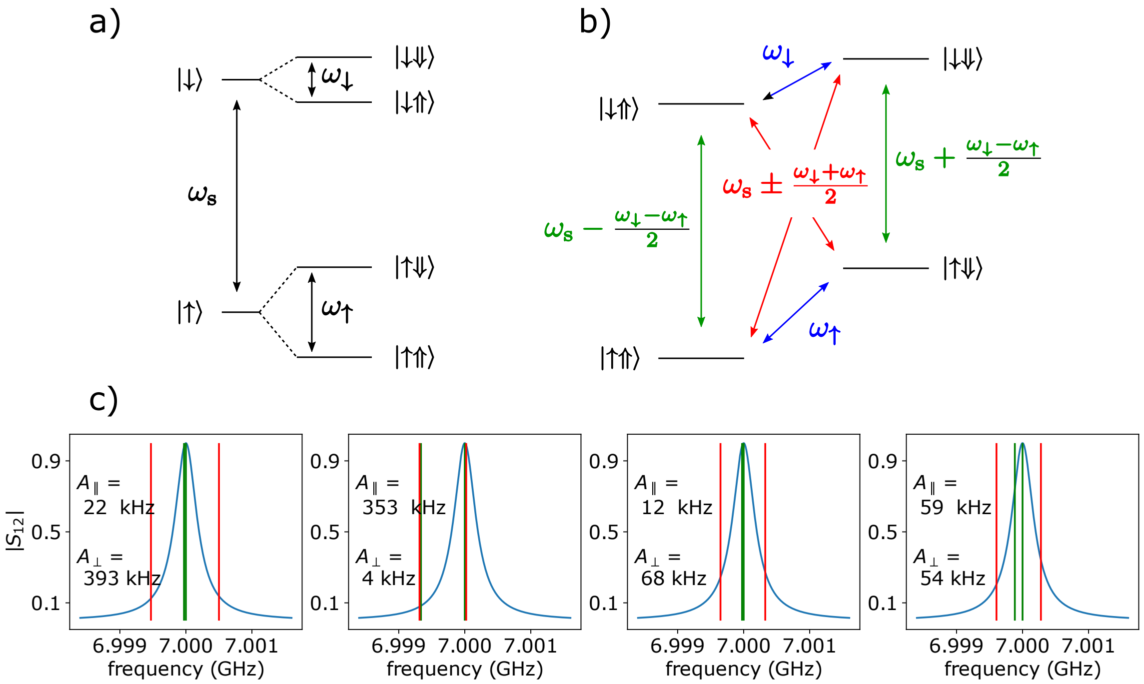

Figure 9.9: **Energy diagram**. a) Energy diagram of the electron spin and the nuclear spin. b) Energy transition between the hybridized states. $\omega_{\downarrow\uparrow}$ are the nuclear frequency re normalized by the electron state. Green transition and blue transition represent individual spin flip. Red transitions represent a collective transition of the spins allowed by the transverse hyperfine coupling term $A_\perp$. c) Illustration of the filtering issue. The S_{21} parameter amplitude of a 7 GHz resonator of width 400 kHZ is represented as the function of the frequency. The spin transition $|\uparrow\Uparrow\rangle \leftrightarrow |\downarrow\Uparrow\rangle$ is put at resonance with the cavity. Green and red vertical transitions represent the transitions for 4 ^{183}W located on 4 different sites.

Experimentally, we set the π-pulse duration to 700 ns which constitute a trade-off between a fast enough pulse and an acceptable rate of spurious thermal photon generated by the high energy microwaves sent to the fridge.

9.2.2.2 Pulse filtering caused by the superconducting resonator and finite length

An additional experimental consideration comes from the the superconducting resonator that allows to couple the electron spin to the microwave line. At 186 mT, its total linewitdh is $\kappa_t/2\pi = 401$ kHz (see Figure 8.4).

This provokes a filtering of the control-pulses which that could compromise our ability to control nuclear spin. Indeed, the nuclear spin Larmor frequency being $\omega_L = 332$ kHz, the flip-flop transition are located on the edges of resonance. More problematically, for the nuclear spins closest to the electronic spin, we have seen in Section 9.1.2.1 that the coupling is of the order of more than a hundred kHz. This reinforces the shift between the centre frequency and the forbidden frequencies as illustrated on Figure 9.9c. These strongly coupled nuclear spins could therefore be impossible to address.

In addition, compare to the experiment performed via optically transition, the duration of our $\pi-$pulse (700 ns) is not small compare to the precession time $2\pi/\omega_L = 3$ μs. This could cause a non-canonical behaviour of the dynamical decoupling experiment.

These two potential issues are not addressed in this thesis and will be the subject of future work in the group. As the reader is aware of the limitations of the experiment, the result of the nuclear spin detection is presented in the next section.

9.2.2.3 CPMG sequence

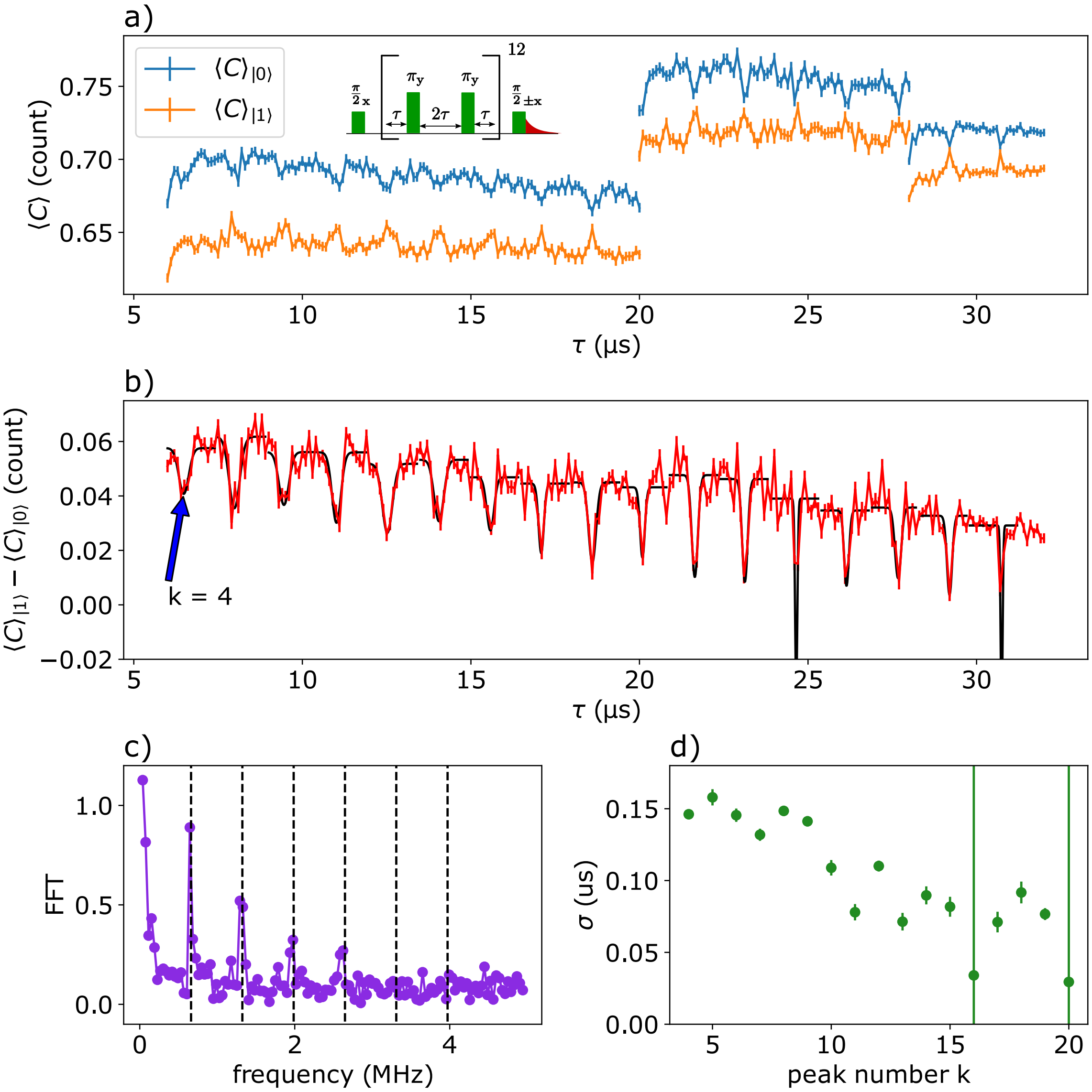

Figure 9.10: **Dynamical decoupling experiment** $N_\pi = 24$. a) Dynamical decoupling experiment based on a 24-pulses CPMG sequence (see inset). The average count plotted as the function of the time τ shows the projection of electron spin on final state on the ground $\langle C\rangle_{|0\rangle}$ and on the excited state $\langle C\rangle_{|1\rangle}$ (phase cycling). The curves are from 3 different data sets which explains the 3 different offsets. b) Contrast between the two projections representing the probability P_x to retrieve the electron state in its initial state, the dips spaced by $\Delta\tau = \pi/\omega_L = 1.52$ μs are caused by interaction with the ^{183}W nuclear spin bath. The first dip at $\tau_4 = 6.44$ μs is the fourth order resonance. Red lines are data, solid black lines are Gaussian fit of each dips c) Fourier transform of the contrast. The harmonics are spaced by $\Delta f = 1/\Delta\tau = \omega_L/\pi = 664$ kHz. d) Evolution of dips witdh extracted from Gaussian fit as the function of the order of resonance k.

In this section we perform a dynamical decoupling experiment with a CPMG sequence (corresponding to Figure 9.7a). $N_\pi = 24$ π-pulses are applied on the electron spin described in the previous section.

As for the the measurement of the coherence time depicted in Section 9.1.4.3 we use a phase cycling to project the final electron spin state on $|0\rangle$ or $|1\rangle$. The results presented in Figure 9.10 are from 3 different data sets, which explains the different count offset coming from a variation of the SMPD dark count between the experiment.

Figure 9.10a are the raw data showing the two projections of the phase cycling $\langle C\rangle_{|1\rangle}$ and $\langle C\rangle_{|0\rangle}$. On Figure 9.10b we plot the contrast $\langle C\rangle_{|1\rangle} - \langle C\rangle_{|0\rangle}$. This contrast is proportional to P_x the probability to find the electron in the $|x\rangle$ state at the end of the sequence (see Section 9.2.1.2). Several regularly spaced dips appear, the measurement starting from $\tau = 6\ \mu$s, the first dip corresponds to $k = 4$. The contrast baseline decreases to zero during the experiment due to the loss of coherence (see Section 9.1.4.3).

The separation $\Delta\tau = \tau_{k+1} - \tau_k = 1.52\ \mu$s between the dips can be expressed by using the Equation 9.23 as $\Delta\tau = \pi/\omega\mathrm{L}$. The corresponding frequency $\omega/2\pi = 1/(2\Delta\tau) = 332$ kHz matches perfectly the expected ^{183}W Larmor frequency which is also visible on the FFT signal (see Figure 9.10c).

The pattern of dips being regular, we know from the simulations realized in Section 9.2.1.3 that the closest site of W are not populated by ^{183}W. Moreover, as expected, we do not see individual peaks separating from the bath.

Finally, we fit each dips with a Gaussian function to estimate their width σ that we plot as the function of k in Figure 9.10d. Counter-intuitively, the width of the dips decreases when one would expect them to widen [Tam+12; Kol+12]. We do not yet understand this phenomenon, and we lack the data to try to explain it.

9.2.2.4 Variation of the pulse number at fixed τ

In this section, we select the dip $k = 6$ and we vary the number of π-pulses applied on the electron spin. If coherent interactions take place between the electron spin and a nuclear spin, we should obtain a population inversion i.e. P_x should reach 0 for a certain N_π.

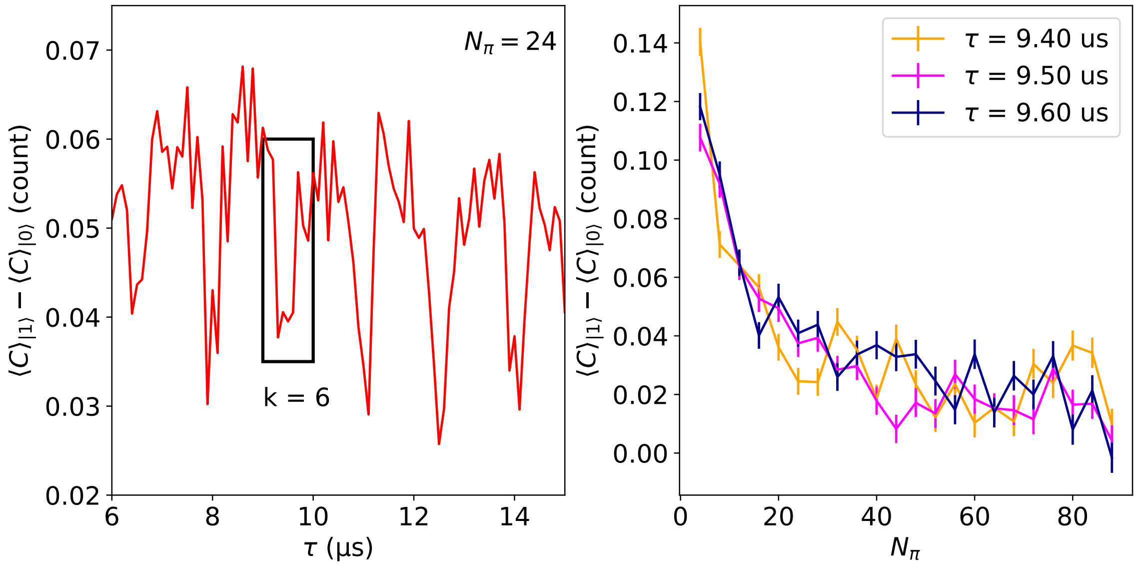

Figure 9.11: **Variation of N_π for k = 6**. a) Magnification of the signal presented in Figure 9.10b, The dip located at $\tau_6 = 9.5\ \mu$s is selected to measure the effect of the variation of N_π. b) Contrast as the function of the number of refocusing pulses N_π for 3 different τ centered on the sixth dips. The contrast saturates around 0 for the 3 τ corresponding to $P_\mathrm{x} = 0.5$.

In term of contrast, this means that $\langle C\rangle_{|1\rangle}$ - $\langle C\rangle_{|0\rangle}$ would become negative. Figure 9.11 shows the result of the experiment, we follow 3 points located near to the lowest level of the dip. As shown on the right panel, no population inversion takes place, on the contrary, the contrast saturates at 0, which corresponds to $P_\mathrm{x} = 0.5$. This typically corresponds to the signal produced by the spin bath where a multitude of individual signals overlap and cause P_x to tend towards ≈ 0.5.

This definitely confirms that we cannot access coherent control of an individual nuclear spin with this experience.

9.3 Conclusion

In this chapter, we show that the ability to measure a single Er^{3+} electron spin allows access to its local magnetic environment. In particular, we detect the bath of $^{183}\mathrm{W}$ nuclear spin using a pulsed dynamical decoupling method. The detection is based on the measurement of the electron spin coherence, which collapses when the pulse sequence puts the electron spin-flip in resonance with the nuclear spins. Here we push magnetic resonance detection to its ultimate limits of sensitivity. The oscillating field that will set the nuclear spin in motion is directly produced by the electron spin. Similar experiments have already been performed, but only for impurities with an optical transition [Tam+12; Riz+22]. Our method, on the other hand, is more general and applies to any type of impurity with a spin degree of freedom.

9.3.1 Experimental limitations

Contrary to a similar experiment realized with NV of diamond [Tam+12], here we do not access the individual nuclear spin control. This is due to the effective spin number $m_\mathrm{s} = 1/2$ of the Er^{3+} electron spin, which imposes the same resonance condition on all nuclear spins regardless of their hyperfine coupling to the electron spin. We therefore just have access to the signal due to the coupling between the electron spin and the overall nuclear spin bath.

In this experiment, we explore the potential of our detection method for the first time. The setup was not initially designed for this purpose, and we are operating at the limits of its detection sensitivity. In fact, we need two days of averaging to acquire the complete CPMG sequence shown in Figure 9.10b. The electron spin relaxation dynamics driven by the Purcell rate $\Gamma_\mathrm{p} \approx 0.63\ \mathrm{ms}^{-1}$ is too slow for faster acquisition, while the SMPD sensitivity $\mathcal{S} = 10^{-22}\ \mathrm{W}/\sqrt{\mathrm{Hz}}$ is not sufficient to decrease the amount of averaging required.

Moreover, we do not account for the non-ideality of the π-pulses due to the filtering imposed by the spin resonator. This could impact the detection of the most strongly coupled nuclear spins. To better understand these effects, numerical simulations are needed and will be conducted in another thesis project within our group.

In addition to the measures carried out in this chapter, we realized Hartman-Hahn double resonance experiment with the same electron spin (see Appendix A). Combined with the CMPG measurement, we can make some assumptions about the nuclear spin distributions on the surrounding tungsten sites (see Section A.6.1), notably that the 7 most coupled sites are not occupied. However, these hypotheses must be qualified in view of the experimental limitations mentioned above.

9.3.2 Perspectives

The potential for improvements in this experiment is vast.

Regarding acquisition time, both the SMPD performance and the Purcell rate can be enhanced. For the latter, several strategies can be employed, such as reducing the width of the nanowire to concentrate the magnetic field more intensely. Another option is to change the host crystal to increase the g-factor. For example, Er^{3+} in a TiO_2 crystal has a $\boldsymbol{g}$-tensor component almost twice as large as the $g_\perp$ of erbium in $CaWO_4$.

For individual nuclear spin manipulation, the spin resonator can be modified by adding Bragg mirrors to implement a radio-frequency drive. By applying a variant of the dynamical decoupling sequence using both microwave and radio frequency pulses, it becomes possible to address nuclear spins individually [Bra+19]. This experiment could lay the groundwork for a hybrid quantum computer that uses nuclear spins as memory and superconducting qubits as processors.

The prospects for quantum sensing are also quite promising. Individual control of nuclear spins could enable atomic-resolution imaging of a sample [Abo+19]. Given the generality of our detection method, it is conceivable to achieve atomic-resolution images of individual molecules, as long as they possess a spin degree of freedom.

Chapter 10

Conclusion

10.1 Detection of a single electron spin and its local environment by photon counting

This thesis describes the detection of single erbium ions embedded in a scheelite crystal by electron spin resonance techniques using a single microwave photon detector. The experiment, performed at 10 mK, is based on an interweaving of concepts, each experimental block gives access to the next concept, which in turn reveals another part of the experiment.

The first link in the chain is the use of a Travelling Parametric Wave Amplifier, to amplify the output signal by adding the minimum of noise allowed by quantum mechanics. Based on a chain of Josephson junction, it allows the single shot readout of superconducting qubit. This device has benefited greatly from the rapid development of the cQED field. In a few years it has grown from a research project to a common device used in numerous cQED experiments.

The second link is the single microwave photon detector. Based on a superconducting transmon qubit and a 4-wave mixing [Les+20], the concept of SMPD that we use in this thesis has already been proven to work in previous work of the group [Alb+21; Bil23]. However, the sensitivity of this initial design was not sufficient for single spin detection, and half the time of this PhD was spent improving the detector's performance by modifying its fabrication and architecture. At the end of the development, the new version of the SMPD had a sensitivity $\mathcal{S} = 10^{-22}$ W/$\sqrt{\text{Hz}}$ an order of magnitude better than the state of the art.

The third link is the superconducting resonator placed at the top of the scheelite crystal. Composed by a large interdigitated capacitor and a nanowire, it allows to force the radiative relaxation of the coupled spins by Purcell effect [Bie+16]. The new generation of resonators, developed in parallel of this thesis, imposed a relaxation rate of $\hbar\omega\Gamma_\text{P} = 3 \cdot 10^{-21}$ W. This emission power, combined with the new sensitivity of the photon counter, has made it possible to detect individual electron spins [Wan+23]. We showed that the SNR of the single spin detection reaches 1.9 for an integrating time of 1 s. Compared to other single spin detection methods, this method is applicable to all types of paramagnetic impurities and has a large detection volume ($\approx 10\ \mu\text{m}^3$). Furthermore, as it is based on the detection of the incoherent photon emitted by spontaneous emission, it does not require a long coherence time.

The fourth link is the electron spin itself. Once the single detection is achieved, it becomes a probe of its local magnetic environment mostly composed of ^{183}W nuclear spin 1/2 in CaWO_4 crystal. In this thesis, we demonstrated the feasibility to detect the bath of ^{183}W nuclear spin using dynamical decoupling technique.

10.2 Possible improvement of the experiment and prospects

This experiment represents the first demonstration of ESR spectroscopy for a single paramagnetic impurity. While the setup presented in this thesis is adequate for this purpose, it is not sufficient for single nuclear spin detection, which necessitates a higher overall sensitivity. As a pioneering effort, there is significant room for improvement.

10.2.1 SMPD improvements

Significant enhancements in sensitivity, $\mathcal{S} = \hbar\omega\sqrt{\alpha_\mathrm{d}}/\eta_\mathrm{d}$, are being achieved by the newest generation of devices under development in the laboratory.

A higher efficiency, η_d, can be reached by enhancing the T_1 of the transmon qubit. The rapid advancements in cQED are continuously pushing the boundaries of our understanding of transmon radiative losses. Presently, T_1 values of several hundred microseconds are routinely accomplished [Wan+22].

As for the dark count rate, α_d, it was demonstrated in the thesis that most false positives originated from thermal photons in equilibrium. The corresponding dark count formula is: $\alpha_\mathrm{th} = \bar{n}_\mathrm{b}\eta\mathrm{d}\kappa_\mathrm{d}/4$. To reduce this contribution, we could consider increasing the frequency of the resonators to decrease $\bar{n}$. Additionally, we could tune the detector bandwidth, κ_d, to adjust it to the source to be detected. This can be done by incorporating a SQUID into the buffer resonator Purcell filter. This adjustment to the filter frequency provides a natural degree of freedom for the resonator linewidth since the Purcell effect that connects the two components depends on their frequency detuning.

10.2.2 Spin-resonator coupling improvements and new features

The spin-resonator coupling $g_0 \propto \mathrm{g}\delta B$ is crucial in determining the experiment's sensitivity, as it gauges our capacity to swiftly extract information from the spin system. Increasing the confinement of the magnetic field δB can enhance the coupling, for example, by narrowing the nanowire's width, altering its shape, or more radically, considering a dual geometry where two current sheets create a magnetic field in a thin trench. A complementary approach involves increasing the resonator capacitance to produce a stronger current in the wire, which can be achieved by using a dielectric material with higher permittivity, such as $\mathrm{TiO_2}$, or by modifying the capacitor geometry to parallel plate capacitor for instance.

The coupling also depends on the Landé factor g, so the choice of the host crystal is essential. For example, if an Er^{3+} ion is embedded in a $\mathrm{TiO_2}$ crystal, one component of the **g**-tensor will be $\mathrm{g_{zz}} = 15.1$ [Err63], twice as large as $\mathrm{g}_\perp = 8$ in $\mathrm{CaWO_4}$. This would quadruple the Purcell rate and significantly reduce the acquisition time.

Modifications can also be made to the superconducting resonator atop the host crystal to introduce new features for nuclear spin detection. By incorporating a Bragg mirror with the spin resonator, it becomes possible to apply a radio frequency drive to the spin sample. In this case, individual nuclear spins can be addressed, as demonstrated in the NV center of diamond [Bra+19].

10.2.3 Let's dream a bit...

The ability to manipulate individual nuclear spins presents numerous potential applications in the medium term.

First, in terms of quantum sensing, the individual control of nuclear spins could enable 3D imaging of the local environment surrounding the impurity. This could be utilized to create atomically resolved 3D images of molecules by using either a native unpaired electron spin (e.g., metallic ions in metalloenzymes or radicals in molecules) or by deliberately implanting a paramagnetic impurity (see Figure 10.1b).

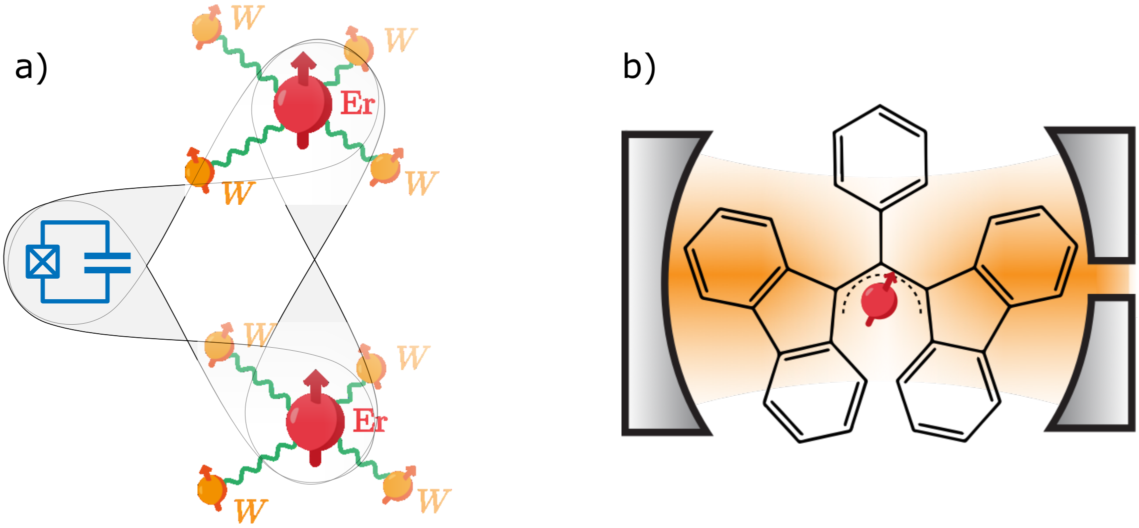

Figure 10.1: **Potential applications of single spin detection by ESR**.a) Hybrid quantum calculation. Based on the SMPD presented in this thesis, and hybrid quantum architecture using the nuclear spin as long-term memory can be considered. b) The electron spin is a powerful probe of its environment and can be used to create atomically resolved images of molecules.

Another intriguing possibility is to use the capability of addressing nuclear spins to create dense multi-qubit registers with potentially hour-long storage times, as already demonstrated with NV centers in diamond [Tam+14] and, more recently, with ytterbium ions in yttrium orthovanadate [Rus+21]. This could lead to the development of a hybrid architecture, where information is processed by superconducting qubits acting as processors, while the spins store quantum states (see Figure 10.1a).

The Quantronics Group plans to explore these various opportunities in the coming years.

Appendix A

Hartman Hahn double resonance (HHDR)

In this section, we perform another nuclear spin detection experiment based on a phenomenon known in nuclear magnetic resonance as the Hartmann-Hahn double resonance (HHDR) [HH62]. This effect allows two spins of different frequency to exchange energy coherently when driven at the same Rabi frequency via cross relaxation. Similarly this effect can occur when the Rabi frequency of one spin matches the Larmor frequency of the other.

In the experiment realized here, we drive the Er^{3+} electron spin with a Rabi frequency that matches the Larmor frequency of the surrounding $^{183}\mathrm{W}$ nuclear spins. As for the experiment presented in Chapter 9, this experiment has already been carried out in NV diamond centres [Lon+13]. It is the continuous version of the pulsed dynamical decoupling experiment based on CPMG sequence.

In this appendix, we demonstrate the ability to cool the nuclear spin bath using the HHDR. We also make some assumptions about the tungsten sites occupied by $^{183}\mathrm{W}$. As the data from this measurement campaign is less clear, we have decided to include it in the appendix.

A.1 Principle of the experiment

The experiment is based on the spin-locking sequence (see Figure A.1a). The electron spin is placed in the $|x\rangle = (|\uparrow\rangle + |\downarrow\rangle)/\sqrt{2}$ state with a $\pi_{\mathrm{x}}/2$-pulse, then a microwave drive along the $y-$axis is applied to lock its position.

The locked spin can be considered as a new two-level system whose energy difference corresponds to the Rabi frequency. From this point of view one can defined the energy relaxation time of this effective spin T_1^{ρ}, corresponding to the life time of the locked $|x\rangle$ state.

The system can also exchange energy with the environment. By calibrating the Rabi frequency such as it matches the Larmor frequency $\omega_{\mathrm{L}}/2\pi = 332$ kHz of the surrounding $^{183}\mathrm{W}$ nuclear spins, one can create a resonant coupling and therefore polarization exchange.

In the next section we describe this interaction quantitatively.

A.2 Hamiltonian and coherent evolution

One can describe the Hamiltonian of the experiment by introducing a drive term acting on the electron spin space in Equation 9.2. In the expression below, we place ourselves directly in the frame rotating at the drive speed:

$$\hat{H}/\hbar = \Omega \hat{S}_{\mathrm{x}} + \delta \hat{S}_{\mathrm{z}} + \omega_{\mathrm{L}} \hat{I}_{\mathrm{z}} + \hat{S}_{\mathrm{z}}(A_{\perp} \hat{I}_{\mathrm{x}} + A_{\parallel} \hat{I}_{\mathrm{z}}) \tag{A.1}$$

with $\delta = \omega_{\mathrm{s}} - \omega_{\mathrm{d}}$ the frequency detuning between the drive frequency ω_{d} and the electron spin frequency ω_{s} and Ω the Rabi frequency depending on the drive amplitude.

The locked spin can be considered as a effective spin with a quantization axis along y (see Figure A.1b). To materialize this effect, we change the basis of the electron spin from $(\left|\uparrow\right\rangle, \left|\downarrow\right\rangle)$ to $(\left|x\right\rangle, \left|y\right\rangle)$ with $\left|x\right\rangle = (\left|\uparrow\right\rangle + \left|\downarrow\right\rangle)/\sqrt{2}$, $\left|y\right\rangle = (\left|\uparrow\right\rangle - \left|\downarrow\right\rangle)/\sqrt{2}$.

The spin operators associated with this basis read:

$$\hat{S}_{\mathrm{z}}^{(\mathrm{x,y})} = \frac{1}{2}(\left|x\right\rangle \left\langle x\right| - \left|y\right\rangle \left\langle y\right|) \tag{A.2}$$

$$\hat{S}_{\mathrm{x}}^{(\mathrm{x,y})} = \frac{1}{2}(\left|x\right\rangle \left\langle y\right| + \left|x\right\rangle \left\langle y\right|). \tag{A.3}$$

$$\tag{A.4}$$

Since, $\hat{S}_{\mathrm{z}}^{(\mathrm{x,y})} = \hat{S}_{\mathrm{x}}$ and $\hat{S}_{\mathrm{x}}^{(\mathrm{x,y})} = \hat{S}_{\mathrm{z}}$, one can write Equation A.1 as:

$$\hat{H}^{(\mathrm{x,y})}/\hbar = \Omega \hat{S}_{\mathrm{z}}^{(\mathrm{x,y})} + \delta \hat{S}_{\mathrm{x}}^{(\mathrm{x,y})} + \omega_{\mathrm{L}} \hat{I}_{\mathrm{z}} + \hat{S}_{\mathrm{x}}^{(\mathrm{x,y})}(A_{\perp} \hat{I}_{\mathrm{x}} + A_{\parallel} \hat{I}_{\mathrm{z}}). \tag{A.5}$$

From now on, we will no longer write the indices $^{(\mathrm{x,y})}$ to make the expressions more readable. Moreover, we will consider that the microwave drive is at resonance with the electron spin ie $\delta = 0$.

We write Equation A.5 by introducing the ladder operators: $\hat{S}_{\pm} = \hat{S}_{\mathrm{x}} \pm \hat{S}_{\mathrm{y}}$:

$$\hat{H} = \Omega \hat{S}_{\mathrm{z}} + \omega_{\mathrm{L}} \hat{I}_{\mathrm{z}} + \frac{A_{\perp}}{4}(\hat{S}_{+}\hat{I}_{+} + \hat{S}_{-}\hat{I}_{-} + \hat{S}_{-}\hat{I}_{+} + \hat{S}_{+}\hat{I}_{-}) + \frac{A_{\parallel}}{2}(\hat{S}_{+}\hat{I}_{\mathrm{z}} + \hat{S}_{-}\hat{I}_{\mathrm{z}}). \tag{A.6}$$

We then change the reference frame both for the electron and the nuclear spin by applying the unitary operator $\hat{U}^{\dagger} = \exp\Big(i\Omega \hat{S}_{\mathrm{z}} t\Big) \otimes \exp\Big(i\Omega \hat{I}_{\mathrm{z}} t\Big)$. We then only keep the non-rotating terms (RWA approximation) yielding to:

$$\boxed{\hat{H}/\hbar = \Delta \hat{I}_{\mathrm{z}} + \frac{A_{\perp}}{4}(\hat{S}_{+}\hat{I}_{-} + \hat{S}_{-}\hat{I}_{+})} \tag{A.7}$$

with $\Delta = \omega_{\mathrm{L}} - \Omega$ the difference between the nuclear spin Larmor frequency and the Rabi frequency of the electron spin. The flip-flop terms $\hat{S}_{\pm}\hat{I}_{\mp}$ represent the polarization exchange between the nuclear spin and the electronic spin.

With this Hamiltonian we calculate the coherent evolution of a state initially in the $\left|\downarrow\Uparrow\right\rangle$ state (electron spin excited, nuclear spin in ground state) and then the probability $P_{\left|\uparrow\Downarrow\right\rangle}$ that an exchange occurs:

$$P_{\left|\uparrow\Downarrow\right\rangle}(t) = \frac{g^2}{\sqrt{g^2 + \Delta^2}} \sin^2\left(\frac{t}{2}\sqrt{\Delta^2 + g^2}\right) \tag{A.8}$$

with $g = A_{\perp}/2$. The transition probability shows temporal oscillation behavior control by the detuning Δ and the hyperfine parameter $A_{\perp}$. This is a manifestation of the coherent nature of the interaction. Spins become entangled and disentangled as they evolve. For $\Delta = 0$ ie for the Rabi frequency perfectly tuned with the nuclear Larmor frequency, the frequency of the oscillation is simply $A_{\perp}/4\pi$.

This experience is in some way two-dimensional both the optimal Rabi frequency leading to $\Delta = 0$ and the oscillation rate at resonance contain information on the nuclear spin.

The probability $P_{|\uparrow\Downarrow\rangle}(t)$ can be directly follow by measuring the electron spin state. As in the dynamic decoupling experiment, the electron spin serves as both a drive and a probe.

A.3 Experiment calibration

A.3.1 Rabi frequency calibration

The first step is to correctly calibrate the Rabi frequency as a function of the drive amplitude sent to the electron spin. As we consider the same spin as in Chapter 9, the calibration is the same (see Figure 9.4).

A.3.2 Longitudinal relaxation time T_1^ρ

The second step of calibration is to verify if the longitudinal relaxation time T_1^ρ i.e. the life time of the locked state is sufficiently long to resolve the oscillation at frequency $A_\perp/4\pi$ causes by the double resonance.

To measure T_1^ρ we perform a spin locking experiment depicted in Figure A.1a. The spin of the electron is sent to the equator, then the microwave drive locks its position on the y-axis. We use a Rabi frequency of 230 kHz, detuned from the nuclear spins Larmor frequency. The last $\pi/2$ pulse projects the final state either to the ground or to the excited state. In this sequence, the phase of the last $\pi/2$-pulse is modified with the function $\phi(\tau) = 2\pi\Delta\tau + \phi_0$ with $\Delta = 1$ kHz and ϕ_0 alternating between 0 and $\pi/2$. This complicated phase modification is an adaptation from the Ramsey sequence that we used to calibrate the electron spin frequency. It could have been replaced by a simple phase cycling. The evolution of the electron spin during this locking sequence is showed in Figure A.1b.

The average total number of count $\langle C\rangle$ as the function of the locking time for the two different projections ($\phi_0 = 0$ or $\pi/2$) is presented in Figure A.1c. The projections oscillate with a frequency of approximately 1 kHz as set by $\phi(t)$. The linear increase of $\langle C\rangle$ is due to the fridge heating causes by the microwave drive.

To extract the longitudinal relaxation time , we take the difference between the two projections as for the phase cycling (see Figure A.1d). An exponentially damped sinusoidal fit allows to extract $T_1^\rho = 2.85$ ms which corresponds roughly to $2T_1$ with $T_1 = 1.57$ ms the energy relaxation time measured in Section 9.1.4.2.

This coherence time is superior to the one found in Section 9.1.4.3 for a dynamical decoupling sequence of 16 refocusing pulses. Indeed, the spin locking sequence can be seen as a continuous version of the dynamical decoupling sequence containing an infinity of refocusing pulses which naturally push the coherence time to its maximum.

This $T_1^\rho = 2.85$ ms will allow to resolve oscillation of typically $1/T_1^\rho \approx 0.4$ kHz which corresponds to an hyperfine parameter $A_\perp/2\pi = 0.8$ kHz. From Section 9.1.2.1, we know that the maximum value of $A_\perp/2\pi$ is 400 kHz for the most coupled spins (the 4 nearest neighbors). We can therefore detect all the ^{183}W nuclear spin with $A_\perp/2\pi$ comprises between 0.8 and 400 kHz which corresponds to ~ 750 sites.

A.4 Spin locking and HHDR

A.4.1 Adapted spin locking sequence

Once the experiment is properly calibrated, we move to the nuclear spin detection by setting the Rabi frequency of the electron spin close to the nuclear spin Larmor frequency. The experiment is performed with the spin locking sequence described in the last section.

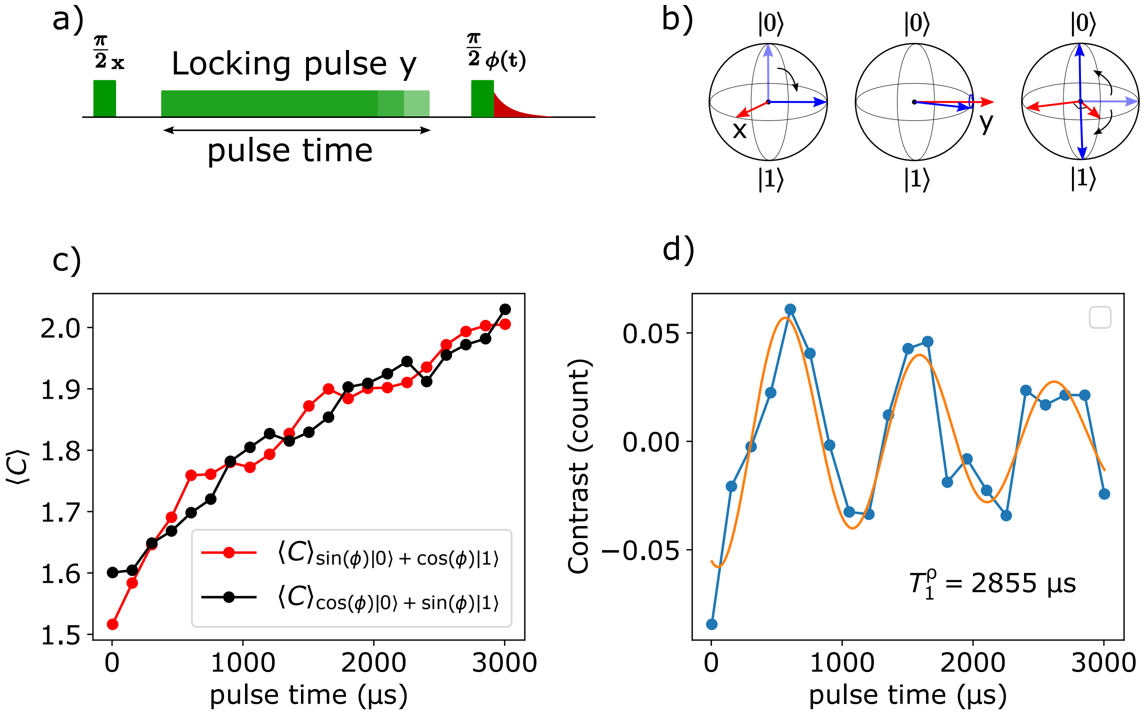

Figure A.1: **Measurement of the longitude relaxation time T_1^ρ.** a) Spin locking sequence. The electron spin is initialize in the $|x\rangle$ state by a $\pi/2_\text{x}$-pulse and locked in this position with a drive applied along the y-axis. The phase of the last $\pi/2$-pulse evolves as $\phi(\tau) = 2\pi\Delta\tau + \phi_0$ with $\Delta = 1$ kHz and ϕ_0 alternating between 0 and $\pi/2$ b) Representation of the sequence in the electron spin Bloch sphere. c) Total average count $\langle C\rangle$ as the function of the drive duration. The red (resp. black) curve corresponds to $\phi_0 = 0$ (resp. $\phi_0 = \pi/2$). the increase of $\langle C\rangle$ with the drive duration is due to the fridge heating. d) Difference between the $\phi_0 = 0$ and $\phi_0 = \pi/2$ curves. Solid orange line is an exponentially damped sinusoidal fit allowing to extract $T_1^\rho = 2855$ μs

The energy transmitted from the electron spin to the nuclear spins during the double resonance tends to polarise the nuclear spin bath. Indeed, while the electron spin state is reset at the beginning of each sequence, the nuclear spins accumulate polarization throughout the experiment.

This effect can be used to actively cool the spin bath [Lon+13] as we will show in the next section but it also causes the reduction of polarisation exchanges. Indeed, if all the nuclear spins are already in the excited state, the probability $P_{|\uparrow\Downarrow\rangle}$ (see Equation A.8) to exchange energy from the electron spin to the nuclear spin is null.

To overcome this difficulty, we alternate the phase of the locking drive from y to $-y$ (see Figure A.2a). The initial state of the electron spin will therefore alternate between $|\uparrow\rangle^{(\text{x,y})}$ and $|\downarrow\rangle^{(\text{x,y})}$ in the $(|x\rangle, |y\rangle)$ basis avoiding the nuclear spin polarization.

To finish the sequence, we project the electron state either on the ground or on the excited state (phase cycling). The contrast will be positive (resp. negative) if the electron spin was in $|\uparrow\rangle^{(\text{x,y})}$ (resp. $|\downarrow\rangle^{(\text{x,y})}$) at the end of the locking sequence. The oscillation between $|\uparrow\rangle^{(\text{x,y})}$ and $|\downarrow\rangle^{(\text{x,y})}$ will allow us to reconstruct the exchange probability $P_{|\uparrow\Downarrow\rangle}$ (see Equation A.8)

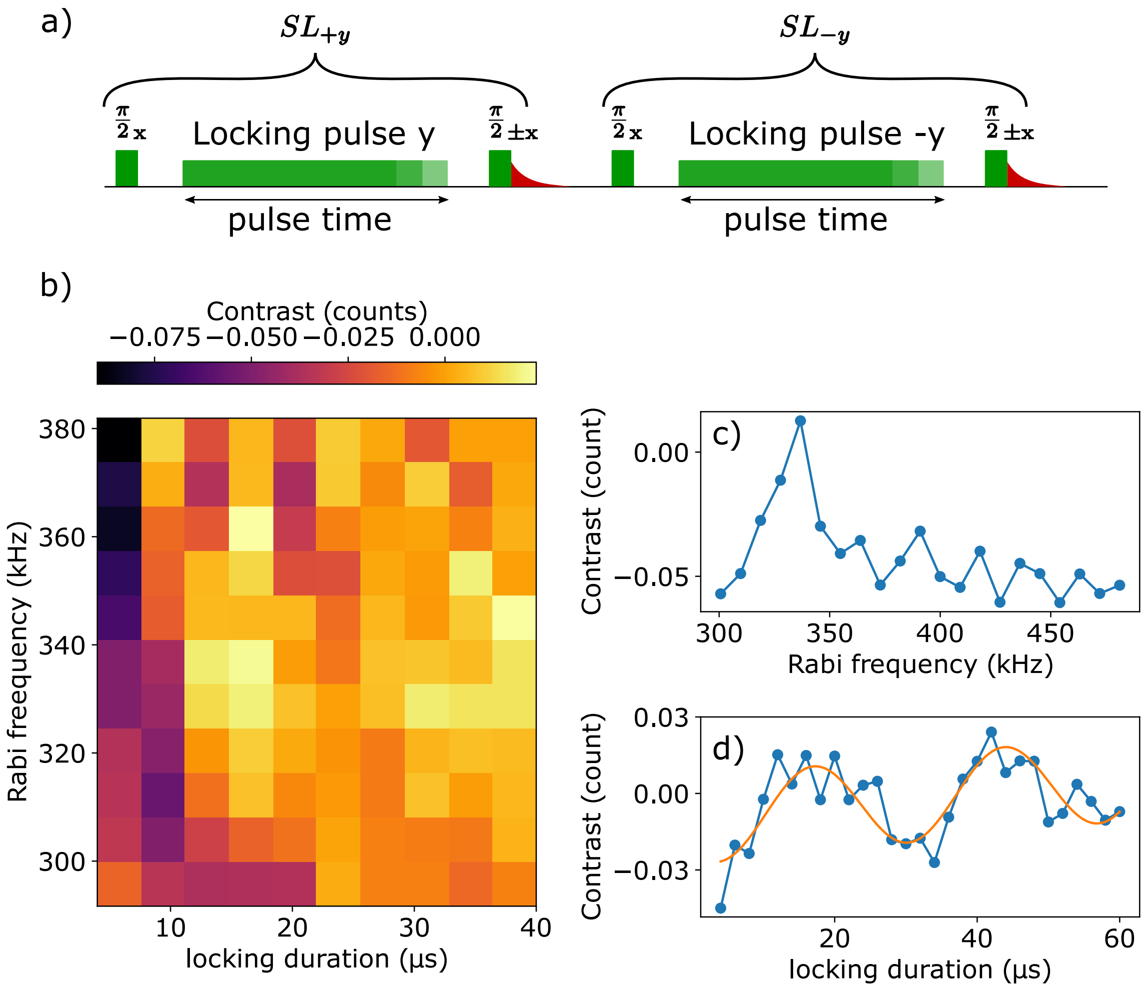

Figure A.2: **Hartmann-Hahn double resonance**.a) Spin locking sequence for the HHDR experiment. The drive is alternatively applied in the y and $-y$ direction in order to avoid the nuclear spins polarization. The sequences are called $SL_{\pm y}$. Phase cycling is added in the last $\pi/2-$pulse. b) Contrast as the function of the locking duration and the Rabi frequency of the electron spin. An oscillation is visible around 340 kHz proving the existence of a double resonance phenomena. c) Spectroscopy in Rabi frequency realized with a locking duration fixed at 120 μs. The HHDR is now clearly visible at 340 kHz. The contrast sign inversion at 340 kHz indicates that the final state of the electron spin is on average more often $|-x\rangle$ than $|x\rangle$. d) Spin locking experiment realized with the Rabi frequency corresponding to the resonant condition. The contrast is plotted as the function on the locking duration and shows a clear oscillation whose frequency $f_{\text{osc}} = 36$ kHz is extracted with a sinusoidal fit (solid orange line).

A.4.2 HHDR

To capture the two pieces of information accessible via the double resonance, i.e. the Larmor frequency and the hyperfine parameters of the nuclear spins, we vary both the amplitude and the duration of the drive. Figure A.2b presents the result of the experiment. The contrast coming from phase cycling (see Figure A.2a) is plotted as the function of the locking duration and the electron spin Rabi frequency (calculated from the drive amplitude). An oscillation appears in the contrast around 330 kHz that would correspond to a HHDR signal , however, as the data from this first experiment was quite noisy,we decided to refine our measurement. We first take a simple spectroscopy by varying the Rabi frequency for a locking time of 120 μs in order to precise the resonant condition. Figure A.2c corresponds to this experiment and exhibit a clear peaks centered around $\Omega = 340$ kHz which confirms that the double resonance occurs.

We then fix the Rabi frequency on the resonant condition and we vary the locking duration. The result are presented in Figure A.2d where the contrast is plotted as the function of the locking duration. A clear oscillation appears, we extract the oscillation frequency $\mathrm{f}_{\mathrm{osc}} = 36$ kHz with a sinusoidal fit. From Equation A.8 and assuming that the Rabi frequency is perfectly tuned, we can infer that this oscillation is caused by the coherent energy exchange between the electron spin and an ^{183}W nuclear spin with $A_\perp = 72$ kHz.

A.4.3 Search for matching W sites

To verify the relevance of this hypothesis, it is necessary to check with the simulations conducted in Section 9.1.2.1 whether tungsten sites can host ^{183}W with such a hyperfine parameter. On the histogram presenting the distribution of the $A_\perp$ (see Figure 9.2) we can observe that 4 sites are eligible for candidate status. Their positions with the respect to the erbium ion (see Figure 9.2a for the axis definition) and their hyperfine parameters are presented in the table Table A.1. These 4 sites are equivalent 2 to 2 and have a very similar $A_\perp \approx 68.5$ kHz. These parameters could correspond to the observed oscillation $\mathrm{f}_{\mathrm{osc}} = A_\perp/2 = 36$ kHz insofar as the Rabi frequency is slightly detuned from the Larmor frequency, which has the consequence of accelerating the oscillation.

site	x (Å)	y (Å)	z (Å)	$A_\parallel$ (kHz)	$A_\perp$ (kHz)
1	0	0	-5.67	12.38	68.52
2	0	0	-5.67	12.38	68.52
3	-5.24	-2.62	2.84	34.90	68.48
4	-5.24	-2.62	2.84	34.90	68.48

Table A.1: **Tungsten site compatible with the HHDR signal**

Finally one can say from this analysis that the observed signal is caused by ^{183}W atoms occupying one or several sites depicted in Table A.1. As the $A_\perp$ of the 4 sites is very similar it is complicated to establish the number of populated sites by observing a beating in the oscillations.

A.4.4 Conclusion and comparison with the Dynamical decoupling experiment

To summarize this section, one observed a clear Hartmann-Hahn double resonance between an electron spin ER^{3+} and ^{183}W nuclear spins. A fit of the observed oscillation in Figure A.2d and a research among the simulated hyperfine parameters allows us to establish that the HHDR signal is certainly caused by ^{183}W populating one to four sites depicted in Table A.1.

the Dynamical decoupling and the HHDR experiments are consistent in that they both confirm the absence of ^{183}W at the sites with the highest hyperfine parameters. indeed, there is no trace of higher frequency oscillation in the HHDR signal Figure A.2d and the DD signal Figure 9.10b are incompatible with the presence of strongly coupled nuclear spin. To go further in the analysis, and try to locate other populated sites, we could have increased the spin locking time and conducted a frequency analysis of the signal obtained. These more in-depth analyses will be the subject of future thesis projects.

A.5 Polarization of the nuclear spin bath

A.5.1 Principle and interest of the experiment

As mentioned in Section A.4, an other interesting feature of the HHDR experiment is the possibility to actively cool the nuclear spin bath. This can be done by keeping the drive axis in the same direction during several spin locking sequences. If the locking time is calibrated such as the energy exchange is maximum at the end of the interaction i.e. $P_{|\uparrow\Downarrow\rangle} = 1$ (see Equation A.8), the nuclear spin bath will be progressively polarized. As the ^{183}W nuclear spins interact little with their magnetic environment due to their low gyromagnetic ration $\gamma_{\mathrm{W}} = \mu_{\mathrm{N}} g_{\mathrm{W}} = 1.78$ kHz/mT, their energy relaxation time is very large, probably $\gg 1$ hour. Therefore the polarization should remain effective over long time scale.

Polarizing the nuclear spin bath can increase the FID time of the electron spin if the magnetic fluctuations it causes are the main source of decoherence. In the case of diamond NV centres, this experiment has allowed to freeze the ^{13}C nuclear spin bath and to increase the free induction decay time by an order of magnitude [Lon+13].

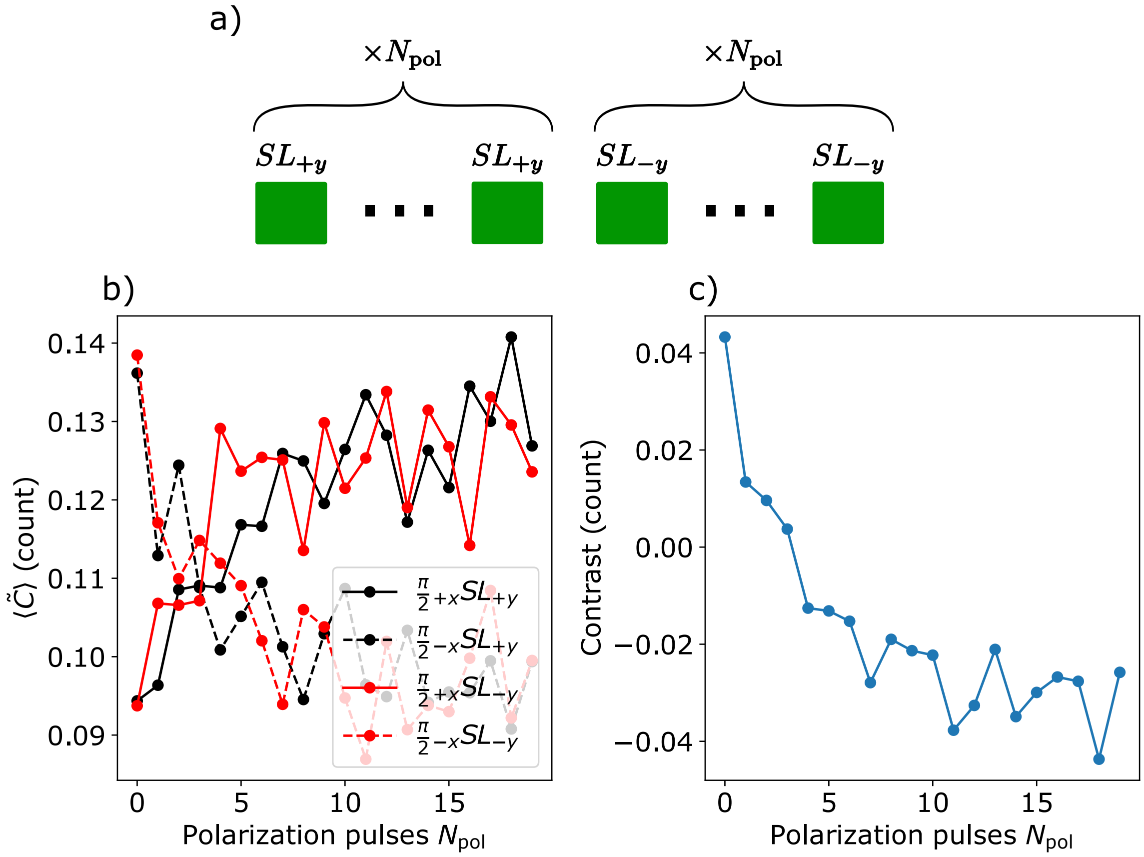

Figure A.3: **Nuclear spin bath polarization**. a) Polarization sequence. The spin locking sequences $SL_\pm$ corresponding to a drive in the $\pm\, y$ direction are applied alternatively N_{pol} times. b) Background corrected average count for the two drive directions and the two phase cycling projections as the function of N_{pol}. As expected the signal given by the $SL_\pm$ sequences is similar. A population inversion occurs progressively between $N_{\mathrm{pol}} = 1$ and $N_{\mathrm{pol}} = 20$ due to gradual nuclear spin bath polarization. c) Contrast between the phase cycling projections obtained by averaging on the two drive directions. The population inversion is complete, the contrast ranging from 0.04 to -0.04 count.

A.5.2 Effective polarization of the ^{183}W nuclear spin bath

The polarization sequence is depicted in Figure A.3a. Contrarily to the HHDR experiment the polarization experiment is composed of blocks of N_{pol} spin locking sequence (referred to as $SL_{\pm \mathrm{y}}$ from Figure A.2a) with the same drive direction (see Figure A.3a). The locking time is fixed to 15 μs which corresponds to a half period of the coherent HHDR oscillation presented in Figure A.2d. This locking duration maximizes the energy transfer between the electron spins and the identified nuclear spins.

As for the last section, the signal come from the measurement of the electron spin state after the polarization sequence. The raw data are thus composed of 4 series depending on the phase cycling and on the drive direction, a plot as the function of the number of sequence polarization is shown in Figure A.3b. A population inversion is clearly visible between $N_{\mathrm{pol}} = 1$ and $N_{\mathrm{pol}} = 20$, moreover, the signal coming from the $SL_{+\mathrm{y}}$ and the $SL_{-\mathrm{y}}$ is identical as expected.

In Figure A.3c we sum the two contribution coming from the $\pm y$ drive and we plot the contrast between the two phase cycling projections. The evolution of the contrast value from 0.04 to -0.04 count shows clearly that the final electron state is reversed.

The building-up of this inversion is simply linked to the progressive polarization of the nuclear spin bath which increasingly prevents the electron spin from exchanging its energy. In an extreme way, when $N_{\mathrm{pol}} = 1$, the electron exchanges its polarization with the nuclear spin bath with a unit probability, whereas for $N_{\mathrm{pol}} = 20$, it does not exchange it at all and remains in its initial state.

this experiment clearly shows that, like what has already been done in the NV centres, we are able to polazise the ^{183}W nuclear spin bath around the Er^{3+} ion.

In the next section we move to the impact of this polarization on the electron spin free induction decays time.

A.5.3 Polarization impact on the free induction decay time

To study the impact of polarization on FID time, we use the sequence described in Figure A.4a. we first polarize the nuclear spin bath by applying $N_{\mathrm{pol}} = 10$ spin-locking sequences with the same locking drive direction. A series of Ramsey sequences is then played with different delays τ. At the beginning of each Ramsey sequence, we apply a spin locking sequence to secure the polarisation during the acquisition of the Ramsey curve.

The average count rate as the function of the Ramsey waiting time τ is shown in Figure A.4b. The oscillation is imposed by the linearly increasing phase $\phi(\tau) = 2\pi\Delta\tau$ of the last $\pi/2-$ pulse with $\Delta = 100$ kHz. We extract the FID time $T_2^* = 4.68$ μs with an exponentially damped sinusoidal fit. Figure A.4c shows the phase cycling signals of the electron spin at the beginning of the additional spin locking sequence. The contrast remains constant indicating a good polarisation maintenance throughout the acquisition of the FID curve.

The FID time found, $T_2^* = 4.68$ μs is equivalent to the one found in Section 9.1.4.2. This proves that the FID time of this particular Er^{3+} electron spin is not limited by the magnetic noise caused by the ^{183}W nuclear spin bath.

A.6 About the environment of the electron spin

Finally, after the measurements carried out in this chapter, we have acquired a certain amount of information about the electron spin environment.

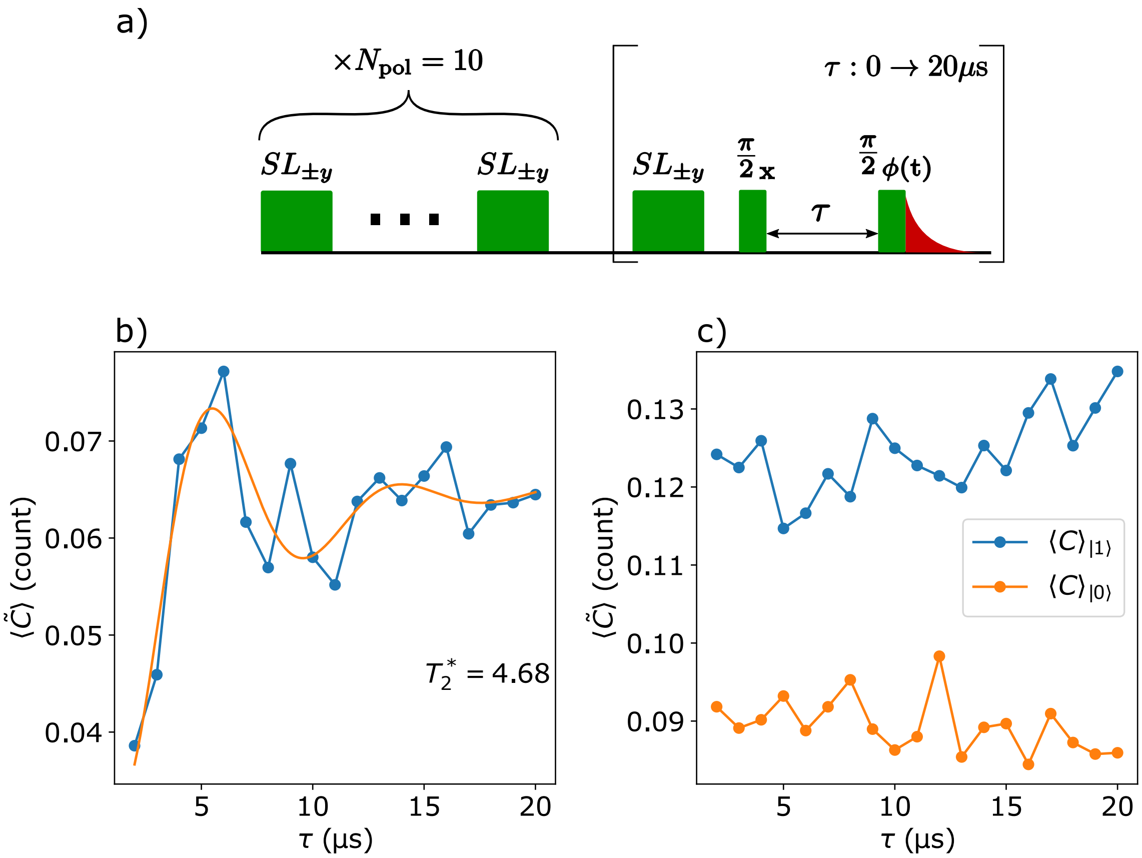

Figure A.4: **Free induction decay time after nuclear spin polarization**. a) Sequence measuring the FID time after a nuclear spin bath polarization. The bath is polarize with $N_{\mathrm{pol}} = 10$ spin locking sequences $SL_{\pm}$. A Ramsey sequence is then applied and repeated with 19 τ value ranging from 1 μs to 20 μs. The phase $\phi(\tau) = 2\pi\Delta\tau$ of the last $\pi/2$-pulse is linearly increase with $\Delta = 100$ kHz. The polarization stability is checked before each Ramsey sequence by a $SL_{\pm}$ sequence. b) Background corrected average number of count $\langle\tilde{C}\rangle$ as the function of the waiting time τ. The FID time T_2^* is extracted with an exponentially damped sinusoidal fit (solid orange line). c) $\langle\tilde{C}\rangle$ measure after the spin locking sequence of checking. The stability of the phase cycle projection proves the stability of the nuclear spin polarization.

A.6.1 Position of the ^{183}W atoms

From the dynamical decoupling measurement and the Hartmann-Hahn double resonance, we can assume that the 4 closest tungsten sites are not populated by ^{183}W. The two measurement are coherent on this point. However, this assumption must be balanced by the fact that we do not detect the effect of pulse filtering by the cavity discussed in Section 9.2.2.1. This could lead to an intrinsic inability to address the more strongly coupled spins.

The HHDR experiment includes additional information on hyperfine coupling and allows to establish that at least one site among the site depicted in Table A.1 is populated. These sites are located respectively at 5.7 Å and 6.5 Å to the electron spins an correspond to the 3rd and 4th closest neighbor.

A.6.2 Electron spin FID time and information about the electromagnetic environment

We have also studied the free induction decay time of the electron spin in different experimental configurations (see Table A.2). The basic configuration consists of placing the X and Y coils in persistent mode and controlling the stability of Z via a feed-back loop. In this case we obtain $T_2^* = 6.57\ \mu$s. To eliminate the assumption that this coherence time is limited by the stability of Z coil, we remeasured the coherence time by placing the z-axis in persistent mode (measurement not shown in the thesis). In this case $T_2^* = 4.62$ proving that the field stability is not the limiting factor of the electron spin coherence.

Another source of magnetic noise that could limit coherence is the ^{183}W nuclear spin bath. The HHDR experiment offers us the possibility to efficiently polarize this bath, suppressing its fluctuations. The experiment is realized in Section A.5.3 and yields to $T_2^* = 4.68$. This value, close to the previous one, proves that the coherence time is not limited by the nuclear spin bath either.

Finally, we can return to the coherence measure realized with the CPMG sequences in the section Section 9.1.4.3. As shown on Figure 9.6d the coherence time increases as a function of the square root of the number of refocusing pulses. This dynamic indicates that the spin undergoes a $1/f$ noise spectral density [YSH11; ÁS11; Med+12],characteristic of fluctuation caused by interface defects [Mye+14; Yon+18]. The most likely conclusion is that this particular electron spin is very close to the resonator nanowire (which is also supported by the short value of $T_mathrm1$) and that its coherence is intrinsically limited by surface defects causing magnetic or electrical fluctuations..

Experimental conditions	T_2^* (μs)
X, Y coils in presistent mode	6.57
X, Y, Z coils in presistent mode	4.62
After nuclear spin polarization	4.68

Table A.2: **Free induction decay time in different experimental configurations**

Appendix B

CPMG versus XY sequence

Before turning to the CPMG sequence, we used the XY-4 sequence to perform our first dynamical decoupling measurement. As shown on Figure B.1b, the XY-4 sequence is a CPMG sequence with a π_{x}-pulse replacing a π_{y}-pulse. This modification involves that we need 2 basic $\tau - \pi_{\mathrm{x}} - 2\tau - \pi_{\mathrm{y}} - \tau$ units of π-pulse to retrieve the original $|x\rangle$ state.

The comparison between the DD signal from XY-4 and CPMG are depicted in Figure B.1c for $N_\pi = 24$. The XY-4 signal presents a lot of spurious dips around the expected resonant position. This results in the appearance of high frequency harmonics in the Fourier transform of the signal. In contrast, these harmonics are rapidly attenuated in the case of the CPMG.

We later understood that this perturbed signal was specifically due to the XY-4 sequence as shown in this article [Lor+15]. We then decided to move to the CPMG sequence which produced a much clearer signal.

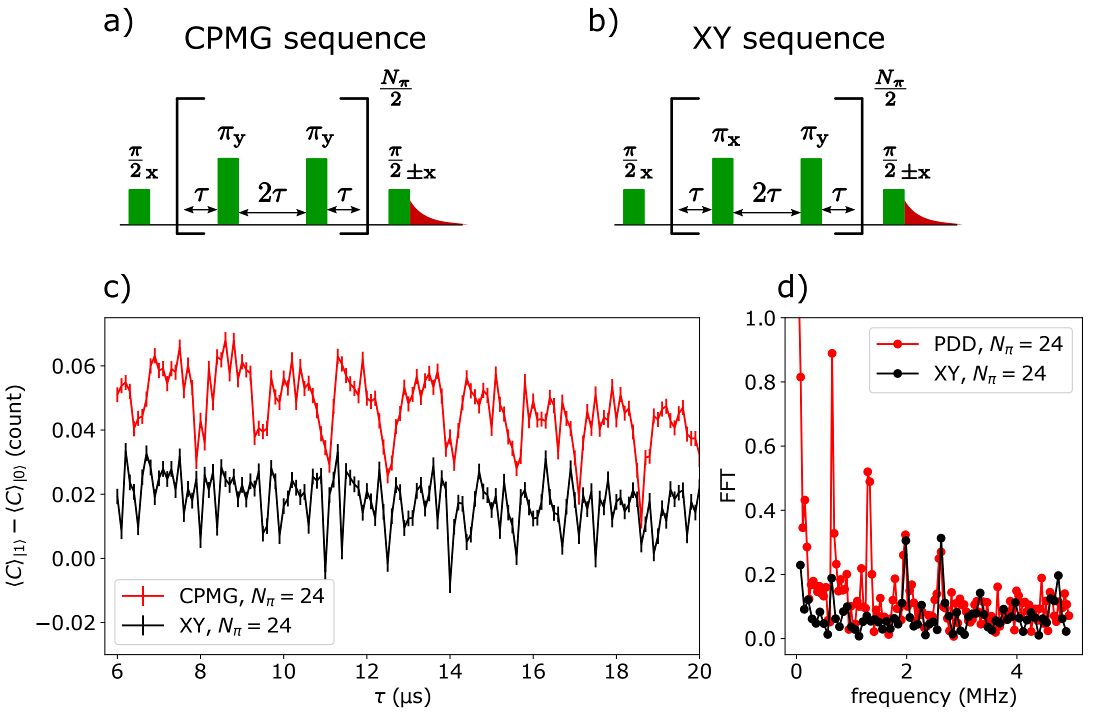

Figure B.1: **Comparison between CPMG and XY-4 sequence**. CPMG sequence (a) compare to the XY-4 sequence (b). c) Contrast coming from the CPMG sequence (red) and the XY-4 (black). Spurious dips appears in the XY-4 case causing high frequency harmonics in the Fourrier transform signal (d)

Bibliography

[AB12] A. Abragam and B. Bleaney. *Electron Paramagnetic Resonance of Transition Ions*. OUP Oxford, June 2012 (cit. on p. 123).

[Abh+22] Nandita Abhyankar et al. “Recent advances in microresonators and supporting instrumentation for electron paramagnetic resonance spectroscopy”. In: *Review of Scientific Instruments* 93.10 (Oct. 2022), p. 101101 (cit. on pp. 2, 14).

[Abo+19] M. H. Abobeih et al. “Atomic-scale imaging of a 27-nuclear-spin cluster using a single-spin quantum sensor”. In: *Nature* 576.7787 (Dec. 19, 2019), pp. 411–415. arXiv: `1905.02095[cond-mat,physics:quant-ph]` (cit. on pp. 155, 157, 176).

[Abo+22] M. H. Abobeih et al. “Fault-tolerant operation of a logical qubit in a diamond quantum processor”. In: *Nature* 606.7916 (June 2022), pp. 884–889 (cit. on p. 117).

[Alb+21] Emanuele Albertinale et al. “Detecting spins by their fluorescence with a microwave photon counter”. In: *Nature* 600.7889 (2021), pp. 434–438 (cit. on pp. 3, 5, 15, 17, 51, 71, 72, 74, 94, 117, 151, 177).

[Alb21] Emanuele Albertinale. “Measuring spin fluorescence with a microwave photon detector”. In: (2021) (cit. on pp. 44, 47, 51, 61, 71, 75, 97, 103, 106).

[ÁS11] Gonzalo A. Álvarez and Dieter Suter. “Measuring the Spectrum of Colored Noise by Dynamical Decoupling”. In: *Physical Review Letters* 107.23 (Nov. 30, 2011), p. 230501 (cit. on pp. 164, 190).

[Ber+09] S. Bertaina et al. “Spin-Orbit Qubits of Rare-Earth-Metal Ions in Axially Symmetric Crystal Fields”. In: *Physical Review Letters* 103.22 (Nov. 2009), p. 226402 (cit. on pp. 8, 19).

[Bes+18] Jean-Claude Besse et al. “Single-Shot Quantum Non-Demolition Detection of Itinerant Microwave Photons”. In: *APS March Meeting Abstracts*. Vol. 2018. 2018, A39–007 (cit. on p. 71).

[Bie+16] A. Bienfait et al. “Controlling spin relaxation with a cavity”. In: *Nature* 531.7592 (Mar. 2016), pp. 74–77 (cit. on pp. 3, 7, 15, 19, 129, 130, 153, 177).

[Bil+22] Eric Billaud et al. *Microwave fluorescence detection of spin echoes*. Aug. 29, 2022. arXiv: `2208.13586[quant-ph]` (cit. on pp. 3, 8, 19, 79, 153).

[Bil23] Eric Billand. “Electron spin resonance spectroscopy of rare earth ions in scheelite detected by microwave fluorescence at millikelvin temperature”. PhD thesis. Université Paris-Saclay, Feb. 8, 2023 (cit. on pp. 8, 19, 130, 131, 161, 177).

[Bla+07] Alexandre Blais et al. “Quantum-information processing with circuit quantum electrodynamics”. In: *Phys. Rev. A* 75 (3 Mar. 2007), p. 032329 (cit. on p. 46).

[Bla+21] Alexandre Blais et al. "Circuit Quantum Electrodynamics". In: *Reviews of Modern Physics* 93.2 (May 19, 2021), p. 025005. arXiv: `2005.12667[quant-ph]` (cit. on pp. 3, 14, 41).

[Blo46] F. Bloch. "Nuclear Induction". In: *Physical Review* 70.7-8 (Oct. 1946), pp. 460–474 (cit. on pp. 1, 13).

[Bou+98] V. Bouchiat et al. "Quantum Coherence with a Single Cooper Pair". In: *Physica Scripta* T76.1 (1998), p. 165 (cit. on pp. 27, 42).

[Bra+19] C. E. Bradley et al. "A Ten-Qubit Solid-State Spin Register with Quantum Memory up to One Minute". In: *Physical Review X* 9.3 (Sept. 11, 2019), p. 031045 (cit. on pp. 157, 176, 178).

[Bro+19] D. A. Broadway et al. "Microscopic Imaging of the Stress Tensor in Diamond Using in Situ Quantum Sensors". In: *Nano Letters* 19.7 (July 2019), pp. 4543–4550 (cit. on p. 147).

[Bru+19] Claudio Bruschini et al. "Single-photon avalanche diode imagers in biophotonics: review and outlook". In: *Light: Science & Applications* 8.1 (Sept. 2019), p. 87 (cit. on p. 51).

[Cla+88] John Clarke et al. "Quantum Mechanics of a Macroscopic Variable: The Phase Difference of a Josephson Junction". In: *Science* 239.4843 (Feb. 26, 1988), pp. 992–997 (cit. on p. 27).

[Cle+10] A. A. Clerk et al. "Introduction to quantum noise, measurement, and amplification". In: *Reviews of Modern Physics* 82.2 (Apr. 15, 2010), pp. 1155–1208 (cit. on p. 32).

[Cro+23] Kevin D. Crowley et al. *Disentangling Losses in Tantalum Superconducting Circuits*. Jan. 18, 2023. arXiv: `2301.07848[cond-mat,physics:quant-ph]` (cit. on pp. 72, 77).

[Dan22] Marianne Le Dantec. "Electron spin dynamics of erbium ions in scheelite crystals, probed with superconducting resonators at millikelvin temperatures". PhD thesis. Université Paris-Saclay, Jan. 24, 2022 (cit. on pp. 4, 15, 120, 126, 153, 161).

[Dib+18] A. M. Dibos et al. "Atomic Source of Single Photons in the Telecom Band". In: *Physical Review Letters* 120.24 (June 2018), p. 243601 (cit. on pp. 145, 149).

[DS13] M. H. Devoret and R. J. Schoelkopf. "Superconducting Circuits for Quantum Information: An Outlook". In: *Science* 339.6124 (Mar. 8, 2013), pp. 1169–1174 (cit. on p. 76).

[Dun+17] A. Dunsworth et al. "Characterization and reduction of capacitive loss induced by sub-micron Josephson junction fabrication in superconducting qubits". In: *Applied Physics Letters* 111.2 (July 10, 2017), p. 022601 (cit. on pp. 77, 78).

[Elz+04] J. M. Elzerman et al. "Single-shot read-out of an individual electron spin in a quantum dot". In: *Nature* 430.6998 (July 2004), pp. 431–435 (cit. on p. 118).

[Enr71] Bernal G. Enrique. "Optical Spectrum and Magnetic Properties of Er3+ in CaWO4". In: *The Journal of Chemical Physics* 55.5 (Sept. 1971), pp. 2538–2549 (cit. on pp. 8, 19, 120).

[Err63] H. J. Erritsen. "Paramagnetic Resonance of Transition Metal Ions in Rutile (TiO_2)". In: *Paramagnetic Resonance: Proceedings of the First International Conference*. Ed. by W. Low. Academic Press, 1963, pp. 3–12 (cit. on p. 178).

[Est+89] D Esteve et al. “Observation of the Temporal Decoupling Effect on the Macroscopic Quantum Tunneling of a Josephson Junction”. In: *Physica Scripta* T29 (Jan. 1, 1989), pp. 121–124 (cit. on p. 27).

[Flu14] Emmanuel Flurin. “The Josephson mixer: a swiss army knife for microwave quantum optics”. In: (2014), p. 251 (cit. on p. 32).

[Gam+06] Jay Gambetta et al. “Qubit-photon interactions in a cavity: Measurement-induced dephasing and number splitting”. In: *Physical Review A* 74.4 (2006), p. 042318 (cit. on p. 47).

[Gri+20] Arne L. Grimsmo et al. “Quantum metamaterial for nondestructive microwave photon counting”. In: *arXiv:2005.06483 [quant-ph]* (May 2020) (cit. on p. 51).

[Gru+97] A. Gruber et al. “Scanning Confocal Optical Microscopy and Magnetic Resonance on Single Defect Centers”. In: *Science* 276.5321 (1997), pp. 2012–2014 (cit. on pp. 2, 14, 117).

[HH62] S. R. Hartmann and E. L. Hahn. “Nuclear Double Resonance in the Rotating Frame”. In: *Physical Review* 128.5 (Dec. 1, 1962), pp. 2042–2053 (cit. on pp. 163, 181).

[HR06] S. Haroche and J. -M Raimond. *Exploring the quantum*. Oxford University Press, Aug. 2006 (cit. on pp. 3, 14, 28).

[Ino+16] Kunihiro Inomata et al. “Single microwave-photon detector using an artificial Λ-type three-level system”. In: *Nature communications* 7.1 (2016), pp. 1–7 (cit. on p. 71).

[Jef+14] Evan Jeffrey et al. “Fast Accurate State Measurement with Superconducting Qubits”. In: *Physical Review Letters* 112.19 (May 15, 2014), p. 190504 (cit. on p. 48).

[JL05] Bernard Jacquier and Guokui Liu. *Spectroscopic properties of rare earths in optical materials*. 83. Berlin Tsinghua: Springer Tsinghua University Press, 2005 (cit. on p. 120).

[Joh28] J. B. Johnson. “Thermal Agitation of Electricity in Conductors”. In: *Physical Review* 32.1 (July 1, 1928), pp. 97–109 (cit. on p. 67).

[Jos62] B. D. Josephson. “Possible new effects in superconductive tunnelling”. In: *Physics Letters* 1.7 (1962), pp. 251–253 (cit. on p. 38).

[Kan+22] Shun Kanai et al. “Generalized scaling of spin qubit coherence in over 12,000 host materials”. In: *Proceedings of the National Academy of Sciences* 119.15 (Apr. 2022), e2121808119 (cit. on p. 118).

[KDM77] H. J. Kimble, M. Dagenais, and L. Mandel. “Photon Antibunching in Resonance Fluorescence”. In: *Physical Review Letters* 39.11 (Sept. 1977), pp. 691–695 (cit. on p. 51).

[Kie66] A. Kiel. “Theory of Electric Shifts of the Optical and Magnetic Resonance Properties of Paramagnetic Ions in Crystals”. In: *Physical Review* 148.1 (Aug. 1966), pp. 247–256 (cit. on p. 125).

[Kim98] H. J. Kimble. “Strong interactions of single atoms and photons in cavity QED”. In: *Physica Scripta* 1998 (T76 Jan. 1, 1998), p. 127 (cit. on p. 28).

[Kin+20] Jonathan M. Kindem et al. “Control and single-shot readout of an ion embedded in a nanophotonic cavity”. In: *Nature* 580.7802 (Apr. 2020), pp. 201–204 (cit. on p. 145).

[Koc+07] Jens Koch et al. “Charge-insensitive qubit design derived from the Cooper pair box”. In: *Phys. Rev. A* 76 (4 Oct. 2007), p. 042319 (cit. on pp. 28, 42).

[Kol+12] Shimon Kolkowitz et al. “Sensing distant nuclear spins with a single electron spin”. In: *Physical Review Letters* 109.13 (Sept. 25, 2012), p. 137601. arXiv: `1204.5483[cond-mat,physics:quant-ph]` (cit. on pp. 10, 23, 157, 159, 166, 167, 174).

[Kos+15] Kazuki Koshino et al. “Theory of microwave single-photon detection using an impedance-matched Λ system”. In: *Physical Review A* 91.4 (2015), p. 043805 (cit. on p. 51).

[Kra30] HA Kramers. “General theory of paramagnetic rotation in crystals”. In: *Proc. Acad. Sci. Amsterdam* 33 (1930), p. 959 (cit. on pp. 7, 19, 120).

[Le +21] Marianne Le Dantec et al. “Twenty-three–millisecond electron spin coherence of erbium ions in a natural-abundance crystal”. In: *Science Advances* 7.51 (Dec. 2021), eabj9786 (cit. on pp. 4, 8, 15, 19).

[Leg+15] Z. Leghtas et al. “Confining the state of light to a quantum manifold by engineered two-photon loss”. In: *Science* (2015). arXiv: `1412.4633` (cit. on p. 52).

[Leg80] A. J. Leggett. “Macroscopic Quantum Systems and the Quantum Theory of Measurement”. In: *Progress of Theoretical Physics Supplement* 69 (Mar. 1, 1980), pp. 80–100 (cit. on p. 27).

[Les+20] Raphaël Lescanne et al. “Irreversible Qubit-Photon Coupling for the Detection of Itinerant Microwave Photons”. In: *Phys. Rev. X* 10 (2 May 2020), p. 021038 (cit. on pp. 3, 5, 15, 17, 51, 71, 177).

[Lon+13] P. London et al. “Detecting and Polarizing Nuclear Spins with Double Resonance on a Single Electron Spin”. In: *Physical Review Letters* 111.6 (Aug. 5, 2013), p. 067601 (cit. on pp. 10, 23, 157–159, 165, 181, 184, 187).

[Lor+15] M. Loretz et al. “Spurious Harmonic Response of Multipulse Quantum Sensing Sequences”. In: *Physical Review X* 5.2 (Apr. 22, 2015), p. 021009 (cit. on pp. 166, 191).

[MC15] Anja Metelmann and Aashish A Clerk. “Nonreciprocal photon transmission and amplification via reservoir engineering”. In: *Physical Review X* 5.2 (2015), p. 021025 (cit. on p. 52).

[McL+23] Russell A. McLellan et al. *Chemical profiles of the oxides on tantalum in state of the art superconducting circuits.* Jan. 20, 2023. arXiv: `2301.04567[cond-mat,physics:quant-ph]` (cit. on pp. 72, 77).

[Med+12] J. Medford et al. “Scaling of Dynamical Decoupling for Spin Qubits”. In: *Physical Review Letters* 108.8 (Feb. 23, 2012), p. 086802 (cit. on pp. 164, 190).

[MG67] W. B. Mims and R. Gillen. “Local Electric Fields and the Paramagnetic Resonance of Charge-Compensated Sites in (Ca, Ce)WO_4”. In: *The Journal of Chemical Physics* 47.9 (Nov. 1967), pp. 3518–3532 (cit. on p. 121).

[Mim65] W. B. Mims. “Electric Field Shift in Paramagnetic Resonance for Four Ions in a Calcium Tungstate Lattice”. In: *Physical Review* 140.2A (Oct. 1965), A531–A535 (cit. on p. 125).

[Min+21] Zlatko K. Minev et al. *Energy-participation quantization of Josephson circuits.* Aug. 16, 2021. arXiv: `2010.00620[cond-mat,physics:quant-ph]` (cit. on pp. 74, 76).

[Muh+14] Juha T. Muhonen et al. “Storing quantum information for 30 seconds in a nanoelectronic device”. In: *Nature Nanotechnology* 9.12 (Oct. 2014), pp. 986–991 (cit. on p. 154).

[Mur+12] KW Murch et al. “Cavity-assisted quantum bath engineering”. In: *Physical review letters* 109.18 (2012), p. 183602 (cit. on p. 52).

[Mye+14] B. A. Myers et al. “Probing Surface Noise with Depth-Calibrated Spins in Diamond”. In: *Physical Review Letters* 113.2 (July 2014), p. 027602 (cit. on pp. 154, 164, 190).

[Ner+19] Ani Nersisyan et al. *Manufacturing low dissipation superconducting quantum processors*. Jan. 23, 2019. arXiv: `1901.08042[physics,physics:quant-ph]` (cit. on p. 76).

[NPT99] Y. Nakamura, Yu A. Pashkin, and J. S. Tsai. “Coherent control of macroscopic quantum states in a single-Cooper-pair box”. In: *Nature* 398.6730 (Apr. 1999), pp. 786–788 (cit. on p. 27).

[Nyq28] H. Nyquist. “Thermal Agitation of Electric Charge in Conductors”. In: *Physical Review* 32.1 (July 1, 1928), pp. 110–113 (cit. on p. 67).

[OB90] M. Orrit and J. Bernard. “Single pentacene molecules detected by fluorescence excitation in a p-terphenyl crystal”. In: *Physical Review Letters* 65.21 (Nov. 1990), pp. 2716–2719 (cit. on pp. 10, 20, 145).

[Pal+09] A Palacios-Laloy et al. “Spectral measurement of the thermal excitation of a superconducting qubit”. In: *Physica Scripta* T137 (Dec. 2009), p. 014015 (cit. on p. 110).

[Pla+12] Jarryd J. Pla et al. “A single-atom electron spin qubit in silicon”. In: *Nature* 489.7417 (Sept. 2012), pp. 541–545 (cit. on p. 118).

[Pla+18] J. J. Pla et al. “Strain-Induced Spin-Resonance Shifts in Silicon Devices”. In: *Physical Review Applied* 9.4 (Apr. 2018), p. 044014 (cit. on p. 146).

[Pla+21] Alexander P. M. Place et al. “New material platform for superconducting transmon qubits with coherence times exceeding 0.3 milliseconds”. In: *Nature Communications* 12.1 (Mar. 19, 2021), p. 1779 (cit. on pp. 72, 75, 77, 80, 81).

[Pol06] Martin Polovka. “EPR spectroscopy: A tool to characterize stability and antioxidant properties of foods”. In: *Journal of Food and Nutrition Research* 45.1 (2006), pp. 1–11 (cit. on pp. 2, 13).

[Poz11] David M. Pozar. *Microwave Engineering*. John Wiley & Sons, Nov. 2011 (cit. on p. 34).

[PTP46] E. M. Purcell, H. C. Torrey, and R. V. Pound. “Resonance Absorption by Nuclear Magnetic Moments in a Solid”. In: *Physical Review* 69.1-2 (Jan. 1946), pp. 37–38 (cit. on pp. 1, 13).

[Pur46] E. M Purcell. “Spontaneous emission probabilities at radio frequencies”. In: *Phys. Rev.* 69 (1946), p. 681 (cit. on pp. 7, 19, 47).

[Rab+38] I. I. Rabi et al. “A New Method of Measuring Nuclear Magnetic Moment”. In: *Physical Review* 53.4 (Feb. 1938), pp. 318–318 (cit. on pp. 1, 13).

[Rah+20] Mouktik Raha et al. “Optical quantum nondemolition measurement of a single rare earth ion qubit”. In: *Nature Communications* 11.1 (Mar. 2020), p. 1605 (cit. on p. 117).

[Ran+20] Vishal Ranjan et al. “Electron spin resonance spectroscopy with femtoliter detection volume”. In: *Applied Physics Letters* 116.18 (2020), p. 184002 (cit. on pp. 3, 14, 15, 117, 151).

[Ran+21] V. Ranjan et al. “Spatially-resolved decoherence of donor spins in silicon strained by a metallic electrode”. In: *arXiv:2101.04391 [cond-mat, physics:quant-ph]* (Jan. 2021) (cit. on pp. 146, 154).

[Rea+22] Alexander P. Read et al. *Precision measurement of the microwave dielectric loss of sapphire in the quantum regime with parts-per-billion sensitivity.* June 28, 2022. arXiv: `2206.14334[cond-mat,physics:quant-ph]` (cit. on p. 72).

[RHM65] L. G. Rowan, E. L. Hahn, and W. B. Mims. “Electron-Spin-Echo Envelope Modulation”. In: *Physical Review* 137.1 (Jan. 4, 1965), A61–A71 (cit. on p. 171).

[Riz+22] R. Rizzato et al. “Polarization Transfer from Optically Pumped Ensembles of N- V Centers to Multinuclear Spin Baths”. In: *Physical Review Applied* 17.2 (Feb. 2022), p. 024067 (cit. on pp. 2, 14, 175).

[Roy+18] Baptiste Royer et al. “Itinerant microwave photon detector”. In: *Physical review letters* 120.20 (2018), p. 203602 (cit. on p. 51).

[Rus+21] Andrei Ruskuc et al. “Nuclear spin-wave quantum register for a solid state qubit”. In: *arXiv:2108.12723 [quant-ph]* (Aug. 2021) (cit. on p. 179).

[Sag+15] Erhan Saglamyurek et al. “Quantum storage of entangled telecom-wavelength photons in an erbium-doped optical fibre”. In: *Nature Photonics* 9.2 (Feb. 2015), pp. 83–87 (cit. on p. 118).

[Sha+13] Shyam Shankar et al. “Autonomously stabilized entanglement between two superconducting quantum bits”. In: *Nature* 504.7480 (2013), p. 419 (cit. on p. 52).

[SJ01a] A. Schweiger and G. Jeschke. *Principles of pulse electron paramagnetic resonance.* Oxford University Press, 2001 (cit. on p. 117).

[SJ01b] Arthur Schweiger and Gunnar Jeschke. *Principles of pulse electron paramagnetic resonance.* Oxford University Press on Demand, 2001 (cit. on pp. 1, 13).

[Sli+15] K. M. Sliwa et al. “Reconfigurable josephson circulator/directional amplifier”. In: *Physical Review X* 5.4 (2015), pp. 1–10. arXiv: `1503.00209` (cit. on p. 52).

[Sli55] Charles P. Slichter. “Spin Resonance of Impurity Atoms in Silicon”. In: *Physical Review* 99.2 (July 1955), pp. 479–480 (cit. on pp. 2, 14).

[SMK15] Eyob A. Sete, John M. Martinis, and Alexander N. Korotkov. “Quantum theory of a bandpass Purcell filter for qubit readout”. In: *Phys. Rev. A* 92 (1 July 2015), p. 012325 (cit. on p. 48).

[Som+21] Aaron Somoroff et al. *Millisecond coherence in a superconducting qubit.* Mar. 15, 2021. arXiv: `2103.08578[cond-mat,physics:quant-ph]` (cit. on p. 28).

[Tam+12] T. H. Taminiau et al. “Detection and Control of Individual Nuclear Spins Using a Weakly Coupled Electron Spin”. In: *Physical Review Letters* 109.13 (Sept. 25, 2012), p. 137602 (cit. on pp. 10, 23, 123, 157, 159, 166, 174, 175).

[Tam+14] T. H. Taminiau et al. “Universal control and error correction in multi-qubit spin registers in diamond”. In: *Nature Nanotechnology* 9.3 (Mar. 2014), pp. 171–176 (cit. on p. 179).

[Thi+14] Stefan Thiele et al. “Electrically driven nuclear spin resonance in single-molecule magnets”. In: *Science* 344.6188 (June 2014), pp. 1135–1138 (cit. on p. 118).

[Vin+12] Romain Vincent et al. “Electronic read-out of a single nuclear spin using a molecular spin transistor”. In: *Nature* 488.7411 (Aug. 2012), pp. 357–360 (cit. on p. 118).

[Vio+02] D. Vion et al. “Manipulating the Quantum State of an Electrical Circuit”. In: *Science* 296.5569 (May 3, 2002), pp. 886–889 (cit. on p. 27).

[VKL99] Lorenza Viola, Emanuel Knill, and Seth Lloyd. “Dynamical Decoupling of Open Quantum Systems”. In: *Physical Review Letters* 82.12 (Mar. 22, 1999), pp. 2417–2421. arXiv: `quant-ph/9809071` (cit. on pp. 10, 23, 157).

[Wal+04] A. Wallraff et al. “Strong coupling of a single photon to a superconducting qubit using circuit quantum electrodynamics”. In: *Nature* 431.7005 (Sept. 2004), pp. 162–167 (cit. on p. 28).

[Wan+22] Chenlu Wang et al. “Towards practical quantum computers: transmon qubit with a lifetime approaching 0.5 milliseconds”. In: *npj Quantum Information* 8.1 (Jan. 13, 2022), pp. 1–6 (cit. on pp. 28, 77, 178).

[Wan+23] Zhiren Wang et al. *Single electron-spin-resonance detection by microwave photon counting*. Jan. 6, 2023. arXiv: `2301.02653[cond-mat,physics:quant-ph]` (cit. on pp. 9, 20, 79, 106, 144, 177).

[WB64] M. J. Weber and R. W. Bierig. “Paramagnetic Resonance and Relaxation of Trivalent Rare-Earth Ions in Calcium Fluoride. I. Resonance Spectra and Crystal Fields”. In: *Physical Review* 134.6 (June 15, 1964), A1492–A1503 (cit. on p. 121).

[WEH18] Stephanie Wehner, David Elkouss, and Ronald Hanson. “Quantum internet: A vision for the road ahead”. In: *Science* 362.6412 (Oct. 2018) (cit. on p. 51).

[Wei83] M. Weissbluth. *Atoms and Molecules Student Edition*. New York: Academic Press, 1983 (cit. on p. 118).

[Wra+93] J Wrachtrup et al. “Optical detection of magnetic resonance in a single molecule”. In: *Nature* 363 (1993), pp. 244–245 (cit. on p. 117).

[Xia+04] M. Xiao et al. “Electrical detection of the spin resonance of a single electron in a silicon field-effect transistor”. In: *Nature* 430.6998 (July 2004), pp. 435–439 (cit. on pp. 2, 14).

[Yon+18] Jun Yoneda et al. “A quantum-dot spin qubit with coherence limited by charge noise and fidelity higher than 99.9%”. In: *Nature Nanotechnology* 13.2 (Feb. 2018), pp. 102–106 (cit. on pp. 164, 190).

[Yos+96] Tetsuhiko Yoshimura et al. “In vivo EPR detection and imaging of endogenous nitric oxide in lipopolysaccharide-treated mice”. In: *Nature Biotechnology* 14.8 (Aug. 1996), pp. 992–994 (cit. on pp. 2, 13).

[YSH11] Tatsuro Yuge, Susumu Sasaki, and Yoshiro Hirayama. “Measurement of the Noise Spectrum Using a Multiple-Pulse Sequence”. In: *Physical Review Letters* 107.17 (Oct. 18, 2011), p. 170504 (cit. on pp. 164, 190).

[Zha+12] Nan Zhao et al. “Sensing single remote nuclear spins”. In: *Nature Nanotechnology* 7.10 (Oct. 2012), pp. 657–662 (cit. on p. 166).

université
PARIS-SACLAY

ÉCOLE DOCTORALE
Physique en
Île-de-France (PIF)

Titre : Résonance magnétique d'un spin électronique unique et de son environnement magnétique par comptage de photons

Mots clés : résonance magnétique, résonance de spin électronique, circuits supraconducteurs, fluorescence, compteur de photon micro-onde

Résumé : La résonance magnétique est une branche de la science qui vise à détecter les spins via leur absorption et émission de rayonnement électromagnétique. On distingue deux sous-branches : la Résonance Magnétique Nucléaire (RMN) qui s'applique aux spins atomiques et la Résonance Paramagnétique Electronique (RPE) qui s'applique aux spins électroniques non appariés. Dans les deux cas, les appareils commerciaux sont limités à la mesure de vastes ensembles de spins et ne fournissent que des moyennes de leur réponse collective. Dans cette thèse, nous réalisons la RPE d'ion Erbium individuels insérés dans un cristal de scheelite en utilisant une nouvelle méthode de détection basée sur la fluorescence micro-onde émise par les spins pendant leur relaxation. Pour favoriser l'émission de photon, les spins sont couplés à un résonateur supraconducteur ayant un petit volume de mode et de faibles pertes, générant un effet Purcell. La sortie du résonateur est connectée à un compteur de photon micro-onde basé sur un qubit supraconducteur et un mélange à 4 ondes. La grande sensibilité de ce détecteur $\mathcal{S} = 10^{-22}\ \mathrm{W}/\sqrt{\mathrm{Hz}}$ est une des clés de la réussite de cette expérience. Notre méthode s'applique à tous types d'impuretés paramagnétiques sans nécessiter une transition optique ni un grand temps de cohérence. Nous mesurons les caractéristiques de plusieurs spins individuels, les résultats varient fortement d'un spin à l'autre, mettant en avant l'inhomogénéité de leurs environnements électromagnétiques. Les temps de cohérence atteignent plusieurs millisecondes et sont limités radiativement. Finalement, nous réalisons une expérience visant à sonder l'environnement magnétique d'une impureté particulière grâce à une séquence de découplage dynamique. Le signal à résonance nous permet de mettre en évidence la présence de spin nucléaire de $^{183}\mathrm{W}$. Nous émettons finalement quelques hypothèses préliminaires sur leur disposition autour de l'ion erbium étudié.

Title : Magnetic resonance of a single electron spin and its magnetic environment by photon counting

Keywords : magnetic resonance, electron spin resonance, superconducting circuits, fluorescence, single microwave photon detector

Abstract : Magnetic resonance is a branch of science that aims to detect spins via their absorption and emission of electromagnetic radiation. There are two sub-branches : Nuclear Magnetic Resonance (NMR), which applies to atomic spins, and Electronic Paramagnetic Resonance (EPR), which applies to unpaired electron spins. In both cases, commercial instruments are limited to measuring large ensembles of spins and only provide averages of their collective response. In this thesis, we perform EPR of individual Erbium ions inserted in a scheelite crystal using a new detection method based on the microwave fluorescence emitted by the spins during their relaxation. To promote photon emission, the spins are coupled to a superconducting resonator with a small mode volume and low losses, generating a Purcell effect. The output of the resonator is connected to a microwave photon detector based on a superconducting qubit and a 4-wave micing. The high sensitivity of this detector $\mathcal{S} = 10^{-22}\ \mathrm{W}/\sqrt{\mathrm{Hz}}$ is one of the keys to the success of this experiment. Our method is applicable to all types of paramagnetic impurities without requiring an optical transition or a large coherence time. We measure the characteristics of several individual spins, the results vary strongly from one spin to another, highlighting the inhomogeneity of their electromagnetic environments. The coherence times reach several milliseconds and are radiatively limited. Finally, we perform an experiment to probe the magnetic environment of a particular impurity using a dynamic decoupling sequence. The resonance signal allows us to demonstrate the presence of $^{183}\mathrm{W}$ nuclear spin. We finally make some preliminary hypotheses on their arrangement around the erbium ion studied.